UNIVERSITAT DE BARCELONA

A Comprehensive Validation of Global Precipitation Measurement Satellite Products Over a Western Mediterranean Region

Eric Peinó Calero

DOCTORAL DISSERTATION

A Comprehensive Validation of Global Precipitation Measurement Satellite Products Over a Western Mediterranean Region

Author:

Eric Peinó Calero

Supervised by:

Dr. Joan Bech Rustullet

Dra. Mireia Udina Sistach

LIBERTAS PERFVNDET · OMNIA LVCE

UNIVERSITAT DE BARCELONA

A Comprehensive Validation of Global Precipitation Measurement Satellite Products Over a Western Mediterranean Region

Memoria presentada para optar al grado de Doctor por la Univeristat de Barcelona

Programa de Doctorado en Física

Autor:

Eric Peinó Calero

Directores:

Dr. Joan Bech Rustullet

Dra. Mireia Udina Sistach

Tutor:

Dr. Joan Bech Rustullet

Barcelona, Septiembre de 2024

UNIVERSITAT DE BARCELONA

"...Caminante, no hay camino, se hace camino al andar..."

—Antonio Machado

Acknowledgements

Han pasado 3 años y algunos meses desde que llegué a esta increíble ciudad y “sin quitarme el polvo del camino” empezar una etapa que me enseñaría aún más los tantos matices de la vida. Una de las mejores cosas de hacer una tesis (y lo digo porque esta es la tercera y espero la última) es que puedes hacer balance y te permite agradecer muy humildemente a algunos de los que han hecho mejor tu camino.

- Vull donar un agraïment especial als meus directors Joan i Mireia, per donar-me l’oportunitat i el suport per continuar amb el meu propòsit. Per la seva ajuda i atenció en tot moment, pels bons consells i per l’alè i l’ànim que tant fan falta. Des del punt de vista professional, impecables, però personalment encara millors. La meva gratitud, confiança i lleialtat són amb vosaltres per sempre.
- Quiero agradecer a todos los del Grupo Meteo especialmente: Javi (eres genial, mejor persona), Francesc, Laura, Mario, Eulalia, Yolanda, Carmen, Montse, Marta y Raúl. Siempre amables, con buena conversación y dispuestos a ayudar.
- Quiero agradecer a los profesionales del CNR-ISAC que me recibieron y brindaron su ayuda durante 3 meses de mi estancia en Roma, especialmente a Marco y a Elisa.
- A Sergi y a Enric por su colaboración y su rápida respuesta cuando solicité de su ayuda.

"... Questo posto è maledetto. Vattene, vattene e non tornare più. E se un giorno ti prende la nostalgia e decidi di tornare, non cercarmi. Non bussare alla mia porta, perché non ti aprirò. Cerca qualcosa che ami con passione, e qualunque cosa fai, amala... "

—Alfredo (Philippe Noiret) en Cinema Paradiso

Alejarte de tu familia, de tu tierra, de tu casa, nunca es fácil, pero siempre hay algo más grande.

- A mi mamá, mi papá, mi Tata y a mi abuela. Nunca la frase "estar lejos" ha resultado tan inútil en sí misma. Nunca había dejado de cumplir tanto su propósito. Simpre juntos. Gracias por caminar conmigo!
- A mi abuelo por estar al pie del cañón por no descansar nunca.
- A mi tío (te prometo que ya es el último) y a mi tía Cosette por estar siempre ahí y salvarnos tantas veces.
- A mi otro hermano. Una vez más y 7 años después de la última vez que lo dije, gracias por vivir juntos los momentos más importantes de nuestras vidas.

- A Armando, siempre es un alivio saber que estás.
- A mis primas-hermanas, Gracias!!
- A Sandra por complementar mi familia.
- A mi Lauri por salvarme. Eres el vivo ejemplo de mis mejores elecciones.
- A Alejandro, mi otro hermano, y a Imi. Hay veces que el tiempo no cambia nada.
- A mi Bea que siempre está.
- A Marien y a Enrique. Los buenos amigos siempre aparecen.
- A mi gente de la Resistencia: Alejandro, Jesús, Lyex y Diana (estos agradecimientos son de mi tesis DOCTORAL, no es de máster). Una pequeña familia, con todo lo que eso incluye.
- A mis amigos de la universidad, siempre se los debo.
- Al resto de mi familia y amigos, que afortundamente no son pocos.

A todos, Mi Corazón!

I would like to acknowledge the support from the Secretariat for Universities and Research of the Ministry of Business and Knowledge of the Government of Catalonia, and the European Social Fund. In addition, this research was supported by the projects WISE-PreP (RTI2018-098693-B-C32), ARTEMIS (PID2021-124253OB-I00) and PANDORA (PDC2022-133207-I00). We would like to thank the Water Research Institute (IdRA) of the University of Barcelona and Observatory Fabra of the Royal Academy of Sciences and Arts of Barcelona. I am also grateful to the Montcelimar Foundation for funding my research stay and to the Institute of Atmospheric Sciences and Climate (CNR-ISAC) for hosting me. Finally, this work has been made possible thanks to the data provided by NASA/JAXA, the Meteorological Service of Catalonia, the Spanish Meteorological Agency (AEMET), and the European Organisation for the Exploitation of Meteorological Satellites (EUMETSAT), which has played a key role over the years through various training courses and workshops.

Summary

Quantitative precipitation estimation is not only essential for understanding atmospheric processes, but also a key factor in water resource management, weather forecasting, and climate modeling. Advances in remote sensing have enabled significant progress in this area, with satellite systems providing near-continuous global precipitation coverage, including remote and oceanic regions where other methods prove insufficient. The Global Precipitation Measurement (GPM) mission, using an international constellation of satellites, aims to enhance our understanding of the Earth's water cycle and energy balance. This mission represents one of the most comprehensive and accurate efforts to quantify precipitation on a global scale. Since its launch in 2014, the mission's derived products have undergone continuous updates to improve their retrieval algorithms. This, combined with the complexity of Mediterranean regions—characterized by high climate variability and significant uncertainties in precipitation projections—makes rigorous validation of these products crucial.

Accordingly, this study aims at performing a comprehensive validation of GPM products in a Western Mediterranean region. The research is structured around six specific objectives:

SO1. **To evaluate the precipitation estimates from the three Integrated Multi-satellitE Retrievals for GPM (IMERG) runs (Early, Late, and Final) at various temporal scales (half-hourly, hourly, daily, monthly, seasonal, and annual).**

SO2. **To analyze the IMERG estimates at the highest temporal resolution (30 minutes), considering different orographic features, climatic conditions, and precipitation intensity thresholds.**

SO3. **To quantify the errors associated with IMERG in estimating heavy rainfall events at daily and sub-daily scales, to identify and address sources of error.**

SO4. **To investigate the impact of the contribution of different sensors to IMERG retrievals and their linkage to microphysical properties of precipitating cloud tops, with a focus on estimating heavy rainfall events.**

SO5. **To compare the performance of three Operational Hydrology and Water Management (H SAF) products and the Early and Late versions of IMERG in estimating extreme precipitation events at hourly and daily scales.**

SO6. **To evaluate the precipitation intensity, radar reflectivity factors, and drop size distribution (DSD) parameters of GPM's Dual-frequency Precipitation Radar (DPR) Level 2 version 07B considering a network of disdrometers.**

This doctoral thesis, structured into three fundamental parts, addresses the main objectives of the research based on three scientific publications and a preprint. The narrative of the thesis begins with a direct validation of the IMERG runs, one of the key products of the GPM mission, at multiple temporal scales. It continues with the quantification of the errors in detecting intense rainfall events in the Mediterranean region, also considering the impact of the precipitating cloud top phase on satellite retrievals. A comparison with H SAF mission products is included, and the errors in the retrievals of extreme events are quantified using 18 case studies. Finally, the rain estimates and drop size distributions derived from the GPM Dual-frequency Precipitation Radar (DPR) are validated.

Although in recent years the number of validation studies for GPM and its derived products has increased, many of them had recurrent shortcomings, such as the lack of evaluations at sub-daily scales or in mountainous regions under different climatic regimes and/or considering precipitation intensity. Accordingly, the first part of the thesis focuses on evaluating the precipitation estimates of the three IMERG runs (Early, Late, and Final) at various temporal scales, including half-hourly, in the Catalonia region. A dense network of automatic stations from the Meteorological Service of Catalonia, covering the 2015-2020 period, was used as reference data. While Early and Late runs of IMERG overestimate precipitation, IMERG Final reduces the error at all temporal scales. However, the calibration to which a Final run is subjected causes underestimation in some areas, such as the Pyrenees mountains. The proportion of false alarms is a problem for IMERG, especially during the summer, mainly associated with the detection of false precipitation in the form of light rainfall. At sub-daily scales, IMERG showed high bias and very low correlation values, indicating the remaining challenge for satellite retrievals to estimate precipitation at high temporal resolution. This behaviour is more evident in flat areas and cold semi-arid climates, wherein overestimates of more than 30% were found. In contrast, rainfall classified as very heavy and torrential showed significant underestimates, higher than 80%, reflecting the inability of IMERG to detect extreme sub-daily precipitation events.

Building on this investigation, the study continued, this time focusing on IMERG products with lower latency in their outputs (Early and Late), to evaluate retrievals associated with extreme precipitation events. The validation strategy also sought to identify the contribution of different sensors (IR and PMW) involved in IMERG retrievals. Subsequently, the results were stratified according to their relationship with the microphysical properties of precipitating clouds, using data from the Nowcasting and Very Short-Range Forecasting (NWC) Satellite Application Facility (SAF) of the European Organisation for the Exploitation of Meteorological Satellites (EUMETSAT). The results showed a marked tendency to underestimate precipitation compared to rain gauges which increases with rainfall intensity and temporal resolution. A weaker negative bias was also found for retrievals with PMW, an increased bias when filling PMW gaps by including IR information, and an improved performance in the presence of precipitating ice clouds compared to warm and mixed-phase clouds. In line with these studies, the second part of this research analyzed 18 extreme precipitation cases in Catalonia and compared IMERG retrievals with various products from the Support to Operational Hydrology and Water Management (H SAF) program managed by EUMETSAT, including, among others, products H64 and H68. These studies employed a pixel-to-point comparison method to reduce uncertainties associated with comparing satellite data obtained on a regular grid with point-scale observations from rain gauges. The results showed that while all satellite products tend to overestimate observed precipitation, H64 performs best at the daily scale, and H68 stands out in hourly detection. However, the accuracy of all products significantly decreases with increasing precipitation intensity, with H68 exhibiting the largest errors in high-intensity events. Despite significant biases, the IMERG Late product proved to be the most effective in detecting intense precipitation events. This study offers critical insights into their comparative performance, enhancing their application in hydrometeorological management and disaster response.

Finally, the GPM Core satellite Dual-frequency Precipitation Radar, one of the few instruments currently providing spaceborne three-dimensional precipitation field observations, was evaluated. Unlike the rest of the studies where precipitation level 3 products are taken, in this analysis the limited GPM CO overpasses over a given region play a fundamental role, which implies a low probability of coincidence with the observation of precipitation over the disdrometer sites. This analysis included retrievals of precipitation intensity, radar reflectivity factor (Ka and Ku bands), and drop size distribution parameters such as intercept parameter (N_w), shape parameter (μ), and mass-weighted mean diameter (D_m), all obtained from version 07, the latest available. Seven OTT Parsivel disdrometers, located in various topographic areas of the Western Mediterranean between 2014 and 2023, were used as ground references. Four spatial comparison techniques were applied between satellite estimates and surface observations, using both continuous and categorical statistics to quantify associated errors. Overall, GPM DPR products captured the variability of the observed DSD well at different rainfall intensities. However, overestimation of the mean D_m and underestimation of the mean N_w were observed, being much more sensitive to errors in drop diameters larger than 1.5 mm. Moreover, the lowest errors were found for radar reflectivity factor and D_m, and the highest for N_w and rainfall rate. In addition, the GPM DPR convective and stratiform classification was tested, and a substantial overestimation of stratiform cases compared to disdrometer observations were found.

This research represents one of the first studies in the Iberian Peninsula to validate IMERG products with a detailed focus on orographic, climatic, and precipitation intensity factors at high temporal resolution. The comparison with H SAF products and the evaluation of the latest updates to version 7 of the DPR expands the scope of validation and lays the groundwork for future research on the use of satellite data in precipitation estimation.

Resumen

La estimación cuantitativa de la precipitación no solo es esencial para comprender los procesos atmosféricos, sino que también es un factor clave en la gestión de recursos hídricos, la previsión meteorológica y la modelización climática. Los avances en la teledetección han permitido un progreso significativo en esta área, con sistemas satelitales que proporcionan una cobertura casi continua y global de las precipitaciones, incluyendo zonas remotas y oceánicas donde otros métodos resultan insuficientes. La misión Global Precipitation Measurement (GPM), usando una constelación internacional de satélites, tiene como objetivo mejorar nuestra comprensión del ciclo del agua y el balance energético de la Tierra. Esta misión representa uno de los esfuerzos más completos y precisos para cuantificar la precipitación a escala global. Desde su lanzamiento en 2014, los productos derivados de la misión han experimentado actualizaciones constantes para mejorar sus algoritmos de estimación. Esto, sumado a la complejidad en las regiones mediterráneas, caracterizadas por una alta variabilidad climática y grandes incertidumbres en las proyecciones de precipitación, hace que la validación rigurosa de estos productos sea crucial.

De acuerdo con lo planteado, este estudio está orientado a realizar una validación exhaustiva de los productos del GPM en una región del Mediterráneo occidental. La investigación se estructura en torno a seis objetivos específicos:

SO1. **Evaluar las estimaciones de precipitación de las tres ejecuciones del Integrated Multi-satellitE Retrievals for GPM (IMERG: Early, Late y Final) en diversas escalas temporales (semi-horaria, horaria, diaria, mensual, estacional y anual)**

SO2. **Analizar las estimaciones de IMERG a la mayor resolución temporal (30 minutos), teniendo en cuenta distintas características orográficas, condiciones climáticas y umbrales de intensidad de precipitación.**

SO3. **Cuantificar los errores asociados con IMERG en la estimación de eventos de lluvia intensa en escalas diarias y subdiarias, identificando las fuentes de error.**

SO4. **Investigar la contribución de los distintos sensores en las estimaciones de IMERG y su relación con las propiedades microfísicas de las nubes precipitantes, centrándose en la estimación de eventos de lluvia intensa.**

SO5. **Comparar el rendimiento de tres productos del programa H SAF y las versiones Early y Late de IMERG en la estimación de eventos de precipitación extrema a escalas horarias y diarias.**

SO6. **Evaluar la intensidad de la precipitación, el factor de reflectividad radar y los parámetros de la distribución del tamaño de gotas (DSD) del Dual-Frequency Precipitation Radar (DPR) de GPM, utilizando una red de disdrómetros.**

Esta tesis doctoral, estructurada en tres partes fundamentales, aborda los principales objetivos de la investigación basados en tres publicaciones científicas y un *preprint*. La narrativa de la tesis comienza con una validación directa de las ejecuciones de IMERG, uno de los productos clave de la misión GPM, a múltiples escalas temporales. Continúa con la cuantificación de los errores de estos productos en la detección de eventos de lluvia intensa en la región mediterránea, considerando además el impacto de la fase del tope de las nubes que precipitan en las estimaciones satelitales. Se incluye una comparación con productos de la misión H SAF y se cuantifican los errores en las recuperaciones de eventos extremos tomando 18 casos de estudio. Finalmente, se validan las estimaciones de lluvia y las distribuciones del tamaño de gotas derivadas del Dual-Frequency Precipitation Radar (DPR) a bordo del GPM.

Aunque en los últimos años ha aumentado el número de estudios de validación del GPM y sus productos derivados, muchos de ellos presentaban deficiencias recurrentes, como la falta de evaluaciones a escalas subdiarias o en regiones montañosas bajo distintos regímenes climáticos y/o teniendo en cuenta la intensidad de las precipitaciones. A partir de ello, la primera parte de la tesis se centra en la evaluación de las estimaciones de precipitación de las tres ejecuciones de IMERG (Early, Late y Final) a diversas escalas temporales, incluida la semi-horaria, en la región de Cataluña. Como datos de referencia, se utilizó una red densa de estaciones automáticas del Servicio Meteorológico de Cataluña, abarcando el período 2015-2020. Mientras que las ejecuciones Early y Late de IMERG sobreestiman la precipitación, IMERG Final reduce el error en todas las escalas temporales. Sin embargo, la calibración a la que se somete la ejecución Final provoca una subestimación en zonas de montaña como los Pirineos. La proporción de falsas alarmas es un problema para IMERG, especialmente durante el verano, asociado principalmente a la detección de falsas precipitaciones en forma de lluvia débil. A escalas subdiarias, IMERG mostró un sesgo elevado y valores de correlación muy bajos, lo que indica el reto que aún tienen los sensores de satélite para estimar la precipitación a alta resolución temporal. Este comportamiento es más evidente en zonas llanas y climas semiáridos fríos, donde se encontraron sobreestimaciones de más del 30%. Por el contrario, las precipitaciones clasificadas como muy fuertes y torrenciales mostraron subestimaciones significativas, superiores al 80%, lo que refleja la incapacidad de IMERG para detectar eventos extremos de precipitación subdiaria.

A partir de esta investigación, se continuó el estudio, esta vez centrado en los productos IMERG con menor latencia en sus salidas (Early y Late), para evaluar las recuperaciones asociadas a eventos extremos de precipitación. La estrategia de validación también buscó identificar la contribución de los diferentes sensores (IR y PMW) que participan en las recuperaciones de IMERG. Posteriormente, los resultados se estratificaron según su relación con las propiedades microfísicas de las nubes precipitantes, utilizando datos del Support to Nowcasting and Very Short Range Forecasting (NWC) Satellite Application Facility (SAF) de la Organización Europea para la Explotación de Satélites Meteorológicos (EUMETSAT por sus siglas en inglés). Los resultados mostraron una marcada tendencia a subestimar la precipitación en comparación con los pluviómetros que aumenta con la intensidad de la precipitación y la resolución temporal, un sesgo negativo más débil para las estimaciones con datos de PMW, un sesgo mayor cuando se rellenan los huecos de PMW incluyendo información IR, y un mejor rendimiento en presencia de nubes de hielo precipitantes en comparación con las nubes cálidas y de fase mixta. En línea con estos estudios, la segunda parte de esta investigación analizó 18 casos de precipitación extrema en Cataluña y comparó las estimaciones IMERG con varios productos del programa de Apoyo a la Hidrología Operativa y la Gestión del Agua (H SAF, por sus siglas en inglés) gestionado por EUMETSAT, incluyendo, entre otros, los productos H64 y H68. Estos estudios emplearon un método de comparación píxel a punto para reducir las incertidumbres asociadas a la comparación de datos de satélite obtenidos en una cuadrícula regular con observaciones a escala de punto procedentes de pluviómetros. Los resultados mostraron que, si bien todos los productos satelitales tienden a sobreestimar la precipitación observada, el H64 obtiene los mejores resultados a escala diaria, y el H68 destaca en la detección horaria. Sin embargo, la precisión de todos los productos disminuye significativamente con el aumento de la intensidad de la precipitación, siendo el H68 el que presenta mayores errores en eventos de alta intensidad. A pesar de los importantes sesgos, el producto IMERG Late demostró ser el más eficaz en la detección de eventos de precipitación intensa. Este estudio ofrece una visión crítica de su rendimiento comparativo, mejorando su aplicación en la gestión hidrometeorológica y la respuesta a catástrofes.

Finalmente, se evaluó el Dual-Frequency Precipitation Radar a bordo del satélite GPM Core (CO), uno de los pocos instrumentos satelitales que actualmente proporciona observaciones tridimensionales de los campos de precipitación. A diferencia del resto de estudios en los que se toman productos de precipitación de nivel 3, en este análisis juegan un papel fundamental el limitado nombre de sobrevuelos del GPM CO sobre una región determinada, lo que implica una baja probabilidad de coincidencia con la observación de precipitación sobre los emplazamientos de los disdrómetros. Este análisis incluyó las estimaciones de la intensidad de la precipitación, el factor de reflectividad del radar (en banda Ka y Ku) y parámetros de la distribución del tamaño de gotas como el parámetro de intercepción (N_w), el parámetro de forma (μ), y el diámetro medio ponderado (D_m), todos obtenidos de la versión 07, la más reciente disponible. Para ello, se utilizaron observaciones de siete disdrómetros OTT Parsivel ubicados en diversas zonas topográficas del Mediterráneo occidental entre 2014 y 2023. Mediante cuatro técnicas de comparación espacial entre las estimaciones por satélite y las observaciones en superficie, se aplicaron tanto estadísticos continuos como categóricos para cuantificar los errores asociados. En general, los productos GPM DPR capturaron bien la variabilidad de la DSD observada en diferentes intensidades de precipitación. Sin embargo, se observó una sobreestimación de la D_m media y una subestimación de la N_w media siendo mucho más sensibles a los errores en los diámetros de gota superiores a 1.5 mm. Los errores más bajos se encontraron para el factor de reflectividad del radar y D_m, y los más altos para N_w e intensidad de precipitación. Además, se evaluó la clasificación convectiva y estratiforme del GPM DPR, y se encontró una sobreestimación sustancial de los casos estratiformes en comparación con las observaciones del disdrómetro.

Esta investigación representa uno de los primeros estudios en la península Ibérica que valida los productos de IMERG con un enfoque detallado en factores orográficos, climáticos y de intensidad de precipitación, a alta resolución temporal. La comparación con productos del programa H SAF y la evaluación de las actualizaciones más recientes de la versión 7 del DPR amplía el ámbito de la validación y sienta las bases para futuras investigaciones sobre el uso de datos satelitales en la estimación de la precipitación.

Resum

L'estimació quantitativa de la precipitació no només és essencial per comprendre els processos atmosfèrics, sinó que també és un factor clau en la gestió de recursos hídrics, la previsió meteorològica i la modelització climàtica. Els avenços en la teledetecció han permès un progrés significatiu en aquesta àrea, amb sistemes satel·litaris que proporcionen una cobertura gairebé contínua i global de les precipitacions, incloent zones remotes i oceàniques on altres mètodes resulten insuficients. La missió Global Precipitation Measurement (GPM), usant una constel·lació internacional de satèl·lits, té com a objectiu millorar la nostra comprensió del cicle de l'aigua i el balanç energètic de la Terra. Aquesta missió representa un dels esforços més complets i precisos per quantificar la precipitació a escala global. Des del seu llançament el 2014, els productes derivats de la missió han experimentat actualitzacions constants per millorar els seus algorismes de recuperació. Això, sumat a la complexitat de les regions mediterrànies, caracteritzades per una alta variabilitat climàtica i grans incerteses en les projeccions de precipitació, fa que la validació rigorosa d'aquests productes sigui crucial.

D'acord amb això, aquest estudi està orientat a realitzar una validació exhaustiva dels productes del GPM en una regió del Mediterrani occidental. La investigació s'estructura al voltant de sis objectius específics:

SO1. **Avaluar les estimacions de precipitació de les tres execucions de l'Integrated Multi-satellitE Retrievals for GPM (IMERG: Early, Late i Final) a diverses escales temporals (semi-horària, horària, diària, mensual, estacional i anual).**

SO2. **Analitzar les estimacions d'IMERG a la màxima resolució temporal (30 minuts), tenint en compte diferents característiques orogràfiques, condicions climàtiques i llindars d'intensitat de precipitació.**

SO3. **Quantificar els errors associats amb IMERG en l'estimació d'esdeveniments de pluja intensa a escales diàries i subdiàries, identificant les fonts d'error.**

SO4. **Investigar la contribució dels diferents sensors en les estimacions d'IMERG i la seva relació amb les propietats microfísiques dels núvols precipitants, centrant-se en l'estimació d'esdeveniments de pluja intensa.**

SO5. **Comparar el rendiment de tres productes del programa H SAF i les versions Early i Late d'IMERG en l'estimació d'esdeveniments de precipitació extrema a escales horàries i diàries.**

SO6. **Avaluar la intensitat de la precipitació, el factor de reflectivitat radar i els paràmetres de la distribució de la mida de les gotes (DSD) del Dual-Frequency Precipitation Radar (DPR) de GPM, utilitzant una xarxa de disdròmetres.**

Aquesta tesi doctoral, estructurada en tres parts fonamentals, aborda els principals objectius de la investigació basats en tres publicacions científiques i un *preprint*. La narrativa de la tesi comença amb una validació directa de les execucions d'IMERG, un dels productes clau de la missió GPM, a múltiples escales temporals. Continua amb la quantificació dels errors d'aquests productes en la detecció d'esdeveniments de pluja intensa a la regió mediterrània, considerant a més l'impacte de la fase del cim dels núvols que precipiten en les recuperacions satel · litàries. S'inclou una comparació amb productes de la missió H SAF i es quantifiquen els errors en les estimacions d'esdeveniments extrems prenent 18 casos d'estudi. Finalment, es validen les estimacions de pluja i les distribucions de la mida de les gotes derivades del Dual-frequency Precipitation Radar (DPR) de GPM.

Tot i que en els darrers anys ha augmentat el nombre d'estudis de validació del GPM i els seus productes derivats, molts d'ells presentaven mancances recurrents, com la manca d'avaluacions a escales subdiàries o en regions muntanyoses sota diferents règims climàtics i/o tenint en compte la intensitat de les precipitacions. A partir d'això, la primera part de la tesi se centra en l'avaluació de les estimacions de precipitació de les tres execucions d'IMERG (Early, Late i Final) a diverses escales temporals, inclosa la semi-horària, a la regió de Catalunya. Com a dades de referència, es va utilitzar la xarxa densa d'estacions automàtiques del Servei Meteorològic de Catalunya, que abasten el període 2015-2020. Mentre que les execucions Early i Late d'IMERG sobreestimen la precipitació, IMERG Final redueix l'error en totes les escales temporals. No obstant això, el calibratge al qual es sotmet l'execució Final provoca una subestimació en zones de muntanya com els Pirineus. La proporció de falses alarmes és un problema per a IMERG, especialment durant l'estiu, associat principalment a la detecció de falses precipitacions en forma de pluja feble. A escales subdiàries, IMERG va mostrar un biaix elevat i valors de correlació molt baixos, cosa que indica el repte que encara tenen els sensors de satèl · lit per estimar la precipitació a alta resolució temporal. Aquest comportament és més evident en zones planes i climes semiàrids freds, on es van trobar sobreestimacions de més del 30%. Per contra, les precipitacions classificades com molt fortes i torrencials van mostrar subestimacions significatives, superiors al 80%, cosa que reflecteix la incapacitat d'IMERG per detectar esdeveniments extrems de precipitació subdiària.

A partir d'aquesta investigació, es va continuar l'estudi, aquesta vegada centrat en els productes IMERG amb menor latència en les seves sortides (Early i Late), per avaluar les estimacions associades a esdeveniments extrems de precipitació. L'estratègia de validació també va buscar identificar la contribució dels diferents sensors (IR i PMW) que participen en les estimacions d'IMERG. Posteriorment, els resultats es van estratificar segons la seva relació amb les propietats microfísiques dels núvols precipitants, utilitzant dades del Support to Nowcasting and Very Short Range Forecasting (NWC) Satellite Application Facility (SAF) de l'Organització Europea per a l'Explotació de Satèl · lits Meteorològics (EUMETSAT per les seves sigles en anglès). Els resultats van mostrar una marcada tendència a subestimar la precipitació en comparació amb els pluviòmetres que augmenta amb la intensitat de la precipitació i la resolució temporal, un biaix negatiu més feble per a les recuperacions amb dades de PMW, un biaix major quan es reomplen els buits de PMW incloent-hi informació IR, i un millor rendiment en presència de núvols de gel precipitants en comparació amb els núvols càlids i de fase mixta. En línia amb aquests estudis, la segona part d'aquest estudi va analitzar 18 casos de precipitació extrema a Catalunya i va comparar les recuperacions d'IMERG amb diversos productes del programa de Suport a la Hidrologia Operativa i la Gestió de l'Aigua (H SAF, per les seves sigles en anglès) gestionat per EUMETSAT, incloent, entre d'altres, els productes H64 i H68. Aquests estudis van utilitzar un mètode de comparació píxel a punt per reduir les incerteses associades a la comparació de dades de satèl · lit obtingudes en una quadrícula regular amb observacions a escala de punt procedents de pluviòmetres. Els resultats van mostrar que, tot i que tots els productes satel · litaris tendeixen a sobreestimar la precipitació observada, l'H64 obté els millors resultats a escala diària, i l'H68 destaca en la detecció horària. No obstant això, la precisió de tots els productes disminueix significativament amb l'augment de la intensitat de la precipitació, sent l'H68 el que presenta més errors en esdeveniments d'alta intensitat. Tot i els importants biaixos, el producte IMERG Late va demostrar ser el més eficaç en la detecció d'esdeveniments de precipitació intensa. Aquest estudi ofereix una visió crítica del seu rendiment comparatiu, millorant la seva aplicació en la gestió hidrometeorològica i la resposta a catàstrofes.

Finalment, es va avaluar el Dual-Frequency Precipitation Radar a bord del satèl · lit GPM Core (CO), un dels pocs instruments satel · litaris que actualment proporciona observacions tridimensionals dels camps de precipitació. A diferència de la resta d'estudis en què es prenen productes de precipitació de nivell 3, en aquesta recerca juguen un paper fonamental el limitat nombre de sobrevols del GPM CO sobre una regió determinada, cosa que implica una baixa probabilitat de coincidència amb l'observació de precipitació sobre els emplaçaments dels disdròmetres. Aquesta anàlisi va incloure les recuperacions de la intensitat de la precipitació, el factor de reflectivitat del radar (en banda Ka i Ku) i paràmetres de la distribució de la mida de les gotes com el paràmetre d'intercepció (N_w), el paràmetre de forma (μ) i el diàmetre mitjà ponderat (D_m), tots obtinguts de la versió 07, la més recent disponible. Per a això, es van utilitzar observacions de set disdròmetres OTT Parsivel ubicats en diverses zones topogràfiques del Mediterrani occidental entre 2014 i 2023. Mitjançant quatre tècniques de comparació espacial entre les estimacions per satèl · lit i les observacions en superfície, es van aplicar tant estadístics continus com categòrics per quantificar els errors associats. En general, els productes GPM DPR van capturar bé la variabilitat de la DSD observada en diferents intensitats de precipitació. No obstant això, es va observar una sobreestimació de la D_m mitjana i una subestimació de la N_w mitjana, sent molt més sensibles als errors en els diàmetres de gota superiors a 1.5 mm. Els errors més baixos es van trobar per al factor de reflectivitat del radar i D_m, i els més alts per a N_w i la intensitat de precipitació. A més, es va avaluar la classificació convectiva i estratiforme del GPM DPR, i es va trobar una sobreestimació substancial dels casos estratiformes en comparació amb les observacions del disdròmetre.

Aquesta investigació representa un dels primers estudis a la península Ibèrica que valida els productes d'IMERG amb un enfocament detallat en factors orogràfics, climàtics i d'intensitat de precipitació, a alta resolució temporal. La comparació amb productes del programa H SAF i l'avaluació de les actualitzacions més recents de la versió 7 del DPR amplia l'àmbit de la validació i posa les bases per a futures investigacions sobre l'ús de dades satel · litàries en l'estimació de la precipitació.

Contents

Acknowledgements **iii**

List of Figures **xxi**

List of Tables **xxiii**

Acronyms **xxv**

1 Introduction **1**

1.1 Precipitation Characteristics 1

1.2 Observing Global Precipitation. Quantitative Precipitation Estimation 2

1.2.1 Satellite precipitation measurements (LEO observing systems, GEO observing systems) 5

1.2.2 Precipitation retrievals 7

1.2.3 Satellite Precipitation Products 9

1.2.4 Limitations and Errors 11

1.3 Global Precipitation Measurement Mission 12

1.3.1 Satellite Sensors and Characteristics 14

1.3.2 GPM Constellation 15

1.3.3 IMERG products 16

1.3.4 Applications 18

1.3.5 Validation and Comparison 19

2 Objectives **21**

2.1 Motivation 21

2.2 General Objective 22

2.3 Specific Objectives 23

2.4 Structure of the thesis 24

3 Multiscale Direct Validation: Effective Temporal Resolution of IMERG **27**

3.1 Performance Assessment of GPM IMERG Products at Different Time Resolutions, Climatic Areas and Topographic Conditions in Catalonia 27

3.1.1 Summary 27

3.1.2 Article 28

4 Detection of Heavy Rainfall in the Mediterranean Area: Impact of Cloud Top Phase on Spaceborne Precipitation Estimation **51**
4.1 Disentangling Satellite Precipitation Estimate Errors of Heavy Rainfall at the Daily and Sub-Daily Scales in the Western Mediterranean 51
4.1.1 Summary 51
4.1.2 Article 51
4.2 Intercomparison of HSAF and IMERG satellite precipitation products over a Mediterranean coastal region 75
4.2.1 Summary 75
4.2.2 Preprint Article 75

5 Physical validation **103**
5.1 Validation of GPM DPR rainfall and Drop Size Distributions using disdrometer observations in the Western Mediterranean 103
5.1.1 Summary 103
5.1.2 Article 104

6 Conclusions **129**
6.1 Original Contributions 129
6.2 Key Findings 129
6.3 Main research limitations 132
6.4 Future Perspectives 133

References **145**

A Contributions **147**
A.1 Peer-reviewed Papers 147
A.2 Research Stays 147
A.3 Conference presentations 148
A.4 Posters 149
A.5 Relevant Training Courses 149
A.6 Teaching 150

List of Figures

1.1 Representation of the global water cycle: (A) stores (in thousands of km^3) and (B) flows (thousands of km^3 per year) (Allan et al., 2020). 1

1.2 Global maps of GPCC gauge density (version 2022) for July 2024. Source: Oficial GPCC web page, https://kunden.dwd.de/GPCC/Visualizer 3

1.3 (a) Disdrometer (OTT Parsivel 2) located in Cendrosa, Catalonia during the LIASE Campaign (2021) (b) Conceptual model illustrating the dominant mechanisms for the six groups objectively determined from the surface disdrometers using Principal component analysis (PCA) in $logN_w - D_0$ space (Note that N$_w$ is the normalized intercept parameter and D_0 is median drop diameters) (Dolan et al., 2018) 4

1.4 Weather radar global coverage (assumed 200 km range for each radar (Saltikoff et al., 2019) 4

1.5 A timeline of several missions together with the relevance of their radar operating bands to the detection of clouds and precipitation, modified from Battaglia et al. (2020) 6

1.6 (a) Global Precipitation Measurement Core Satellite in orbit (b) Structure of Typhoon Hagupit as it headed towards the Philippines captured by GPM's DPR and GMI sensors (c) Snowstorm over the US east coast captured by GPM CO on March 17, 2014. Source: https://svs.gsfc.nasa.gov/gallery/gpm. 13

1.7 (a) GPM Core Observatory showing the GMI and DPR instruments and other important components (b) The GPM-CO measuring over a mid-latitude storm. GMI swath, DPR Ku-band (or KuPR) swath and DPR Ka-band (or KaPR) swath are represented. Source: https://svs.gsfc.nasa.gov/gallery/gpm. 14

1.8 The GPM constellation in April 2019. Source: https://gpm.nasa.gov/missions/GPM/constellation). 16

1.9 (a) Near-real-time dataset of precipitation within several hours of data acquisition. This visualization shows precipitation data obtained from IMERG on September 17, 2024 (b) Newly improved Grand Average Precipitation Climatology dataset covering June 2000 to May 2023. The Grand Average Precipitation Climatology dataset takes the entire record of global precipitation from 2000 to 2023 and calculates the average precipitation for the entire globe. Source: https://gpm.nasa.gov/data/imerg/precipitation-climatology. 17

2.1 Number of IMERG validation studies published between 2016 and 2019 (Pradhan et al., 2022). 22

6.1 An example of the IMERG PMW gridder geolocation error and the necessary correction corresonding to July 12, 2019. a) GPROF climate product (GPROF-CLIM) V05B precipitation estimates computed from the GMI footprint measurements. b) The original gridding of the GPROF-CLIM V05B precipitation estimates by the IMERG V06B algorithm, which includes the geolocation error. c) Corrected version of the IMERG V06B gridding (showing a 0.1° one-pixel shift westward for all grid boxes). The red box highlights cases where the geolocation error in the IMERG gridding is clear; however, note that the one-gridbox offset applies to all gridboxes. Also, note that these gridded values are not yet calibrated, which happens in computing the HQprecipitation variable (Huffman et al., 2023). . . . 133

List of Tables

1.1 Summary of several satellite precipitation products produced by combining input data from several sensor types, including satellite sensors and precipitation gauges. The information was extracted from the website https://www.eorc.jaxa.jp/IPWG/data/datasets2.html [Last updated July 31, 2021]. 9

3.1 Summary of the impact and quality of the journal in which the first paper in accordance with this thesis was published. The data correspond to the year 2022 (last year available at the date of preparation of this document) according to Scientific Journal Rankings (SJR). IF: Impact Factor. 28

4.1 Summary of the impact and quality of the journal in which the second paper in accordance with this thesis was published. The data correspond to the year 2023 (last year available at the date of preparation of this document) according to Scientific Journal Rankings (SJR). 52

5.1 Summary of the impact and quality of the journal in which the third paper in accordance with this thesis was published. The data correspond to the year 2023 (last year available at the date of preparation of this document) according to Scientific Journal Rankings (SJR). IF: Impact Factor 104

Acronyms

AMSR	Advanced Microwave Scanning Radiometer
AMW	Active Microwave
CARE	Environment Canada Center for Atmospheric Research Experiments
CCS	Cloud Classification System (CCS)
CDRD	Cloud Dynamics and Radiation Database
CHIRPS	Climate Hazards InfraRed Precipitation with Stations
CloudSat	Cloud Satellite
CM SAF	Climate monitoring
CMIC	Cloud Microphysics
CMORPH	Climate Prediction Center Morphing
CNES	Centre National d'Études Spatiales
CO	Core Observatory
CORRA	Combined Radar-Radiometer
COT	Cloud Optical Thikness
DPR	Dual-frequency Precipitation Radar
DSD	Drop Size Distributions
EarthCARE	Earth Clouds, Aerosols and Radiation Explorer
ENSO	El Niño–Southern Oscillation
ESA	European Space Agency
EUMETSAT	European Organisation for the Exploitation of Meteorological Satellites
FCDRs	Fundamental Climate Data Records
FEWS Net	Famine Early Warning System Network
GCPEx	GPM Cold Precipitation Experiment
GEO	Geosynchronous-Earth-orbit
GMAO	Global Modeling and Assimilation Office
GMI	GPM Microwave Imager
GPCC	Global Precipitation Climatology Centre
GPCP	Global Precipitation Climatology Project
GPI	GOES Precipitation Index
GPM	Global Precipitation Measurement
GPROF	Goddard Profiling
GSFC	Goddard Space Flight Center
GSMaP	Global Satellite Mapping of Precipitation
GV	Ground Validation
H SAF	Support to Operational Hydrology and Water Management

ICHARM	International Centre for Water Hazard and Risk Management
IMERG	Integrated Multi-satellitE Retrievals for GPM
IPWG	International Precipitation Working Group
IR	Infrared
ISRO	Indian Space Research Organisation
JAXA	Japan Aerospace Exploration Agency
JMA	Japan Meteorological Agency
KaPR	Ka-band Precipitation Radar
KGE	Kling–Gupta efficiency
KuPR	Ku-band Precipitation Radar
LEO	Low-Earth-orbit
LHASA	Landslide Hazard Assessment for Situational Awareness
LPVEx	Light Precipitation Validation Experiment
MC3E	Mid-latitude Continental Convective Clouds Experiment
MSWEP	Multisource Weighted-Ensemble Precipitation
MW	Microwave
NASA	National Aeronautics and Space Administration
NOAA	National Oceanic and Atmospheric Administration
NWC SAF	Support to Nowcasting and Very Short Range Forecasting
NWP	Numerical Weather Prediction
OLYMPEX	Olympic Mountain Experiment
PERSIANN	Precipitation Estimation from Remotely Sensed Information using Artificial Neural Networks
PMW	Passive Microwave
PNPR	Passive Microwave Neural Network Precipitation Retrieval
PPS	Precipitation Processing System
PR	Precipitation Radar
PRPS	Precipitation Retrieval and Profiling Scheme
RainCube	Radar in a CubeSat
RBIAS	Relative Bias
RMSE	Root Mean Squared Error
SAF	Satellite Application Facility
SMMR	Scanning Multichannel Microwave Radiometer
SSM/I	Special Sensor Microwave/Imager
SSMIS	Special Sensor Microwave – Imager/Sounder
TMI	TRMM Microwave Imager
TMPA	TRMM Multi-satellite Precipitation Analysis
TRMM	Tropical Rainfall Measuring Mission
VIS	Visible
WCRP	World Climate Research Programme
WMO	World Meteorological Organization
XCAL	GPM Intersatellite Calibration Working Group

CHAPTER

1

Introduction

1.1 Precipitation Characteristics

Precipitation, as defined by the World Meteorological Organization (WMO), refers to the fall of hydrometeor particles, including various forms such as rain, drizzle, snow, hail, and ice pellets. This process not only provides essential freshwater resources but also has the potential to contribute to severe weather events that can significantly impact human activities and ecosystems (Kidd et al., 2021). In the water cycle (Figure 1.1), precipitation is vital, involving phase transitions of water throughout the troposphere, from vapor to liquid to solid, down to the Earth's surface. These phase transitions are accompanied by the release of latent heat, which significantly influences the atmospheric energy budget and, consequently, the global climate system (Watters, 2021). Understanding these processes is essential for accurately modeling and predicting weather patterns and climate changes.

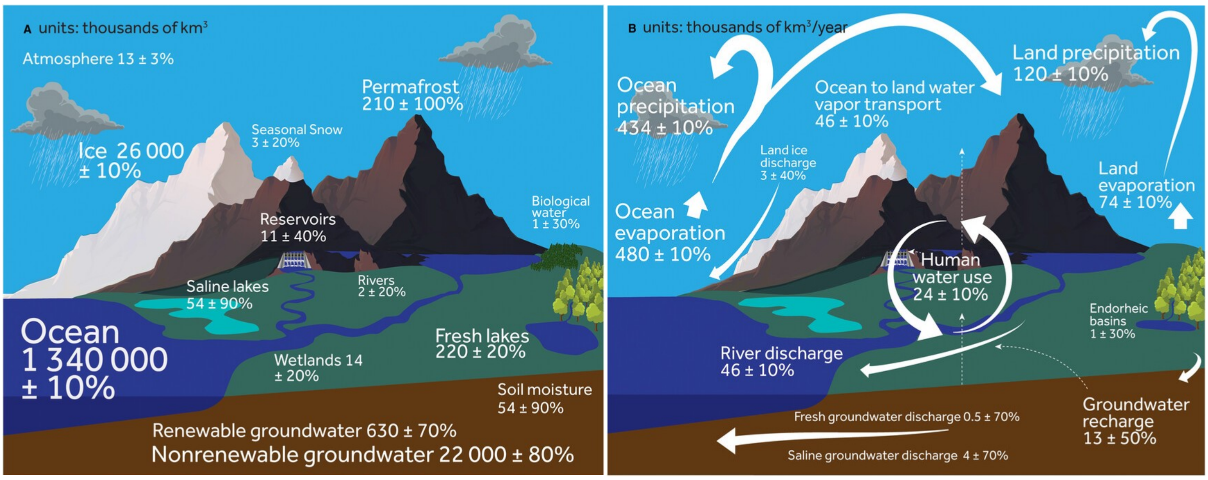

Figure 1.1: Representation of the global water cycle: (A) stores (in thousands of km^3) and (B) flows (thousands of km^3 per year) (Allan et al., 2020).

Observing precipitation presents unique challenges due to the specific temporal and spatial scales and characteristics it exhibits. At the microphysical scale, water is unique in that it coexists in all three phases–vapor, liquid, and solid—within many precipitation systems. The formation of liquid-phase water begins with the condensation of cloud water droplets, approximately 10 µm in size, on cloud condensation nuclei ∼ 0.1 µm, through the growth of cloud droplets, to precipitation-sized particles ∼ 100 µm, up to 4–5 mm (Kidd et al., 2021). Smaller droplets tend to be spherical, but as they grow larger, they become flatter or even umbrella-shaped due to air resistance before breaking apart. In the ice phase, water particles undergo similar growth processes, but with additional physical aggregation and interaction with liquid water (riming), leading to a diverse range of shapes and sizes (Kidd et al., 2021). The characteristics of precipitation can vary depending on cloud type and atmospheric conditions. For example, raindrops smaller than 0.5 mm in diameter are classified as drizzle and may evaporate before reaching the ground, forming virga (Ahrens, 2015). On the other hand, intense rainfall from cumuliform clouds can result in heavy, short-lived showers or cloudbursts, potentially leading to flash floods. Understanding the intensity and timing of precipitation is crucial for managing its impact on soil, urban infrastructure, and water resources (Ahrens, 2015).

At the precipitation system scale, the mechanisms driving the microphysical processes that form clouds and precipitation result in variations in precipitation that range from a few meters to 1000 km or more and from a few seconds to days, weeks, and longer (Trenberth et al., 2009). These variations greatly influence the accuracy of precipitation observations, which depend on the resolution and sampling of the observing system (Luini & Capsoni, 2012). In fact, the statistical properties of precipitation are unusual in that the normal/modal value in both space and time is typically zero, as precipitation does not occur most of the time across much of the globe (Kidd et al., 2021). When precipitation does occur, it is often skewed toward light intensities. The accumulation of precipitation, which depends on both the frequency and intensity of events, tends to follow a log-normal distribution (Ng et al., 2018). As instantaneous measurements are accumulated over time and across areas, this distribution gradually shifts toward a more normal distribution. This characteristic complicates statistical evaluations, requiring extreme care when analyzing and interpreting precipitation datasets. Specifically, the distribution of precipitation intensities is highly dependent on the spatial and temporal scales considered, meaning that observing the same precipitation system with sensors of different resolutions can yield different results (Kidd et al., 2021; Luini & Capsoni, 2012).

1.2 Observing Global Precipitation. Quantitative Precipitation Estimation

Observing and accurately measuring global precipitation is a complex task, essential for understanding weather patterns, managing water resources, and predicting climate changes. The following is a coherent description of some of the main sources of global precipitation measurements:

- **Rain Gauges:** The most direct method for measuring precipitation is through rain gauges, which are devices that collect and measure precipitation, at best (although not the most frequent) with 1 and 30 minutes of temporal resolution. Despite their widespread use, rain gauges have significant limitations. Their measurements are prone to errors due to turbulence around the gauge orifice, especially during light rain or strong winds, leading to potential underestimation of precipitation (Ciach, 2003; Duchon & Essenberg, 2001;

Kochendorfer et al., 2017). Moreover, the global coverage of rain gauges is highly variable (Figure 1.2), with vast areas, particularly over oceans and remote regions, lacking sufficient coverage. Being a point measurement, even in well-monitored regions, a single gauge only represents a very small area, making it difficult to capture the spatial variability of precipitation (Kyriakidis et al., 2001; Lundquist et al., 2019).

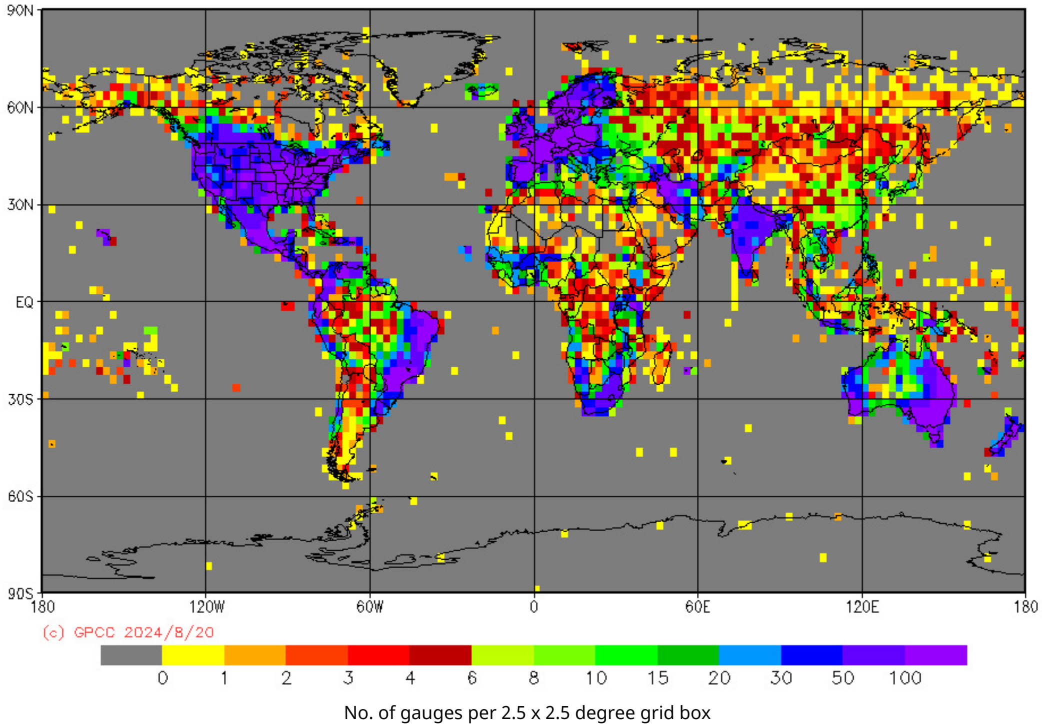

Figure 1.2: Global maps of GPCC gauge density (version 2022) for July 2024. Source: Oficial GPCC web page, https://kunden.dwd.de/GPCC/Visualizer

- **Disdrometer:** Another crucial instrument for precipitation measurement is the disdrometer, which, on a point scale, can measure the size and fall velocity of each hydrometeor (solid or liquid) within its measuring area. Compared to rain gauges, disdrometers provide more comprehensive information about precipitation, offering not only the amount of rainfall but also microphysical measurements such as the drop size distribution (DSD) in the case of rain, radar reflectivity factor (Z), liquid water content (LWC), and the kinetic energy of falling particles. In addition, microphysical data obtained from disdrometers can improve the classification of precipitation types (stratiform and convective regimes) and associated physical mechanisms (Dolan et al., 2018)(Figure 1.3). However, disdrometric measurements are subject to various errors caused by (i) statistical sampling, (ii) instrumental limitations (i.e., resolution and sensitivity), and (iii) environmental factors such as wind effects, splashing, or external interferences like insects (Adirosi et al., 2023). Moreover, despite their potential role, disdrometers are not yet widely used by operational meteorological and hydrological services, leading to a lack of a robust network of these devices and limiting their use to research purposes in specific regions worldwide.

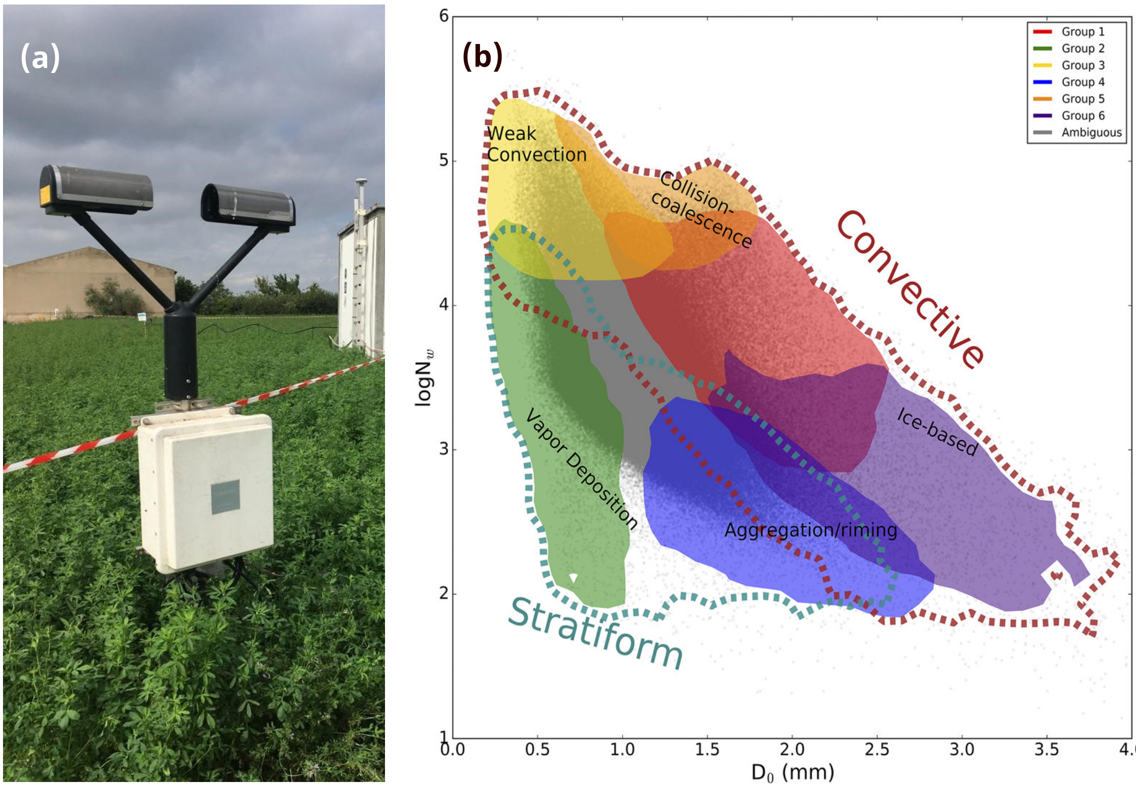

Figure 1.3: (a) Disdrometer (OTT Parsivel 2) located in Cendrosa, Catalonia during the LIASE Campaign (2021) (b) Conceptual model illustrating the dominant mechanisms for the six groups objectively determined from the surface disdrometers using Principal component analysis (PCA) in $logN_w - D_0$ space (Note that N_w is the normalized intercept parameter and D_0 is median drop diameters) (Dolan et al., 2018)

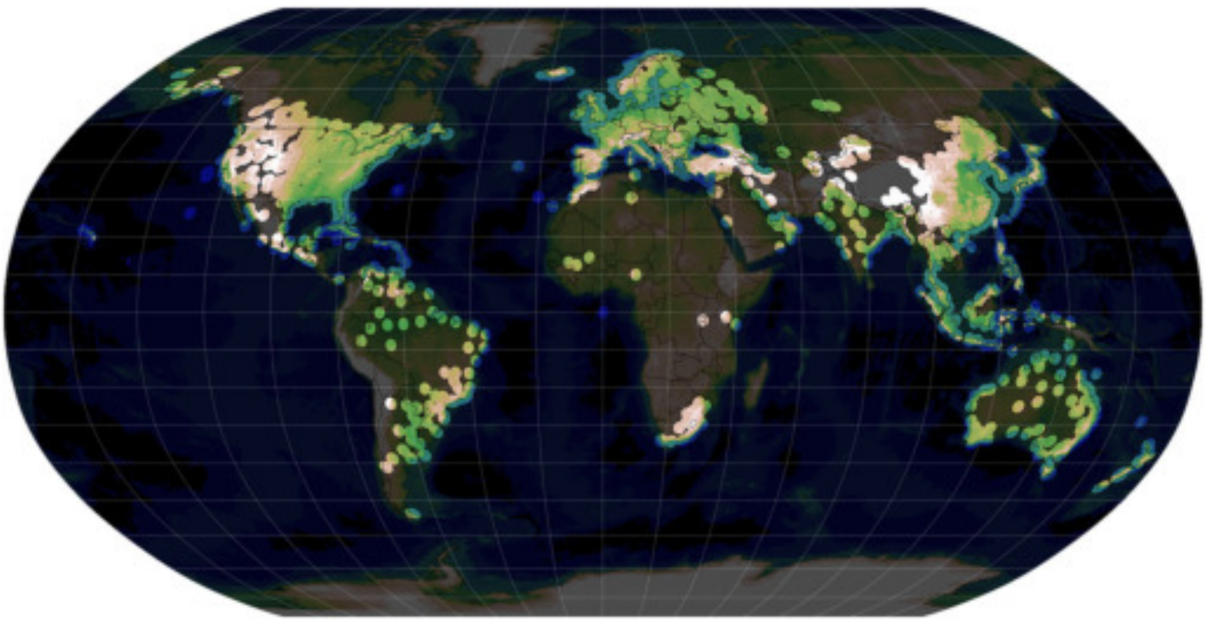

Figure 1.4: Weather radar global coverage (assumed 200 km range for each radar (Saltikoff et al., 2019)

- **Weather radar:** To complement above ground instruments, weather radar systems have been developed to provide more comprehensive precipitation data. Radars can observe precipitation over larger areas and at multiple altitudes, offering three-dimensional views of weather systems. However, the data they provide are indirect, relying on complex algorithms to convert the backscattered signal from raindrops or snowflakes into an estimated precipitation intensity (Fabry, 2018). Additionally, radar beams are typically tilted upwards due to the Earth curvature and usual propagation conditions (Bech et al., 2003), which means they measure precipitation at higher altitudes rather than at the surface, complicating the detection of near-surface precipitation and the differentiation between rain and snow (Casellas et al., 2021; Clark & Slater, 2006). Radar networks are expensive to install and maintain, and their coverage is generally limited to some land regions (Figure 1.4), further limiting their global applicability (Ciach & Krajewski, 1999; Harrison et al., 2000; Saltikoff et al., 2019).

- **Reanalysis models and numerical simulations**: Beyond ground-based observational methods, reanalysis models and numerical simulations have emerged as important tools for quantifying precipitation. These models combine historical weather data, observations, and complex physical equations to generate continuous precipitation estimates over time (Xie et al., 2022). While these models offer valuable insights and can cover areas lacking direct measurements, they also depend on the quality and density of the input data, which means that in regions with sparse observational data, their accuracy may be reduced. Moreover, the outputs of these models often need to be validated against ground-based measurements, which, as mentioned, are not uniformly available worldwide.

The limitations of ground-based methods and reanalysis models have led to the increasing reliance on satellite-based observations for global precipitation estimation. Satellites can provide near-continuous coverage of the Earth's surface, including remote and oceanic regions where other methods fall short. They use various sensors and techniques to estimate precipitation, such as passive microwave and infrared observations, which detect energy emitted or reflected by precipitation particles. These satellite-based estimates have revolutionized global precipitation monitoring, enabling the generation of comprehensive datasets that support a wide range of scientific and societal applications, from flood monitoring to agricultural planning. Despite their advantages, satellite estimates still face challenges related to accuracy and resolution, particularly in distinguishing between different types of precipitation and in regions with complex topography (Kidd & Levizzani, 2019).

1.2.1 Satellite precipitation measurements (LEO observing systems, GEO observing systems)

Satellite observations of clouds and precipitation have been exploited to provide a range of products that may be used to monitor precipitation occurrence and amounts at a range of spatial and temporal scales (Kidd & Levizzani, 2019). The relevance of satellite systems for observing precipitation and applications for hazard monitoring must consider the resolution (temporal and spatial) of the satellite observations; latency, or availability of observational data and/or products within a certain amount of time; accuracy of the results as determined through validation of data products; and usefulness of the resulting products to user community. The precipitation-capable missions typically comprise of two orbital types: the Low Earth Orbiting (LEO) satellites that circle the Earth at about 850 km altitude or lower, and the Geostationary (GEO) satellites that view the Earth from an altitude of about 36000 km.

LEO satellites are often placed in sun-synchronous orbits, allowing them to pass over the same regions at consistent local times, which is crucial for capturing diurnal variations in precipitation. They are equipped with advanced sensors, including passive microwave (PMW) radiometers and active microwave (AMW) radar, which provide more direct and detailed measurements of precipitation. Figure 1.5 shows the chronology of the Tropical Rainfall Measuring Mission(TRMM), GPM, CloudSat, RainCube and EarthCARE missions, intended primarily for cloud and precipitation detection. Missions like TRMM and the Global Precipitation Measurement (GPM) mission are prime examples of LEO systems designed to enhance our understanding of global precipitation patterns. However, the spatial and temporal coverage of any single LEO satellite is limited, with observations available only up to twice per day at the Equator. To mitigate this limitation, multiple LEO satellites are often deployed in a constellation, enabling more frequent observations and improving the temporal resolution of global precipitation data (Kidd & Levizzani, 2019; Watters, 2021).

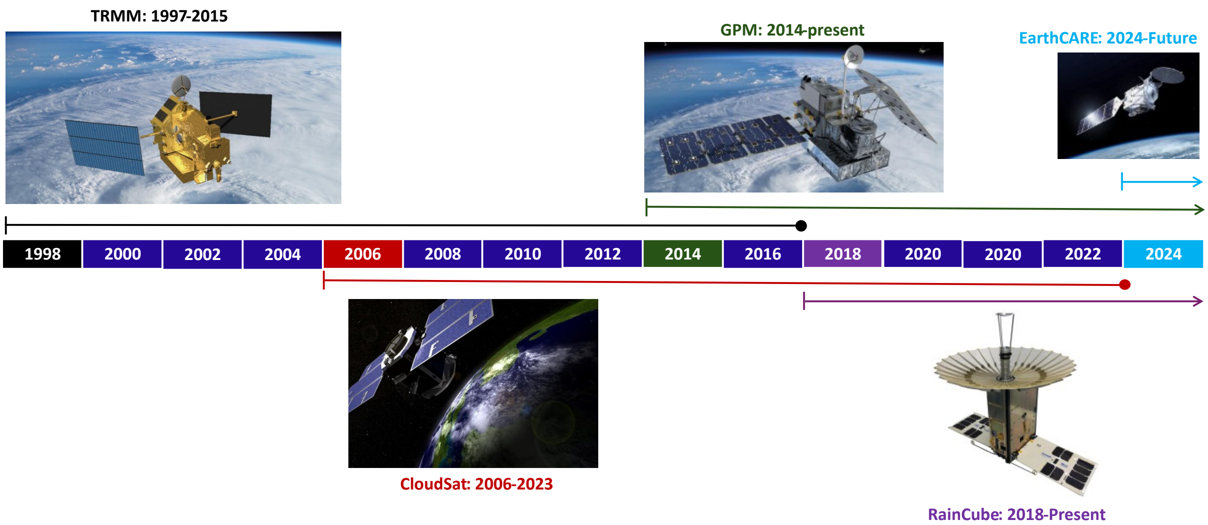

Figure 1.5: A timeline of several missions together with the relevance of their radar operating bands to the detection of clouds and precipitation, modified from Battaglia et al. (2020)

In contrast, Geostationary Earth Orbit (GEO) satellites, also referred to as a geosynchronous equatorial orbit satellites, operate at much higher altitudes, where they remain fixed relative to the Earth's surface. This geostationary position allows GEO satellites to continuously monitor the same region, providing frequent and consistent data over large areas. GEO satellites are particularly valuable for tracking weather systems and providing near-real-time data, which is crucial for operational meteorology and disaster management. These satellites typically carry visible (VIS) and infrared (IR) sensors, which, while less direct in measuring precipitation than microwave sensors, offer high temporal resolution and are essential for continuous monitoring.

However, achieving quasi-global coverage requires a constellation of GEO satellites positioned around the Equator, each covering a specific portion of the Earth's surface (Kidd & Huffman, 2011; Kidd & Levizzani, 2019).

The combination of LEO and GEO satellite systems is crucial to overcoming the limitations of each approach. By integrating data from both systems, scientists can create more accurate and comprehensive global precipitation datasets, essential for weather forecasting, climate studies, and resource management. Therefore, a stable and robust satellite constellation is crucial for providing adequate temporal sampling to capture precipitation variations, especially in data-sparse regions such as the poles or oceans.

1.2.2 Precipitation retrievals

A good number of algorithms, techniques, and schemes exist to estimate precipitation from satellite observations (Kidd & Levizzani, 2019). These methods range from simple, direct relationships to more complex approaches integrating multiple data types and models. Techniques have also been developed or adapted to consider the product latency time to meet user requirements: the typical data delivery time for global IR and MW data is around 2-3 hours, though some regional applications exploit direct broadcast capabilities and significantly reduce the latency to the order of 10-15 minutes (Kidd & Levizzani, 2019). Some of the main algorithms are shown below, grouped according to the method they use to process the data.

- **VIS/IR Methods:** Visible (VIS) and infrared (IR) methods estimate precipitation based on cloud properties observed by geostationary satellites. IR-based techniques often use cloud top temperatures to infer precipitation rates. The GOES Precipitation Index (GPI) (Arkin et al., 1994) is a classic IR-based method that assigns a fixed precipitation rate (3 mm/h) to clouds with temperatures below 235K. While simple and quick, this method's primary disadvantage is its indirect nature, which can lead to inaccuracies. It often misinterprets thin, high-altitude clouds as precipitating clouds or fails to detect precipitation in shallow clouds. Hydro-estimator (Scofield & Kuligowski, 2003) is another IR-based technique that improves upon the GPI by distinguishing between convective and stratiform precipitation areas. This method accounts for variations in cloud top temperatures and surface precipitation rates, offering more accurate estimates for intense convective systems. Similarly, the PERSIANN-CCS technique (Hong et al., 2004) utilizes cloud texture information such as cloud variability and minimum temperatures to refine precipitation estimates. Despite their advancements, IR-based methods generally struggle with detecting precipitation in regions with high thin clouds or shallow, non-precipitating clouds. These methods are particularly effective in tropical regions where cold cloud-top temperatures have a clearer relationship with surface precipitation.

- **Passive Microwave Methods:** In contrast to IR techniques, passive microwave (PMW) methods are more sensitive to the water and ice content within clouds. These methods use microwave radiometers to measure radiation emitted by precipitation-sized hydrometeors. Lower-frequency channels are more effective over oceans, where surface emissivity affects measurements, while higher-frequency channels can be used over both land and sea due to their sensitivity to solid ice particles. The Goddard Profiling (GPROF) scheme (C. D. Kummerow et al., 2015) is a notable PMW-based retrieval method. It estimates both surface precipitation and vertical profiles by integrating model information, such as 2-meter temperature and total precipitable water, with ancillary datasets. This approach helps to constrain possible precipitation retrievals and ensures consistency across various PMW observations. The Passive Microwave Neural Network Precipitation Retrieval v2 (PNPR) (Sanò et al., 2016) utilizes a neural network to retrieve precipitation rates from advanced PMW sensors. Trained with cloud-resolving model simulations, it offers precise estimates across different surface backgrounds. Cloud Dynamics and Radiation Database (CDRD) EUMETSAT product improves on conventional cloud radiation databases by using a regional/mesoscale model to simulate precipitating storms. It generates numerical simulations to enhance precipitation retrieval accuracy, especially over land surfaces (Mugnai et al., 2013). Simpler threshold-based methods (Laviola & Levizzani, 2011; Laviola et al., 2013), such as those using brightness temperature (BT) depression from PMW channels, provide operationally feasible solutions but may require validation with ground-based data.

- **Active Microwave Systems:** Active microwave systems, such as precipitation radars, provide direct measurements of precipitation. The TRMM Precipitation Radar, launched in 1997, and the GPM Dual-frequency Precipitation Radar (DPR), operational since 2014, represent significant advancements in radar technology. These systems convert return power into radar reflectivity to estimate precipitation rates and allow to identify features like bright bands, snowfall, and hail, providing three-dimensional information on precipitation systems, enhancing the establishment of climatological distributions. The radar's ability to measure precipitation directly is a major advantage, but limitations include long revisit times and restricted latitudinal coverage—37°N to 37°S for TRMM and 68°N to 68°S for GPM (Iguchi et al., 2021).

- **Multi-sensor Techniques:** To address the limitations of individual methods, multi-sensor techniques combine data from various sources. The GPM Combined Radar-Radiometer Algorithm (CORRA) (Grecu et al., 2016) integrates PMW and AMW observations to reduce ambiguities in precipitation modeling. This approach builds on the TRMM algorithm (Haddad et al., 1997) and aims to provide consistent precipitation estimates by combining different data types. CMORPH (Joyce et al., 2004), GSMaP (Aonashi et al., 2009; Kubota et al., 2007; Ushio et al., 2009), and IMERG (Huffman et al., 2020) are prominent products that merge PMW and IR data. They follow a three-step process: (1) the individual PMW measurements are generated (or obtained) to detect and estimate any surface precipitation, (2) wind vectors or changes in cloud top temperatures derived from IR data (or more recently models) move the precipitation between the individual PMW overpasses, and (3) (if required) IR-derived estimates are combined with the morphed PMW estimates. These products use surface precipitation gauge data to refine estimates, to minimize bias at a monthly scale. The Multisource Weighted-Ensemble Precipitation (MSWEP) (Beck et al., 2017) is another advanced product that combines multiple datasets into a comprehensive

3-hourly precipitation estimate at high spatial resolution. By integrating various methods and improving temporal and spatial sampling, these multi-sensor techniques enhance the accuracy and coverage of global precipitation datasets, essential for meteorological forecasting and climate studies.

1.2.3 Satellite Precipitation Products

Satellite precipitation products are indispensable tools for a wide array of applications, ranging from climate studies to operational weather forecasting (Kidd & Levizzani, 2019). These products, many of which are freely available online, leverage data from various sensors and platforms to provide global and regional precipitation estimates. They incorporate different algorithms and data sources, such as satellite observations and surface gauges, to deliver accurate and reliable precipitation measurements. Table 1.1 summarizes some of these products and their characteristics according to the nature of the data used. More information can be found on the International Precipitation Working Group (IPWG) web page on Data and Products (https://www.eorc.jaxa.jp/IPWG/data).

Table 1.1: Summary of several satellite precipitation products produced by combining input data from several sensor types, including satellite sensors and precipitation gauges. The information was extracted from the website https://www.eorc.jaxa.jp/IPWG/data/datasets2.html [Last updated July 31, 2021].

Product	**Space/time resolution**	**Areal coverage**	**Time record**	**Update frequency**	**Latency**
GPCP	2.5°/monthly	Global	1979-	Monthly	2 months
TMPA	2.5°/3-hourly	Global 50°N-S	1998-2019	Monthly	Replaced
IMERG Early	0.1°/half-hourly, monthly	Global	2000-	30 min	4 hours
IMERG Late	0.1°/half-hourly, monthly	Global	2000-	30 min	14 hours
IMERG Final	0.1°/half-hourly, monthly	Global	2000-	30 min/Monthly	3.5 months
H SAF (H61)	~0.03°/1h, 24h	60°S-75°N, 80°W-80°E	2020-	Hourly/ Daily	30 min
CHIRPS Final	~0.05°/daily, pentad, monthly	50°N-S	1981-	Monthly	2 weeks
PERSIANN	0.25°/30 min	60°N-S	2000-	Hourly	1 day
CMORPH V1.0 BLD	0.25°/daily	60°N-S regional	1998-	Daily	18 hours
GSMaP Standard	0.1°/hourly	60°N-S	2014-	1 hour	3 days

Among the most widely used long-term datasets is the Global Precipitation Climatology Project (GPCP) (Adler et al., 2018). GPCP combines multisensor information from satellites with surface gauge data to create a comprehensive precipitation climate data record. This dataset is particularly valuable for long-term climate studies and monitoring global precipitation patterns. The ongoing development of climate-scale precipitation data products has highlighted the importance of Fundamental Climate Data Records (FCDRs), which are essential for generating consistent and stable long-term time series. FCDRs consist of intercalibrated passive microwave (PMW) brightness temperatures (BT), which ensure the consistency necessary for reliable climate analysis. Several sources of FCDRs are available, including those from NOAA and Colorado State University, which provide FCDRs for the Special Sensor Microwave/Imager (SSM/I) and Special Sensor Microwave-Imager/Sounder (SSMIS sensors), calibrated to the F13 sensor (Berg et al., 2013; Sapiano et al., 2012) covering the period from July 1987 to the present. Another significant source is the NASA/GSFC Precipitation Processing System, which includes data from the TRMM and GPM constellation sensors, intercalibrated to the GPM Microwave Imager (GMI), with the dataset extending back to July 1987. Additionally, the EUMETSAT Satellite Application Facility on Climate Monitoring (CM-SAF) offers FCDRs for SSM/I, SSMIS, and Microwave Imager Radiances (Fennig et al., 2020), with data extending back to the SMMR radiometer aboard the Nimbus-7 satellite.

EUMETSAT's Satellite Application Facility on Support to Operational Hydrology and Water Management (H SAF) (Mugnai et al., 2013) is another critical product in the field of precipitation estimation. H SAF provides MW-derived rainfall products, which are particularly useful for operational hydrology and water management. This product utilizes a Cloud Dynamics and Radiation Database (CDRD) approach, coupled with a regional/mesoscale model in cloud-resolving mode, to improve the accuracy of precipitation retrievals, especially over land surfaces. H SAF is designed to support real-time applications, offering data with a latency suitable for operational use, making it an essential tool for monitoring and managing water resources in Europe and beyond.

In addition to these global datasets, there are specialized products like the Climate Hazards InfraRed Precipitation with Stations (CHIRPS) (Funk et al., 2015), which integrates satellite IR data with in-situ station data to provide high-resolution precipitation estimates. CHIRPS is widely used for climatic studies, particularly in monitoring droughts and famine-related events in Africa. Recent advances have also led to the development of the Multisource Weighted-Ensemble Precipitation (MSWEP) product, which combines gauge data, satellite observations, and model reanalyses to provide high-resolution, 3-hourly global precipitation estimates. While MSWEP's integration of multiple data sources enhances global performance, it also presents challenges in validation, as the specific contribution of satellite data can be difficult to isolate. Other notable products include the Precipitation Estimation from Remote Sensing Information using Artificial Neural Network (PERSIANN) (Sorooshian et al., 2000), which utilizes artificial neural networks to estimate precipitation from remote sensing data, and the Climate Prediction Center Morphing Technique (CMORPH) (Joyce et al., 2004), which generates high-resolution precipitation estimates by morphing microwave-derived rainfall rates with motion vectors derived from geostationary satellite IR data.

Furthermore, the Global Satellite Mapping of Precipitation (GSMaP) (Kubota et al., 2007) provides high-resolution global precipitation mapping by combining multiple satellite observations, while the TRMM Multisatellite Precipitation Analysis (TMPA) (Huffman et al., 2007) offers a long-term record of global precipitation, particularly focused on the tropics. The Integrated Multi-satellitE Retrievals for GPM (IMERG) (Hou et al., 2014) is another critical product, integrating data from multiple satellites to provide near-real-time and retrospective global precipitation estimates. IMERG is widely used in both research and operational weather forecasting, demonstrating the breadth of applications supported by these advanced satellite precipitation products.

1.2.4 Limitations and Errors

Satellite-derived precipitation products, while valuable, are subject to several limitations and sources of error that can impact on their accuracy and reliability. These limitations are especially critical given that these datasets aim to provide (quasi-) global coverage from a variety of observational samples. All of them were summarized by Kidd and Levizzani (2019).

- Skewed Distribution of Instantaneous Precipitation: Instantaneous precipitation measurements are highly skewed towards zero, with the modal value often being zero. This skewness affects the accuracy of satellite observations. While accumulating these instantaneous samples over time and space can provide a more normal distribution, other errors and uncertainties persist. For instance, representativeness errors arise when satellite measurements do not fully capture the spatial and temporal variability of precipitation (Kidd & Levizzani, 2019).

- Error Quantification and Uncertainty: Accurate quantification of errors and uncertainties is essential for effective use of satellite precipitation products in hydrological applications, climate studies, and water resource management (Maggioni & Massari, 2018; Maggioni et al., 2016). These uncertainties stem from several factors, including the frequency and channels used in satellite sensors, the type of precipitation observed, and the heterogeneity within the sensor's footprint.

- Frequency and Channel Limitations: Satellite sensors use different frequencies and channels to observe precipitation. IR channels provide data on cloud-top characteristics, while high-frequency PMW channels offer information on precipitation-related ice content, and low-frequency PMW channels reveal water content. The complexity of combining these channels, each with different weightings, can introduce retrieval errors (Kidd & Levizzani, 2019).

- Sampling Errors: The skewed distribution of precipitation at the instantaneous scale and the rarity of precipitation events complicates the sampling process. Sampling errors are most significant at scales of 1 hour to monthly, though at these scales, spatial and temporal autocorrelation can mitigate errors. Larger spatial and temporal domains generally lead to lower errors due to more samples, but instantaneous precipitation remains highly variable depending on precipitation type and system.

- Influence of Surface Characteristics: The performance of satellite algorithms can be adversely affected by surface characteristics. For example, decreased algorithm performance has been observed over dry and sparsely vegetated regions, where surface radiation signals may mimic the scattering signatures of frozen hydrometeors (Carr et al., 2015). Additionally, complex terrain can limit the quantitative use of satellite estimates, requiring high-resolution radar data for more accurate error analysis in mountainous regions (Bartsotas et al., 2018; Maggioni et al., 2017).

- Algorithm Performance and Precipitation Types: Satellite algorithms generally perform better in pure stratiform, and convective precipitation regimes compared to mixed precipitation events. The variability in performance across different precipitation types and systems adds another layer of complexity to error quantification (Carr et al., 2015).

- Lack of Standardization and Understanding: There is a notable lack of standardization and clear understanding of the errors and uncertainties associated with precipitation products. The transfer of error metrics across different scales, both temporally and spatially, is not well established, making it challenging for users to effectively incorporate these uncertainties into their applications (Tan et al., 2016).

In summary, while satellite precipitation products are invaluable for global monitoring and various applications, their limitations and errors—stemming from skewed data distributions, sampling challenges, frequency and channel issues, and surface characteristic influences—must be carefully considered. Continued research and development are needed to better quantify, understand, and mitigate these limitations to enhance the accuracy and applicability of satellite-derived precipitation data.

1.3 Global Precipitation Measurement Mission

This section provides a comprehensive overview of the NASA-JAXA Global Precipitation Measurement (GPM) mission, covering both the GPM Core Observatory (GPM CO) and the GPM Constellation. The first part outlines the technical details of the two spaceborne instruments aboard the satellite: the Dual-frequency Precipitation Radar (DPR) and the GPM Microwave Imager (GMI). The second part explores the GPM constellation of international satellites, each equipped with microwave radiometers, operating in different orbits and calibrated by the GPM CO. Additionally, key aspects of NASA's algorithm for the global precipitation product, the Integrated Multi-satellitE Retrievals for GPM (IMERG), derived from mission data, are discussed. Finally, the section highlights the applications and validations of GPM products in enhancing our understanding and quantification of global precipitation.

GPM mission is an international satellite mission that aims to advance our understanding of global precipitation patterns. Jointly operated by NASA and the Japan Aerospace Exploration Agency (JAXA), the GPM mission was launched on February 28, 2014, with the deployment of its Core Observatory (CO) (Hou et al., 2014; Kidd & Huffman, 2011)(Figure 1.6a). This mission serves as the successor to the highly successful TRMM, which was operational from 1997 to 2015 (C. Kummerow et al., 1998; Simpson et al., 1988). Unlike TRMM, which focused primarily on tropical regions, GPM extends its coverage to include mid-latitudes, providing near-global precipitation observations from 68°N to 68°S (GPM: 65° inclination; TRMM: 35° inclination).

The primary objective of the GPM mission is to enhance the measurement of precipitation, including rainfall and snowfall, and to improve our understanding of the spatial and temporal variability of precipitation across the globe. This is critical for addressing key challenges identified by the World Climate Research Programme (WCRP), such as predicting changes in freshwater availability, understanding the frequency and intensity of extreme weather events, and studying convection-cloud feedback mechanisms. By improving precipitation measurements, the GPM mission contributes to a better understanding of the Earth's water and energy cycles, which are vital for managing water resources and assessing environmental impacts.

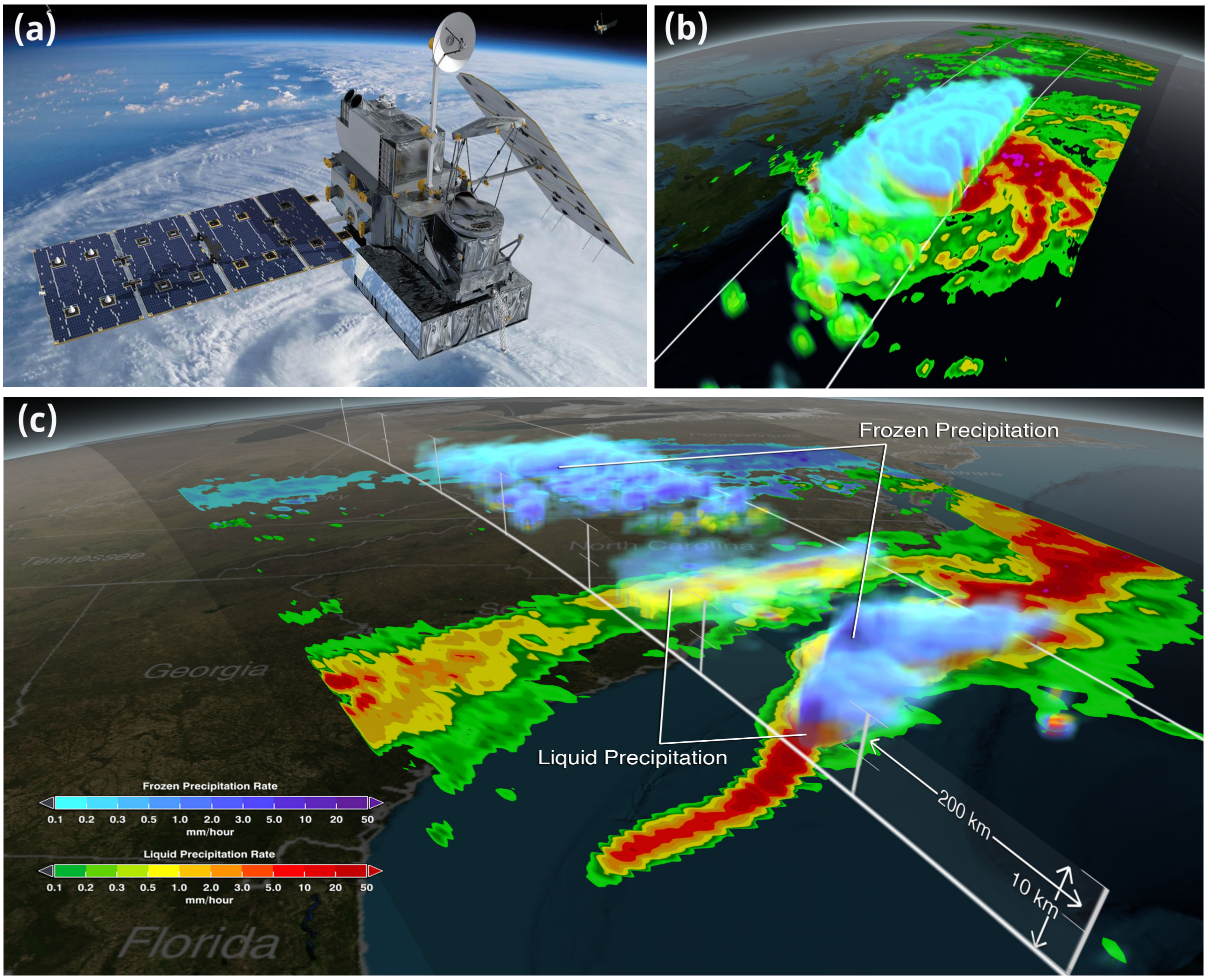

Figure 1.6: (a) Global Precipitation Measurement Core Satellite in orbit (b) Structure of Typhoon Hagupit as it headed towards the Philippines captured by GPM's DPR and GMI sensors (c) Snowstorm over the US east coast captured by GPM CO on March 17, 2014. Source: https://svs.gsfc.nasa.gov/gallery/gpm.

The GPM CO carries two advanced instruments —the DPR and the GMI— designed to provide detailed observations of precipitation (Figure 1.6b). The DPR offers three-dimensional measurements of precipitation structure, while the GMI provides multi-frequency radiometric observations. Together, these instruments enable the GPM-CO to serve as a calibration standard for a constellation of international satellites that contribute to the GPM mission's global precipitation measurements. This constellation, along with additional data from geostationary satellites, allows the generation of high-resolution precipitation products such as the IMERG and GSMaP, which are widely used for various applications (Skofronick-Jackson et al., 2017).

Building on the legacy of TRMM, which provided invaluable data on tropical precipitation, the GPM mission has expanded the observational capability to include light and solid precipitation, particularly at higher latitudes where such measurements are crucial (Figure 1.6c). This expansion has been facilitated by the inclusion of the Ka-band radar in the DPR, which complements the Ku-band radar used in TRMM. The overlapping period of TRMM and GPM observations also allowed for inter-calibration, ensuring continuity and consistency between the datasets (C. Kummerow et al., 1998; C. D. Kummerow et al., 2015). With its advanced instrumentation and international collaboration, the GPM mission plays a pivotal role in improving our ability to monitor and understand precipitation on a global scale.

1.3.1 Satellite Sensors and Characteristics

GPM CO is equipped with two state-of-the-art instruments designed to measure precipitation with unprecedented accuracy and detail: DPR and the GMI (Figure 1.7a). Flying in a low-Earth non-Sun-synchronous orbit, the GPM-CO can capture detailed observations of precipitation systems, particularly over the mid-latitudes, where it provides vertical profiling of precipitation across a 245 km swath and two-dimensional characterizations across a broader 885 km swath using its passive microwave radiometer (Figure 1.7b).

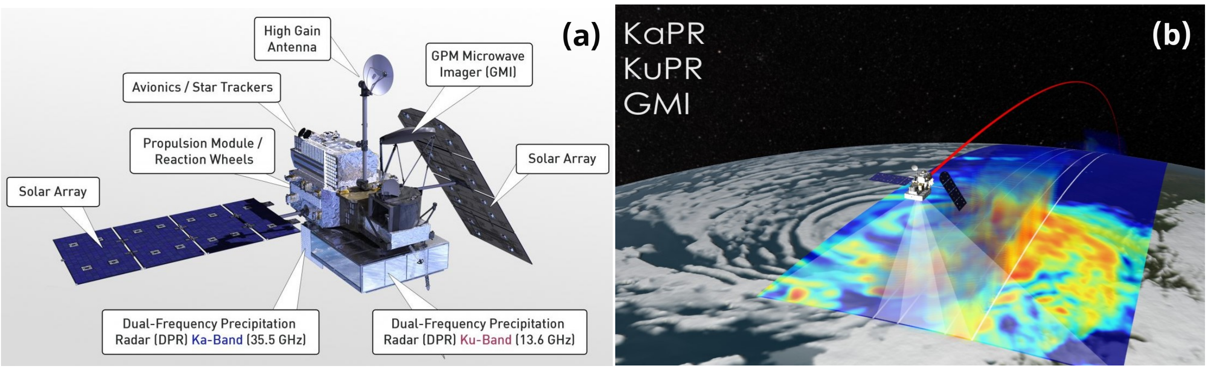

Figure 1.7: (a) GPM Core Observatory showing the GMI and DPR instruments and other important components (b) The GPM-CO measuring over a mid-latitude storm. GMI swath, DPR Ku-band (or KuPR) swath and DPR Ka-band (or KaPR) swath are represented. Source: https://svs.gsfc.nasa.gov/gallery/gpm.

The DPR is a novel instrument as it is the first and only multi-frequency precipitation radar in space, following the TRMM Precipitation Radar (PR) as the second spaceborne precipitation radar ever deployed (Iguchi, 2020; Iguchi et al., 2021). The DPR's ability to sense precipitation throughout the vertical column allows it to capture the three-dimensional structure of precipitating systems, offering measurements of rain rates ranging from 0.2 to 110.0 mm/h. These measurements are provided at a vertical resolution of 0.25 km and a horizontal resolution of 5 km (Hou et al., 2014). The DPR operates at two frequencies: the Ku-band (13.6 GHz) and the Ka-band (35.5 GHz). The Ku-band, with a detection threshold of 0.32 mm/h (15 dBZ), covers a swath of 245 km, while the Ka-band, with a detection threshold ranging from 0.27 to 0.56 mm/h (14-19 dBZ), initially covered the central 120 km of the Ku-band swath but was extended to 245 km in May 2018 (Iguchi, 2020; Iguchi et al., 2021). The addition of the Ka-band enhances the accuracy of precipitation rate estimates, improves the identification of the height at which precipitation changes phase, and aids in characterizing the precipitation drop size distribution. The introduction of GPM DPR measurements in mid-latitude regions has enabled the capture of the three-dimensional structure of extratropical cyclones and snowfall events, and its multi-frequency capability has improved our understanding of tropical cyclone structures.

GMI complements the DPR by providing radiometric information across 13 channels (ranging from 10 to 183 GHz) over a broader swath of 885 km (Hou et al., 2014; Skofronick-Jackson et al., 2017). Although the GMI's retrievals are limited to precipitation estimates up to 60 mm/h due to its lower spatial resolution (15 km) compared to the DPR (5 km), it plays a crucial role in calibrating the GPM satellite constellation of PMW radiometers (Skofronick-Jackson et al., 2018). The GMI stands out as the calibration standard for the constellation, offering the highest spatial resolution among the radiometers within the GPM constellation, particularly in the 166 and 183 GHz channels, which have a footprint resolution of 4.4 km by 7.3 km (Hou et al., 2014). With an accuracy within 0.4 K across all channels, the GMI is recognized as the most accurate spaceborne PMW radiometer currently available (Skofronick-Jackson et al., 2018; Wentz & Draper, 2016).

1.3.2 GPM Constellation

GPM CO plays a central role in a constellation of passive microwave satellites operated by various international space agencies, including NASA, JAXA, NOAA, EUMETSAT, ESA, ISRO, and CNES. This constellation consists of 11 satellites that together achieve global precipitation coverage, sampling over 90% of the Earth's surface at least once every three hours (Hou et al., 2014). The GPM constellation (Figure 1.8) exemplifies the mission's philosophy by providing consistent and calibrated global precipitation data, greatly enhancing our understanding of the global hydrological cycle and energy budget.

The integrated observing system formed by these satellites not only improves the spatial and temporal resolution of precipitation observations but also supports a wide range of applications due to the low latency of the data. These applications include disaster response, agricultural modeling, and monitoring disease risks (D. B. Kirschbaum et al., 2017). The primary goals of the GPM mission—enhancing spaceborne precipitation observations and deepening our understanding of precipitation systems—are addressed through this constellation, which samples Earth's precipitation with a frequency that ensures over 90% of global coverage within a three-hour window (Kidd et al., 2020).

The satellites within the GPM constellation, each in different non-Sun-synchronous or polar orbits, carry PMW radiometers that are intercalibrated by the GPM-CO's GMI instrument. This intercalibration ensures the consistency and accuracy of the data across the constellation, which is crucial for producing NASA's flagship global-gridded precipitation product, IMERG (Huffman et al., 2015, 2020). The evolving nature of this constellation allows it to continuously improve and adapt, maintaining its critical role in global precipitation monitoring.

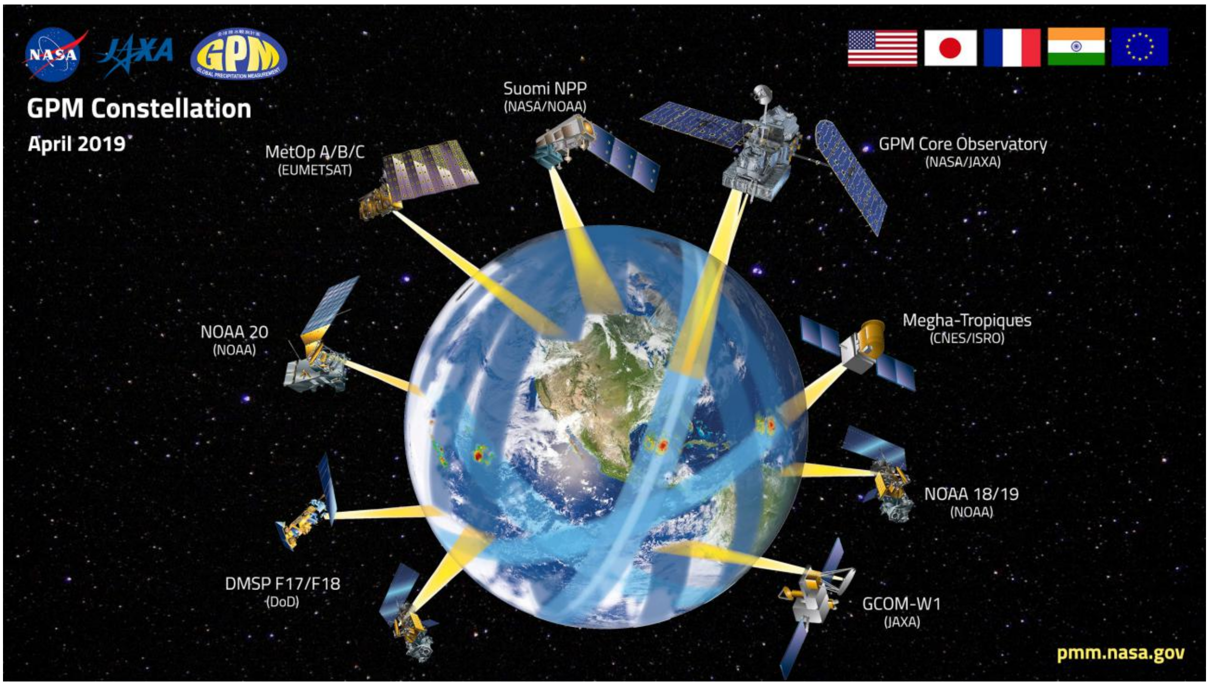

Figure 1.8: The GPM constellation in April 2019. Source: https://gpm.nasa.gov/missions/GPM/constellation).

1.3.3 IMERG products

IMERG product is a comprehensive tool for global precipitation estimation developed as part of the GPM mission. It integrates data from the GPM CO and its constellation of satellites, along with other ancillary data sources, to produce accurate and high-resolution precipitation maps (Figure 1.9a). IMERG operates by leveraging a series of sophisticated algorithms and calibration techniques to ensure data consistency and precision. The process begins with the calibration of the satellite measurements. The GPM Precipitation Processing System (PPS) standardizes incoming data from the GPM-CO and constellation satellites, including both brightness temperatures and orbital data structures. This step is crucial for maintaining consistency across different sensors. The GPM Intersatellite Calibration Working Group (XCAL) plays a key role in this process, employing various methods to align the calibration of different radiometers with the GMI to ensure consistency across all observations.

The primary algorithms used in IMERG are essential for converting raw satellite data into actionable precipitation estimates. The Goddard Profiling Algorithm (GPROF) (Olson et al., 2007) is used to process passive microwave radiometer data, converting brightness temperatures into precipitation estimates. This algorithm is integral to the processing of data from a range of microwave sensors, including the GPM constellation and TRMM satellites. For the Megha-Tropiques satellite, the Precipitation Retrieval and Profiling Scheme (PRPS) provides detailed vertical profiles of humidity, contributing to the accuracy of precipitation retrievals. The Combined Radar-Radiometer Algorithm (CORRA) merges radar and radiometer data to enhance the precision of precipitation estimates. CORRA combines radar reflectivity measurements with microwave brightness temperatures to create a more accurate precipitation profile. This algorithm is particularly useful for integrating data from different sensors and improving overall estimation accuracy.

In addition to microwave data, IMERG incorporates infrared (IR) observations from geostationary satellites to fill gaps in precipitation coverage. This is done using a Kalman Filter, which blends IR estimates with microwave data to provide continuous coverage. The morphing procedure, which involves linearly interpolating precipitation estimates based on the movement of precipitation features, is used to further enhance data coverage. This technique relies on motion vectors derived from reanalysis data to ensure that precipitation estimates are accurately positioned in time and space. Calibration of microwave precipitation estimates to match the CORRA product involves a two-step process. First, estimates from the TRMM/GPM constellation are adjusted to align with TMI/GMI estimates using zonal oceanic histograms and land-based histograms. Next, these adjusted estimates are calibrated to CORRA using a grid-based interpolation method, ensuring that data from different sources are harmonized.

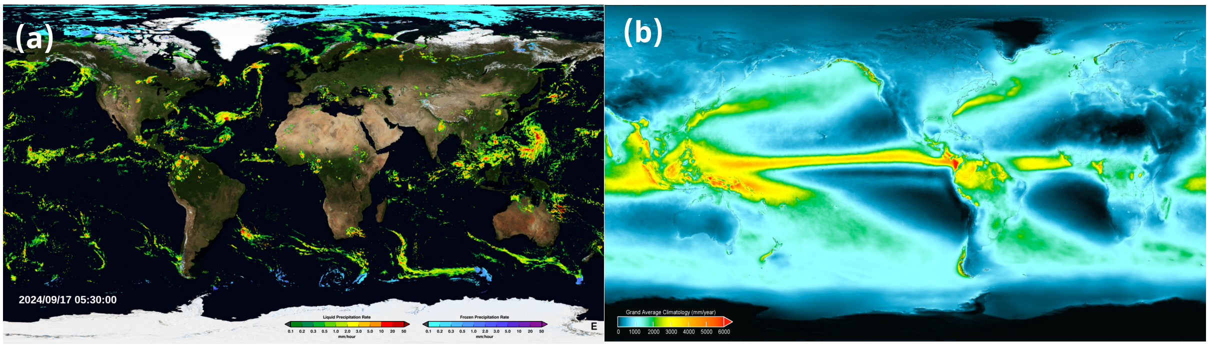

Figure 1.9: (a) Near-real-time dataset of precipitation within several hours of data acquisition. This visualization shows precipitation data obtained from IMERG on September 17, 2024 (b) Newly improved Grand Average Precipitation Climatology dataset covering June 2000 to May 2023. The Grand Average Precipitation Climatology dataset takes the entire record of global precipitation from 2000 to 2023 and calculates the average precipitation for the entire globe. Source: https://gpm.nasa.gov/data/imerg/precipitation-climatology.

IMERG produces several types of products to meet different needs:

- Level 1 products consist of raw and calibrated measurements from the satellites;
- Level 2 products provide instantaneous precipitation retrievals from individual sensors;
- Level 3 products offer global gridded precipitation estimates with high spatial (0.1°) and temporal (half-hour) resolution.

In turn, IMERG algorithm generates three main Level 3 products:

- Early Run, which is produced within 4 hours of observation and propagates forward only;
- Late Run, which includes data processed within 14 hours and includes forward and backward propagation;

- Final Run, which uses both forward and backward propagation and includes monthly gauge analysis, providing the most accurate and research-grade precipitation estimates after ~3.5 month. The Final run uses a month-to-month adjustment, which combines the multisatellite data for the month with the Global Precipitation Climatology Centre (GPCC) gauge (1° × 1° grid), derived from approximately 6700 stations worldwide.

IMERG Version 6 (V06), brought significant improvements over previous versions. It extends the precipitation record to include data from the TRMM era, enhances coverage beyond 60°N/S, and improves the morphing process by using reanalysis data for motion vectors. This version provides a detailed 24-year record of global precipitation (Figure 1.9b), with comprehensive coverage in the 60°N-S region and partial coverage elsewhere. IMERG's detailed and accurate precipitation estimates are vital for applications in weather forecasting, climate research, and disaster management.

1.3.4 Applications

Satellite-derived precipitation products, like those from the GPM mission, play a crucial role in monitoring and analyzing precipitation on a global scale in near real-time. These products are instrumental across a wide range of applications, from enhancing numerical weather prediction (NWP) models to aiding in disaster relief efforts. For instance, GPM data is used to track tropical cyclones and generate rainfall accumulation maps to support emergency responses during severe weather events, such as those detailed by (Skofronick-Jackson et al., 2018). In hydrology, satellite precipitation products are invaluable for modeling and forecasting, especially in regions with sparse ground-based measurements or in large river basins where they provide critical data for predicting river flows and initiating timely responses to potential flooding (Maggioni & Massari, 2018). The complexity of translating satellite rainfall measurements into river flow predictions is a significant challenge, as outlined in the hydrological modeling literature.

Extreme precipitation events, such as those leading to floods or landslides, are monitored using near real-time GPM data. The Landslide Hazard Assessment for Situational Awareness (LHASA) model, for example, utilizes this data to assess landslide risks, as discussed by (D. Kirschbaum & Stanley, 2018). Additionally, JAXA's collaboration with the International Centre for Water Hazard and Risk Management (ICHARM) since 2005 underscores the importance of satellite data in managing water hazards. Conversely, satellite precipitation data are also crucial in monitoring drought conditions, which can impact food security. The variability in precipitation patterns influenced by phenomena like the El Niño Southern Oscillation (ENSO) affects many food-producing regions in Africa, Central, and South America. TRMM satellite data have been used extensively to study these changes (Maidment et al., 2015). Systems like the Famine Early Warning System Network (FEWS Net) use precipitation information to assess drought metrics and the start of growing seasons, helping to mitigate the impacts on agriculture and food security (D. B. Kirschbaum et al., 2017). GPM data has also been used to derive metrics of water stress by comparing global precipitation with population density. The role of satellite data in drought risk management and its implications for agriculture and food security are further explored in the relevant chapters of the referenced volume. Recently, satellite precipitation data have also been applied to assess fire risk, particularly in regions prone to wildfires such as the western coast of the U.S. and Canada. The lack of winter snowfall can significantly impact water availability during the summer, potentially increasing the risk of forest fires (Gergel et al., 2017).

In the realm of operational numerical weather forecasting, GPM data have made significant contributions. The Japan Meteorological Agency (JMA) began operational assimilation of GPM DPR data into its mesoscale NWP system in March 2016, marking the first use of spaceborne radar data in such a system. This assimilation has led to improvements in moisture analysis and rainfall forecasts, as well as reduced errors in tropical cyclone positioning (Ikuta, 2016; Okamoto et al., 2016). NASA's Global Modeling and Assimilation Office (GMAO) incorporated GMI radiances into its Forward Processing System in real-time starting in July 2018. This integration has had a notable impact, improving short-term (0–72 hours) forecasts of specific humidity and enhancing the accuracy of tropical middle and lower tropospheric temperature and wind forecasts. The inclusion of GMI data has been shown to have a significant impact, comparable to that of a single Microwave Humidity Sounder instrument and has helped refine analyses of precipitating snow and other atmospheric parameters.

The GPM mission, building on the legacy of TRMM, has provided a consistent, high-resolution, sub-hourly global precipitation record that now spans over 20 years. This record has enabled the development of a global precipitation climatology based on the IMERG product, which has been compared with other climatological datasets, such as the GPCC gauge product, the GPCP satellite-gauge product, and the ECMWF ERA5 reanalysis. Furthermore, thanks to the vertical profiling capabilities of the GPM-CO's DPR, precipitation has not only been measured but also characterized by its vertical structure, identifying types such as convective, stratiform, and warm rain. With ten years of DPR data, the global distribution of these precipitation types has been detailed (Iguchi et al., 2021; Watters, 2021). Classifying and stratifying precipitation by type is crucial for understanding global energy dynamics, as each type exhibits distinct vertical latent heat profiles (Houze, 1997). In the context of climate change, where extreme events are projected to increase in frequency and intensity (IPCC, 2013), GPM's ability to enhance spaceborne precipitation measurements is essential for better understanding and adapting to our changing climate.

1.3.5 Validation and Comparison

The validation of satellite-derived precipitation products is crucial for ensuring their accuracy and reliability in various applications. The U.S. GPM program, led by NASA, incorporates a ground validation (GV) component designed to verify and validate the precipitation products generated by GPM observations while enhancing understanding of the precipitation processes observed by the GPM sensors. This validation work can be categorized into three primary areas:

- **Direct Validation:** This involves comparing satellite precipitation estimates with ground-based precipitation measurements collected by national and international networks. Large-scale precipitation measurements from sources like Multi-Sensor/Multi-Source radar data are used to assess the accuracy of satellite products. Notable examples include the validation of Level-2 GPROF precipitation products over Europe and the U.S. using surface radar and gauge data (Kidd, 2018), and the evaluation of Level-3 IMERG precipitation products across different spatial and temporal scales (Manz et al., 2017; Navarro et al., 2019; Palomino-Ángel et al., 2019; Prakash et al., 2018; Shawky et al., 2019; Tan et al., 2016, 2017). Other significant works include, who compared DPR and GPROF products against dense gauge networks (Bogerd et al., 2024; Tan et al., 2022), and the ongoing efforts by the International Precipitation Working Group (IPWG) to validate satellite precipitation products globally.

- **Physical Validation:** This area encompasses field campaigns where surface, airborne, and spaceborne measurements are coordinated to provide comprehensive observations of precipitation systems. GPM GV efforts have included several intensive campaigns such as the Light Precipitation Validation Experiment (LPVEx) in Helsinki, Finland (Huang et al., 2015; Iguchi et al., 2014), the GPM Cold Precipitation Experiment (GCPEx) at the Environment Canada Center for Atmospheric Research Experiments (CARE) site (Colle et al., 2017; Skofronick-Jackson et al., 2015), the Mid-latitude Continental Convective Clouds Experiment (MC3E) in Oklahoma (Jensen et al., 2016), and the Olympic Mountain Experiment (OLYMPEX) in the Northwest U.S (Houze et al., 2017; Petersen et al., 2020). These campaigns aim to capture a wide range of meteorological and climatological conditions to validate and refine satellite measurements.

- **Integrated Approach:** This method relates precipitation products to specific applications to assess errors and uncertainties across different spatial and temporal scales. This includes the study of drop-size distribution (DSD) by various sensors and reconciling differences in observations and processes (Adirosi et al., 2021; Bringi et al., 2015; Liao et al., 2014; Seela et al., 2023), as well as identifying and mitigating errors in hydrological modeling using satellite-derived precipitation data products.

Overall, the validation of satellite precipitation products, including IMERG, reveals variations in performance based on climatic conditions, geographical locations, and precipitation types. Continued global studies, particularly in under-represented regions, are essential for a comprehensive evaluation of these products and their integration into climate and hydrological models.

CHAPTER

2

Objectives

This chapter presents the main scientific problems that motivated the thesis and, consequently, the objectives of this work.

2.1 Motivation

GPM mission represents a significant advancement in satellite-based precipitation observation, offering unprecedented global coverage and high-resolution data critical for weather forecasting, climate modeling, and disaster management. However, ten years after its launch, GPM products have undergone seven different versions, reflecting ongoing efforts to improve their accuracy and reliability. This highlights the importance of validating GPM precipitation products to identify and quantify potential errors and biases, guiding future algorithm improvements, and ensuring their reliability for diverse applications.

A considerable number of studies have evaluated the performance of GPM IMERG precipitation products at various temporal and spatial scales worldwide. A study by Pradhan et al. (2022), which reviewed the state of the art in IMERG precipitation product validation, revealed that Europe is one of the regions with the fewest studies (Figure 2.1). If we also consider the evaluation of other GPM mission products, such as those derived from the DPR and/or GMI, the results are even less significant in the region. Specifically, the Western Mediterranean region is characterized by diverse climatic conditions, with Mediterranean, arid and alpine climates, and a complex topography with coastal areas, mountain ranges and valleys. This diversity poses significant challenges for satellite-based precipitation measurements, which are sensitive to variations in terrain and climate. The need thus arises to assess whether GPM precipitation products accurately represent precipitation dynamics in the Western Mediterranean region, given that this is a region marked by significant uncertainties in precipitation projections in the context of climate change. Research efforts in this region should be oriented to answer key scientific questions such as:

1. What are the strengths and weaknesses of IMERG, and how do these vary amongst differing meteorological regimes and microphysical characteristics?
2. What is the accuracy of near real-time IMERG measurements for quantifying extreme events and how do they compare to other satellite products for this purpose?

3. What is the accuracy of measurements from sensors on board the GPM CO, such as the Dual Precipitation Radar, and what can they contribute to the study of precipitation in mid-latitude regions?

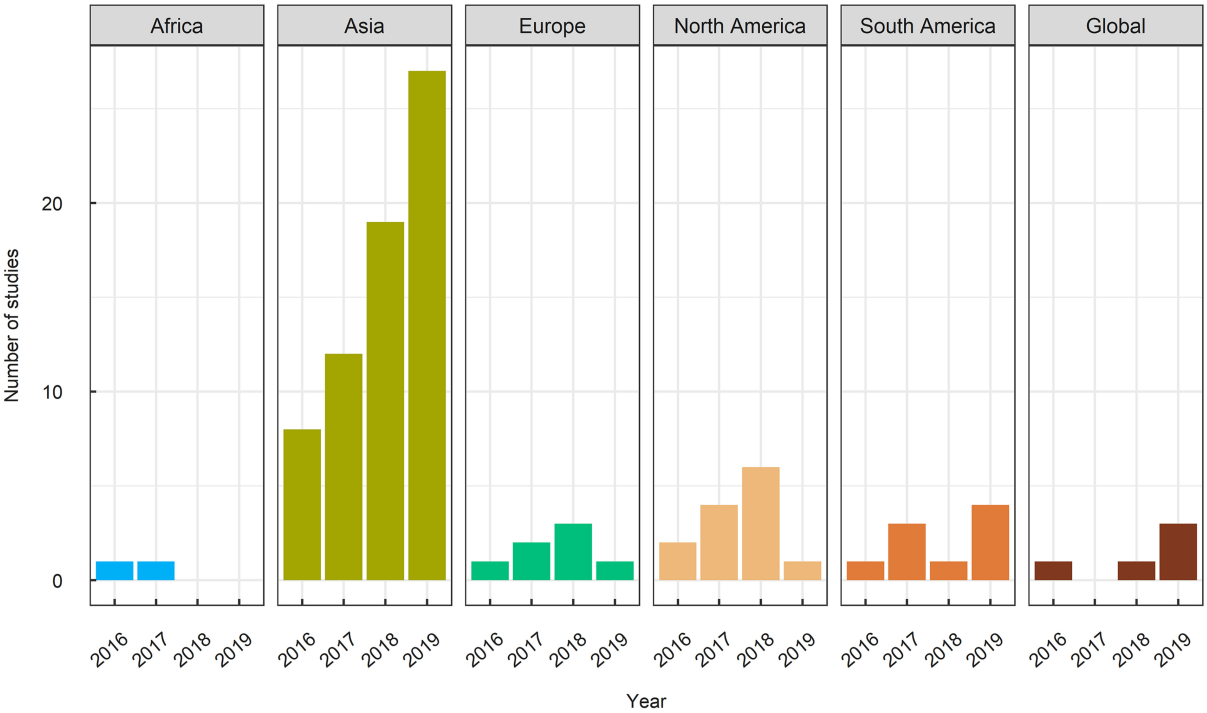

Figure 2.1: Number of IMERG validation studies published between 2016 and 2019 (Pradhan et al., 2022).

2.2 General Objective

Considering the points raised above, the **general objective** of this thesis is: **To validate precipitation estimates obtained from various GPM mission products over a Western Mediterranean region.**

This thesis, centered on a comprehensive validation exercise, is essential for understanding the strengths and limitations of cutting-edge satellite products that estimate precipitation. In a region characterized by complex topography and variable climate, having such tools allows for improved scientific understanding of regional hydrological cycles, weather patterns, and climate variability. Additionally, validating GPM products opens the possibility of incorporating these data into meteorological and climate models, which, in turn, will enable more reliable forecasts and more accurate climate simulations—vital aspects for addressing the challenges of climate change. The research also has direct applications in disaster management, as the region is susceptible to extreme weather events such as heavy rainfall and droughts, and accurate precipitation data are essential for early warning systems and disaster response strategies.

2.3 Specific Objectives

To address the general objective, a set of specific objectives were established, as listed below:

SO1. **To evaluate the precipitation estimates from the three Integrated Multi-satellitE Retrievals for GPM (IMERG) runs (Early, Late, and Final) at various temporal scales (half-hourly, hourly, daily, monthly, seasonal, and annual).**

Understanding the behavior of IMERG products at multiple scales simultaneously, rather than limiting the analysis to a single spatial and temporal resolution, could help elucidate how accuracy and errors vary with spatiotemporal aggregation. Additionally, it will help identify the effective resolution for use in for various hydro-meteorological purposes.

SO2. **To analyze the IMERG estimates at the highest temporal resolution (30 minutes), considering different orographic features, climatic conditions, and precipitation intensity thresholds.**

IMERG is particularly valuable in areas of the Earth's surface that lack ground-based precipitation-measuring instruments, including oceans and remote regions. Moreover, its half-hourly temporal resolution makes it one of the most highly valued products for water resource management and forecasting extreme weather events. Understanding its strengths and limitations in the context of different orographic and climatic characteristics, including mountainous and coastal regions, could enhance our understanding of the product's effectiveness under such conditions.

SO3. **To quantify the errors associated with IMERG in estimating heavy rainfall events at daily and sub-daily scales, to identify and address sources of error.**

IMERG provides near real-time estimates of Earth's precipitation updated every half-hour, enabling a wide range of applications that help communities around the world make informed decisions for disaster management, resource management, energy production, food security, and more. This objective aims to examine the effects of rainfall intensity on the estimates obtained, proposing a methodology to define extreme precipitation events at different temporal aggregations and evaluate the usefulness of these products.

SO4. **To investigate the impact of the contribution of different sensors to IMERG retrievals and their linkage to microphysical properties of precipitating cloud tops, with a focus on estimating heavy rainfall events.**

The evaluation of the Early and Late versions can be approached for different types of microphysical characteristics of precipitating clouds, as well as the effect of the various sensors that contribute to the final IMERG products. In fact, previous studies have recommended an individual evaluation of the underlying passive microwave (PMW) and infrared (IR) sources to detect error cancellation effects. Some works have directly addressed issues related to cloud microphysics in the retrieval process, as well as the behavior of different sensors contributing to IMERG. From this perspective, it is recommended to extend these studies to different regions based on their unique characteristics.

SO5. **To compare the performance of three H SAF products and the Early and Late versions of IMERG in estimating extreme precipitation events at hourly and daily scales.**

Like IMERG, H SAF generates and archives high-quality datasets and products for operational hydrological applications, starting from the acquisition and processing of data from Earth observation satellites in geostationary and polar orbits operated by EUMETSAT and other satellite organizations. The retrieval of products uses data from microwave and infrared instruments and aims to achieve the best possible accuracy compatible with available satellite systems. H SAF applications align with the objectives of other European and international programs, including those focused on mitigating hazards and natural disasters, such as flash floods, forest fires, landslides, and drought conditions, and improving water management. Several investigations using this approach have been carried out in Mediterranean countries. In Europe, there is access to numerous rain gauges and radars from eight European partner countries of the H SAF project, but no data are available in the Iberian Peninsula. According to the consulted literature, few studies evaluate the H SAF precipitation products outside the countries selected in their validation program and directly compare them with other products such as IMERG. This work aims to be one of the first to address this gap.

SO6. **To evaluate the precipitation intensity, radar reflectivity factors, and drop size distribution (DSD) parameters of GPM's Dual-frequency Precipitation Radar (DPR) Level 2 version 07B considering a network of disdrometers.**

GPM CO became the first spaceborne dual-frequency precipitation radar (DPR), operating at Ka- (35.5 GHz) and Ku-band (13.6 GHz) to offer three-dimensional measurements of the precipitation structure. Therefore, it is necessary to identify biases and improve future versions, with ground validation being an important component for evaluating and improving the performance of the DPR algorithm. Some of the DPR-derived variables are estimated at ground level, so specific information about precipitation drop size distributions (DSDs) at that level is needed for their verification. Achieving this objective will constitute one of the first validation exercises in the Mediterranean region using ground-based disdrometers to test the behavior of precipitation intensity, radar reflectivity factor (Z_{Ku} and Z_{Ka}), and DSD parameters (D_m, N_w) of the latest available version of GPM DPR.

2.4 Structure of the thesis

The present thesis is built as a compendium of three publications and an additional manuscript under review that will be considered for future publication.

Chapter 1 contains the current section, which includes an introduction divided into an overview and review of the state of the art on the main topics addressed in the thesis.

Chapter 2 contains the general and specific objectives. The next three chapters form the core of the thesis, each featuring one of the three published papers.

Chapter 3 presents a multiscale direct validation of IMERG products **(linked with SO1 and SO2)**, which is included in:

- Peinó, E., Bech, J., Udina, M., 2022. Performance Assessment of GPM IMERG Products at Different Time Resolutions, Climatic Areas and Topographic Conditions in Catalonia. Remote Sensing 14, 5085. https://doi.org/10.3390/rs14205085

Chapter 4 focuses on the detection of extreme precipitation events and the impact of the precipitation phase on the estimation of various sensors (linked with **SO3** and **SO4**). The performance of various satellite products in detecting these events is also examined. The following article includes the development of the first part:

- Peinó, E., Bech, J., Udina, M., and Polls, F. (2024). Peinó, E., Bech, J., Udina, M., Polls, F., 2024. Disentangling Satellite Precipitation Estimate Errors of Heavy Rainfall at the Daily and Sub-Daily Scales in the Western Mediterranean. Remote Sensing 16, 457. https://doi.org/10.3390/rs16030457

The second part of this chapter is under revision and will be proposed for publication shortly (linked with **SO5**). This topic is addressed in:

- Peinó, E., Bech, J., Petraca M. and Udina, M.(2024). Intercomparison of HSAF and IMERG satellite precipitation products over a Mediterranean coastal region. (Draft)

Chapter 5 is focused on Physical validation of the DPR **(linked with SO6)**. The paper comprising this study is:

- Peinó, E., Bech, J., Polls, F., Udina, M., Petracca, M., Adirosi, E., Gonzalez, S., Boudevillain, B., 2024. Validation of GPM DPR rainfall and Drop Size Distributions using disdrometer observations in the Western Mediterranean. Remote Sensing 16, 2594.

Finally, **Chapter 6**, includes the conclusions and gives the answers to the general and specific objectives proposed in **Chapter 1**. In addition, the main limitation of the study and possible future lines of research for the topics addressed in this thesis are sketched. Finally, **Appendix A** lists the contributions made during pre-doctoral period.

CHAPTER

3

Multiscale Direct Validation: Effective Temporal Resolution of IMERG

3.1 Performance Assessment of GPM IMERG Products at Different Time Resolutions, Climatic Areas and Topographic Conditions in Catalonia

3.1.1 Summary

This chapter addresses the critical need for accurate precipitation estimates in meteorology and climate science, and is focused on a specific precipitation spaceborne product. The study evaluates the performance of three IMERG runs (Early, Late, and Final) across various temporal scales, from half-hourly to annual, using data from the automatic weather station network of the Meteorological Service of Catalonia. This comprehensive evaluation is essential for understanding the reliability of IMERG products in different temporal contexts.

The methodology involves a detailed analysis of IMERG estimates at the highest temporal resolution (30 minutes), considering different orographic features (valley, plain, and ridgetop), climatic conditions (BSk, Csa, Cf, and Df) according to the Köppen classification, and precipitation intensity thresholds (light, moderate, intense, very intense, and torrential). By examining these factors, the study aims to provide a nuanced understanding of how IMERG products perform under varying conditions. This approach is crucial for improving precipitation estimates in regions with complex topography and diverse climatic characteristics. The study found that IMERG Early and IMERG Late tend to overestimate precipitation, while IMERG Final reduces the error at all temporal scales. However, IMERG Final also showed underestimation in some areas, such as the Pyrenees mountains. The proportion of false alarms, especially during summer, and the high bias and low correlation values at sub-daily scales were significant challenges identified in the study.

The novelty and importance of this study lie in its detailed and multi-faceted evaluation of IMERG products, which contributes significantly to the field of remote sensing. The findings help address the specific objectives of evaluating precipitation estimates at various temporal scales and analyzing IMERG estimates under different conditions. This research not only enhances the understanding of IMERG product performance but also provides valuable insights for future improvements in precipitation estimation and validation strategies. The study's results highlight the need for further refinement of IMERG products to improve their accuracy, especially in regions with complex topography and diverse climatic conditions.

3.1.2 Article

Peinó, E., Bech, J., and Udina, M. (2022). Performance assessment of GPM IMERG products at different time resolutions, climatic areas and topographic conditions in Catalonia. Remote Sensing, 14(20), 5085.

Table 3.1: Summary of the impact and quality of the journal in which the first paper in accordance with this thesis was published. The data correspond to the year 2022 (last year available at the date of preparation of this document) according to Scientific Journal Rankings (SJR). IF: Impact Factor.

Journal Name	**Description**	**Journal Metrics**
Remote Sensing	Remote Sensing is an international, peer-reviewed, open access journal about the science and application of remote sensing technology. It is published semimonthly online by Multidisciplinary Digital Publishing Institute (MDPI).	Impact Factor: 5.0 (2022), 5-Year IF: 4.9, CiteScore: 7.9, Quartile: Q1 Earth and Planetary Sciences (miscellaneous)

remote sensing

Article

Performance Assessment of GPM IMERG Products at Different Time Resolutions, Climatic Areas and Topographic Conditions in Catalonia

Eric Peinó [1], Joan Bech [1,2,*] and Mireia Udina [1]

[1] Department of Applied Physics—Meteorology, Universitat de Barcelona, 08028 Barcelona, Spain
[2] Water Research Institute, Universitat de Barcelona, 08028 Barcelona, Spain
* Correspondence: joan.bech@ub.edu

Abstract: Quantitative Precipitation Estimates (QPEs) from the Integrated Multisatellite Retrievals for GPM (IMERG) provide crucial information about the spatio-temporal distribution of precipitation in semiarid regions with complex orography, such as Catalonia (NE Spain). The network of automatic weather stations of the Meteorological Service of Catalonia is used to assess the performance of three IMERG products (Early, Late and Final) at different time scales, ranging from yearly to sub-daily periods. The analysis at a half-hourly scale also considered three different orographic features (valley, flat and ridgetop), diverse climatic conditions (BSk, Csa, Cf and Df) and five categories related to rainfall intensity (light, moderate, intense, very intense and torrential). While IMERG_E and IMERG_L overestimate precipitation, IMERG_F reduces the error at all temporal scales. However, the calibration to which a Final run is subjected causes underestimation regardless in some areas, such as the Pyrenees mountains. The proportion of false alarms is a problem for IMERG, especially during the summer, mainly associated with the detection of false precipitation in the form of light rainfall. At sub-daily scales, IMERG showed high bias and very low correlation values, indicating the remaining challenge for satellite sensors to estimate precipitation at high temporal resolution. This behaviour was more evident in flat areas and cold semi-arid climates, wherein overestimates of more than 30% were found. In contrast, rainfall classified as very heavy and torrential showed significant underestimates, higher than 80%, reflecting the inability of IMERG to detect extreme sub-daily precipitation events.

Keywords: GPM-IMERG; satellite precipitation estimates; remote sensing; assessment; complex orography; extreme precipitation

check for updates

Citation: Peinó, E.; Bech, J.; Udina, M. Performance Assessment of GPM IMERG Products at Different Time Resolutions, Climatic Areas and Topographic Conditions in Catalonia. *Remote Sens.* **2022**, *14*, 5085. https://doi.org/10.3390/rs14205085

Academic Editor: Silas Michaelides

Received: 9 September 2022
Accepted: 9 October 2022
Published: 12 October 2022

1. Introduction

The effects of climate change on future precipitation remain uncertain [1]. However, climate model predictions simulate yearly decreases in semi-arid regions of the Mediterranean [2]. Mountain areas are particularly vulnerable, where the cryosphere is directly affected by global warming, which consequently leads to altered seasonal runoff patterns [3]. Thus, hydrological cycles will gradually shift from being dominated by snow and ice to being determined by rainfall [4]. Accurate precipitation measurements at different spatial and temporal scales are of great significance for validating numerical weather and climate models, managing water resources and predicting natural disasters.

However, quantitative estimates of precipitation often have significant uncertainty [5]. Rain gauges, which are the world's most common method of obtaining accurate and reliable measurements at high temporal resolutions, provide point-scale measurements. This makes them unable to fully capture the spatial variability of the precipitation or to capture extreme local events in many areas wherein the instrument density is low. Ground-based radar-derived estimates are another feasible method, but due to their poor global coverage, the effects of terrain blockage [6] and the difficulties associated with estimating mixed and solid phase precipitation [5,7], there are limitations to obtain reliable estimates. Thus, satellite precipitation estimates (SPEs) offer an excellent way to compensate for some of these limitations and, although they have their own shortcomings, can be considered a complement to other methods [8].

Based on the success of the previous Tropical Rainfall Measurement Mission (TRMM), the Global Precipitation Measurement Mission (GPM) core satellite plus a constellation of satellites from partner countries provide one of the most accurate and fine-grained spatio-temporal resources for global precipitation measurements [9]. GPM has advanced sensors such as the GPM dual frequency precipitation radar (DPR) and microwave imager (GMI), which quantify precipitation more accurately and detect light and solid precipitation [10]. The associated processing, Integrated Multisatellite Retrievals for GPM (IMERG), incorporates, fuses and intercalibrates several infrared, microwave (MW) and gauge observations to provide precipitation estimates at relatively high spatial ($0.1^\circ \times 0.1^\circ$) and temporal (30 min) resolutions [9].

Since the launch of the GPM (February 2014), the chronology of publications evaluating the performance of the IMERG reflects a growing trend of research interest in the subject [11]. Most of the works that take a country or region of study stratify the results of the validation process according to different time scales [12–18], topographic features [15,19–24], climatic conditions [23,25–27] and in terms of precipitation intensity [19,20,28–33]. In this way, a more specific description of IMERG behaviour under different conditions is obtained, leading to the choice of a more suitable use for its application.

Several investigations with this approach have been developed in Mediterranean countries. In Greece, Kazamias et al. [34] explored the performance of IMERG Final across the country at daily, seasonal and annual scales, in different elevation zones and rainfall intensities. Caracciolo et al. [35] studied the influence of morphology and land–sea transition on the reliability of IMERG Final at hourly and daily scales, while Chiaravalloti et al. [36] evaluated and compared the IMERG Early, Late and Final products over complex terrain in southeastern Italy. Tapiador et al. [37] introduced for the first time the results of a validation in Spain based on a comparison with a high-resolution grid of daily precipitation derived from the records of approximately 2300 rain gauges covering the Iberian Peninsula and the Balearic Islands. The study at annual, seasonal and daily resolutions also analysed the spatial structure of precipitation and considered different precipitation thresholds for the three IMERG products. Similarly, Navarro et al. [38] validated the IMERG at the south of the Pyrenees and the Ebro valley according to four parameters: altitude, climate type, seasonality and quality of surface observations. Finally, Tapiador et al. [39] selected the IMERG Late product to evaluate the consistency of ground observations and satellite data during the Storm 'Filomena' in January 2021. Pradhan et al. [11] recently reviewed validation studies of IMERG and identified the most common limitations in this type of work, offering some suggestions to solve them. An important pending issue is the evaluation of IMERG products at multiple time scales, including sub-daily periods, to understand the errors associated with temporal aggregation. Further analysis in mountainous regions, over different climatic regimes, geographical conditions and assessing the effect of rainfall intensity on their accuracy still require the attention of the scientific community.

Based on these research gaps, the objectives of this work are twofold: (1) To evaluate the precipitation estimates obtained from the three IMERG runs (Early, Late and Final) at different time scales (half-hourly, hourly, daily, monthly, seasonal and annual) simultaneously taking as reference the automatic stations of the Meteorological Service of Catalonia and (2) To validate the IMERG estimates at the highest temporal resolution (30 min) according to different orographic features (valley, flat, ridgetop), different climatic conditions (BSk, Csa, Cf, Df) (see Appendix B) and according to different precipitation intensity thresholds (light, moderate, heavy, very heavy, torrential). The study considers the period from 2015 to 2020, so that full calendar years of the GPM core satellite data are employed. We focus on the region of Catalonia, northeast of the Iberian Peninsula, being one of the first studies to evaluate the behaviour of IMERG at a sub-daily temporal resolution in this region. This complements the previous studies done in IP and other areas with complex orography.

Sections 2.1 and 2.2 provide a description of the study area and details of the methodology, data and assessment metrics employed. Sections 3.1 and 3.2 compare the rain gauge observations and estimates of the three IMERG products at different time scales simultaneously. Sections 3.4 and 3.5 focus on the semi-hourly scale, considering different orographic and climatic conditions as well as different precipitation intensity thresholds, respectively. The most significant results are discussed in Section 4, and finally a summary with the most relevant aspects is given in Section 5.

2. Materials and Methods

2.1. Study Area

Catalonia is a region wherein topographic complexity and high climatic variability are a challenge for the remote sensing estimation of precipitation from satellite- or ground-based products, as well as for the estimation of the precipitation field using rain gauge stations [38,40]. The area of study is in the north-east (NE) of the Iberian Peninsula with approximately 32,107 km^2 and over 580 km of coastline facing northeast to southwest towards the Mediterranean Sea (Figure 1a). It is bordered to the north by the Pyrenees (Figure 1a), a mountainous barrier that connects the Iberian Peninsula with the European mainland and has elevations that can exceed 3000 masl. Another distinctive feature is the Central Depression (Figure 1a), characterized by flat land with few orographic contrasts resulting from the erosion of the Ebro and its tributaries.

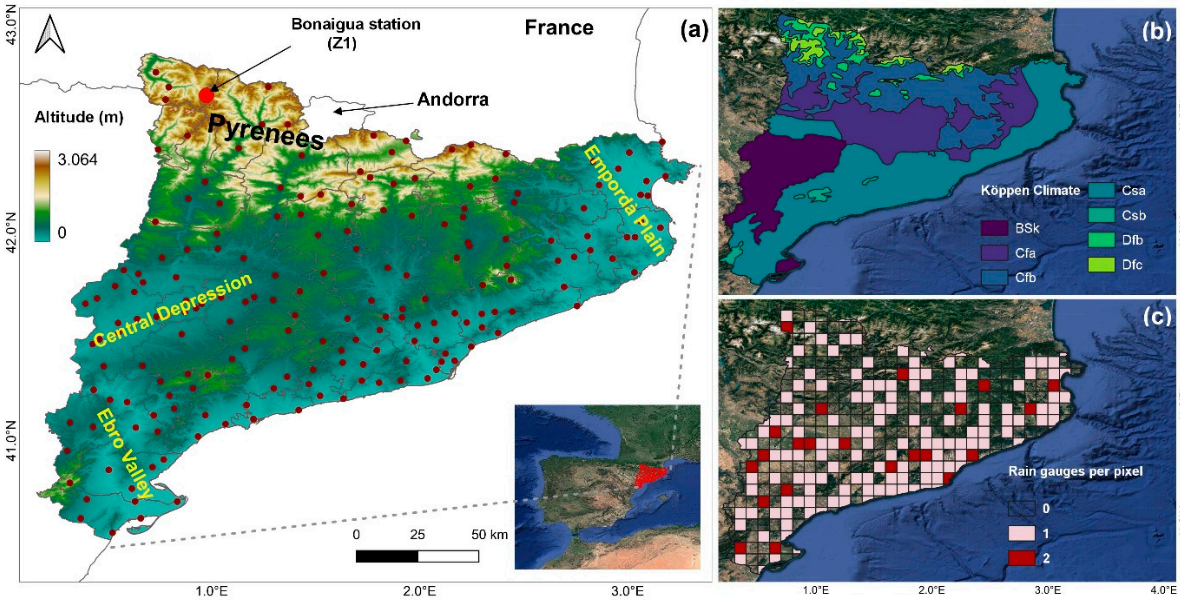

Figure 1. (**a**) Digital elevation model of Catalonia and XEMA stations network distribution. (**b**) Köppen climate classification in the study area. (**c**) Number of XEMA stations per IMERG pixel in the Catalonia domain.

The location of the orographic features and the pronounced topographic gradient of the region influence atmospheric low-level circulations and, particularly, the rainfall distribution over the entire territory [41,42]. On a large scale, it is an area of contact between air masses of different characteristics: cold or polar, coming from mid and high latitudes, and warm or tropical, typical of subtropical and tropical latitudes. The northwestern side of the Pyrenees (Köppen types Dfb, Dfc), which is exposed to the influence of humid air masses from the Atlantic, is where the highest annual accumulations are observed, with average values exceeding 1200 mm. The coastal and pre-coastal mountain chains (Csa) enhance the pluviometric effects of the Mediterranean cyclogenesis along the coast and form a pluviometric screen on the rest of the territory [43].

In inland areas, the climatic regime is highly conditioned by the precipitation deficit, which barely exceeds 400 mm per year. In the Central Depression (BSk), the winter is relatively cold, with frequent fog favoured by thermal inversions [44], and the summer is hot and dry. This impact of the general circulation patterns of the atmosphere modulated by the complex topography of the region promotes heavy rainfall, frequent flash floods and complex mesoscale meteorological events [42,45,46].

2.2. Datasets

2.2.1. IMERG V06B Data

This study validates data obtained from 2015 to 2020 obtained by the Integrated Multisatellite Retrievals for GPM (IMERG) version 06B at different time scales. GPM (2014–present) under the IMERG algorithm calibrates, fuses and interpolates precipitation estimates from various passive microwave sensors, infrared sensors and monthly rain gauge records [47] every 30 min, at a spatial resolution of $0.1^{\circ} \times 0.1^{\circ}$ and with a global coverage from -90°S to 90°N latitude.

The IMERG system provides three products: Early (latency of ~4 h after observation and forward propagation only), Late (latency of ~14 h after observation and includes forward and backward propagation) and Final run (~3.5 months after observation, using both forward and backward propagation and including monthly gauge analysis). The Final run also uses a month-to-month adjustment, which combines the multisatellite data for the month with the Global Precipitation Climatology Centre (GPCC) gauge ($1^{\circ} \times 1^{\circ}$ grid), derived from approximately 6700 stations worldwide [38]. Its influence in each half-hour slot is a ratio multiplier that is fixed for the month, but spatially varying [9].

IMERG data were obtained in UTC time and were downloaded through the NASA Goddard Earth Sciences Data and Information Services Center (GES DISC) [48]. Precipitation estimation data (combined microwave–infrared in the Early and Late products and precipitation estimates with post-processing gauge calibration in the Final product ("*PrecipitationCal*" variable, in all cases)) were analysed. Initially, the data had a resolution of 30 min and was aggregated at different time intervals: hourly, daily, monthly, seasonal and annual.

2.2.2. XEMA Data

The validation of the different IMERG products was conducted taking as a reference rainfall data from the automatic stations network (XEMA) managed by the Meteorological Service of Catalonia [49]. Semi-hourly rainfall records with a resolution of 0.1 mm were obtained in UTC time, between 1 January 2015 and 31 December 2020. Quality control applied to rain gauge data includes comparisons with close stations and correlation analysis [50,51]. From these initial data, hourly accumulation was generated, in which we verified that the data from the two 30-minute intervals corresponding to the hour did exist. Two criteria were applied to perform the comparison between the XEMA and IMERG data. The first criterion (Criterion 1) consists of requiring that there are at least 80% of records for each tested time scale. The second criterion (Criterion 2) restricts the comparison to couples of IMERG and XEMA data equal to or greater than 0.1 mm (this threshold is explained in Section 2.3.1). The results of applying these criteria are shown in Appendix A (Table A1). This distribution means that of the 417 IMERG pixels covering the region, 40% contain at least one rain gauge and 5% contain two rain gauges for validation (Figure 1c). The GPCC rain gauges used to calibrate the IMERG Final come from first order stations of the AEMET network [38], so all our data are independent from those used for calibration.

2.3. Methodology

2.3.1. Overview

Figure 2 shows a diagram summarizing the validation process of the three IMERG products based on the comparison with ground-based observations from XEMA rain gauges. To overcome the spatial mismatch between the two datasets, a pixel-to-point method [20,28] was applied to obtain the satellite information at each coordinate of the meteorological stations. This method allowed for a direct pairwise comparison between the rainfall data and the IMERG pixel value where the station is located. In case there was over one rain gauge in an IMERG pixel, the independence of the precipitation records in each one was maintained for the comparison. This method offers us the advantage of avoiding additional uncertainties derived from interpolation, considering the complexity of the topography in the region. Finally, the information from 164 IMERG pixels was associated with the 186 rain gauges, which corresponds to an overall density of 1.13 rain gauges per 100 km^2. This value represents more than six times the threshold recommended by the World Meteorological Organisation (WMO) for the interior flat and undulating areas [52].

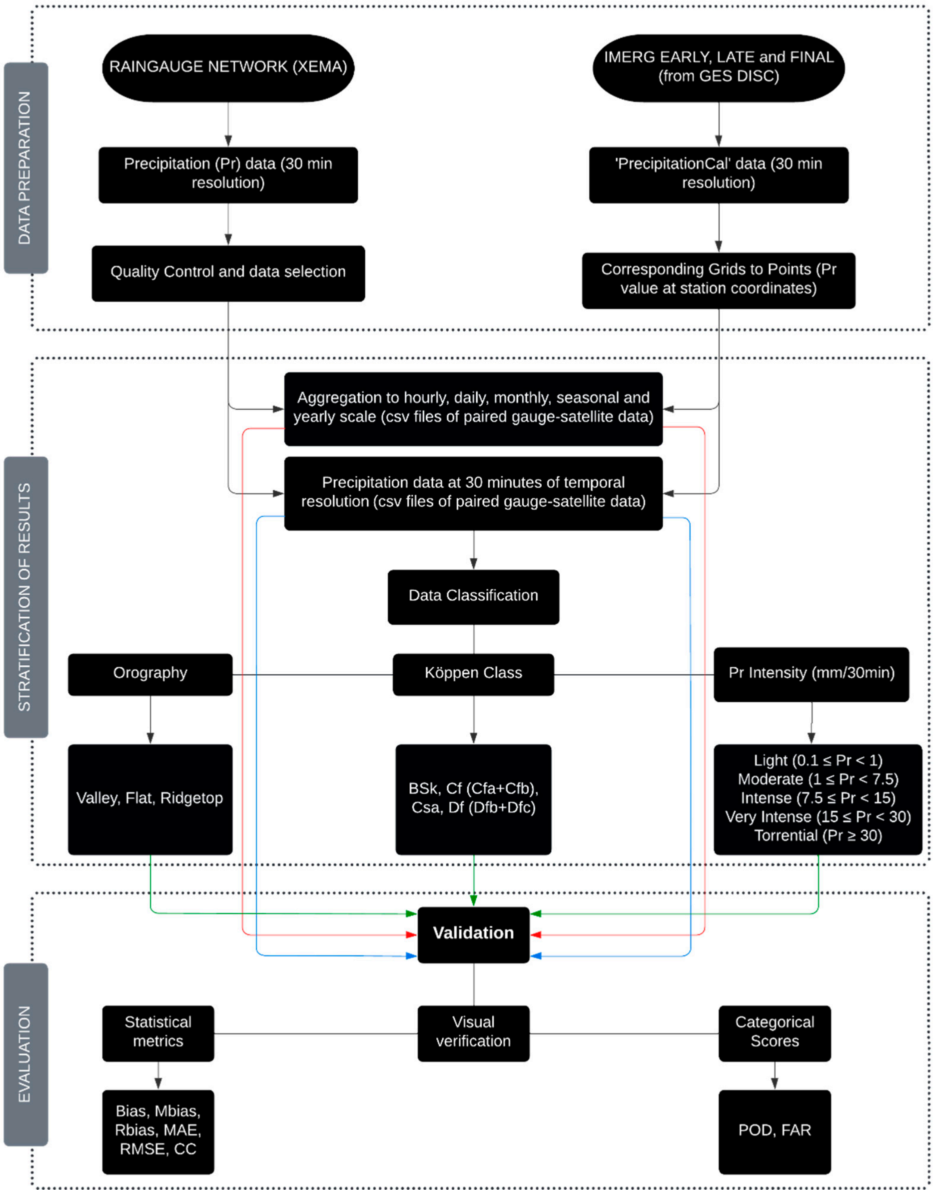

Figure 2. Schematic methodology applied in the data preparation, classification, and validation.

The first part of the study focused on evaluating and comparing the performance in the three IMERG products (Early, Late and Final) at multiple time scales: half-hourly, hourly, daily, monthly, seasonal, annual and annual mean over the period of 2015–2020. The different datasets were obtained from the aggregation of the semi-hourly precipitation accumulations (mm), considering only those records with at least 0.1 mm in both the IMERG and XEMA products (Criterion 2 described in Section 2.2.2). Note that 0.1 mm is the minimum rainfall detected by XEMA rain gauge. In this way, only precipitation periods are considered, and no further biases are introduced due to the different minimum precipitation amounts provided by each dataset, as discussed by Trapero et al. [42] in their Appendix A.

The second part of the research focuses only on the evaluation of the IMERG products on a half-hourly time scale and under various classifications. In order to achieve the classifications, the IMERG pixels were grouped and classified according to common orographic features and Köppen climatic conditions (Table A2).

The stratification of the results according to orography was based on a 5 m DEM [53] of the region of Catalonia. For each pixel, the topographic position index (TPI) was calculated [54] and with the tool "Corridor Designer" [55,56] a raster file was obtained in which each grid was classified as valley (TPI ≤ -12 m), flat (-12 m $<$ TPI $<$ 12 m, slope $< 6°$) and ridgetop (TPI $\geq$ 12 m).

Similarly, the process to divide the domain according to different climatic conditions started from a vector file with the Köppen classification in Catalonia [57], which was rasterised at a high spatial resolution (0.01°) to better preserve the vector characteristics. Four climatic categories were thus determined: BSk, Cf (fusion of Cfa and Cfb), Csa and Df (fusion of Dfb and Dfc).

Finally, the raster files were resampled to IMERG resolution using the so-called majority interpolation method [58] and the corresponding labels were extracted at the station level at both resolutions (initial high resolution and IMERG resolution). The station points where the orographic and climatic labels at different spatial resolutions coincided were taken for the IMERG evaluation process. Figure 3 shows the distribution of the pixels and weather stations used for validation, according to the category they represent.

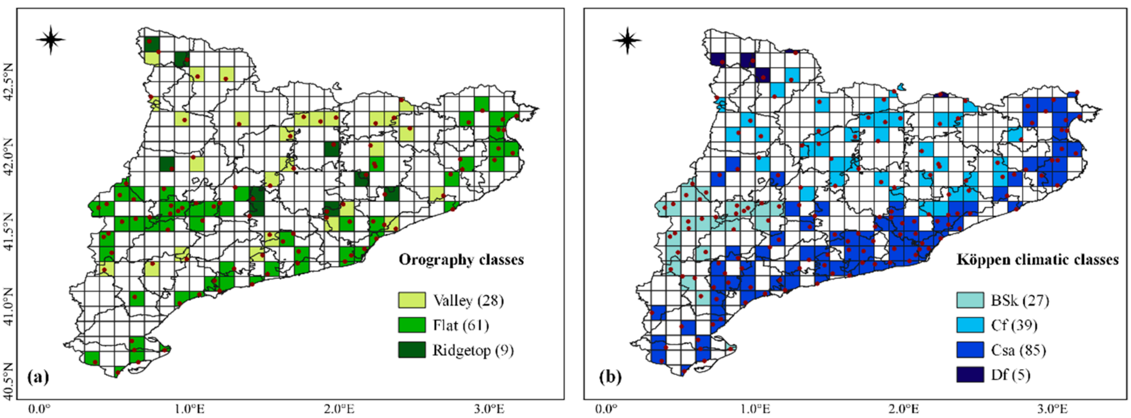

Figure 3. Distribution of IMERG pixels and stations (red dots) classified according to (**a**) orography (**b**) Köppen climate classification used for validation. The numbers in brackets represent the number of stations under that classification.

Half-hourly XEMA data were classified into five categories of precipitation intensity: light, moderate, heavy, very heavy and torrential (Figure 2). These categories were obtained by scaling the thresholds in mm/h established by AEMET [59].

2.3.2. Categorical and Continuous Verification Scores

To validate IMERG's ability to detect rainfall events correctly, categorical verification scores calculated from a 2×2 contingency table classifying events exceeding thresholds are used (Table 1). The recognition of the different possible situations (hits, false alarms, true positives, and misses) was done for various intensity thresholds. The categorical verification scores used were the probability of detection (*POD*) and the false alarm rate (*FAR*) (Table 2). The *POD* represents the proportion of events correctly detected by IMERG out of the total observed rainfall events, while the *FAR* represents the fraction of false detected rainfall events.

Table 1. Contingency table for comparing rainfall observed by XEMA and estimated by IMERG for a given threshold.

Estimated Rainfall	Observed Rainfall	
	Gauge Rain $\geq$ Threshold	Gauge Rain < Threshold
IMERG rain $\geq$ threshold	*Hits (H)*	*False alarms (F)*
IMERG rain < threshold	*Misses (M)*	*Correct Negatives*

Table 2. List of categorical verification metrics used to evaluate IMERG products.

Name	Formula	Perfect Score
Probability of detection (*POD*)	$POD = \frac{Hits}{Hits + Misses}$	1
False alarm ratio (*FAR*)	$FAR = \frac{False\ alarms}{False\ alarms + Hits}$	0

Additional continuous statistical metrics were used (Table 3). The Spearman correlation coefficient, used in cases such as this wherein there is no normality or homoscedasticity in the data, ranges from -1 to 1 and measures of the monotonicity of the relationship [60] between the IMERG and XEMA estimates. We also calculated the confidence interval for this statistic and tested for statistical significance at 95% of confidence. The other five metrics are used to quantify the associated error. *Bias* is a measure of the average error between IMERG and XEMA, while *Rbias* describes the systematic error. Positive (negative) values of *Bias* and *Rbias*, as well as those greater than unity (less than unity) of *Mbias*, denote the overestimation (underestimation) by the satellite products. The *MAE* shows the average magnitude of the absolute errors and, finally, the *RMSE* measures the magnitude of the average error, giving more weight to large errors without indicating the direction of deviation between IMERG and XEMA.

Table 3. List of the continuous verification metrics used to evaluate IMERG products.

Name	Formula	Unit	Perfect Score
Spearman's correlation coefficient	$r = \frac{cov(R(S_i),\ R(O_i))}{\sigma_{R(S_i)}\ \sigma_{R(O_i)}}$	-	1
Mean error (*Bias*)	$Bias = \frac{1}{n}\sum_{i=1}^{n}(S_i - O_i)$	mm	0
Relative bias (*Rbias*)	$Rbias = \frac{\sum_{i=1}^{n}(S_i - O_i)}{\sum_{i=1}^{n} O_i} \times 100$	%	0
Multiplicative bias (*Mbias*)	$Mbias = \frac{\sum_{i=1}^{n} S_i}{\sum_{i=1}^{n} O_i}$	-	1
Mean absolute error (*MAE*)	$MAE = \frac{\sum_{i=1}^{n}\lvert S_i - O_i\rvert}{n}$	mm	0
Root mean square error (*RMSE*)	$RMSE = \sqrt{\frac{1}{n}\sum_{i=1}^{n}(S_i - O_i)^2}$	mm	0

S_i is the value of satellite/model precipitation estimates for the i^{th} event, O_i is the value of rain gauge observation for the i^{th} event, n is the number of observed records, $cov(R(S_i), R(O_i))$ is the covariance of the rank variables, $\sigma_{R(S_i)}$ and $\sigma_{R(O_i)}$ are the standard deviations of the rank variables.

3. Results

3.1. Mean Annual Precipitation 2015–2020

A comparison of mean annual precipitation amounts was made between IMERG products and XEMA data. Figure 4 shows the spatial distribution of the mean annual precipitation of IMERG products compared with rain gauge recorded from 2015 to 2020. In addition, the probability of occurrence of annual precipitation and the kernel density estimation (KDE) curve associated with the distribution of each dataset are plotted (lower panel).

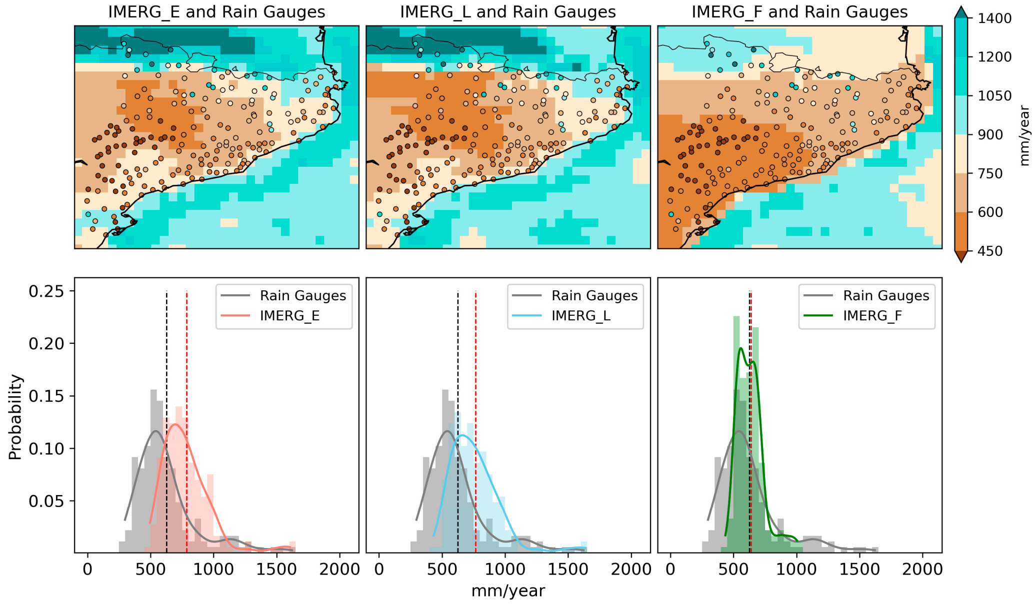

Figure 4. (**Top panel**) Mean annual precipitation accumulations of IMERG products and XEMA stations, in the period of 2015–2020. (**Bottom panel**) KDE curve associated with the distribution of each dataset, the black (red) dashed line represents the mean of the XEMA observations (IMERG).

According to rain gauge data, the average annual rainfall in Catalonia during this period varies between 300 mm and 1600 mm/year. The lowest records are observed in the Central Depression, where they do not exceed 450 mm/year, followed by the coastal areas with values around 600 mm/year. In contrast, stations close to the Pyrenees have accumulations usually exceeding 900 mm/year and those located above 2000 masl typically are over 1600 mm/year, which represents the maximum values for the region under study, and also some of the highest of the Iberian Peninsula. This high spatial variability is consistent with previous precipitation climatologies [61–63] in the studied region, which guarantees the representativeness of the selected sample.

The comparative analysis between the products shows a very similar performance between IMERG_E and IMERG_L, while in IMERG_F there is evidence of the unbiased effect thanks to the calibration with GPCC rainfall. It is also worth noting that the three IMERG products broadly reproduce the spatial rainfall pattern in the region, characterized by a marked latitudinal gradient that decreases from north to south. However, there are discrepancies in magnitude that are substantial. IMERG_E and IMERG_L overestimate precipitation by over 20% in almost all the territory with biases of 160 and 140 mm/year, respectively. This overestimation is notable in the areas of the Central Depression, characterized by a dry continental climate with low pluviometric values. Similar results were detected by Kazamias et al. [34], wherein the *IMERG_unCal* show the largest discrepancies in the areas of Greece with low annual accumulations. Similarly, Navarro et al. [38] also found a general overestimation of precipitation over the Ebro Delta river, and Tapiador et al. [37] reported an underestimation in the Pyrenees mountain massif.

Although the tendency of IMERG_E and IMERG_L to overestimate is shown in the same way at the pre-coastal, coastal and Ebro basin areas, the correction carried out in IMERG_F is effective and generally reflects annual mean values very similar to the rain gauge records (Figure 4, bottom panel). However, IMERG_F generally reduces and smooths the precipitation field over the Pyrenees and some high-altitude stations show an increased bias exceeding 600 mm/year.

3.2. Continuous Verification Scores for Different Time Scales

Table 4 shows a summary of various statistics calculated at half-hourly, hourly, daily, monthly and annual scales considering all valid records between 2015 and 2020. The *Bias*, *MAE* and *RMSE* are standardized to the mean of the observations at the different time scales, which allows for comparisons to be made between them.

Table 4. Continuous statistics calculated at different scales for the three IMERG products.

	N	*Bias* (mm)	*Mbias*	*Rbias* (%)	*MAE* (mm)	*MAE* (%)	*RMSE* (mm)	*RMSE* (%)	*CC*
					30 min				
IMERG_F	277616	−0.07	0.95	−4.85	1.19	87.36	2.37	173.30	0.33
IMERG_L	277616	0.20	1.15	14.59	1.39	101.76	2.70	197.15	0.29
IMERG_E	277616	0.26	1.19	18.86	1.49	109.18	2.89	211.11	0.23
					Hourly				
IMERG_F	199255	−0.05	0.98	−2.16	1.88	87.27	3.51	162.81	0.37
IMERG_L	199255	0.39	1.18	18.25	2.23	103.26	4.21	195.35	0.33
IMERG_E	199255	0.42	1.20	19.60	2.35	109.01	4.46	206.85	0.26
					Daily				
IMERG_F	70399	−0.12	0.99	−1.44	6.22	72.62	10.68	124.66	0.58
IMERG_L	70399	1.71	1.20	19.94	7.93	92.56	14.68	171.42	0.53
IMERG_E	70399	1.57	1.18	18.35	8.01	93.56	14.72	171.91	0.49
					Monthly				
IMERG_F	12802	0.81	1.02	1.53	20.32	38.50	30.60	57.97	0.85
IMERG_L	12802	11.75	1.22	22.27	33.17	62.84	51.13	96.87	0.67
IMERG_E	12802	13.44	1.25	25.46	33.79	64.01	51.49	97.55	0.66
					Spring				
IMERG_F	996	−3.65	0.98	−1.97	48.25	26.03	70.15	37.85	0.83
IMERG_L	996	8.02	1.04	4.33	75.46	40.71	101.30	54.65	0.54
IMERG_E	996	6.61	1.04	3.57	73.81	39.82	100.31	54.12	0.56
					Summer				
IMERG_F	1020	11.39	1.10	9.64	43.41	36.74	59.73	50.55	0.85
IMERG_L	1020	97.23	1.82	82.28	105.47	89.26	143.32	121.29	0.65
IMERG_E	1020	97.84	1.83	82.80	106.46	90.10	142.63	120.70	0.62
					Autumn				
IMERG_F	1032	2.34	1.01	1.15	52.09	25.55	70.80	34.73	0.80
IMERG_L	1032	33.69	1.17	16.53	84.27	41.33	109.55	53.73	0.61
IMERG_E	1032	46.89	1.23	23.00	89.53	43.91	114.42	56.12	0.61
					Winter				
IMERG_F	820	−2.42	0.98	−1.91	37.79	29.83	60.58	47.82	0.91
IMERG_L	820	7.77	1.06	6.14	56.20	44.36	93.27	73.62	0.83
IMERG_E	820	14.11	1.11	11.14	54.51	43.03	88.75	70.06	0.84
					Yearly				
IMERG_F	6204	9.65	1.02	1.55	139.36	22.35	194.17	31.14	0.86
IMERG_L	6204	139.76	1.22	22.41	226.11	36.26	280.06	44.92	0.60
IMERG_E	6204	159.22	1.26	25.54	230.12	36.91	285.82	45.84	0.63

In terms of *Rbias*, IMERG_E and IMERG_L present an overestimation of precipitation close to 20% at all time scales, except at the seasonal and yearly levels. In contrast, this behaviour only occurs in IMERG_F at monthly and annual scales, although it does not exceed 2%. At daily and sub-daily scales, IMERG_F slightly underestimates precipitation relative to observations, with values ranging between −0.05 mm/h and −0.12 mm/day, which is relatively small compared to the mean of the observations at these scales (2.16 mm and 8.56 mm, respectively).

The analysis of the average error (*Bias*) reflects a significant improvement in the IMERG_F at all scales, although much more appreciable at the monthly and annual scales. At the latter, the *Bias* decreases to 9.65 mm compared to the 159.22 mm recorded by

IMERG_E, which means a reduction of the error close to 90%. At the monthly scale, the error value decreases by about 16 times compared to the Early and Late products. While this significant error reduction could represent a good indicator of the improvement in precipitation estimation with IMERG_F, we must consider the limitations of this statistic and its relationship with the possible cancellation of positive and negative errors [64] between IMERG_F and ground-based observations.

As expected, as the temporal resolution decreases, there is a decrease in the *MAE* and the normalised *RMSE* regarding the mean for all products, with few differences at sub-daily scales. This behaviour is most evident in IMERG_F, in which the *MAE* decreases from 0.87 mm at 30 min to 0.22 mm at the annual scale, and the *RMSE* decreases from 1.73 mm to 0.31 mm. This improvement with a lower scale can be seen in the Taylor plot shown in Figure 5a, which displays the *STD*, *CC* and centred *RMSE* statistics normalised to the standard deviation of the three products for all temporal resolutions. A clear improvement in IMERG_F is observed at the monthly and annual scales, with values close to the benchmark (correlation and standard deviation equal to 1). The worst results are shown at the sub-daily scales with low correlation values and in the Early and Late products, with standard deviations higher than the benchmark unit. These differences between IMERG_F and the rest of the products, which grow with the increasing scale, highlight a gradual improvement as more information is integrated into the algorithm. Finally, while this product is expected to provide the most reliable estimates for research [47], the other two products can also be used for related to low latency applications [65].

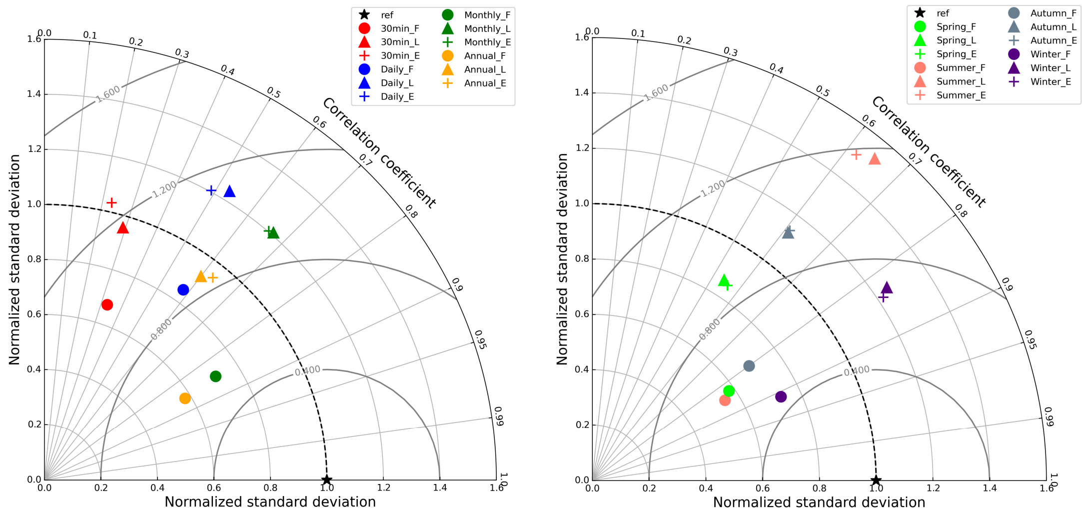

(**a**) (**b**)

Figure 5. (**a**) Taylor diagram at sub-daily, daily, monthly, and annual scales of the products IMERG_E, IMERG_L and IMERG_F. (**b**) Same as the (**a**) figure but shows seasonal scales.

In the seasonal analysis (Figure 5b), IMERG_E and IMERG_L overestimate the precipitation values substantially. These errors are more noticeable during the summer period with a systematic error of over 97 mm and *MAE* and *RMSE* values around 105 mm and 143 mm, respectively. Interestingly, in this period, IMERG_F introduces significant improvements that reduce the overestimation to less than 10%, but it is still the season of the year wherein the worst results are obtained. Precipitation in the summer months is low throughout the Iberian Peninsula and Catalonia, but local storms with convective development usually occur, wherein the amount of precipitation fallen is not adequately captured by IMERG.

The values of the errors in autumn, although lower than in summer, also show overestimates of precipitation in all products and *MAE* and *RMSE* values, which, even with the unbiasing of the Final product, remain relatively high (*MAE* equal to 52.09 mm and *RMSE* equal to 70.80 mm). A similar behaviour is observed in the rest of the seasons of the year, although the *RMSE* values practically double the *MAE* values, which may be caused by the occurrence of extreme phenomena and bring into play the sensitivity of this statistic in such records.

IMERG_F reproduces the annual cycle of precipitation relatively accurately, identifying the spring and autumn months as those that make the overall greatest contribution to the annual cycle amount, while the winter and summer months show the lowest accumulations with very few differences between them. On the other hand, IMERG_E and IMERG_L represent the summer period as the second highest contribution with an average of approximately 215 mm, higher than that recorded in the observations (118 mm), which is consistent with the overestimation made by these products during this period.

The correlation coefficient calculated at the different time scales showed statistical significance at 95% of confidence in all cases. In Figure 5a, at sub-daily scales, similar correlation values are shown among all products, and although a slight improvement appears in IMERG_F, it does not exceed 0.37. IMERG_E and IMERG_L at scales higher than daily show moderate linear correlations close to 0.6, and it is IMERG_F that represents high correlations, higher than 0.8. Similarly, there is a decrease in the standard deviation, closer to the reference point (*STD* = 1), as a result of the unbiasing to which it is subjected. The performance shown demonstrates that this product would be the most suitable for the analysis of precipitation at seasonal and annual scales.

3.3. Categorical Verification Scores for Different Time Scales

Figure 6 shows a summary of the contingency table verification score at the different time scales. For each dataset shown, a threshold greater than or equal to the mean of the observations recorded at each time step is applied.

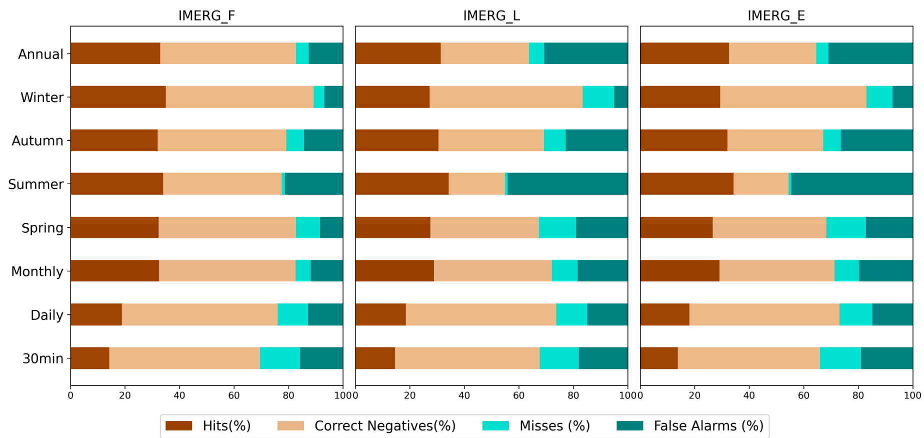

Figure 6. Fraction of events detected as hits, false alarms, misses and correct negatives for the three IMERG products at different time scales. The thresholds selected for each time scale coincide with the mean of the observations at that scale: Half-hourly (1.4 mm), Daily (8.6 mm), Monthly (52.8 mm), Spring (185.8 mm), Summer (118.8 mm), Autumn (203.9 mm), Winter (126.7 mm) and Annual (623.5 mm).

As shown in Figure 6, IMERG_F has a higher ability to detect correct negatives with values close to 50% at all scales, although IMERG_L and IMERG_E are also very similar at sub-daily and daily scales. The percentage of hits tends to increase at scales higher than daily, while the percentage of misses decreases. According to the selected thresholds, the ability of IMERG to estimate precipitation is affected by the detected false alarms. These represent the highest percentage during the summer period in IMERG_E and IMERG_L.

Figure 7 provides the performance of the *POD*, and the *FAR* values at different time scales for different precipitation thresholds. The error associated with the calculation of the statistic at each point, as outlined by Jolliffe and Stephenson [64], is also shown. The figure shows a clear improvement of IMERG estimates as time scale increases. At a half-hourly scale, the ability of IMERG to estimate events at different thresholds is remarkably poor.

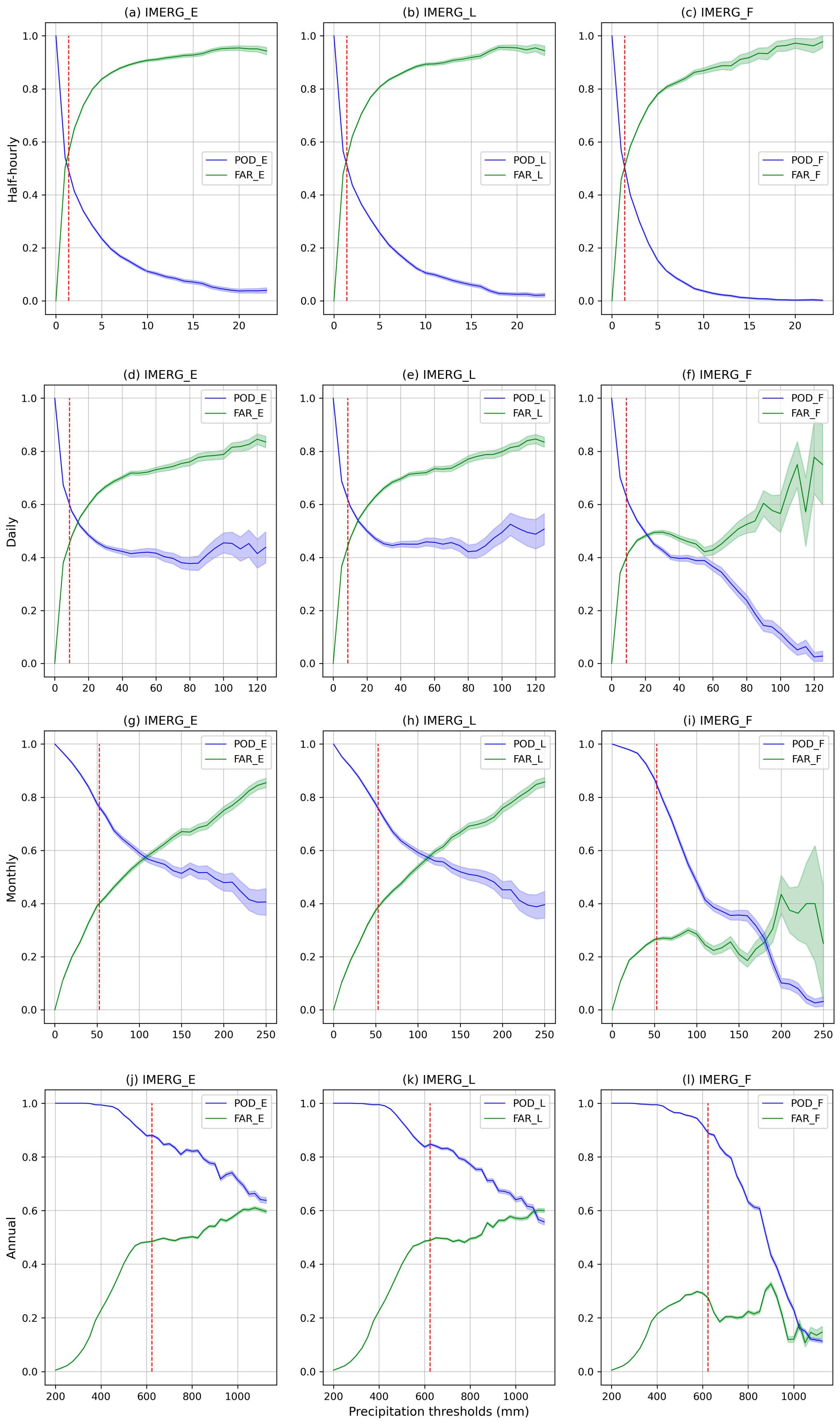

Figure 7. *POD*, *FAR* and errors associated at different time scales and precipitation thresholds. The vertical dashed red line represents the mean of the observations at each time scale.

If we consider the cut-off point between the *POD* and *FAR* line as a limit from which the satellite shows some decay in its event detection ability, we observe that it increases considerably with decreasing temporal resolution. At daily scales, this cut-off point occurs at around 20 mm/day, a value well above the 75th percentile of the sample, which indicates a much better performance compared to the estimation of events at the half-hourly scale, where a value slightly lower than the mean of the recorded observations at this scale is observed (1.4 mm/30 min).

Similarly, for the analysis at monthly and annual scales with cut-off points above 100 mm and 1000 mm, respectively, it ensures the correct identification of rainfall events up to this threshold. As higher thresholds of rainfall in the domain are assessed, the ability of the satellite decreases, highlighting the difficulty of IMERG to detect rainfall extremes at any scale.

Although the three products behave similarly, IMERG_F gives worse results, especially on scales above the monthly scale, wherein the *POD* values decrease faster than in the rest of the products, which is associated with the unbiasing effect induced by the calibration of GPCC stations. These results are consistent with Shawky et al. [66], which found no significant improvement of IMERG_F over IMERG_E in the arid environment of Oman. This result is in line with Sharifi et al. [16], Behrangi et al. [67] and Gosset et al. [68] when positing that the gauge adjustment product (IMERG_F) can change the precipitation amounts, but it cannot modify the occurrence of precipitation.

3.4. Half-Hourly IMERG Products for Different Terrain and Climate Conditions

This section will test the abilities and shortcomings of the three IMERG products at a high temporal resolution (30 min). In addition, differences in the estimation of precipitation by satellite products will be analysed when considering the terrain over which they are estimated and under different climatic conditions.

Figure 8 shows the differences over each station between IMERG and the rainfall records of the XEMA network. In valley areas, the analysis of the systematic error shows a marked underestimation of precipitation in IMERG_F, with mean values of −0.15 mm/30 min, which represents an underestimation of 10% regarding the rain gauges. IMERG_L and IMERG_E show a tendency to overestimate the accumulated values and show *MAE* and *RMSE* values even higher than 100% relative to the mean.

There is a more marked tendency in the behaviour of IMERG in areas representing ridgetops. While IMERG_E and IMERG_L overestimate precipitation, and this could be verified in all time scales, the effect of the calibration incorporated in IMERG_F causes a significant smoothing, such that the *Rbias* reaches critical values lower than −30% sometimes, as in the Bonaigua station (Z1) (Figure 2) at 2266 masl This marked underestimation and change in behaviour from one product to another is probably related to the low density of GPCC reference stations in high altitude areas for calibration. The *CC* shows a pattern in all three products with poor values, barely exceeding 0.3.

The largest errors occur in the stations in flat areas (Flat) with an average bias higher than 0.4 mm/30 min and *Rbias* values higher than 30% in IMERG_E and IMERG_L (Figure 8). Although IMERG_F significantly decreases the error, the tendency to overestimate the values is still maintained, and under this terrain classification the highest *MAE* and *RMSE* values regarding the mean are obtained (higher than 100% and 200%, respectively). In these areas, 43% of the automatic stations are located and analysed, which corresponds to the entire central inland part of the region of Catalonia, the coastal strip, the Ebro basin and the north-western part of the territory. This plays a significant role in the global results regardless of terrain classification.

Figure 9 evaluates the *Rbias* of the three IMERG products under different climatic classifications. For example, IMERG_E presents a large overestimation over the BSk stations and IMERG_F shows a high underestimation over the Df stations. Overall, a clear improvement in bias reduction is found for BSk and Csa stations when IMERG_F is compared to IMERG_E. The improvement is not so evident for the Cf stations, and in contrast, there is a clear bias increase for the Df stations. These results obtained for 30 min records coincide with previous studies by Navarro et al. [38] in the Ebro basin for seasonal and annual scales.

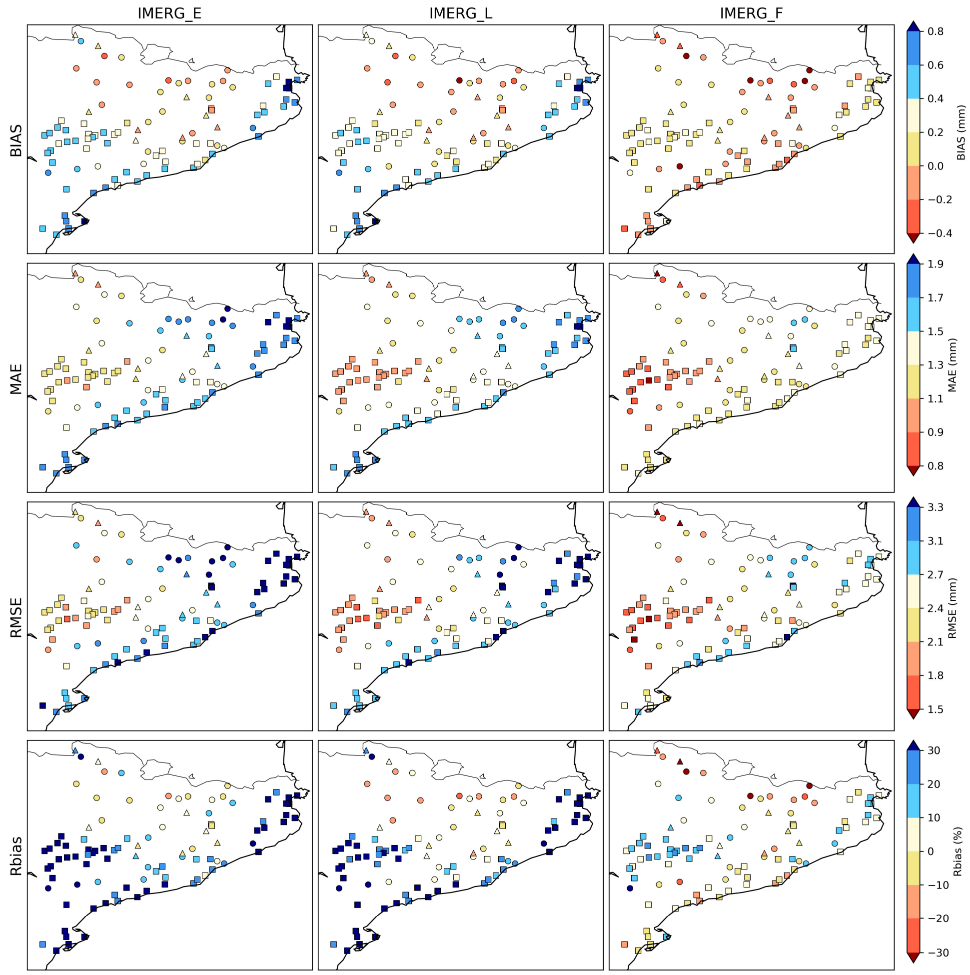

Figure 8. Distribution of Bias, MAE, RMS and Rbias errors at each station point and according to the orography type where they are located: Ridgetop (triangle), Flat (square), Valley (circle).

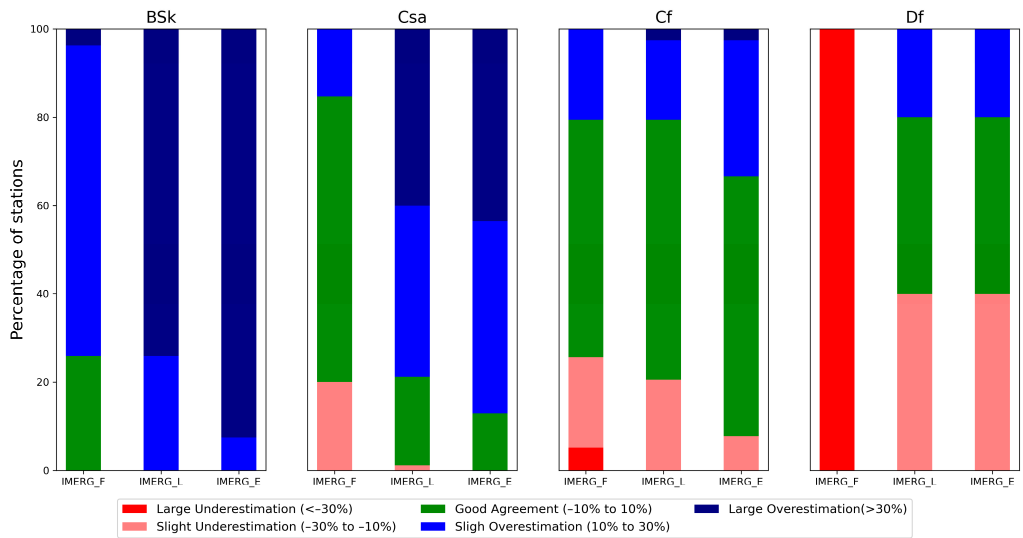

Figure 9. Stacked bars of the half-hourly relative error (*Rbias*) computed for each group of station for each climatic group. The colours represent the five categories of *Rbias* described in the legend.

3.5. Intensity

Table 5 shows a summary of the statistics obtained in the validation process of three IMERG products, considering five categories of rainfall intensity recorded in 30 min. The categories of light, moderate, intense, very intense and torrential rain were scaled from a previous classification of rainfall intensity in 1 h, according to sources from the Spanish Meteorological Agency (AEMET) [59].

Table 5. Summary of statistics calculated according to the intensity of rainfall recorded by rain gauges in 30 min.

	N	*BIAS* (mm)	*Mbias*	*Rbias* (%)	*MAE* (mm)	*RMSE* (mm)
			light (0.1 ≤ Pr < 1)			
IMERG_F	177039	0.56	2.35	134.83	0.70	1.25
IMERG_L	177039	0.76	2.81	181.30	0.90	1.81
IMERG_E	177039	0.85	3.04	203.89	1.00	2.06
			moderate (1 ≤ Pr < 7.5)			
IMERG_F	94589	−0.62	0.74	−25.68	1.55	2.15
IMERG_L	94589	−0.28	0.88	−11.54	1.81	2.70
IMERG_E	94589	−0.27	0.89	−11.31	1.91	2.89
			heavy (7.5 ≤ Pr < 15)			
IMERG_F	4553	−7.37	0.28	−71.98	7.55	8.12
IMERG_L	4553	−6.36	0.38	−62.12	7.07	7.79
IMERG_E	4553	−6.56	0.36	−64.04	7.34	8.05
			very heavy (15 ≤ Pr < 30)			
IMERG_F	1296	−16.54	0.16	−83.65	16.63	17.32
IMERG_L	1296	−14.89	0.25	−75.32	15.18	16.16
IMERG_E	1296	−15.07	0.24	−76.23	15.41	16.40
			torrential (Pr ≥ 30)			
IMERG_F	139	−32.57	0.11	−89.47	32.57	33.19
IMERG_L	139	−29.63	0.19	−81.40	29.63	30.70
IMERG_E	139	−28.98	0.20	−79.60	28.98	30.53

The results obtained show substantial overestimation discrepancies for all rainfall intensity categories and in all IMERG products. Light rainfall, represented by the highest number of records, is overestimated by twice as much *Mbias* by IMERG_F and nearly three times as much by the rest of the products. This implies a relative error rate (*Rbias*) higher than 100% in all cases and a systematic error significantly higher than the mean of the observations. The best performance based on the *MAE* and *RMSE* is obtained by IMERG_F, although they are still quite high compared to the average of the studied records. Such indicators of overestimation in this category have been reported in previous studies [23,27].

On the contrary, at precipitation thresholds above 1 mm/30 min (moderate, heavy, very heavy and torrential), IMERG shows a tendency to underestimate precipitation, which becomes more significant as the intensity of precipitation increases (Figure 10). For the classes heavy, very heavy and torrential, the satellite shows errors ranging between −60% and −90% of the deficit in relation to the rain gauges. The systematic errors in these groups are similar in magnitude to the mean absolute errors and to the mean of the values recorded by the stations in each of the corresponding thresholds, which register a more realistic, significant underestimation.

Among the three products, IMERG_F provides the worst results, while IMERG_L presents the best values, although these differences are not marked. These results are in agreement with studies by Mazzoglio et al. [69] and show the challenge of detecting precipitation extremes at this resolution. Many of these extremes occur in the form of short and local intense rainfall, so they cannot be correctly captured due to the spatial and temporal resolution of satellite sensors. Precipitation at the daily and sub-daily scales is much more variable than monthly precipitation, and regional effects such as topography and local circulation play an important role in rainfall occurrence and distribution [16].

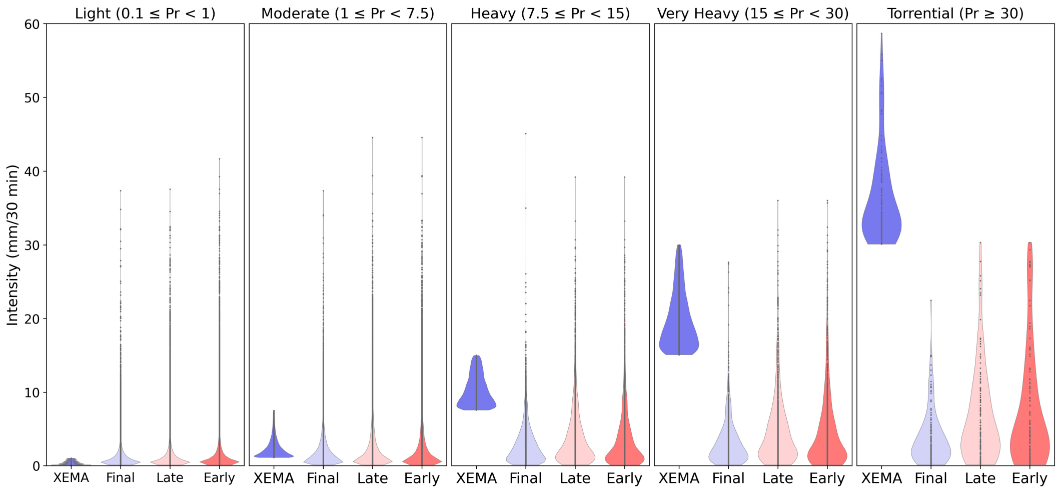

Figure 10. Violin plots of half-hourly rain gauge observations (XEMA) and IMERG products for the five rainfall intensity classes considered. Rainfall rate thresholds are given in mm/30 min.

4. Discussion

In line with previous work, IMERG roughly reproduces the spatial pattern and temporal variability of rainfall in the region of study [17,24,70]. However, there are differences in the magnitude estimation for the different run types: Early, Late and Final. While there is a tendency to overestimate the accumulations in the Early and Late products across the whole territory, IMERG_F reduces the errors and shows a better ability to estimate the amount of precipitation at all time scales, with higher accuracy at monthly, seasonal and annual scales. However, for this product, there is again a tendency to underestimate in areas with complex topography, i.e., high mountain areas such as the Pyrenees. This result is reasonable and has been reported in other high mountain areas [17]. Navarro et al. [38] and Tapiador et al. [37] suggested that this may be due to the lack of rain gauges contributing to the GPCC in high altitude areas, as well as to the low resolution of the GPCC grid ($1^\circ \times 1^\circ$), which makes detection difficult in areas wherein precipitation is highly variable at small scales. Finally, Navarro et al. [38] also mentioned the reduced detection capacity of IMERG in the identification of convective orographic rainfall, mainly related to mesoscale factors.

At the seasonal scale, a similar underestimation is observed in the Final product at all temporal scales. However, in the Early and Late products, significant errors appear during the summer with a tendency to overestimate the cumulates producing high *MAE* and *RMSE* errors. This differs from the studies of Moazam and Najafi, [13] and Navarro et al. [71], wherein the worst results were obtained mainly during winter, when the ground surface is covered with snow and ice [24]. However, our results are in line with Retalis et al. [15], in which the best results were obtained in the rainy seasons (winter and autumn). In semi-arid areas, the summer period is represented by low precipitation values, which makes detection by satellite sensors difficult [17]. Another important issue to consider is that precipitation can be affected by a high rate of evaporation, where some of the liquid water evaporates during the fall process and is no longer part of the effective precipitation [26,31,72], a virga being the extreme case wherein no precipitation reaches the ground. This phenomenon, coupled with the fact that satellite retrievals of precipitation are based on the structure of cloud systems [73] and may not adequately account for the level of evaporation, may lead to the overestimation of precipitation in arid regions.

The effect of not accounting for evaporation in semi-arid areas further explains that, in terms of precipitation event detection, the error in IMERG is dominated by the occurrence of false alarms, especially in summer. In the occurrence of typical deep convective clouds with relatively cold cloud tops (anvils) and, with the absence of PMW measurements, the IR algorithm may falsely assign precipitation to pixels with cold brightness temperature values [74]. Furthermore, in terms of IMERG's ability to detect events given a continuous threshold of cumulates, no significant improvement of one product over the other is observed. In fact, IMERG_E and IMERG_L offer better performance as the thresholds grow with more stable *POD* and *FAR* values and lower uncertainty in the statistics. This is related to the inability of IMERG_F to detect extremes, similarly associated to the calibration of GPCC.

Few studies include the validation of IMERG at the highest temporal resolution (30 min). Even so, the authors of [26,75] agree on the decreased estimation capability of the three products with increasing temporal resolution. The repetition time of the GPM and the downscaling and interpolation procedures to 30 min [76] are some of the main causes of the errors obtained. At this scale, the largest errors occur in flat areas, which coincides with the BSk climate, with a tendency to overestimate. The authors of [38] found that in these areas, IMERG tended to overestimate precipitation equally. These regions, mainly represented in our study by inland depressions (Ebro valley) and coastal areas, are affected by extreme precipitation events occurring at local scales. Orographic factors and mesoscale conditions generate an uneven distribution of precipitation over the territory, resulting in a very spatially uncorrelated precipitation field [37] and therefore an added challenge for satellite estimates.

Finally, the overestimation of lightprecipitation associated with the detection of false alarms and the underestimation of precipitation extremes reflects a similar behaviour to that found in the Tibetan Plateau [27]. Along these lines, it is important to be aware of the limitations of the assessment procedure, which may influence the accuracy of the results. Firstly, it is worth mentioning that the rain gauge data used were not corrected for the effect of wind, so the measurements may suffer from systematic biases caused by wind-induced evaporation loss and the underestimation of trace values [24]. On the other hand, in terms of the pixel-to-point method, although it has advantages over other methods [70], it is very difficult for a (point-scale) rain gauge to represent the actual precipitation situation in an IMERG pixel-scale range. These inherent differences between the rain gauge estimate and the precipitation in the satellite area can directly influence the high values of false alarms, as well as the detection of extreme precipitation events occurring at the local scale. Especially in a region like Catalonia, characterised by its orographic complexity and climatic variability, more rain gauges per IMERG cell may provide better results.

5. Conclusions

The main purpose of the current study focused on a comprehensive evaluation of IMERG precipitation estimates in its three Early, Late and Final runs based on information from 186 automatic weather stations, managed by the Meteorological Service of Catalonia (NE Spain). The evaluation was carried out at different time scales (semi-hourly, hourly, daily, monthly, seasonal and annual) over a period of 6 years (2015–2020), based on the analysis of several metrics that quantify the error in precipitation accumulations. Similarly, the behaviour of IMERG was evaluated at a high resolution (30 min) under different topographic conditions (valley, flat, ridgetop), climatic conditions (BSk, Csa, Csb, Dfb) and under different precipitation intensity thresholds (light, moderate, heavy, very heavy, torrential). The main findings of the study are:

1. IMERG generally captures the spatial–temporal pattern and variability of annual mean precipitation. However, discrepancies appear in the estimation of the magnitude. While IMERG_E and IMERG_L overestimate precipitation by 20% in practically the whole territory, IMERG_F reduces the error significantly, yielding only 2%. The calibration performance in this run may even cause an underestimation of precipitation in areas of complex orography such as the Pyrenees.

2. The calculated statistics showed a significant improvement with decreasing temporal resolutions, with the monthly, seasonal and annual scales showing the best results in the estimation of precipitation accumulations. In contrast, the sub-daily scales showed high *Bias* values and very low correlation values, indicating the remaining challenge for satellite sensors to estimate precipitation at very high temporal resolutions. IMERG_F showed much better error statistics compared to IMERG_E and IMERG_L, wherein a generalised overestimation was evident and especially marked during the summer period.
3. Similarly, the analysis of the *POD* and *FAR* showed a greater ability of IMERG to identify precipitation events at scales greater than daily, wherein a stable behaviour of the statistics is observed well above the mean values, although with deficiencies in the identification of extreme events at all scales. The proportion of false alarms is a problem for IMERG especially during the summer, which is mainly associated with the detection of false precipitation in the form of lightrainfall (which is likely influenced by evaporation processes not assimilated by the algorithm), as well as the underestimation of locally occurring heavy precipitation.
4. The worst results were obtained on a semi-hourly scale represented by flat areas and under a BSk climate, wherein IMERG shows a tendency to overestimate rainfall.
5. IMERG tends to overestimate light precipitation, while it tends to underestimate accumulated precipitation in the rest of the intensity thresholds studied, especially those marked by high intensity precipitation. Associated with these errors is the fundamental role of taking rainfall gauges on a point scale that may not represent the spatial and temporal variability of rainfall in a region where this variable is spatially uncorrelated.

The evaluation of IMERG products presented here, although not the first one in Spain, is the first to address in detail the orographic and climatic factors at high temporal resolutions. Furthermore, we attempted to cover some of the most common weaknesses of this type of research by extending the analysis simultaneously to different temporal resolutions and by emphasising the analysis at high temporal resolutions. This study can be used by other researchers and developers involved in the IMERG algorithm to introduce improvements in future versions. Additionally, although with the limitation of latency, time observation and monitoring could be considered in operational work. For more applications based on the results presented here, and to try to answer some of the questions raised, in future work we intend to study in greater depth the capacity of IMERG to detect extreme events and to identify the specific behaviour of IMERG contributing sensors such as MW and IR.

Author Contributions: Conceptualization, E.P. and J.B.; methodology, E.P. and J.B.; formal analysis, E.P.; data curation, E.P.; writing—original draft preparation, E.P.; writing—review and editing, all the authors.; visualization, E.P.; supervision, J.B. and M.U. All authors have read and agreed to the published version of the manuscript.

Funding: This research was partly funded by the project "Analysis of Precipitation Processes in the Eastern Ebro Subbasin" (WISE-PreP, RTI2018-098693-B-C32 and ARTEMIS, PID2021-124253OB-I00 MINECO/FEDER) and the Water Research Institute (IdRA) of the University of Barcelona.

Data Availability Statement: IMERG data were downloaded from https://gpm.nasa.gov/data/directory and meteo.cat data were downloaded from https://www.meteo.cat/wpweb/serveis/cataleg-de-serveis/serveis-oberts/dades-obertes/.

Acknowledgments: Satellite and gauge data for this study were provided by NASA/JAXA and meteo.cat, respectively. The authors wish to thank the support from the Secretariat for Universities and Research of the Ministry of Business and Knowledge of the Government of Catalonia and the European Social Fund.

Conflicts of Interest: The authors declare no conflict of interest.

Appendix A

Table A1 provides an overview of the data available for each temporal resolution considered in the study. The first column lists the maximum number of possible data records for each temporal resolution, calculated considering the number of existing stations for each year, which varies from 183 to 188 stations depending on the year. The second and third columns show the number and percentage of records verifying Criterion 1 (80% minimum availability of records needed for a given temporal period). The fourth and fifth column show the number and percentage of records verifying Criterion 2 (amounts equal to or higher than 0.1 mm for both rain gauge and IMERG products).

Table A1. Data availability for each temporal resolution considered in the study.

Temporal Resolution	Maximum Number of Records	Criterion 1		Criterion 2	
		Number of Records	Percentage (%)	Number of Records	Percentage (%)
half-hourly	19,482,432	18,804,667	97	277,616	1
daily	405,884	391,446	96	70,399	17
monthly	13,332	12,864	96	12,802	96
spring	1111	996	90	996	90
summer	1111	1020	92	1020	92
autumn	1111	1032	93	1032	93
winter	923	820	89	820	89
annual	1111	1034	93	1034	93

Appendix B

Table A2. Different climate areas of the Köppen climate classification [77–79] considered in this study.

Code	Description	Group
BSk	Cold semi-arid (steppe) climate	Arid
Csa	Hot-summer Mediterranean climate	Temperate
Cf	Temperate without dry season	Temperate
Df	Continental without dry season	Cold (continental)

References

1. Collins, M.; Knutti, R.; Arblaster, J.; Dufresne, J.-L.; Fichefet, T.; Friedlingstein, P.; Gao, X.; Gutowski, W.J.; Johns, T.; Krinner, G. Long-Term Climate Change: Projections, Commitments and Irreversibility. In *Climate Change 2013-The Physical Science Basis: Contribution of Working Group I to the Fifth Assessment Report of the Intergovernmental Panel on Climate Change*; Cambridge University Press: New York, NY, USA, 2013; pp. 1029–1136.
2. Lionello, P.; Scarascia, L. The relation between climate change in the Mediterranean region and global warming. *Reg. Environ. Change* **2018**, *18*, 1481–1493. [CrossRef]
3. AR5 Climate Change 2013: The Physical Science Basis—IPCC. Available online: https://www.ipcc.ch/report/ar5/wg1/ (accessed on 14 July 2022).
4. Kohler, T.; Giger, M.; Hurni, H.; Ott, C.; Wiesmann, U.; Wymann Von Dach, S.; Maselli, D. Mountains and Climate Change: A Global Concern. *Mt. Res. Dev.* **2010**, *30*, 53–55. [CrossRef]
5. Clark, M.P.; Slater, A.G. Probabilistic Quantitative Precipitation Estimation in Complex Terrain. *J. Hydrometeorol.* **2006**, *7*, 3–22. [CrossRef]
6. Bech, J.; Codina, B.; Lorente, J.; Bebbington, D. The Sensitivity of Single Polarization Weather Radar Beam Blockage Correction to Variability in the Vertical Refractivity Gradient. *J. Atmos. Ocean. Technol.* **2003**, *20*, 845–855. [CrossRef]
7. Casellas, E.; Bech, J.; Veciana, R.; Pineda, N.; Rigo, T.; Miró, J.R.; Sairouni, A. Surface precipitation phase discrimination in complex terrain. *J. Hydrol.* **2021**, *592*, 125780. [CrossRef]
8. Scofield, R.A.; Kuligowski, R. Status and Outlook of Operational Satellite Precipitation Algorithms for Extreme-Precipitation Events. *Weather Forecast.* **2003**, *18*, 1037–1051. [CrossRef]
9. Huffman, G.J.; Bolvin, D.T.; Braithwaite, D.; Hsu, K.; Joyce, R.; Xie, P.; Yoo, S.-H. NASA Global Precipitation Measurement (GPM) Integrated Multi-Satellite Retrievals for GPM (IMERG). *Algorithm Theor. Basis Doc. ATBD Version* **2015**, *4*, 26.

10. Hou, A.Y.; Kakar, R.K.; Neeck, S.; Azarbarzin, A.A.; Kummerow, C.D.; Kojima, M.; Oki, R.; Nakamura, K.; Iguchi, T. The global precipitation measurement mission. *Bull. Am. Meteorol. Soc.* **2014**, *95*, 701–722. [CrossRef]
11. Pradhan, R.K.; Markonis, Y.; Godoy, M.R.V.; Villalba-Pradas, A.; Andreadis, K.M.; Nikolopoulos, E.I.; Papalexiou, S.M.; Rahim, A.; Tapiador, F.J.; Hanel, M. Review of GPM IMERG performance: A global perspective. *Remote Sens. Environ.* **2022**, *268*, 112754. [CrossRef]
12. Nascimento, J.G.; Althoff, D.; Bazame, H.C.; Neale, C.M.U.; Duarte, S.N.; Ruhoff, A.L.; Gonçalves, I.Z. Evaluating the Latest IMERG Products in a Subtropical Climate: The Case of Paraná State, Brazil. *Remote Sens.* **2021**, *13*, 906. [CrossRef]
13. Moazami, S.; Najafi, M. A comprehensive evaluation of GPM-IMERG V06 and MRMS with hourly ground-based precipitation observations across Canada. *J. Hydrol.* **2021**, *594*, 125929. [CrossRef]
14. Ramadhan, R.; Yusnaini, H.; Marzuki, M.; Muharsyah, R.; Suryanto, W.; Sholihun, S.; Vonnisa, M.; Harmadi, H.; Ningsih, A.P.; Battaglia, A.; et al. Evaluation of GPM IMERG Performance Using Gauge Data over Indonesian Maritime Continent at Different Time Scales. *Remote Sens.* **2022**, *14*, 1172. [CrossRef]
15. Retalis, A.; Katsanos, D.; Tymvios, F.; Michaelides, S. Comparison of GPM IMERG and TRMM 3B43 Products over Cyprus. *Remote Sens.* **2020**, *12*, 3212. [CrossRef]
16. Sharifi, E.; Steinacker, R.; Saghafian, B. Multi time-scale evaluation of high-resolution satellite-based precipitation products over northeast of Austria. *Atmos. Res.* **2018**, *206*, 46–63. [CrossRef]
17. Zhang, Y.; Hanati, G.; Danierhan, S.; Liu, Q.; Xu, Z. Evaluation and Comparison of Daily GPM/TRMM Precipitation Products over the Tianshan Mountains in China. *Water* **2020**, *12*, 3088. [CrossRef]
18. Zhou, Z.; Guo, B.; Xing, W.; Zhou, J.; Xu, F.; Xu, Y. Comprehensive evaluation of latest GPM era IMERG and GSMaP precipitation products over mainland China. *Atmos. Res.* **2020**, *246*, 105132. [CrossRef]
19. Lei, H.; Li, H.; Zhao, H.; Ao, T.; Li, X. Comprehensive evaluation of satellite and reanalysis precipitation products over the eastern Tibetan plateau characterized by a high diversity of topographies. *Atmos. Res.* **2021**, *259*, 105661. [CrossRef]
20. Mahmoud, M.T.; Mohammed, S.A.; Hamouda, M.A.; Mohamed, M.M. Impact of Topography and Rainfall Intensity on the Accuracy of IMERG Precipitation Estimates in an Arid Region. *Remote Sens.* **2021**, *13*, 13. [CrossRef]
21. Mayor, Y.G.; Tereshchenko, I.; Fonseca-Hernández, M.; Pantoja, D.A.; Montes, J.M. Evaluation of Error in IMERG Precipitation Estimates under Different Topographic Conditions and Temporal Scales over Mexico. *Remote Sens.* **2017**, *9*, 503. [CrossRef]
22. Rojas, Y.; Minder, J.R.; Campbell, L.S.; Massmann, A.; Garreaud, R. Assessment of GPM IMERG satellite precipitation estimation and its dependence on microphysical rain regimes over the mountains of south-central Chile. *Atmos. Res.* **2021**, *253*, 105454. [CrossRef]
23. Sharifi, E.; Steinacker, R.; Saghafian, B. Assessment of GPM-IMERG and Other Precipitation Products against Gauge Data under Different Topographic and Climatic Conditions in Iran: Preliminary Results. *Remote Sens.* **2016**, *8*, 135. [CrossRef]
24. Sharma, S.; Chen, Y.; Zhou, X.; Yang, K.; Li, X.; Niu, X.; Hu, X.; Khadka, N. Evaluation of GPM-Era Satellite Precipitation Products on the Southern Slopes of the Central Himalayas Against Rain Gauge Data. *Remote Sens.* **2020**, *12*, 1836. [CrossRef]
25. Anjum, M.N.; Ahmad, I.; Ding, Y.; Shangguan, D.; Zaman, M.; Ijaz, M.W.; Sarwar, K.; Han, H.; Yang, M. Assessment of IMERG-V06 Precipitation Product over Different Hydro-Climatic Regimes in the Tianshan Mountains, North-Western China. *Remote Sens.* **2019**, *11*, 2314. [CrossRef]
26. Chen, C.; Chen, Q.; Duan, Z.; Zhang, J.; Mo, K.; Li, Z.; Tang, G. Multiscale Comparative Evaluation of the GPM IMERG v5 and TRMM 3B42 v7 Precipitation Products from 2015 to 2017 over a Climate Transition Area of China. *Remote Sens.* **2018**, *10*, 944. [CrossRef]
27. Wang, X.; Ding, Y.; Zhao, C.; Wang, J. Similarities and improvements of GPM IMERG upon TRMM 3B42 precipitation product under complex topographic and climatic conditions over Hexi region, Northeastern Tibetan Plateau. *Atmos. Res.* **2019**, *218*, 347–363. [CrossRef]
28. Fang, J.; Yang, W.; Luan, Y.; Du, J.; Lin, A.; Zhao, L. Evaluation of the TRMM 3B42 and GPM IMERG products for extreme precipitation analysis over China. *Atmos. Res.* **2019**, *223*, 24–38. [CrossRef]
29. Hosseini-Moghari, S.; Tang, Q. Can IMERG Data Capture the Scaling of Precipitation Extremes With Temperature at Different Time Scales? *Geophys. Res. Lett.* **2022**, *49*, e2021GL096392. [CrossRef]
30. Sungmin, O.; Foelsche, U.; Kirchengast, G.; Fuchsberger, J.; Tan, J.; Petersen, W.A. Evaluation of GPM IMERG Early, Late, and Final rainfall estimates using WegenerNet gauge data in southeastern Austria. *Hydrol. Earth Syst. Sci.* **2017**, *21*, 6559–6572. [CrossRef]
31. Wang, S.; Liu, J.; Wang, J.; Qiao, X.; Zhang, J. Evaluation of GPM IMERG V05B and TRMM 3B42V7 Precipitation Products over High Mountainous Tributaries in Lhasa with Dense Rain Gauges. *Remote Sens.* **2019**, *11*, 2080. [CrossRef]
32. Yang, M.; Liu, G.; Chen, T.; Chen, Y.; Xia, C. Evaluation of GPM IMERG precipitation products with the point rain gauge records over Sichuan, China. *Atmos. Res.* **2020**, *246*, 105101. [CrossRef]
33. Zhang, D.; Yang, M.; Ma, M.; Tang, G.; Wang, T.; Zhao, X.; Ma, S.; Wu, J.; Wang, W. Can GPM IMERG Capture Extreme Precipitation in North China Plain? *Remote Sens.* **2022**, *14*, 928. [CrossRef]
34. Kazamias, A.-P.; Sapountzis, M.; Lagouvardos, K. Evaluation of GPM-IMERG rainfall estimates at multiple temporal and spatial scales over Greece. *Atmos. Res.* **2022**, *269*, 106014. [CrossRef]
35. Caracciolo, D.; Francipane, A.; Viola, F.; Noto, L.V.; Deidda, R. Performances of GPM satellite precipitation over the two major Mediterranean islands. *Atmos. Res.* **2018**, *213*, 309–322. [CrossRef]
36. Chiaravalloti, F.; Brocca, L.; Procopio, A.; Massari, C.; Gabriele, S. Assessment of GPM and SM2RAIN-ASCAT rainfall products over complex terrain in southern Italy. *Atmos. Res.* **2018**, *206*, 64–74. [CrossRef]
37. Tapiador, F.J.; Navarro, A.; García-Ortega, E.; Merino, A.; Sánchez, J.L.; Marcos, C.; Kummerow, C. The Contribution of Rain Gauges in the Calibration of the IMERG Product: Results from the First Validation over Spain. *J. Hydrometeorol.* **2020**, *21*, 161–182. [CrossRef]

38. Navarro, A.; García-Ortega, E.; Merino, A.; Sánchez, J.L.; Tapiador, F.J. Orographic biases in IMERG precipitation estimates in the Ebro River basin (Spain): The effects of rain gauge density and altitude. *Atmos. Res.* **2020**, *244*, 105068. [CrossRef]
39. Tapiador, F.; Villalba-Pradas, A.; Navarro, A.; Martín, R.; Merino, A.; García-Ortega, E.; Sánchez, J.; Kim, K.; Lee, G. A Satellite View of an Intense Snowfall in Madrid (Spain): The Storm 'Filomena' in January 2021. *Remote Sens.* **2021**, *13*, 2702. [CrossRef]
40. Trapero, L.; Bech, J.; Rigo, T.; Pineda, N.; Forcadell, D. Uncertainty of precipitation estimates in convective events by the Meteorological Service of Catalonia radar network. *Atmos. Res.* **2009**, *93*, 408–418. [CrossRef]
41. Martín-Vide, J.; Vallvé, M.B. The use of rogation ceremony records in climatic reconstruction: A case study from Catalonia (Spain). *Clim. Change* **1995**, *30*, 201–221. [CrossRef]
42. Trapero, L.; Bech, J.; Duffourg, F.; Esteban, P.; Lorente, J. Mesoscale numerical analysis of the historical November 1982 heavy precipitation event over Andorra (Eastern Pyrenees). *Nat. Hazards Earth Syst. Sci.* **2013**, *13*, 2969–2990. [CrossRef]
43. Lana, X.; Serra, C.; Burgueño, A. Patterns of monthly rainfall shortage and excess in terms of the standardized precipitation index for Catalonia (NE Spain). *Int. J. Clim.* **2001**, *21*, 1669–1691. [CrossRef]
44. Casellas, E.; Bech, J.; Veciana, R.; Miró, J.R.; Sairouni, A.; Pineda, N. A meteorological analysis interpolation scheme for high spatial-temporal resolution in complex terrain. *Atmos. Res.* **2020**, *246*, 105103. [CrossRef]
45. Llasat, M.C.; Marcos, R.; Turco, M.; Gilabert, J.; Llasat-Botija, M. Trends in flash flood events versus convective precipitation in the Mediterranean region: The case of Catalonia. *J. Hydrol.* **2016**, *541*, 24–37. [CrossRef]
46. Llasat, M.C.; Puigcerver, M. Total Rainfall and Convective Rainfall in Catalonia, Spain. *Int. J. Climatol.* **1997**, *17*, 1683–1695. [CrossRef]
47. Huffman, G.J.; Bolvin, D.T.; Braithwaite, D.; Hsu, K.-L.; Joyce, R.J.; Kidd, C.; Nelkin, E.J.; Sorooshian, S.; Stocker, E.F.; Tan, J. Integrated multi-satellite retrievals for the Global Precipitation Measurement (GPM) mission (IMERG). In *Satellite Precipitation Measurement*; Advances in Global Change Research; Levizzani, V., Kidd, C., Kirschbaum, D.B., Kummerow, C.D., Nakamura, K., Turk, F.J., Eds.; Springer International Publishing: Cham, Switzerland, 2020; Volume 1, pp. 343–353. ISBN 978-3-030-24568-9.
48. GES DISC. Available online: https://disc.gsfc.nasa.gov/ (accessed on 22 July 2022).
49. Servei Meteorològic de Catalunya. Dades Obertes. Available online: https://www.meteo.cat/wpweb/serveis/cataleg-de-serveis/serveis-oberts/dades-obertes/ (accessed on 22 July 2022).
50. Llabrés-Brustenga, A.; Rius, A.; Rodríguez-Solà, R.; Casas-Castillo, M.C.; Redaño, A. Quality control process of the daily rainfall series available in Catalonia from 1855 to the present. *Arch. Meteorol. Geophys. Bioclimatol. Ser. B* **2019**, *137*, 2715–2729. [CrossRef]
51. Llabrés-Brustenga, A.; Rius, A.; Rodríguez-Solà, R.; Casas-Castillo, M.C. Influence of regional and seasonal rainfall patterns on the ratio between fixed and unrestricted measured intervals of rainfall amounts. *Arch. Meteorol. Geophys. Bioclimatol. Ser. B* **2020**, *140*, 389–399. [CrossRef]
52. WMO. *Guide to Hydrological Practices: Data Aquisition and Processing, Analysis, Forecasting and Other Applications*; WMO: Geneva, Switzerland, 1994.
53. Connector QGIS Open ICGC. Institut Cartogràfic i Geològic de Catalunya. Available online: http://www.icgc.cat/es/Aplicaciones/Herramientas/Connector-QGIS-Open-ICGC (accessed on 30 September 2022).
54. De Reu, J.; Bourgeois, J.; Bats, M.; Zwertvaegher, A.; Gelorini, V.; De Smedt, P.; Chu, W.; Antrop, M.; De Maeyer, P.; Finke, P.; et al. Application of the topographic position index to heterogeneous landscapes. *Geomorphology* **2013**, *186*, 39–49. [CrossRef]
55. Jenness, J.; Brost, B.; Beier, P. Land Facet Corridor Designer. Rocky Mountain Research Station | RMRS—US Forest Service. 2013. Available online: http://corridordesign.org/dl/tools/CorridorDesigner_EvaluationTools.pdf (accessed on 10 April 2022).
56. Majka, D.; Beier, P.; Jenness, J. CorridorDesigner ArcGIS Toolbox Tutorial. Environmental. Research, Development and. Education for the New Economy. (ERDENE) Initiative from. Northern Arizona University. 2007. Available online: http://corridordesign.org/downloads (accessed on 14 April 2022).
57. Clima. Available online: http://atlasnacional.ign.es/wane/Clima (accessed on 22 July 2022).
58. Resampling. Available online: https://docs.qgis.org/2.6/en/docs/user_manual/processing_algs/saga/grid_tools/resampling.html (accessed on 28 April 2022).
59. AEMET-Agencia Estatal de Meteorología Intensidad de Precipitación. Available online: https://meteoglosario.aemet.es/es/termino/427_intensidad-de-precipitacion (accessed on 28 April 2022).
60. Functions—Pingouin 0.5.2 Documentation. Available online: https://pingouin-stats.org/api.html (accessed on 22 July 2022).
61. Romero, R.; Guijarro, J.A.; Ramis, C.; Alonso, S. A 30-Year (1964–1993) Daily Rainfall Data Base for the Spanish Mediterranean Regions: First Exploratory Study. *Int. J. Climatol.* **1998**, *18*, 541–560. [CrossRef]
62. Gonzalez, S.; Bech, J. Extreme point rainfall temporal scaling: A long term (1805-2014) regional and seasonal analysis in Spain. *Int. J. Clim.* **2017**, *37*, 5068–5079. [CrossRef]
63. Sumner, G.; Homar, V.; Ramis, C. Precipitation seasonality in eastern and southern coastal Spain. *Int. J. Clim.* **2001**, *21*, 219–247. [CrossRef]
64. Jolliffe, I.T.; Stephenson, D.B. *Forecast Verification: A Practitioner's Guide in Atmospheric Science*; John Wiley & Sons: Hoboken, NJ, USA, 2012; ISBN 978-1-119-96107-9.
65. Tan, J.; Huffman, G.J.; Bolvin, D.T.; Nelkin, E.J. IMERG V06: Changes to the Morphing Algorithm. *J. Atmos. Ocean. Technol.* **2019**, *36*, 2471–2482. [CrossRef]
66. Shawky, M.; Moussa, A.; Hassan, Q.K.; El-Sheimy, N. Performance Assessment of Sub-Daily and Daily Precipitation Estimates Derived from GPM and GSMaP Products over an Arid Environment. *Remote Sens.* **2019**, *11*, 2840. [CrossRef]

67. Behrangi, A.; Tian, Y.; Lambrigtsen, B.H.; Stephens, G.L. What Does CloudSat Reveal about Global Land Precipitation Detection by Other Spaceborne Sensors? *Water Resour. Res.* **2014**, *50*, 4893–4905. [CrossRef]
68. Gosset, M.; Viarre, J.; Quantin, G.; Alcoba, M. Evaluation of several rainfall products used for hydrological applications over West Africa using two high-resolution gauge networks. *Q. J. R. Meteorol. Soc.* **2013**, *139*, 923–940. [CrossRef]
69. Mazzoglio, P.; Laio, F.; Balbo, S.; Boccardo, P.; Disabato, F. Improving an Extreme Rainfall Detection System with GPM IMERG data. *Remote Sens.* **2019**, *11*, 677. [CrossRef]
70. Yu, C.; Hu, D.; Liu, M.; Wang, S.; Di, Y. Spatio-temporal accuracy evaluation of three high-resolution satellite precipitation products in China area. *Atmos. Res.* **2020**, *241*, 104952. [CrossRef]
71. Navarro, A.; García-Ortega, E.; Merino, A.; Sánchez, J.L.; Kummerow, C.; Tapiador, F.J. Assessment of IMERG Precipitation Estimates over Europe. *Remote Sens.* **2019**, *11*, 2470. [CrossRef]
72. Wang, X.; Ding, Y.; Zhao, C.; Wang, J. Validation of TRMM 3B42V7 Rainfall Product under Complex Topographic and Climatic Conditions over Hexi Region in the Northwest Arid Region of China. *Water* **2018**, *10*, 1006. [CrossRef]
73. Michaelides, S.; Levizzani, V.; Anagnostou, E.; Bauer, P.; Kasparis, T.; Lane, J.E. Precipitation: Measurement, Remote Sensing, Climatology and Modeling. *Atmos. Res.* **2009**, *94*, 512–533. [CrossRef]
74. Cui, W.; Dong, X.; Xi, B.; Feng, Z.; Fan, J. Can the GPM IMERG Final Product Accurately Represent MCSs' Precipitation Characteristics over the Central and Eastern United States? *J. Hydrometeorol.* **2020**, *21*, 39–57. [CrossRef]
75. Xu, J.; Ma, Z.; Tang, G.; Ji, Q.; Min, X.; Wan, W.; Shi, Z. Quantitative Evaluations and Error Source Analysis of Fengyun-2-Based and GPM-Based Precipitation Products over Mainland China in Summer, 2018. *Remote Sens.* **2019**, *11*, 2992. [CrossRef]
76. Gaona, M.F.R.; Overeem, A.; Leijnse, H.; Uijlenhoet, R. First-Year Evaluation of GPM Rainfall over the Netherlands: IMERG Day 1 Final Run (V03D). *J. Hydrometeorol.* **2016**, *17*, 2799–2814. [CrossRef]
77. Peel, M.C.; Finlayson, B.L.; McMahon, T.A. Updated world map of the Köppen-Geiger climate classification. *Hydrol. Earth Syst. Sci.* **2007**, *11*, 1633–1644. [CrossRef]
78. Beck, H.E.; Zimmermann, N.E.; McVicar, T.R.; Vergopolan, N.; Berg, A.; Wood, E.F. Present and future Köppen-Geiger climate classification maps at 1-km resolution. *Sci. Data* **2018**, *5*, 180214. [CrossRef] [PubMed]
79. Dirección General del Instituto Geográfico Nacional. *Atlas Nacional de España del siglo XXI*; Centro Nacional de Información Geográfica (Ministerio de Fomento): Madrid, Spain, 2015.

CHAPTER

4

Detection of Heavy Rainfall in the Mediterranean Area: Impact of Cloud Top Phase on Spaceborne Precipitation Estimation

4.1 Disentangling Satellite Precipitation Estimate Errors of Heavy Rainfall at the Daily and Sub-Daily Scales in the Western Mediterranean

4.1.1 Summary

In recent years, significant advancements have been made in quantitative satellite precipitation estimates, which are crucial for various applications. This section evaluates the performance of Integrated Multi-satellitE Retrievals for GPM (IMERG V06B) at sub-daily and daily scales over the Western Mediterranean region. The study spans ten years of half-hourly precipitation records aggregated at different sub-daily periods. The analysis focuses on the contribution of passive microwave (PMW) and infrared (IR) sources in IMERG estimates and their relationship with various microphysical cloud properties using Cloud Microphysics (CMIC–NWC SAF) data.

The results reveal a marked tendency to underestimate precipitation compared to rain gauges, with this underestimation increasing with rainfall intensity and temporal resolution. Retrievals with PMW data exhibit a negative bias, while the inclusion of IR information to fill PMW gaps increases the bias. Additionally, the performance improves in the presence of precipitating ice clouds compared to warm and mixed-phase clouds. These findings can contribute for understanding the errors associated with IMERG in estimating heavy rainfall events and the impact of different sensors on these estimates.

4.1.2 Article

Peinó, E., Bech, J., Udina, M., and Polls, F. (2024). Disentangling Satellite Precipitation Estimate Errors of Heavy Rainfall at the Daily and Sub-Daily Scales in the Western Mediterranean. Remote Sensing, 16(3), 457.

Table 4.1: Summary of the impact and quality of the journal in which the second paper in accordance with this thesis was published. The data correspond to the year 2023 (last year available at the date of preparation of this document) according to Scientific Journal Rankings (SJR).

Journal Name	**Description**	**Journal Metrics**
Remote Sensing	Remote Sensing is an international, peer-reviewed, open access journal about the science and application of remote sensing technology. It is published semimonthly online by Multidisciplinary Digital Publishing Institute (MDPI).	Impact Factor: 4.2 (2023), 5-Year IF: 4.9, CiteScore: 8.3, Quartile: Q1 Earth and Planetary Sciences (miscellaneous)

remote sensing

Article

Disentangling Satellite Precipitation Estimate Errors of Heavy Rainfall at the Daily and Sub-Daily Scales in the Western Mediterranean

Eric Peinó [1,*], Joan Bech [1,2], Mireia Udina [1] and Francesc Polls [1]

[1] Department Applied Physics—Meteorology, Universitat de Barcelona, 08028 Barcelona, Spain; joan.bech@ub.edu (J.B.); mudina@meteo.ub.edu (M.U.); fpolls@meteo.ub.edu (F.P.)
[2] Water Research Institute, Universitat de Barcelona, 08028 Barcelona, Spain
* Correspondence: epeino@meteo.ub.edu

Abstract: In the last decade, substantial improvements have been achieved in quantitative satellite precipitation estimates, which are essential for a wide range of applications. In this study, we evaluated the performance of Integrated Multi-satellitE Retrievals for GPM (IMERG V06B) at the sub-daily and daily scales. Ten years of half-hourly precipitation records aggregated at different sub-daily periods were evaluated over a region in the Western Mediterranean. The analysis at the half-hourly scale examined the contribution of passive microwave (PMW) and infrared (IR) sources in IMERG estimates, as well as the relationship between various microphysical cloud properties using Cloud Microphysics (CMIC–NWC SAF) data. The results show the following: (1) a marked tendency to underestimate precipitation compared to rain gauges which increases with rainfall intensity and temporal resolution, (2) a weaker negative bias for retrievals with PMW data, (3) an increased bias when filling PMW gaps by including IR information, and (4) an improved performance in the presence of precipitating ice clouds compared to warm and mixed-phase clouds. This work contributes to the understanding of the factors affecting satellite estimates of extreme precipitation. Their relationship with the microphysical characteristics of clouds generates added value for further downstream applications and users' decision making.

Keywords: GPM IMERG; extreme precipitation; cloud microphysics; NWC SAF; PMW sources

check for updates

Citation: Peinó, E.; Bech, J.; Udina, M.; Polls, F. Disentangling Satellite Precipitation Estimate Errors of Heavy Rainfall at the Daily and Sub-Daily Scales in the Western Mediterranean. *Remote Sens.* **2024**, *16*, 457. https://doi.org/10.3390/rs16030457

Academic Editors: Vincenzo Levizzani and Ehsan Sharifi

Received: 30 December 2023
Revised: 19 January 2024
Accepted: 22 January 2024
Published: 24 January 2024

1. Introduction

The Mediterranean basin is a particularly challenging mid-latitude area for remote rainfall estimation, as precipitation may be caused by weather systems of different natures, such as mesoscale convective systems, intense extratropical cyclones, and tropical-type cyclones [1–5]. This fact, coupled with the uncertainties involved in precipitation projections and the expected intensification of extreme precipitation in the coming decades [6,7], makes studies in this area an important issue [8]. Reliable detection of the most intense precipitation events is crucial for the development of early warning systems, disaster management strategies, and water resource management.

Satellite precipitation estimates such as the Integrated Multi-satellitE Retrievals for GPM (IMERG) products provide valuable information over areas not covered by ground-based weather radars or rain gauge networks [9]. The main basis of IMERG is to incorporate, merge, and intercalibrate various infrared and microwave (MW) observations [10]. The resulting high spatiotemporal resolution (0.1° × 0.1° and 30 min) on a global scale makes IMERG one of the most interesting products for the study of convective phenomena that generate extreme precipitation [11–13]. Version 06B (V06B) spans a period of more than 20 years with three different latency runs targeting disaster response (Early), agricultural modelling and public health applications (Late), and research (Final). The validation of IMERG is of paramount importance for understanding and addressing estimation errors, both for algorithm improvements and for documenting the capabilities and limitations of further applications developed by the scientific and operational communities [14]. Several studies have confirmed the ability of IMERG to reproduce the global spatial characteristics of precipitation fields on annual and seasonal scales [15–17]. However, spaceborne precipitation estimates at shorter timescales, particularly in the case of heavy rainfall events, pose more challenges, with a general tendency to underestimate [13,17–22]. In addition, despite the large amount of work aimed at evaluating IMERG in different regions around the world, the authors of [23] reviewed a number of limitations, gaps, and suggestions provided in recent studies. A relevant conclusion they reported was that the evaluation of IMERG products at multiple scales simultaneously, rather than constraining the analysis to a single spatial and temporal resolution, could help to better understand how the accuracy and errors vary with spatiotemporal aggregation and under different precipitation conditions. The latter can be addressed for different types of microphysical features of precipitating clouds, as well as the effect of different sensors contributing to the final IMERG products. Indeed, the works by [24,25] recommend an individual evaluation of the underlying passive microwave (PMW) and infrared (IR) sources to detect error cancelation effects. Some works, such as [12,26] have addressed issues directly related to cloud microphysics in the retrieval process, as well as the behavior of the different sensors contributing to the IMERG. From this perspective, they recommend extending these studies to different regions based on their own characteristics.

Based on these considerations and taking as a reference a previous study comparing IMERG products at different time scales with a dense rain gauge network over Catalonia on the northeast of the Iberian Peninsula, the objective of this study was to evaluate IMERG V06B in the estimation of heavy rainfall events at the daily and sub-daily scales in this region considering different intensity thresholds. The validation strategy further seeks to identify the contribution of different sensors (IR and PMW) that contribute to IMERG retrievals and, in a subsequent step, to identify the linkage of various microphysical properties of the precipitating cloud top in the estimation of heavy rainfall. Semi-hourly temporal evaluation based on IMERG sources and cloud properties can provide valuable information on the behavior, strengths, and weaknesses of IMERG in the detection of such events.

The remainder of this paper is organized as follows. Section 2 provides a detailed description of the methodology, data, and assessment metrics used. Section 3.1 describes the different intensity thresholds found for each aggregation period, according to the methodology introduced in Section 2. Section 3.2 compares the rain gauge observations and IMERG estimates at different time scales under different intensity thresholds. Section 5 focus on the half-hourly scale, considering sensor contributions and their relationship with cloud microphysical properties. The most significant results are discussed in Section 6, and a summary of the most relevant aspects is provided in Section 7.

2. Materials and Methods

2.1. Study Area

The study area covers the region of Catalonia, located in the northeast of the Iberian Peninsula (southwestern Europe, Figure 1). With approximately 32,107 km^2, it is characterized by a relatively wide range of climates derived from its latitudinal situation, the influence of the Mediterranean Sea, and complex orography [27]. It is limited to the north by the Pyrenees mountains with elevations exceeding 3000 m ASL, whereas the inland area is characterized by mostly flat terrain with a few orographic contrasts resulting from the erosion of the Ebro River and its tributaries. These irregularities generate a marked average annual rainfall gradient that ranges between 350 mm in inland plains and over 1200 mm in the Pyrenees Mountains. The number of rainy days range from approximately 35 days on the southern coast to 135 days in the northwest Pyrenees (Figure 1). In addition, the coastal and pre-coastal mountain ranges—oriented northeast to southwest toward the Mediterranean Sea—may enhance the pluviometric effects of Mediterranean cyclogenesis along the coast, which favors the occurrence of heavy rainfall, flash floods, and complex mesoscale meteorological events [28–30], especially during autumn. The combination of these characteristics represents a challenge for the remote sensing of precipitation from satellites, ground-based weather radar, and traditional measurements from rain gauge stations [31,32].

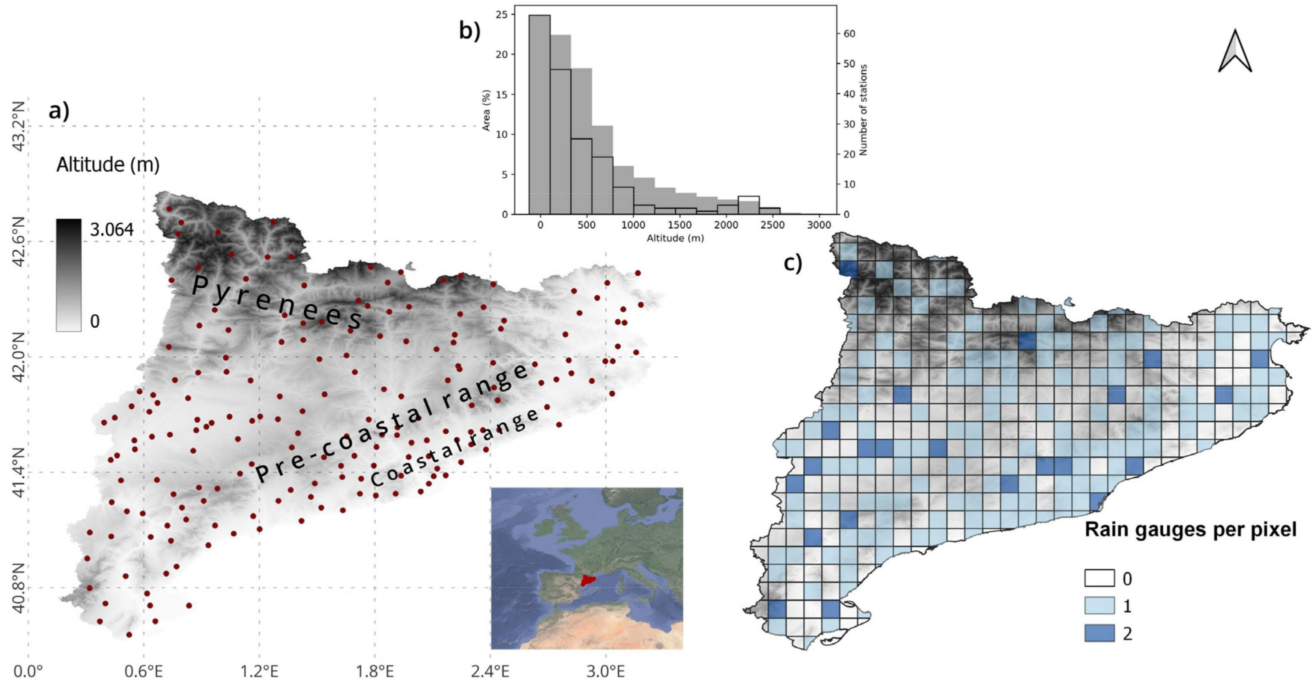

Figure 1. (**a**) Digital elevation model of the study region and network of automatic weather stations (red dots); (**b**) Histograms of altitude distribution of the terrain (% of Catalonia's area, dark shaded gray) and automatic weather stations (unfilled contours); (**c**) Number of rain gauges per IMERG pixel.

2.2. Datasets

2.2.1. GPM IMERG V06B Data

The GPM core satellite and the rest of the GPM constellation satellites contribute to the IMERG algorithm [10], where data are used to calibrate, fuse, and interpolate precipitation estimates from several microwave and infrared sensor sources every 30 min, at a spatial resolution of 0.1° × 0.1° and global coverage from −90° S to 90° N latitude. The GPM core satellite has a dual-frequency precipitation radar and 13-channel PMW GMI imager. The IMERG Early and Late V06B Level 3 data with latencies of 4 h and 14 h, respectively, were considered in this study focused on the low-latency IMERG products. The IMERG Final run, with 3.5 months' latency required for gauge data climatological adjustment, was discarded due to its much higher latency and because it provided worse results for heavy rainfall at the daily and sub-daily scales according to some studies [17,33].

The IMERG algorithm starts from an initial calibration of all PMW sensors associated with the GPM Combined Radar-Radiometer (CORRA) precipitation estimates and merges them from their original spatial resolution into the IMERG grid [14]. In areas without a direct PMW pass, these are spatiotemporally transformed forward in the Early version and backward and forward in the Late product using numerical model-derived motion vectors of total column water vapor (through the so-called Climate Prediction Center morphing (MORPH) method) [34]. Beyond a forecast time of ± 30 min from near-direct PMW observation, PMW-calibrated precipitation estimates from geostationary IR satellites via Kalman filter principles are included [14,35].

IMERG semi-hourly NetCDF files (downloaded from https://disc.gsfc.nasa.gov/, accessed on 13 October 2023) contained explicit information on the data type used in the precipitation estimate through the "PrecipitationCal" variable. In this study, we consider four categories associated with each precipitation estimate: (1) direct PMW overpasses

(PMW-direct), (2) MORPH, (3) combination of PMW and transformed IR, and (4) direct IR. These categories were obtained from the IMERG variables "HQprecipitation" (high-quality precipitation from all available passive microwave sources) and "IRKalmanFilterWeight" (IR-data weights in MW Kalman smoothing). While the former is used to identify direct PMW, the latter quantifies the weight of IR observations wherever PMW direct is absent and varies from 0% (MORPH-only) to 100% (IR-only) [12].

2.2.2. Rain Gauge Data

The IMERG products were validated using rain gauge records (hereafter RG) from the network of automatic stations of the Meteorological Service of Catalonia (SMC). Semi-hourly records with a resolution of 0.1 mm were obtained in the UTC time between 1 March 2014 and 11 October 2023, a period starting with the availability of GPM data. A quality control scheme was applied to SMC rain gauge records based on comparisons with nearby stations and correlation analysis [36,37]. Of the 417 IMERG pixels covering the Catalonia region, 164 were associated with 186 rain gauges considered in this study. According to the spatial distribution, 40% of the IMERG pixels contained at least one rain gauge, and 5% contained two rain gauges (Figure 1). This corresponds to an overall density of 1.13 rain gauges per 100 km^2, which represents more than six times the threshold recommended by the World Meteorological Organization (WMO) for inland flat and undulating areas [38].

2.2.3. CMIC NW SAF Product

The relationship between heavy rainfall events recorded both by rain gauges and IMERG estimates with cloud top microphysical properties was investigated from data provided by the Cloud Microphysics (CMIC) product, developed by the EUMETSAT's Nowcasting Satellite Application Facility (NWC SAF) [39].

CMIC was developed to support nowcasting applications, allowing the characterization of rapidly developing storms [40]. In this study, four CMIC variables were used: (1) cloud top phase, of which only those time intervals with liquid, ice, or mixed presence are analyzed; (2) cloud top effective radius (R_{eff}), defined as the weighted mean of the droplet size distribution; (3) cloud optical thickness (COT); and (4) cloud liquid water path (LWP) and cloud ice water path (IWP), which quantify the vertically integrated amount of liquid and frozen water droplets, respectively. These two quantities can be estimated from

$$LWP,\ IWP = \frac{2}{3}\rho_{(l,i)} COT\ R_{eff(l,i)}, \quad (1)$$

where the subindices $_l$ and $_i$ refer to liquid and ice, respectively, and $\rho_{(l,i)}$ and $R_{eff(l,i)}$ represent the density and cloud top effective particle radius of liquid water and ice [12].

The CMIC product has a spatial resolution of 3 km and 15 min of temporal resolution. To compensate for spatial differences in the rain gauges and IMERG, the values were taken at the closest grid point to each meteorological station. In terms of temporal resolution, the 15 min CMIC data were aggregated to a 30 min resolution. The cloud top phase variable was aggregated according to the criteria described in Appendix A, Table A1, and for the rest of the variables, the mean value of the two 15 min intervals was taken. When one 15 min interval detected ice and the other liquid, the phase was defined as mixed. For these cases, the variable total water path (TWP) was generated as the sum of the IWP and the LWP recorded in the two 15 min intervals that contributed to the semi-hourly aggregation.

2.3. Methodology

2.3.1. Definition and Selection of Extreme Precipitation Events

The IMERG validation process performed here was based on a pixel-to-point comparison [18,41] applied in such a way that information was obtained from the grid closest to each weather station. This method allows a pairwise comparison between the concurrent precipitation data of the RG and IMERG pixels at each time step. This approach avoids uncertainties arising from interpolating RG data in a region characterized by high orographic and climatic variability [17]. As mentioned in Section 2.2.2, the IMERG pixels contained two rain gauges, but as the gauge data were independent, they were treated as two different data points.

The first part of this study focused on evaluating the behavior of the IMERG Early and Late versions in the estimation of intense precipitation, considering different sub-daily temporal aggregations in the period 2014–2023. Temporal resolutions of 1, 3, 6, 9, 12, and 24 h were obtained from the aggregation of the semi-hourly accumulations of the initially created database. This database was constructed with records of at least 0.1 mm accumulated in 30 min present in both the rain gauges and IMERG. Note that 0.1 mm is the minimum precipitation threshold detected by the RG and GPM Ka band radar [42].

To obtain the different extreme precipitation thresholds for different temporal aggregations, the method described by [43] and recent studies [44–47] was applied. This method is based on the fact that a linear relationship between the maximum precipitation amount P and the temporal duration D in a log-log space can be found, so that the data follow a power-law equation:

$$P = aD^b, \tag{2}$$

where a is the prefactor and b is the scaling coefficient [43]. All rain gauge data for the study period and region were used to obtain the fitted function.

Instead of directly using the curve fit of the extreme data to characterize the extreme precipitation records in Catalonia, the upper envelope method was used, that is, a curve that was greater than or equal to all the data, with a power-law scaling line. The specific method for deriving the envelope line is described in the work of [46], and allows the generation of curves that estimate the maximum precipitation amounts for different time periods based on observed records. The scaling law of the adjusted extreme precipitation derived from Equation (2), expressed as a linear function, is

$$\log(P) = a + b\log(D), \tag{3}$$

Once the upper envelope fitting curve corresponding to the reference data from the rain gauges was created, proportional curves (1%, 5%, 10%, and 18%) of equal slope were produced to generate various intensity thresholds. The results and thresholds selected using this method are presented in Section 3.1.

The second part of the paper focuses on the evaluation of only the IMERG Early product and sources at half-hourly resolution under different extreme precipitation criteria based on the envelope curve. The results were stratified according to the characteristics of the precipitating cloud phase: liquid, ice, or mixed. Owing to the availability of the NWC SAF data, 17 case studies between 2021 and 2023 were selected for this analysis. The selected cases were characterized by extreme precipitation events in both RG and IMERG at multiple weather station locations, exceeding the heavy rainfall threshold set by the Meteorological Service of Catalonia (20 mm in 30 min). In this way, the sample was selected to allow for a detailed study of the properties of clouds related to episodes of intense precipitation observed at ground level by RG and estimated by IMERG.

2.3.2. Point-Pixel Validation Measures

IMERG products were validated using two approaches: categorical scores based on contingency tables and continuous statistical scores. The first approach considered a 2×2 contingency table with four possible scenarios for a given threshold (see Table 1), from which several categorical scores were computed (Table 2): the probability of detection (POD), representing the proportion of events correctly detected by IMERG out of the total observed rainfall events, and the false-alarm ratio (FAR) representing the fraction of false detected rainfall events.

The continuous statistical scores used were Spearman's correlation coefficient, BIAS, Rbias, MAE, and RMSE (Table 3). BIAS is a measure of the average error between IMERG and RG, while Rbias describes the systematic error. Positive (negative) values of BIAS and Rbias denote overestimation (underestimation) of the satellite products. MAE shows the average size of the absolute errors and, finally, RMSE measures the size of the average error, giving more weight to large errors without showing the direction of deviation between IMERG and RG.

Table 1. Contingency table comparing observed rainfall by rain gauges and estimated rainfall by IMERG for a given threshold.

Estimated Rainfall	Observed Rainfall	
	Gauge ≥ Threshold	Gauge < Threshold
IMERG ≥ threshold	Hits (H)	False alarms (F)
IMERG < threshold	Misses (M)	Correct Negatives

Table 2. List of categorical verification metrics used to evaluate IMERG products.

Name	Formula	Perfect Score
Probability of detection (POD)	$POD = \frac{Hits}{Hits+Misses}$	1
False-Alarm Ratio (FAR)	$FAR = \frac{False\ alarms}{False\ alarms+Hits}$	0
False-Alarm Rate (POFD)	$POFD = \frac{False\ alarms}{False\ alarms+correct\ negatives}$	0
Hansen and Kuipers (HK)	$HK = POD - POFD$	1

Table 3. List of continuous verification scores used to evaluate IMERG products.

Name	Formula	Unit	Perfect Score
Spearman's correlation coefficient	$r = \frac{cov(R(S_i),R(O_i))}{\sigma_{R(S_i)}\sigma_{R(O_i)}}$	-	1
Mean Error (Bias)	$BIAS = \frac{1}{n}\sum_{i=1}^{n}(S_i - O_i)$	Mm	0
Relative Bias (Rbias)	$Rbias = \frac{\sum_{i=1}^{n}(S_i-O_i)}{\sum_{i=1}^{n}O_i} \times 100$	%	0
Mean Absolute Error (MAE)	$MAE = \frac{\sum_{i=1}^{n}\lvert S_i-O_i\rvert}{n}$	Mm	0
Root Mean Square Error (RMSE)	$RMSE = \sqrt{\frac{1}{n}\sum_{i=1}^{n}(S_i - O_i)^2}$	Mm	0

S_i is the value of satellite/model precipitation estimates for the ith event, O_i is the value of rain gauge observation for the ith event, n is the number of observed records, $cov(R(S_i), R(O_i))$ is the covariance of the rank variables, and $\sigma_{R(S_i)}$ and $\sigma_{R(O_i)}$ are the standard deviations of the rank variables.

3. Results

3.1. General Characteristics of Extreme Precipitation Events

Figure 2 shows the log-log plot of the precipitation accumulations or depth (mm) versus duration (D) in minutes of the extreme precipitation records from 2014 to 2023 in Catalonia from both the RG and IMERG Early and Late runs taken at the grid points closest to the location of the rainfall events. In all three datasets, the linear fit (Equation (2)) was calculated by least-squares linear regression and expressed in the power law. Using the method described in Section 2.3.1, the envelope curve for the RG records was also plotted.

A graphical inspection allows us to detect a great similarity between the maximum values estimated by IMERG Early and Late. Both products show a large underestimation of the maximum threshold detected by the RG in time aggregations below 6 h, which is more marked on the half-hourly scale. In fact, from 6 h to 18 h, IMERG showed a change in the trend of overestimating precipitation records compared to the upper envelope curve of RG. The higher exponent of b in the fitting equation of the IMERG products suggests that satellite estimates of extreme rainfall increase at a higher rate with duration than RG extreme precipitation records. This is related to the higher frequency of extreme precipitation events (Figure 3), especially in northeastern Catalonia. It should be mentioned that these IMERG extremes are only evaluated on the pixels closest to the location of RG rainfall events, discarding other IMERG values that can be higher.

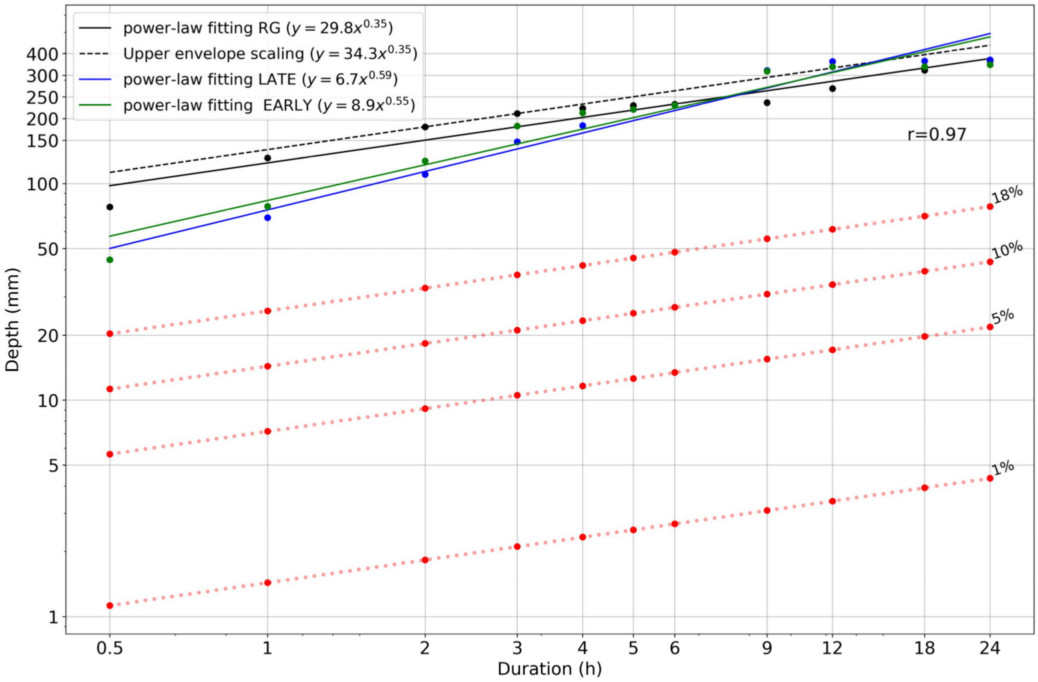

Figure 2. Point precipitation extremes for different temporal aggregations observed by RG (black) and estimated by IMERG Late (blue) and Early (green) in Catalonia between 2014 and 2023. The solid lines correspond to the power-law fits, and the black dashed line corresponds to the scaling of the upper envelope of the observed data. The dashed red lines show different ratios of the upper reference envelope.

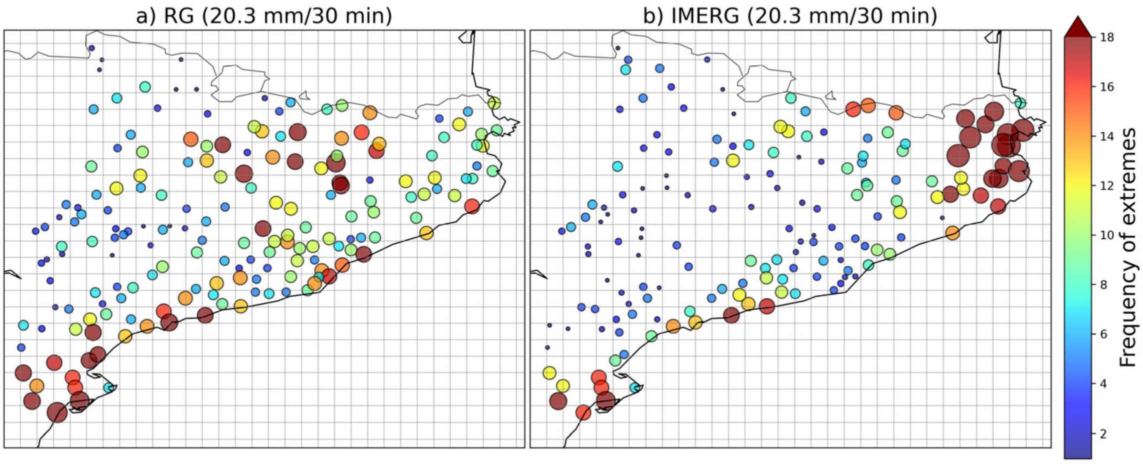

Figure 3. Spatial representation of the half-hourly IMERG and RG extremes, accounting for 18% of the envelope curve. The frequency of IMERG extremes included events identified by both the Early and Late products. The grid represents that at the original IMERG resolution.

Finally, 1%, 5%, 10%, and 18% of the envelope curve of the RG were considered to obtain the threshold values of the reference intensity in each temporal aggregation. Table 4 lists the precipitation threshold values that were used as references for each temporal aggregation. Note that 18% of the envelope curve at the half-hourly scale represents an amount of 20 mm in 30 min, a considerable precipitation amount at this scale, and a value very close to the reference threshold for short-term heavy rainfall considered by the Meteorological Service of Catalonia [48].

Table 4. Precipitation thresholds taken for each temporal aggregation from the upper envelope curve of extreme precipitation of the RG.

Temporal Aggregation (h)	1% (mm)	5% (mm)	10% (mm)	18% (mm)
0.5	1.1	5.6	11.3	20.3
1	1.4	7.2	14.3	25.8
3	2.1	10.5	21.1	37.9
6	2.7	13.4	26.8	48.3
9	3.1	15.4	30.9	55.6
12	3.4	17.1	34.2	61.5
24	4.4	21.8	43.5	78.3

3.2. Evaluation of IMERG at Multiple Time Scales and Intensity Thresholds

The evaluation of IMERG Early and Late products compared with RG records was performed for selected sub-daily and daily time aggregations. Figure 4 shows the boxplots of BIAS and MAE for both products, considering a precipitation intensity threshold of 18% of the envelope curve. In this figure, the first quartile, median, and third quartile of the distribution are identifiable considering errors calculated at all stations in the study region; boxplot whiskers extend to the 1.5 interquartile range and outliers extending further away are also plotted. For consistency between the aggregations, the results are shown in mm/h.

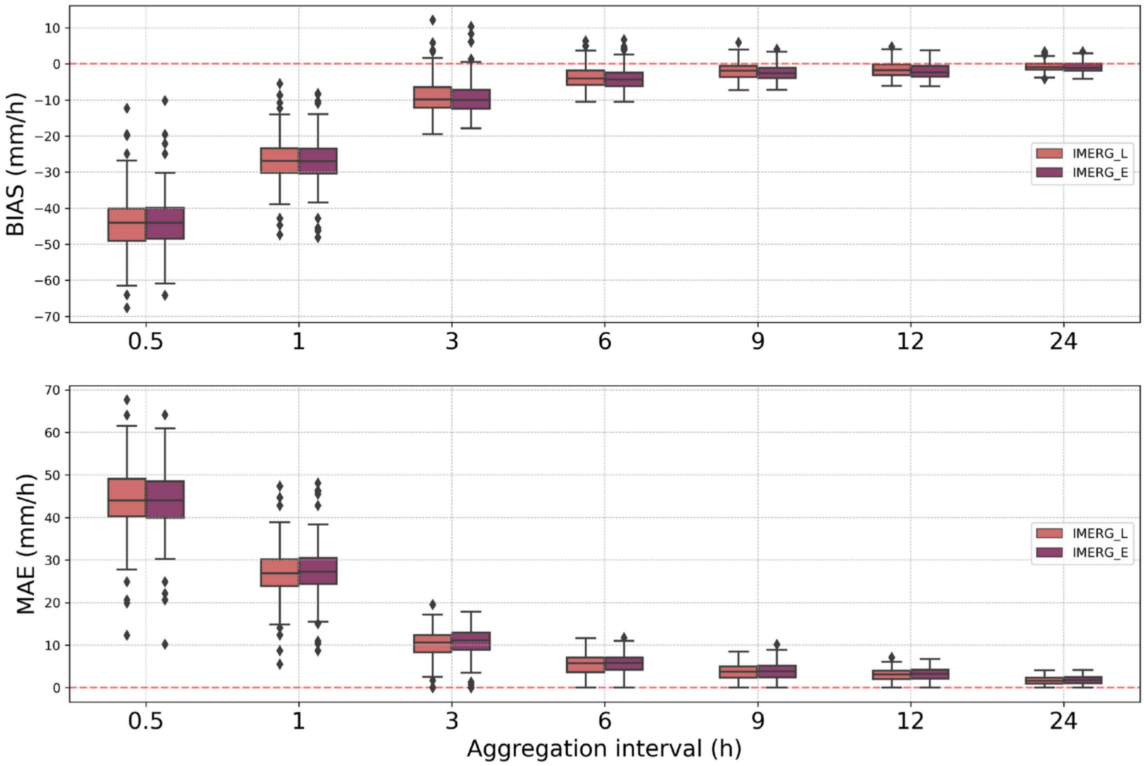

Figure 4. (**Top panel**) BIAS and (**Bottom panel**) MAE comparing IMERG Early (IMERG_E) and IMERG Late (IMERG_L) products and RG records greater than or equal to 18% of the envelope curve. For reference, the dotted red lines indicate perfect scores.

According to the BIAS, there was a tendency for IMERG rainfall values to be underestimated, decreasing for longer aggregation periods. Underestimation increased as the precipitation intensity threshold increased. The best results with values between −0.07 and −0.03 mm/h of BIAS and 0.74 mm/h of MAE are observed at daily scales for the lowest intensity threshold evaluated (1%) (see Table 5). A similar result was found when examining the Rbias values, although the underestimation varied more (Table A2, Appendix B). On the other hand, the worst results were observed on a semi-hourly scale, which shows the deficiencies of IMERG in the quantification of extreme precipitation at the shortest time resolution available. This agrees with previous studies [13,19,49,50] where similar results were obtained.

Table 5. Mean values of BIAS and MAE (both in mm/h) for each temporal aggregation and different precipitation intensity threshold considered (1%, 5%, 10%, and 18% of the maximum envelope curve).

Score	IMERG	0.5 h	1 h	3 h	6 h	9 h	12 h	24 h
				≥1%				
BIAS	E	−1.81	−0.88	−0.21	−0.08	−0.05	−0.02	−0.07
	L	−1.83	−0.79	−0.11	0.00	0.02	0.03	−0.03
MAE	E	4.87	3.52	2.06	1.37	1.03	0.86	0.74
	L	4.63	3.39	2.02	1.36	1.03	0.86	0.74
				≥5%				
BIAS	E	−14.42	−7.16	−2.09	−1.03	−0.75	−0.55	−0.33
	L	−14.20	−6.80	−1.82	−0.85	−0.59	−0.44	−0.26
MAE	E	16.01	9.30	4.24	2.62	1.93	1.57	0.92
	L	15.58	8.94	4.09	2.56	1.90	1.56	0.92
				≥10%				
BIAS	E	−26.75	−15.07	−4.92	−2.18	−1.55	−1.17	−0.68
	L	−26.54	−14.68	−4.51	−1.87	−1.23	−0.98	−0.52
MAE	E	27.48	16.30	6.80	4.01	2.94	2.34	1.39
	L	27.17	15.86	6.46	3.87	2.89	2.29	1.34
				≥18%				
BIAS	E	−44.02	−26.83	−9.24	−3.94	−2.55	−2.00	−1.05
	L	−44.21	−26.68	−8.82	−3.62	−2.01	−1.63	−0.79
MAE	E	44.17	27.30	10.65	5.69	3.74	3.15	1.71
	L	44.31	27.02	10.13	5.44	3.65	3.00	1.61

A good approximation for the detection of heavy precipitation with near real-time application was obtained for aggregation intervals equal to or greater than 6 h, with an average error mean absolute of 1.36 mm/h for a 1% threshold and 5.44 mm/h for an 18% threshold. Although IMERG Late shows slight improvements over the Early version for most aggregations, it is not possible to identify a statistically significant difference. The use of one over the other would be conditioned to the advantages that the latency in which the data are generated may offer.

Additional analyses stratifying the results according to seasonality, the altitude of the stations, climatic regime, and terrain orography for each temporal aggregation (not shown) did not show remarkable differences.

Categorical Scores

Figure 5 shows POD and FAR values based on the contingency table elements for each temporal aggregation, and according to the envelope curve-based precipitation intensities. The detection of precipitation events with acceptable skill (dark reddish-shaded colors in Figure 5, that is, POD $\geq$ 0.5 and FAR $\leq$ 0.5) is limited in both products mostly for precipitation intensities greater than or equal to 1% and greater than 6 h of temporal aggregation. The ability of IMERG to identify extreme rainfall events decreased substantially with increasing rainfall intensity and temporal resolution. If we consider thresholds greater than or equal to 5% of the envelope curve, no temporal aggregation exceeds 50% of correctly detected cases. This behavior is more critical in the detection of events at 30 min and 1 h, where thresholds higher than 10% of the curve do not exceed 8% (30 min) and 15% in 1 h, respectively. According to these results, IMERG cannot detect events above or equal to 5% of the envelope curve.

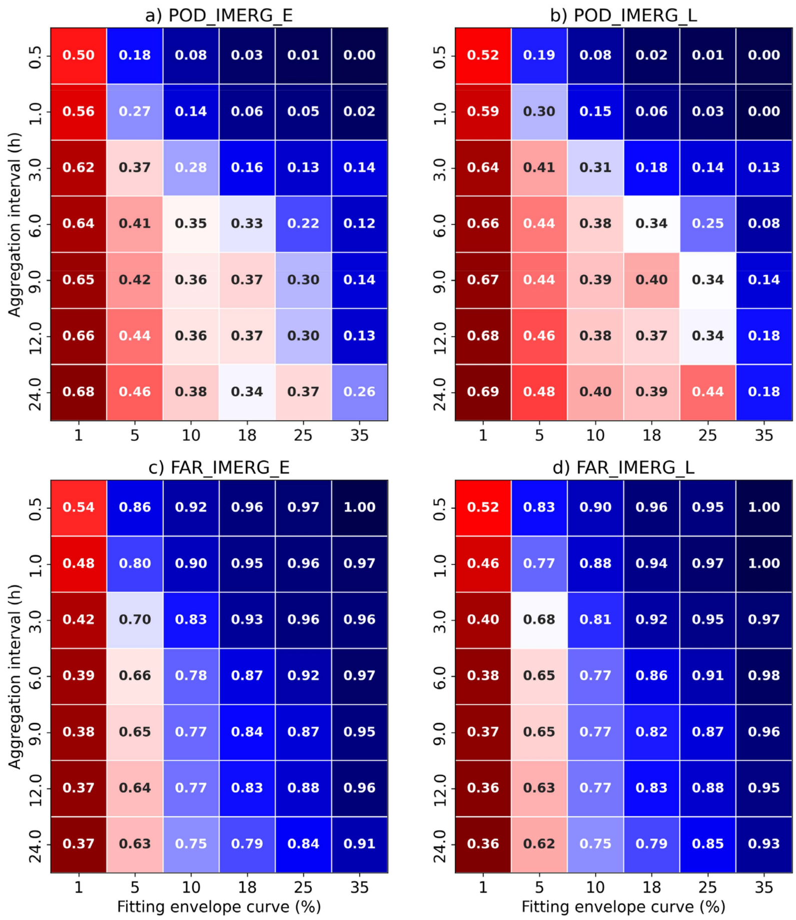

Figure 5. (**a**,**b**) POD and (**c**,**d**) FAR scores for different temporal aggregations and precipitation intensity thresholds of the IMERG Early (IMERG_E) and Late (IMERG_L) products.

While the event detection may be acceptable (greater or equal than 0.50) for 1% rainfall rate envelope thresholds, these values decrease rapidly for higher rainfall rates, reaching only 0.02 or 0.03 at 30 min for the 18% threshold: the SMC standard for heavy rainfall. IMERG products also exhibit significant deficiencies in the generation of false alarms. For both the Early and Late products, limitations were significant at all temporal aggregations with intensities above 5% of the envelope curve, and even at a half-hourly timescale at or above 1% of the envelope curve, FAR exceeded 0.50 values systematically.

For thresholds above 10% of the curve for time aggregations below 3 h, the false-alarm rates were close to 0.90 (1.0 at 30 min) and above 0.70 for lower resolutions, illustrating the low skill of IMERG products with heavy rainfall at a high temporal resolution.

4. Assessing the Contribution of Sensors on a Semi-Hourly Scale

To gain a better understanding of the limitations of the IMERG 30 min precipitation estimates, a deeper analysis using precipitation cloud microphysical characteristics was performed, considering 17 heavy rainfall days that occurred from 2021 to 2023. The analysis was performed with both IMERG Early and Late runs, but only the results based on Early runs are presented here, as they were very similar, and the shorter latency of the Early products compared to the Late runs (4 h instead of 14 h) makes them more useful for near-real-time applications. This is of particular interest to early warning systems devoted to the surveillance of extreme precipitation and subsequent flash floods.

IMERG precipitation estimates are based on direct PMW overpasses (PMW-direct), spatiotemporal advected PMW information (MORPH), a combination of MORPH and IR (MORPH+IR), and observations based on IR information only. In the semi-hourly data for the 17 selected days, IMERG precipitation estimates from MORPH+IR sources dominated (61.6%), followed by PMW-direct (20.2%), and MORPH (16%). A small fraction was represented by IR-only sources (2.1%), which were not considered in the error analysis.

In Figure 6 (top row), a clear underestimation for all IMERG sources is evident, as all fit lines and the associated 90% error areas are well below the diagonal of the scatter plot. This was even more marked in the case of MORPH+IR for higher rainfall intensity thresholds. Figure 6 (bottom row) shows the elements of the contingency table for each source contributing to the IMERG estimate, according to the selected intensity threshold. Note that the correct negatives, which represent more than 90% of the cases, are not shown. As expected, the hit fraction degrades with increasing rainfall rate thresholds, and in all cases, the estimates showing the highest skill in event detection come from the direct PMW sensors, followed by MORPH. In fact, for thresholds greater than or equal to 20 mm/30 min, the few cases detected by IMERG are due to the PMW sensors. Previous studies [14,51,52] have shown that PMW data generally represent precipitation rates better than IR data because PMW radiometers are sensitive to hydrometeor precipitation in the atmospheric column, unlike IR sensors, which are limited to cloud top measurements. In particular, the authors of [12] mentioned that IR retrievals misjudge cold cloud features as rain and not precipitation anvils.

While the underestimation of high rainfall rates in IMERG comes from all sources, the negative bias is the lowest for the PMW-direct and low rainfall rate thresholds (i.e., 1% of the envelope curve, close to ideal top-left location of Figure 7). However, this bias appears to be an inherent problem with the PMW algorithm, which is amplified by MORPH and IR data. In contrast, the worst results were obtained for MORPH+IR and the highest rainfall rate threshold considered (18%), located at the worst location (bottom right) of Figure 7.

The benefits of filling the IMERG PMW gaps by including MORPH and IR information come at the expense of increasing Rbias and MAE for heavy rainfall rates. The above analysis of categorical variables agreed with the trend observed in the analysis of continuous errors. The BIAS errors for thresholds $\geq$18% of the curve are close to 20 mm, which indicates an almost null ability of IMERG to detect the amounts observed by the rain gauges. Note that a few IMERG estimates based on PMW detected values exceeding the 18% threshold; however, they were false alarms corresponding to lower rain gauge records.

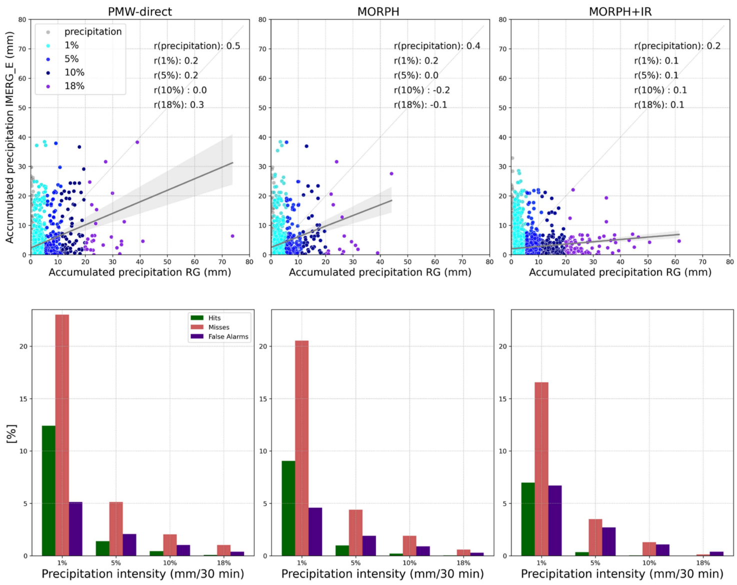

Figure 6. (**Top row**) Scatter plot for each IMERG source versus rain gauge observations. The RG rainfall intensities stratified into different envelope curve thresholds (1%, 5%, 10%, and 18%) are plotted in different colors. The regression adjustment line with 95% confidence error is also plotted (gray line with grayish shading). (**Bottom row**) Percentage of distributions of hits, false alarms, and misses for each IMERG source and for each rain gauge precipitation intensity.

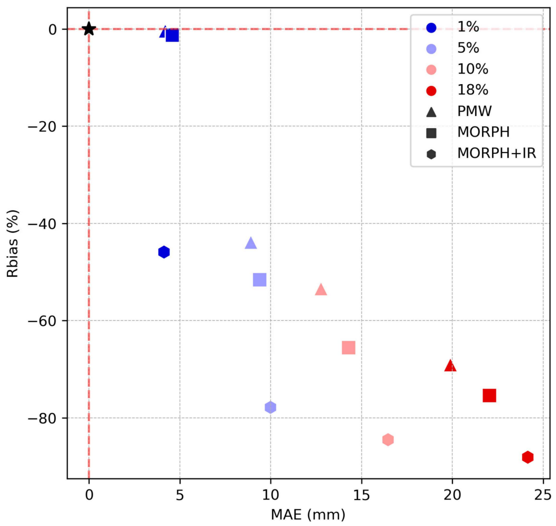

Figure 7. Scatter plot of Rbias (mm) versus MAE (mm) for each IMERG data source (PMW, MORPH, and MORPH+IR) and stratified according to rain gauge precipitation intensities (1%, 5%, 10%, and 18%). The marked point (black star) is the reference for no errors, whereas the bottom right is the location with the highest errors.

5. Relationship between IMERG Sources and Microphysical Properties of the Clouds

In this section, the IMERG comparison with rain gauges is broken down according to the cloud phases and the different microphysical properties of the precipitating clouds. The incorporation of high-resolution cloud top information from CMIC NWC SAF provides additional and independent information that allows us to better understand the behavior of IMERG and its data sources under different RG rainfall intensity thresholds.

Table 6 shows the error and skill measures from IMERG and its sources stratified by warm, ice, or mixed heavy precipitation clouds. In our study area, as expected, the highest number of heavy precipitation events occurred under ice clouds in the order of 4601:117:275 (ice, liquid, mixed), where the numbers indicate the individual 30 min records.

Table 6. Summary of IMERG error statistics for each cloud phase, considering a rainfall threshold intensity of 1%.

		Contingency-Table-Based Measures			Continuous Errors Measures			
Cloud Phase	**Source**	**POD**	**HK**	**FAR**	**BIAS (mm)**	**Rbias (%)**	**MAE (mm)**	**RMSE (mm)**
Ice phase	IMERG_E	0.61	0.38	0.68	−1.28	−27.44	4.30	6.98
	PMW-direct	0.76	0.46	0.64	0.23	4.91	4.36	7.12
	MORPH-only	0.69	0.44	0.69	−0.35	−7.62	4.15	6.71
	MORPH+IR	0.54	0.33	0.68	−2.04	−43.89	3.89	6.44
Liquid phase	IMERG_E	0.16	0.07	0.91	−3.00	−82.24	3.22	4.98
	PMW-direct	0.11	0.02	0.88	−2.32	−84.79	2.42	3.28
	MORPH-only	0.24	0.12	0.88	−2.43	−79.35	2.43	2.96
	MORPH+IR	0.21	0.10	0.92	−3.74	−85.43	3.85	6.66
Mixed phase	IMERG_E	0.22	0.11	0.80	−2.64	−71.55	3.58	5.63
	PMW-direct	0.26	0.16	0.64	−2.26	−70.55	2.87	4.01
	MORPH-only	0.44	0.29	0.72	−1.34	−42.11	2.90	4.28
	MORPH+IR	0.14	0.02	0.89	−3.12	−78.87	3.70	6.11

The cases of heavy precipitation associated with warm clouds showed the worst results, similar to those with clouds in the mixed phase. In the latter cases, the BIAS and Rbias values were greater than twice the errors reported in ice cases in all sources simultaneously, with the PMW-direct records showing the largest differences between one class and the other. For intensities greater than or equal to 1%, the PMW sources in ice conditions were the only ones that overestimated precipitation, thus cutting the underestimation trend of the rest of the IMERG data sources. The MAE and RMSE values are higher in ice clouds precisely because heavy rainfall is mainly associated with deep moist convection; however, it should be noted that they also present lower BIAS and Rbias values.

Similarly, POD values were much higher for glaciated clouds, especially at lower precipitation intensities. In observations from PMW-direct and MORPH sources in the ice phase, POD values reflect a hit rate of 0.76 and 0.69 compared to only 0.11 and 0.24 in the liquid phase. Although false-alarm rates also increase from ice-phase to liquid-phase clouds, they follow the same pattern of the best scores for PMW-based estimates compared with those where IR sources are considered.

For events above 5% precipitation thresholds, the cases under liquid and mixed clouds provided poor results. For events above the 18% threshold, the ability of IMERG was almost null under all cloud phases, but specifically in the liquid and mixed phases (with two cases each), it was totally null.

Figure 8 compares the probability distribution of cloud top properties around all time steps of intense precipitation greater than or equal to 1%. IMERG Early estimates and different sources were considered for comparison with RG. Only daytime precipitation samples were represented, as COT and R_{eff} retrievals were not available during the night. Although available, IWP, LWP, and TWP are limited to the same time set for consistency.

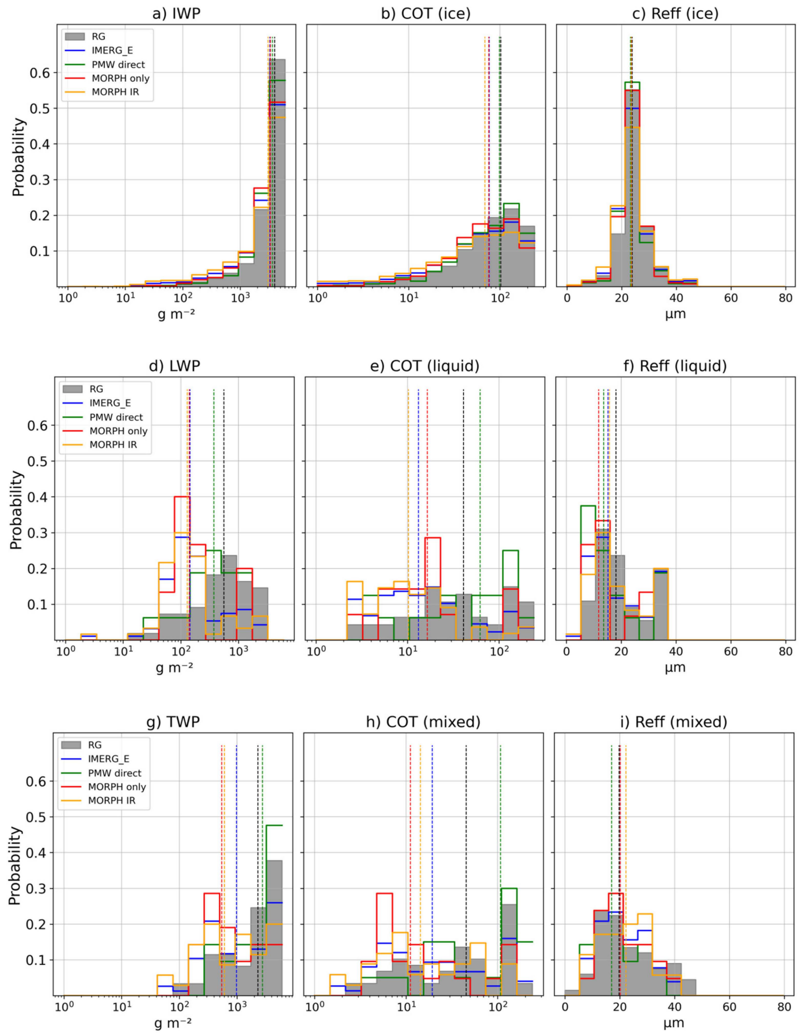

Figure 8. Probability distributions of the cloud properties described in Section 2.2.3, based on all time steps of intense precipitation greater than or equal to 1% of the envelope curve in the RG (gray shading), IMERG, and its sources (colored lines), separated into (**a**–**c**) ice cloud tops and (**d**–**f**) warm/liquid cloud tops and (**g**–**i**) mixed cloud tops. The vertical colored lines in each plot indicate the median values of the respective distribution.

It should be noted that the case studies selected for the analysis were chosen precisely because of the occurrence of heavy rainfall. This behavior is reflected in the high probability of occurrence of high IWP, LWP, and TWP values. IMERG and its sources overestimated the precipitation related to IWP values below 500 g m^{-2} and underestimated the precipitation rates related to higher IWP values compared with RG. This oversensitivity was also evident for lower COT values. The estimates generated by PMW-direct were the closest to the RG distribution, and their median values were very similar. The distributions of sensors related to warm clouds was much more pronounced. A high overestimation is observed for all sources related to TWP values < 1000 g m^{-2}, and for higher values, an underestimation is observed, especially for IMERG MORPH+IR. Although once again, this behavior is reflected in the lower COT values, overestimation is observed for higher values.

Regarding R_{eff}, IMERG and its sources do quite well for ice clouds but show significant overestimates, particularly below 10 µm, and underestimates when R_{eff} is equal to or higher than the median of the observations. In the mixed phase, although there was an overestimation related to low TWP values, it is worth noting that the PMW-direct estimates maintained this overestimation directly related to a marked sensitivity to high COT values.

The PMW-direct sources, although the most accurate, are often the most sensitive to different cloud phases. While uncertainties in rainfall occurrence associated with ice and mixed clouds are directly related to COT characteristics during the liquid phase, they are also related to COT and R_{eff} behavior.

In the context of more intense precipitation (5%, 10%, and 18%) (see Figure A1, Appendix C) associated with ice clouds, a large oversensitivity related to high IWP and COT values, especially by PMW-direct, can be noted. In all cases, extreme precipitation was overestimated, with R_{eff} values close to the median of those recorded by RG. While observations associated with PMW-direct played a key role for intensities of 5% and 10%, MORPH+IR sources played a key role for intensities $\geq$ 18%.

Origin of Hits, Misses, and False Alarms

Figure 9 shows the distributions of the percentages of each IMERG source causing hits, false alarms, and misses compared to RG. This analysis was also performed considering various precipitation intensity thresholds according to all case study data and divided according to the phase of the precipitating cloud.

For intensity thresholds above 1%, there are no clear differences between the IMERG sources that contribute the most to the hits; this behavior changes for the strongest intensity extremes (above 5%). The PMW-direct source was responsible for the detection of these more intense precipitation events coupled with MORPH. In fact, extremes greater than or equal to 18% represent 100% of the detected cases. However, just as they contribute to the hits, they are responsible for the generation of high false-alarm rates, especially in the ice phase.

As far as the miss rate is concerned, it is the MORPH+IR sensors, even IR direct (although in very few cases), that have the most influence. This is evident for cases related to ice clouds from thresholds $\geq$ 1% and is rather clear for liquid and mixed phases with thresholds $\geq$ 5%. The missing of extreme events $\geq$20 mm/30 min is entirely associated with sensors with IR information.

A similar analysis to that performed in the previous section is shown in Figure 10, which focuses on the distribution of the elements of the contingency table for IMERG based on precipitation events above 1%.

The distribution of hits was very similar to that of RG. This implies that by taking the IWP as a reference, especially for high values, IMERG can detect precipitation events measured by RG. It is also evident that for lower values of IWP, the rate of false alarms and misses increases dramatically, which is directly related to the COT detection behavior. Although very similar to [12] in this case, hits, false alarms, and misses can hardly be predicted using R_{eff}.

In the case of liquid and mixed-phase clouds, as indicated by the low POD and high FAR values in Table 6, the IMERG performance decreases dramatically. Taking LWP as a reference, there are predominantly false alarms towards low LWP values, and many losses are associated with higher values. The fact that the median of the distribution of losses in the COT and R_{eff} is almost identical to the distribution of the RG suggests that during this phase, IMERG misinterprets the results. In the mixed phase, false alarms were associated with low TWP and COT values. In contrast, the highest frequency of hits occurred when TWP values were quite high.

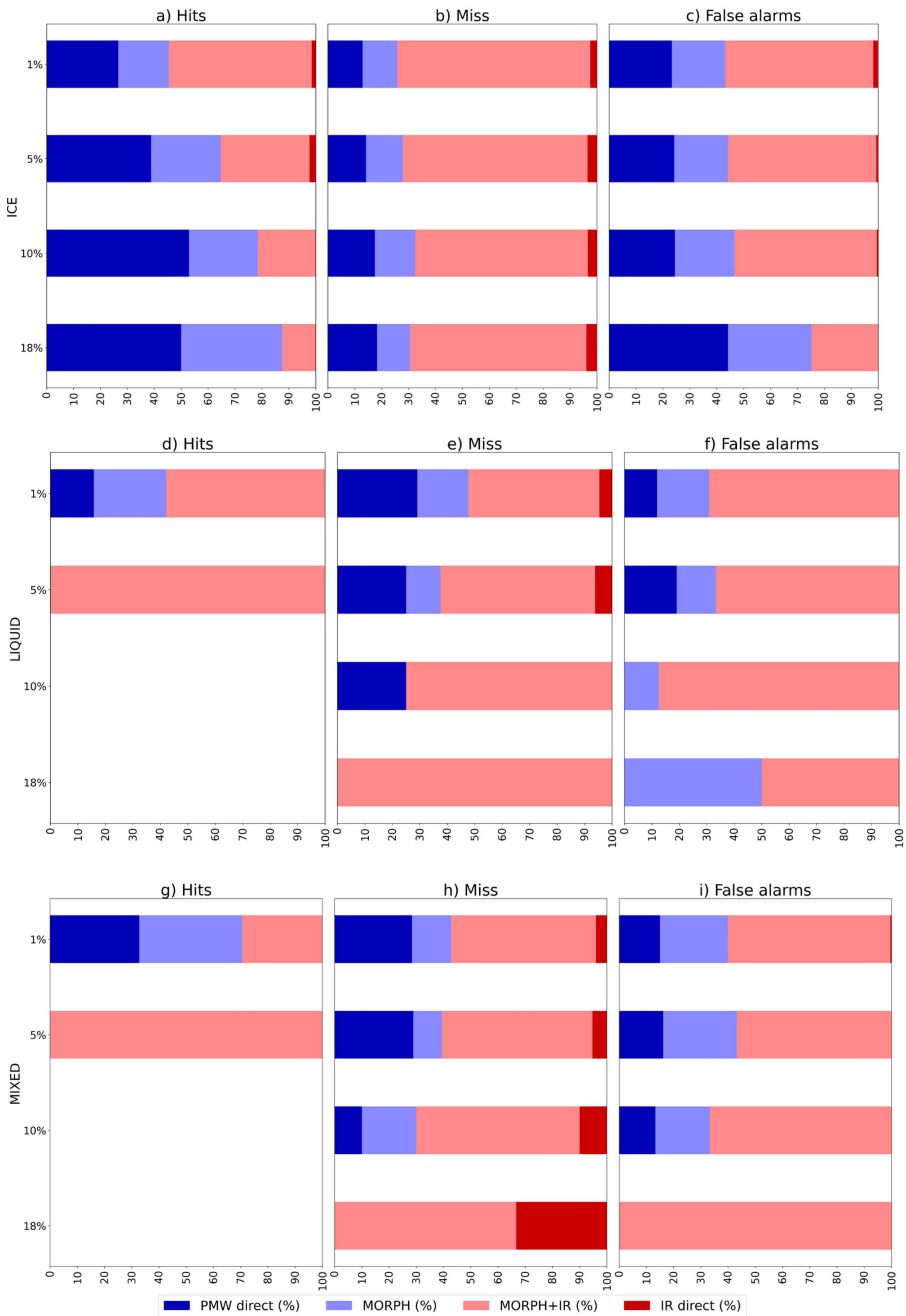

Figure 9. Percentage of sensors contributing to hits, false alarms, and misses of IMERG estimates according to cloud phase (**a**–**c**) ice, (**d**–**f**) liquid, and (**g**–**i**) mixed and RG intensity thresholds. The missing intensity representation (panels d and g) is due to the absence of data for these cases.

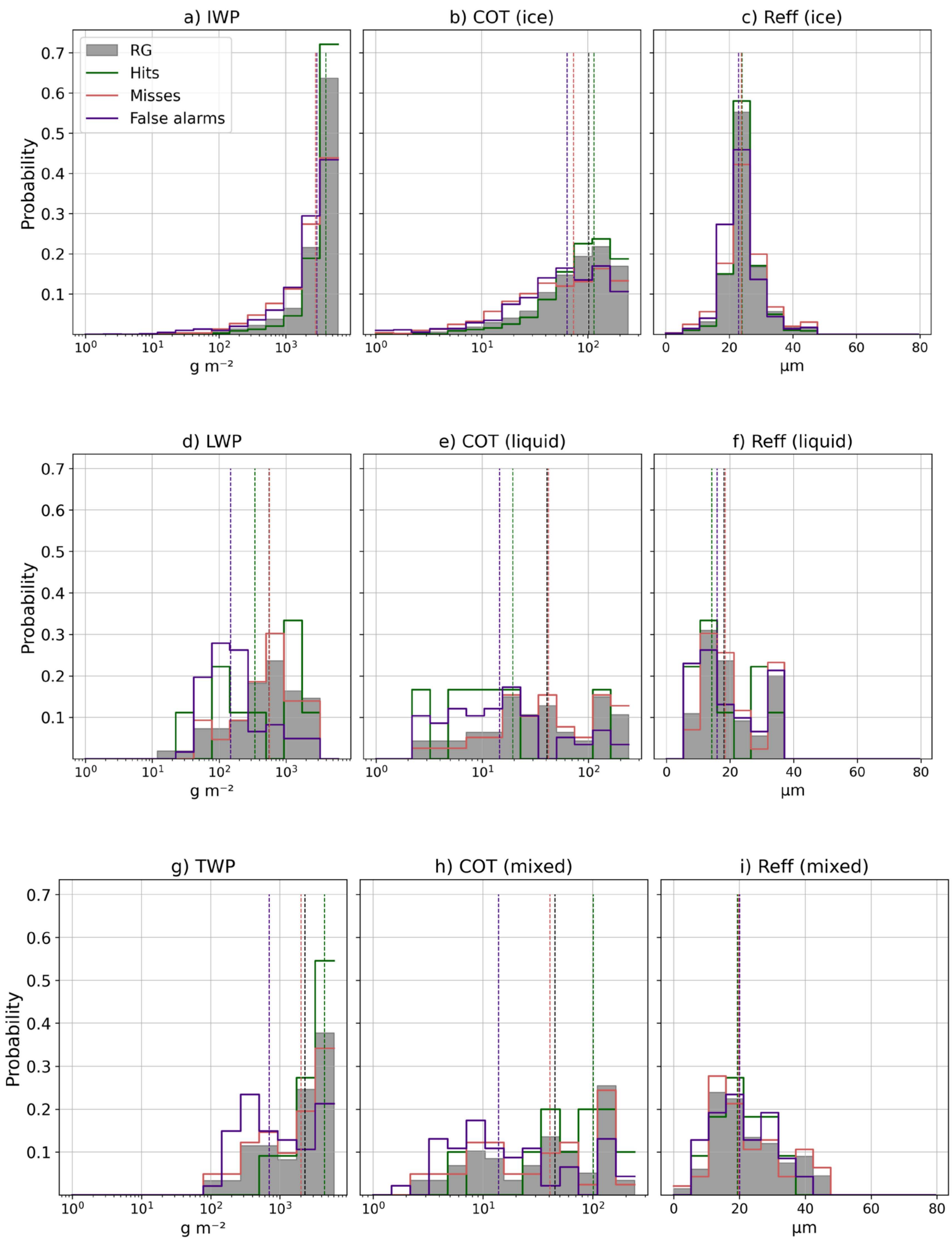

Figure 10. As in Figure 8, but for the elements of the standard contingency table.

6. Discussion

The errors found in IMERG at the daily and sub-daily temporal aggregations and under different precipitation intensity thresholds for heavy rainfall show several limitations that should be considered by users of these products. There is a clear underestimation of the precipitation rain gauge records, which becomes much more marked as the precipitation intensity threshold increases and as the temporal aggregation becomes shorter. The best performance in terms of the ability to detect precipitation events by IMERG is limited to relatively moderate rainfall rates (1% of the extreme rain gauge envelope curve). The errors measuring the accuracy of the estimates indicate that for temporal aggregations greater than 6 h, they start to become acceptable in terms of standard criteria (that is, POD > FAR, POD $\geq$ 0.5, FAR $\leq$ 0.5). The authors in [13] showed similar results when defining an unacceptable probability of detection for aggregation intervals of less than 12 h. Similarly, works such as [13,53] show that with decreasing temporal resolution, the ratio between observations and satellite estimates improves due to the balancing effect of the temporal aggregation of rainfall over a longer period. According to the results shown in this work, for intensity thresholds higher than the 5% envelope curve, a high underestimation of IMERG, lack of detection, and the manifestation of high false-alarm rates start to be inherent in all temporal aggregations.

Another important aspect to consider is related to the fact that IMERG Late shows little improvement and, in some cases, no improvement over IMERG Early. This means that IMERG_E, because of its shorter latency, is the most reliable source in a near-real-time rainfall detection system. This strongly suggests that the negative BIAS in the identification of heavy rainfall events is not solved by increasing the amount of satellite data available later, but it is intrinsic to the algorithm used for the detection and estimation of these events.

Understanding the relationship and contribution of the different data sources used in IMERG estimates is essential for understanding their limitations. Information from direct microwave sensors (PMW-direct) provides the best results in the estimation of rainfall extremes, while those that rely more on IR information are linked to the poorest verification scores. This is directly related to the fact that microwave estimates are often better at representing precipitation than IR retrievals [51,52], because they are more sensitive to hydrometeor precipitation in the atmospheric column, unlike IR sensors, which are mostly limited to cloud top measurements [14].

Despite the advantages of direct microwave sources in event detection, they are associated with the highest false-alarm rate, which is higher than the miss rate under all intensity thresholds. This means that, using these sources, IMERG can detect high precipitation intensity values, but they do not generally coincide with the time and space of rain gauge records. In this sense, it should be noted that in addition to the instrumental limitations, the results of this study must be understood from the perspective of pixel-to-point evaluation. By comparing area-averaged rainfall data within a 0.1° grid with a point measurement within this area, we assume that each rain gauge represents the average rainfall of this area with sufficient accuracy, which entails certain limitations [54–56] much more dominant at sub-daily scales [14].

Considering the microphysical characteristics of precipitating clouds, IMERG sources, especially PMW-direct data, are sensitive to different cloud phases and other cloud characteristics. The worst results were often related to warm and mixed clouds. This reflects the dependence of IMERG on the time at which the ice particles finally form within a convective cloud. The results reported here, although representative of a semiarid climate area in the Western Mediterranean, are largely in agreement with those of [12] carried out in a forested area of West Africa. Although there were slight differences, the biases found in this study, especially for higher intensities, seem to be related to the IMERG processing algorithm and not to the dynamic mechanisms that originate from precipitation in each region.

7. Conclusions

The present study focused on the evaluation of IMERG Early and Late in the estimation of extreme precipitation. Based on information from 186 meteorological stations located in the Western Mediterranean region (Catalonia), several intensity thresholds derived from rain gauge records were used as a reference. The evaluation also considered different temporal aggregations, from the original GPM maximum temporal resolution to a daily scale, between 2014 and 2023. A selection of cases with semi-hourly episodes of extreme precipitation was considered to evaluate the dependencies of IMERG retrievals and their sources on cloud microphysical properties and rain gauge observations. The main conclusions of this study are as follows.

1. IMERG shows a marked tendency to underestimate precipitation as the rainfall intensity threshold increases and the temporal resolution increases. IMERG_L does not offer relevant advantages over the IMERG_E product in the detection of extreme events.
2. Although the underestimate of intense precipitation in IMERG is found for all source types, the negative bias is weaker when recoveries are due to PMW-direct data and increases when information from IR sensors is incorporated.
3. PMW-direct sensors generate high false-alarm rates, while the recovery algorithm with MORPH+IR sources is associated with the highest miss rates of precipitation events.
4. IMERG performs dramatically better in the presence of precipitating ice clouds than in warm and mixed clouds. Uncertainties in the occurrence of extreme precipitation associated with ice clouds are related to COT characteristics, as in the mixed phase. However, the estimation of intense precipitation associated with warm clouds shows the worst results and is related to other microphysical characteristics, such as COT and R_{eff}.

The assessment presented here is made during the changeover from IMERG 06 to 07, which includes significant changes, such as the introduction of the SHARPEN scheme. Therefore, this study contributes to the understanding of the mechanisms of extreme precipitation satellite estimates and their relationship to cloud microphysical features. This is one of the few works that considers a semi-hourly resolution to study this type of event in the Mediterranean and mid-latitudes in general. Future studies will focus, on the one hand, on the evaluation of the V07 version and check if the updates to the algorithm improve its performance regarding V06. On the other, it will also be a priority to focus on the validation of GPM core satellite observations, such as DPR and GMI, in the estimation of heavy rainfall events.

Author Contributions: Conceptualization, E.P. and J.B.; methodology, E.P. and J.B.; formal analysis, E.P.; data curation, E.P.; writing—original draft preparation, E.P. and J.B.; writing—review and editing, all the authors; visualization, E.P.; supervision, J.B. and M.U. All authors have read and agreed to the published version of the manuscript.

Funding: This research was partly funded by the ARTEMIS project (PID2021-124253OB-I00 MINECO/FEDER) and the Water Research Institute (IdRA) of the University of Barcelona.

Data Availability Statement: Data are contained within the article.

Acknowledgments: Satellite and gauge data for this study were provided by NASA/JAXA and the Meteorological Service of Catalonia, respectively. CMIC NWC SAF data were provided by the Spanish State Meteorological Agency (AEMET) as the leading entity and approved by EUMETSAT. The authors wish to acknowledge the support from the Secretariat for Universities and Research of the Ministry of Business and Knowledge of the Government of Catalonia and the European Social Fund.

Conflicts of Interest: The authors declare no conflicts of interest.

Appendix A

Table A1. Semi-hourly configuration of the new cloud phases from the original resolution phases (15 min) of the CMIC NW SAF product.

Interval 1 (15 min)	Interval 2 (15 min)	Resulting Phase (30 min)
liquid	ice	mixed
liquid	liquid	liquid
ice	ice	ice
mixed	mixed	mixed
liquid/ice	mixed	liquid/ice
liquid/ice/mixed	cloud-free/undefined	liquid/ice/mixed

Appendix B

Table A2. Rbias (%) for each temporal aggregation and different precipitation intensity threshold considered (1%, 5%, 10%, and 18% of the maximum envelope curve).

Score	IMERG	0.5 h	1 h	3 h	6 h	9 h	12 h	24 h
				≥1%				
Rbias	E	−29.25	−19.80	−7.91	−3.78	−3.00	−0.65	−0.35
	L	−29.64	−17.96	−3.99	0.71	1.85	3.34	3.57
				≥5%				
Rbias	E	−68.45	−54.79	−33.52	−25.82	−24.42	−21.44	−20.63
	L	−67.40	−52.02	−29.12	−21.19	−19.26	−17.02	−15.76
				≥10%				
Rbias	E	−77.22	−68.32	−46.72	−32.33	−29.47	−27.34	−25.05
	L	−76.58	−66.52	−42.66	−27.70	−23.20	−22.91	−19.15
				≥18%				
Rbias	E	−83.20	−77.01	−56.39	−36.50	−32.58	−30.16	−27.69
	L	−83.39	−76.57	−53.57	−33.38	−25.43	−24.69	−20.73

Appendix C

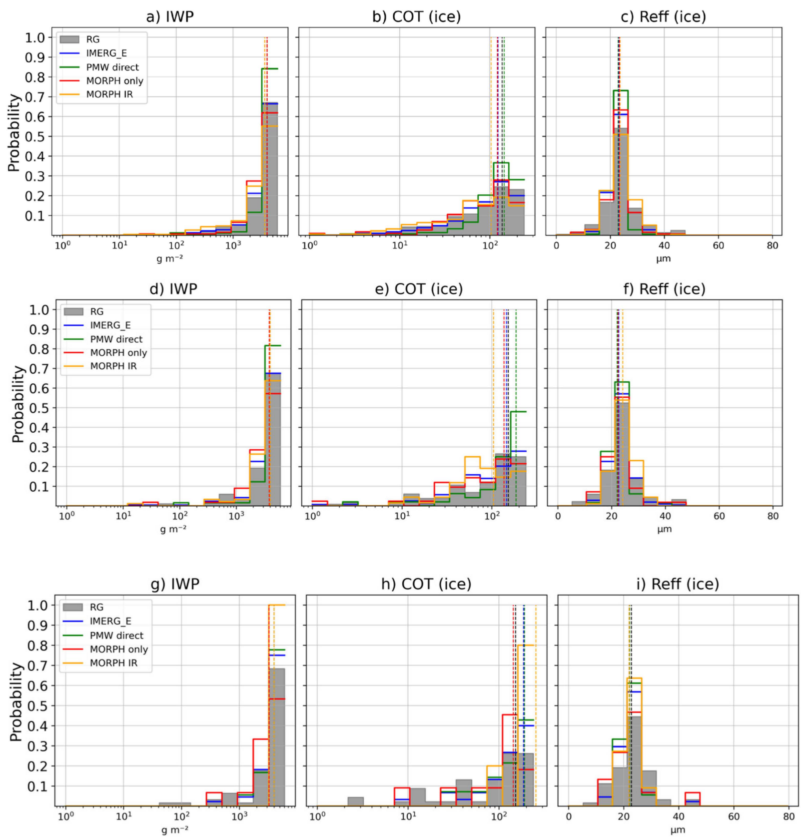

Figure A1. Probability distributions of the cloud properties described in Section 2.2.3 based on all time steps of intense precipitation greater than or equal to (**a**–**c**) 5%, (**d**–**f**) 10%, and (**g**–**i**) 18% of the envelope curve in the RG (gray shading), IMERG, and its sources (colored lines), only for ice cloud tops. The vertical colored lines in each plot indicate the median values of the respective distribution.

References

1. Insua-Costa, D.; Lemus-Cánovas, M.; Miguez-Macho, G.; Llasat, M.C. Climatology and Ranking of Hazardous Precipitation Events in the Western Mediterranean Area. *Atmos. Res.* **2021**, *255*, 105521. [CrossRef]
2. Michaelides, S.; Karacostas, T.; Sánchez, J.L.; Retalis, A.; Pytharoulis, I.; Homar, V.; Romero, R.; Zanis, P.; Giannakopoulos, C.; Bühl, J. Reviews and Perspectives of High Impact Atmospheric Processes in the Mediterranean. *Atmos. Res.* **2018**, *208*, 4–44. [CrossRef]
3. Panegrossi, G.; Casella, D.; Dietrich, S.; Marra, A.C.; Sanò, P.; Mugnai, A.; Baldini, L.; Roberto, N.; Adirosi, E.; Cremonini, R.; et al. Use of the GPM Constellation for Monitoring Heavy Precipitation Events Over the Mediterranean Region. *IEEE J. Sel. Top. Appl. Earth Obs. Remote Sens.* **2016**, *9*, 2733–2753. [CrossRef]
4. Rigo, T.; Llasat, M.C. A Methodology for the Classification of Convective Structures Using Meteorological Radar: Application to Heavy Rainfall Events on the Mediterranean Coast of the Iberian Peninsula. *Nat. Hazards Earth Syst. Sci.* **2004**, *4*, 59–68. [CrossRef]
5. Siena, M.; Levizzani, V.; Marra, F. A Method to Derive Satellite-Based Extreme Precipitation Return Levels in Poorly Gauged Areas. *J. Hydrol.* **2023**, *626*, 130295. [CrossRef]
6. del Jesus, M.; Diez-Sierra, J. Climate Change Effects on Sub-Daily Precipitation in Spain. *Hydrol. Sci. J.* **2023**, *68*, 1065–1077. [CrossRef]
7. Toreti, A.; Naveau, P.; Zampieri, M.; Schindler, A.; Scoccimarro, E.; Xoplaki, E.; Dijkstra, H.A.; Gualdi, S.; Luterbacher, J. Projections of Global Changes in Precipitation Extremes from Coupled Model Intercomparison Project Phase 5 Models. *Geophys. Res. Lett.* **2013**, *40*, 4887–4892. [CrossRef]
8. Zittis, G.; Bruggeman, A.; Lelieveld, J. Revisiting Future Extreme Precipitation Trends in the Mediterranean. *Weather Clim. Extrem.* **2021**, *34*, 100380. [CrossRef] [PubMed]
9. IMERG: Integrated Multi-Satellite Retrievals for GPM | NASA Global Precipitation Measurement Mission. Available online: https://gpm.nasa.gov/data/imerg (accessed on 17 January 2024).
10. Huffman, G.J.; Bolvin, D.T.; Braithwaite, D.; Hsu, K.-L.; Joyce, R.J.; Kidd, C.; Nelkin, E.J.; Sorooshian, S.; Stocker, E.F.; Tan, J.; et al. Integrated Multi-Satellite Retrievals for the Global Precipitation Measurement (GPM) Mission (IMERG). In *Satellite Precipitation Measurement*; Levizzani, V., Kidd, C., Kirschbaum, D.B., Kummerow, C.D., Nakamura, K., Turk, F.J., Eds.; Advances in Global Change Research; Springer International Publishing: Cham, Switzerland, 2020; Volume 1, pp. 343–353. ISBN 978-3-030-24568-9.
11. Li, Z.; Tang, G.; Kirstetter, P.; Gao, S.; Li, J.-L.F.; Wen, Y.; Hong, Y. Evaluation of GPM IMERG and Its Constellations in Extreme Events over the Conterminous United States. *J. Hydrol.* **2022**, *606*, 127357. [CrossRef]
12. Maranan, M.; Fink, A.H.; Knippertz, P.; Amekudzi, L.K.; Atiah, W.A.; Stengel, M. A Process-Based Validation of GPM IMERG and Its Sources Using a Mesoscale Rain Gauge Network in the West African Forest Zone. *J. Hydrometeorol.* **2020**, *21*, 729–749. [CrossRef]
13. Mazzoglio, P.; Laio, F.; Balbo, S.; Boccardo, P.; Disabato, F. Improving an Extreme Rainfall Detection System with GPM IMERG Data. *Remote Sens.* **2019**, *11*, 677. [CrossRef]
14. Watters, D.C.; Gatlin, P.N.; Bolvin, D.T.; Huffman, G.J.; Joyce, R.; Kirstetter, P.; Nelkin, E.J.; Ringerud, S.; Tan, J.; Wang, J.; et al. Oceanic Validation of IMERG-GMI Version 6 Precipitation Using the GPM Validation Network. *J. Hydrometeorol.* **2023**, *1*, 125–142. [CrossRef]
15. Nascimento, J.G.; Althoff, D.; Bazame, H.C.; Neale, C.M.U.; Duarte, N.S.; Ruhoff, L.A.; Gonçalves, I.Z. Evaluating the Latest IMERG Products in a Subtropical Climate: The Case of Paraná State, Brazil. *Remote Sens.* **2021**, *13*, 906. [CrossRef]
16. Moazami, S.; Na, W.; Najafi, M.R.; de Souza, C. Spatiotemporal Bias Adjustment of IMERG Satellite Precipitation Data across Canada. *Adv. Water Resour.* **2022**, *168*, 104300. [CrossRef]
17. Peinó, E.; Bech, J.; Udina, M. Performance Assessment of GPM IMERG Products at Different Time Resolutions, Climatic Areas and Topographic Conditions in Catalonia. *Remote Sens.* **2022**, *14*, 5085. [CrossRef]
18. Fang, J.; Yang, W.; Luan, Y.; Du, J.; Lin, A.; Zhao, L. Evaluation of the TRMM 3B42 and GPM IMERG Products for Extreme Precipitation Analysis over China. *Atmos. Res.* **2019**, *223*, 24–38. [CrossRef]
19. Guo, H.; Chen, S.; Bao, A.; Behrangi, A.; Hong, Y.; Ndayisaba, F.; Hu, J.; Stepanian, P.M. Early Assessment of Integrated Multi-Satellite Retrievals for Global Precipitation Measurement over China. *Atmos. Res.* **2016**, *176–177*, 121–133. [CrossRef]
20. Tian, F.; Hou, S.; Yang, L.; Hu, H.; Hou, A. How Does the Evaluation of the GPM IMERG Rainfall Product Depend on Gauge Density and Rainfall Intensity? *J. Hydrometeorol.* **2018**, *19*, 339–349. [CrossRef]
21. Wang, T.; Li, Z.; Ma, Z.; Gao, Z.; Tang, G. Diverging Identifications of Extreme Precipitation Events from Satellite Observations and Reanalysis Products: A Global Perspective Based on an Object-Tracking Method. *Remote Sens. Environ.* **2023**, *288*, 113490. [CrossRef]
22. Zhang, D.; Yang, M.; Ma, M.; Tang, G.; Wang, T.; Zhao, X.; Ma, S.; Wu, J.; Wang, W. Can GPM IMERG Capture Extreme Precipitation in North China Plain? *Remote Sens.* **2022**, *14*, 928. [CrossRef]
23. Pradhan, R.K.; Markonis, Y.; Vargas Godoy, M.R.; Villalba-Pradas, A.; Andreadis, K.M.; Nikolopoulos, E.I.; Papalexiou, S.M.; Rahim, A.; Tapiador, F.J.; Hanel, M. Review of GPM IMERG Performance: A Global Perspective. *Remote Sens. Environ.* **2022**, *268*, 112754. [CrossRef]
24. Tan, J.; Petersen, W.A.; Tokay, A. A Novel Approach to Identify Sources of Errors in IMERG for GPM Ground Validation. *J. Hydrometeorol.* **2016**, *17*, 2477–2491. [CrossRef]

25. Gebregiorgis, A.S.; Kirstetter, P.-E.; Hong, Y.E.; Gourley, J.J.; Huffman, G.J.; Petersen, W.A.; Xue, X.; Schwaller, M.R. To What Extent Is the Day 1 GPM IMERG Satellite Precipitation Estimate Improved as Compared to TRMM TMPA-RT? *J. Geophys. Res. Atmos.* **2018**, *123*, 1694–1707. [CrossRef]
26. Rajagopal, M.; Zipser, E.; Huffman, G.; Russell, J.; Tan, J. Comparisons of IMERG Version 06 Precipitation at and between Passive Microwave Overpasses in the Tropics. *J. Hydrometeorol.* **2021**, *22*, 2117–2130. [CrossRef]
27. Servei Meteorològic de Catalunya. Atles Climàtic 1991–2020. Available online: https://www.meteo.cat/wpweb/climatologia/el-clima/atles-climatic/ (accessed on 16 January 2024).
28. Trapero, L.; Bech, J.; Duffourg, F.; Esteban, P.; Lorente, J. Mesoscale Numerical Analysis of the Historical November 1982 Heavy Precipitation Event over Andorra (Eastern Pyrenees). *Nat. Hazards Earth Syst. Sci.* **2013**, *13*, 2969–2990. [CrossRef]
29. Llasat, M.C.; Marcos, R.; Turco, M.; Gilabert, J.; Llasat-Botija, M. Trends in Flash Flood Events versus Convective Precipitation in the Mediterranean Region: The Case of Catalonia. *J. Hydrol.* **2016**, *541*, 24–37. [CrossRef]
30. Llasat, M.C.; Puigcerver, M. Total Rainfall and Convective Rainfall in Catalonia, Spain. *Int. J. Climatol.* **1997**, *17*, 1683–1695. [CrossRef]
31. Navarro, A.; García-Ortega, E.; Merino, A.; Sánchez, J.L.; Tapiador, F.J. Orographic Biases in IMERG Precipitation Estimates in the Ebro River Basin (Spain): The Effects of Rain Gauge Density and Altitude. *Atmos. Res.* **2020**, *244*, 105068. [CrossRef]
32. Trapero, L.; Bech, J.; Rigo, T.; Pineda, N.; Forcadell, D. Uncertainty of Precipitation Estimates in Convective Events by the Meteorological Service of Catalonia Radar Network. *Atmos. Res.* **2009**, *93*, 408–418. [CrossRef]
33. Furl, C.; Ghebreyesus, D.; Sharif, H.O. Assessment of the Performance of Satellite-Based Precipitation Products for Flood Events across Diverse Spatial Scales Using GSSHA Modeling System. *Geosciences* **2018**, *8*, 191. [CrossRef]
34. Tan, J.; Huffman, G.J.; Bolvin, D.T.; Nelkin, E.J. IMERG V06: Changes to the Morphing Algorithm. *J. Atmos. Ocean. Technol.* **2019**, *36*, 2471–2482. [CrossRef]
35. Hong, Y.; Hsu, K.-L.; Sorooshian, S.; Gao, X. Precipitation Estimation from Remotely Sensed Imagery Using an Artificial Neural Network Cloud Classification System. *J. Appl. Meteorol. Climatol.* **2004**, *43*, 1834–1853. [CrossRef]
36. Llabrés-Brustenga, A.; Rius, A.; Rodríguez-Solà, R.; Casas-Castillo, M.C.; Redaño, A. Quality Control Process of the Daily Rainfall Series Available in Catalonia from 1855 to the Present. *Theor. Appl. Clim.* **2019**, *137*, 2715–2729. [CrossRef]
37. Llabrés-Brustenga, A.; Rius, A.; Rodríguez-Solà, R.; Casas-Castillo, M.C. Influence of Regional and Seasonal Rainfall Patterns on the Ratio between Fixed and Unrestricted Measured Intervals of Rainfall Amounts. *Theor. Appl. Clim.* **2020**, *140*, 389–399. [CrossRef]
38. WMO E-Library. Available online: https://library.wmo.int (accessed on 30 December 2023).
39. CMIC_description—NWCSAF. Available online: https://www.nwcsaf.org/cmic_description (accessed on 19 December 2023).
40. NWC SAF; EUMETSAT. *Algorithm Theoretical Basis Document for the Cloud Product Processors of the NWC/GEO MTG-I Day-1*; EUMETSAT: Darmstadt, Germany, 2019.
41. Mahmoud, M.T.; Mohammed, S.A.; Hamouda, M.A.; Mohamed, M.M. Impact of Topography and Rainfall Intensity on the Accuracy of IMERG Precipitation Estimates in an Arid Region. *Remote Sens.* **2021**, *13*, 13. [CrossRef]
42. Lasser, M.; Sungmin, O.; Foelsche, U. Evaluation of GPM-DPR Precipitation Estimates with WegenerNet Gauge Data. *Atmos. Meas. Tech.* **2019**, *12*, 5055–5070. [CrossRef]
43. Jennings, A.H. World's Greatest Observed Point Rainfalls. *Mon. Weather Rev.* **1950**, *78*, 4–5. [CrossRef]
44. Breña-Naranjo, J.A.; Pedrozo-Acuña, A.; Rico-Ramirez, M.A. World's Greatest Rainfall Intensities Observed by Satellites. *Atmos. Sci. Lett.* **2015**, *16*, 420–424. [CrossRef]
45. Galmarini, S.; Steyn, D.G.; Ainslie, B. The Scaling Law Relating World Point-Precipitation Records to Duration. *Int. J. Climatol.* **2004**, *24*, 533–546. [CrossRef]
46. Gonzalez, S.; Bech, J. Extreme Point Rainfall Temporal Scaling: A Long Term (1805–2014) Regional and Seasonal Analysis in Spain. *Int. J. Climatol.* **2017**, *37*, 5068–5079. [CrossRef]
47. González-Herrero, S.; Vasallo, F.; Bech, J.; Gorodetskaya, I.; Elvira, B.; Justel, A. Extreme Precipitation Records in Antarctica. *Int. J. Climatol.* **2023**, *43*, 3125–3138. [CrossRef]
48. Servei Meteorològic de Catalunya. Situació Meteorològica de Perill. Available online: https://www.meteo.cat/wpweb/divulgacio/la-prediccio-meteorologica/situacio-meteorologica-de-perill/ (accessed on 11 December 2023).
49. Gaona, M.F.R.; Overeem, A.; Leijnse, H.; Uijlenhoet, R. First-Year Evaluation of GPM Rainfall over the Netherlands: IMERG Day 1 Final Run (V03D). *J. Hydrometeorol.* **2016**, *17*, 2799–2814. [CrossRef]
50. Khodadoust Siuki, S.; Saghafian, B.; Moazami, S. Comprehensive Evaluation of 3-Hourly TRMM and Half-Hourly GPM-IMERG Satellite Precipitation Products. *Int. J. Remote Sens.* **2017**, *38*, 558–571. [CrossRef]
51. Kirstetter, P.-E.; Petersen, W.A.; Kummerow, C.D.; Wolff, D.B. Integrated Multi-Satellite Evaluation for the Global Precipitation Measurement: Impact of Precipitation Types on Spaceborne Precipitation Estimation. In *Satellite Precipitation Measurement*; Levizzani, V., Kidd, C., Kirschbaum, D.B., Kummerow, C.D., Nakamura, K., Turk, F.J., Eds.; Advances in Global Change Research; Springer International Publishing: Cham, Switzerland, 2020; Volume 2, pp. 583–608. ISBN 978-3-030-35798-6.
52. Petersen, W.A.; Kirstetter, P.-E.; Wang, J.; Wolff, D.B.; Tokay, A. The GPM Ground Validation Program. In *Satellite Precipitation Measurement*; Levizzani, V., Kidd, C., Kirschbaum, D.B., Kummerow, C.D., Nakamura, K., Turk, F.J., Eds.; Advances in Global Change Research; Springer International Publishing: Cham, Switzerland, 2020; Volume 2, pp. 471–502. ISBN 978-3-030-35798-6.

53. Kühnlein, M.; Thies, B.; Nauß, T.; Bendix, J. Rainfall-Rate Assignment Using MSG SEVIRI Data—A Promising Approach to Spaceborne Rainfall-Rate Retrieval for Midlatitudes. *J. Appl. Meteorol. Climatol.* **2010**, *49*, 1477–1495. [CrossRef]
54. Kazamias, A.-P.; Sapountzis, M.; Lagouvardos, K. Evaluation of GPM-IMERG Rainfall Estimates at Multiple Temporal and Spatial Scales over Greece. *Atmos. Res.* **2022**, *269*, 106014. [CrossRef]
55. Yu, C.; Hu, D.; Liu, M.; Wang, S.; Di, Y. Spatio-Temporal Accuracy Evaluation of Three High-Resolution Satellite Precipitation Products in China Area. *Atmos. Res.* **2020**, *241*, 104952. [CrossRef]
56. Da Freitas, E.S.; Coelho, V.H.R.; Xuan, Y.; de Melo, C.D.; Gadelha, A.N.; Santos, E.A.; de Galvão, C.O.; Ramos Filho, G.M.; Barbosa, L.R.; Huffman, G.J.; et al. The Performance of the IMERG Satellite-Based Product in Identifying Sub-Daily Rainfall Events and Their Properties. *J. Hydrol.* **2020**, *589*, 125128. [CrossRef]

4.2 Intercomparison of HSAF and IMERG satellite precipitation products over a Mediterranean coastal region

4.2.1 Summary

The well-established scientific collaboration between EUMETSAT H SAF and the GPM program has significantly contributed to the prolific development and advancement of retrieval algorithm techniques (Rysman et al., 2018; Sanò et al., 2018), as well as validation studies over the Mediterranean region (Petracca et al., 2018). Therefore, this section focuses on comparing various H SAF products (H61, H64, H68) and the Early and Late runs of the GPM IMERG. By analyzing hourly and daily data over 17 days with intense precipitation records, continuous and categorical statistical indicators are determined to assess the performance of these products in their estimations.

This section aims to build on the previous section by delving deeper into satellite-derived estimates of extreme precipitation events comparing IMERG and H SAF products. It represents one of the first studies in a Mediterranean and coastal region that validates these products outside the countries included in the H SAF validation program.

The study is the basis of a paper that will be submitted to a high-impact journal on the subject. This future work will provide additional insights into the comparative performance of different satellite precipitation products in the Mediterranean area.

4.2.2 Preprint Article

Peinó, E., Bech, J., Petracca, M. and Udina, M. (2024). Intercomparison of H SAF and IMERG satellite precipitation products over a Mediterranean coastal region.

Intercomparison of H SAF and IMERG heavy rainfall retrievals over a Mediterranean coastal region

Eric Peinó[1], Joan Bech[1,2], Marco Petracca[3], and Mireia Udina[1]

[1]Department of Applied Physics—Meteorology, Universitat de Barcelona, Barcelona, Spain
[2]Water Research Institute, Universitat de Barcelona, Barcelona, Spain
[3]National Research Council of Italy, Institute of Atmospheric Sciences and Climate (CNR-ISAC), Rome, Italy

Abstract: Satellite-based precipitation products play a crucial role in providing global, continuous, and reliable estimates of rainfall, essential for understanding and managing Earth's water cycle. This study aims to evaluate the accuracy of three H SAF products (H61, H64, H68) and compare their performance with the Early and Late IMERG products in the western Mediterranean region, particularly in detecting and estimating extreme precipitation events. The analysis is based on hourly and daily rainfall data collected from 186 rain gauges in Catalonia, using a point-to-pixel as approach method. The results show that while all satellite products tend to overestimate observed precipitation, H64 performs best at the daily scale, and H68 stands out in hourly detection. However, the accuracy of all products significantly decrease with increasing precipitation intensity, with H68 exhibiting the largest errors in high-intensity events. Despite significant biases, the IMERG Late product proved to be the most effective in detecting intense precipitation events. This study offers critical insights into their comparative performance, enhancing their application in hydrometeorological management and disaster response.

1 Introduction

Observing and measuring precipitation on a global scale is crucial to our understanding of the Earth system and has a significant impact on society at multiple levels (Kidd et al., 2021; Kirschbaum et al., 2017; Skofronick-Jackson et al., 2017). Precipitation acts as a direct link between the global energy and water cycles, regulating energy exchange (Trenberth et al., 2009) and is the main factor controlling many natural hazards, such as droughts and floods (Vicente-Serrano et al., 2010). Accurate and reliable precipitation information is of great importance in water resources planning, hydrological simulation, environmental and ecological management, and irrigation management.

Currently, there are three main approaches to obtain observational precipitation estimates: in situ measurements, remote sensing (including weather radar and satellite) and numerical simulation (Xie et al., 2022). Rain gauges are the most common and reliable way to directly measure precipitation on a point scale (Lanza & Stagi, 2008). However, the density and distribution of rain gauge networks vary significantly around the world, with few or nonexistent in marine and mountainous areas making it difficult to provide continuous precipitation information. Because of their ability to provide global and continuous coverage, satellite precipitation products fundamentally present an unprecedented opportunity to overcome the limitations of spatially discontinuous distribution of rain gauges and have shown great potential in a wide range of applications (Serrat-Capdevila et al., 2014). However, these products are derived from indirect precipitation measurements and simulation, so errors in the products exist and vary across different regions, seasons, event types, and precipitation phases.

Since the launch of the first meteorological satellite in 1960, numerous satellites have been developed with sensors capable of providing observations from which surface precipitation can be derived (Kidd & Levizzani, 2019). However, it was not until the launch of the Tropical Rainfall Measuring Mission (TRMM) in December 1997 and, subsequently, the Global Precipitation Measurement Mission (GPM) in February 2014, that missions dedicated specifically to satellite precipitation estimation were initiated. NASA's Integrated Multi-satellitE Retrievals for GPM (IMERG) algorithm (Huffman et al., 2020) is one of the most reliable products for quantitative measurement of precipitation from satellites (Pradhan et al., 2022). The evaluation of IMERG performance has reflected a growing interest in research, with studies stratifying the results according to time scales, topographic features, climatic conditions and precipitation intensity, allowing a more specific description of IMERG behavior in different conditions and its most appropriate application (Lei et al., 2021; Moazami et al., 2022; Rojas et al., 2021; Yang et al., 2020; Zhang et al., 2022).

On the other hand, the Satellite Application Facility (SAF) on support to Operational Hydrology and Water Management (H SAF, or Hydrology SAF) is one of the current eight SAFs managed by European Organisation for the Exploitation of Meteorological Satellites (EUMETSAT). H SAF is the main European concerted effort on satellite precipitation estimates, focusing on precipitation products from available geosynchronous and low-Earth-orbiting satellites using both passive-microwave (PMW) and infrared (IR) data (Mugnai et al., 2013). H SAF generates operational precipitation products that are not only useful for hydrological applications but are also valid in themselves because they are based on a series of advanced and ever-improving algorithms. Since its inception, H SAF has adopted a validation strategy, which is now growing and reaching the critical mass necessary to validate operational and climate products. Specifically, H SAF includes a product validation program and a hydrological validation program, involving several countries and instrumental for evaluating and improving H SAF precipitation products, as well as for assessing their usefulness in fighting floods, landslides, avalanches, and evaluating water resources (Panegrossi et al., 2012; Puca et al., 2014).

Several studies characterize and quantify the errors of satellite precipitation retrievals. Since there is no satellite product that performs best under all conditions, some of these studies have focused on comparing the performance of various satellite products in specific areas to enhance their application in diverse geographic and climatological contexts (Baez-Villanueva et al., 2018; Z. Li et al., 2013; Yu et al., 2020). However, according to the available literature, few studies evaluate the H SAF precipitation products outside the countries selected in their validation program and directly compare them with other products such as IMERG. Therefore, this study aims to evaluate the accuracy of three H SAF products (H61, H64, H68) with hourly and daily temporal aggregations and to intercompare their performance with the Early and Late IMERG products in the western Mediterranean. The validation includes assessing the ability of these products to detect and estimate extreme precipitation events. The methodology, like the H SAF validation program, focuses on two fundamental components: one based on categorical and continuous statistics, and the other on a selection of cases with precipitation events.

The structure of this study is as follows **Section 2** provides a description of the study area, datasets used (H SAF and IMERG products), the comparison methodology adopted in this study and the evaluation metrics employed. **Section 3** shows results and discussions considering the validation of all products based on hourly and daily rainfall data for different intensity thresholds according to the rain gauges. Finally, a summary and conclusion are provided in **Section 4**.

2 Materials and Methods

2.1 Study Area

Catalonia, located in the northeast of the Iberian Peninsula, is characterized by a complex topography that poses challenges for precipitation estimation using remote sensors, as well as for the estimation of the precipitation field using rain gauge stations (Navarro et al., 2020; Peinó et al., 2022; Trapero et al., 2009). Covering approximately 32107 km^2, Catalonia exhibits a wide range of climates due to its latitudinal position, the influence of the Mediterranean Sea, and its complex orography. To the north, it is bordered by the Pyrenees, with elevations exceeding 3000 meters above sea level, while the inland area is predominantly flat with some orographic contrasts resulting from the erosion of the Ebro River and its tributaries (Figure 1a). Additionally, the coastal and pre-coastal mountain ranges, oriented from northeast to southwest towards the Mediterranean Sea, enhance the development of flash floods from both a hydrological perspective (small torrential catchments) and a meteorological perspective (orographic forcing of Mediterranean air masses) (Jansa et al., 2014; Llasat et al., 2016). Consequently, this region experiences thunderstorms and flash floods annually (Llasat et al., 2014).

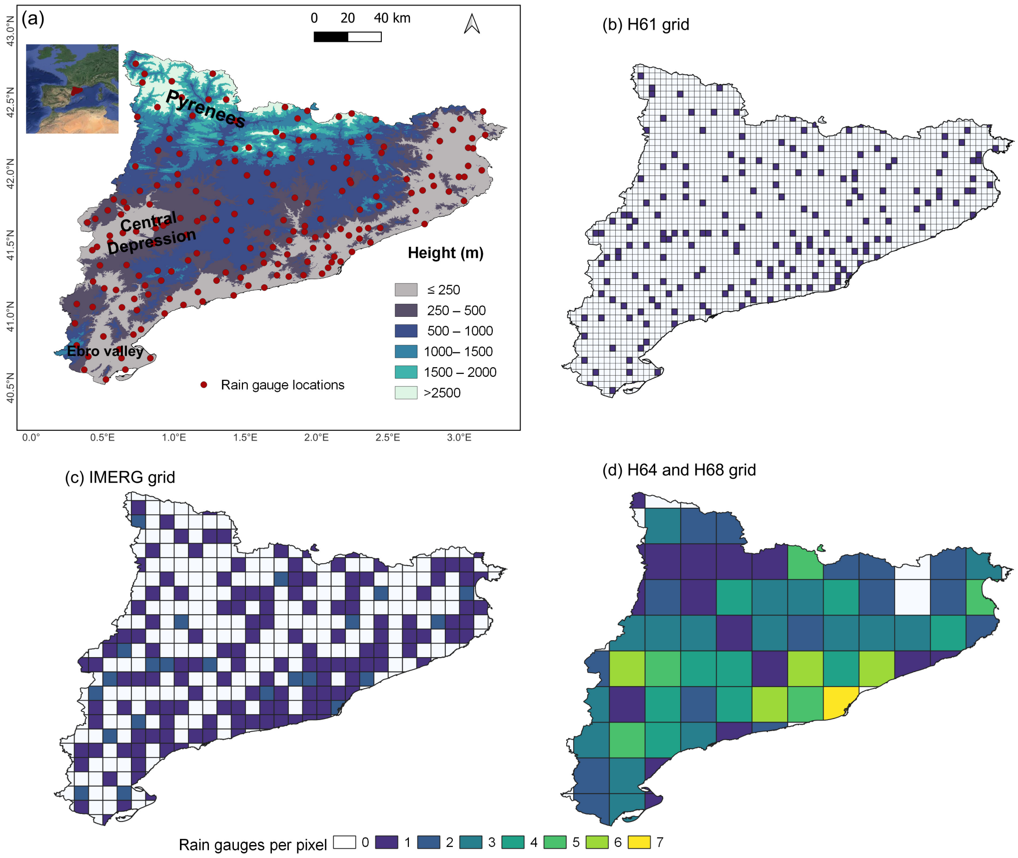

Figure 1: (a) Digital elevation model of Catalonia and rain gauges network distribution (red dots) (b) Number of rain gauges per pixel in H61 product considering the spatial resolution of each satellite grid cell in the Catalonia domain (c) and (d) Same as (b) but for IMERG products and for H64 and H68 products, respectively.

2.2 Data sets

2.2.1 Satellite precipitation products

Table 1 presents a summary of the five satellite precipitation products used in this study. The columns represent the original temporal and spatial resolutions of these products, as well as the method used for extracting data comparable to rain gauge records (see the next section). Finally, we show the temporal resolution used for validating these products, which was selected in order to compare systematically the different products to a common framework (1h or 24h).

Table 1: Summary of satellite precipitation products used.The “Method” column refers to the method of matching with rain gauge data (more details in **Section 2.3**).

Product	Temporal Resolution	Spatial Resolution	Coverage	Method	Temporal aggregation used
H SAF 61	1h/24h	3 km at the sub-satellite point	60°S - 75°N, 80°W - 80°E	Optimal	1h/24h
H SAF 68	30 min	0.25° x 0.25°	60°S - 75°N, 60°W - 60°E	pixel-to-point	1h
H SAF 64	24h	0.25° x 0.25°	60°S - 75°N, 60°W - 60°E	pixel-to-point	24h
IMERG (Early, Late)	30 min	0.1° x 0.1°	90°N - S	pixel-to-point	1h/24h

The NASA Integrated Multi-satellite Retrievals for GPM (IMERG) algorithm (Huffman et al., 2015) intercalibrates, merges, and interpolates precipitation estimates from the GPM/TRMM satellite constellation. It utilizes Passive Microwave (PMW) radiometers in low Earth orbits, calibrated PMW estimates with geostationary IR sensors, and rain gauge records to generate a global-gridded product at a spatial resolution of 0.1° × 0.1° and a temporal resolution of 30 minutes. The algorithm is executed three times (Early, Late, and Final runs) for each gridded spatiotemporal estimate, with estimations improving with latency due to the incorporation of more data and more complex interpolation of PMW estimates (Tan et al., 2019). This study uses data from the Early and Late version 06B level 3 products, which provide better results in retrieving heavy precipitation compared to the IMERG Final product (Furl et al., 2018; Peinó et al., 2022, 2024).

The EUMETSAT Satellite Application Facility on Support to Operational Hydrology and Water Management (H SAF) generates and archives high-quality datasets and products for operational hydrological applications from the acquisition and processing of Earth observation satellite data in both geostationary and polar orbits, operated by EUMETSAT and other satellite organizations (Force, 2024). Specifically, the near-real-time product H61B integrates instantaneous precipitation maps generated by the P-IN-SEVIRI-PMW product, based on intercalibrated PMW Level 2 instantaneous precipitation index estimates combined with the 10.8μm channel of the SEVIRI instrument (ATBD, 2020). This integration provides hourly accumulated precipitation and 24-hour accumulated precipitation at 00, 06, 12, and 18 UTC.

The H64 product (ATBD, 2022) is a gridded daily precipitation product generated by merging PMW precipitation estimates from H-AUX-23 and H67 with soil moisture-derived estimates from the SM2RAIN algorithm (Brocca et al., 2014; Ciabatta et al., 2018; Koster et al., 2016; Massari et al., 2017). Over oceans, the algorithm relies solely on PMW estimates. Factors such as frozen soils, heavily vegetated areas, and complex topography, which affect the reliability of the input product, impact the quality of the H64 product. H64 has a spatial resolution of 0.25° x 0.25°.

The level 3 H68 product (ATBD, 2021) provides a gridded MW precipitation index at regular 30-minute intervals. It is based on instantaneous precipitation index estimates available in P-IN-SSMIS (H01), P-IN-MHS (H02B), P-IN-ATMS (H18), H-AUX-17, and H-AUX-20, combined and intercalibrated. For each 30-minute interval, all available orbits of LEO satellites carrying PMW radiometers (SSMIS, AMSR-2, GMI, ATMS, AMSU/MHS) over the extended H SAF area are considered to provide a single precipitation index estimate for each grid cell.

2.2.2 Rain gauge data

The network of automatic surface weather stations of the Meteorological Service of Catalonia was used for the validation of satellite precipitation products (Peinó et al., 2022, 2024). It includes 186 stations distributed across the region (Figure 1), with an average minimum distance between station of 8.7 km and a density of 1.13 stations per 100 km^2, which is six times the minimum threshold recommended by the WMO for inland flat and undulating areas (WMO, 1994). Semi-hourly precipitation records with a resolution of 0.1 mm were utilized. A quality control scheme was applied to the SMC rain gauge records based on comparisons with nearby stations and correlation analysis (Llabrés-Brustenga et al., 2019, 2020).

2.3 Methodology

2.3.1 Selection of case studies

For the validation exercise, eighteen case studies occurring between 2021 and 2023 were considered (Table 2). The selection of these cases depended not only on the occurrence of precipitation at any station in the region but also on whether any records from both rain gauges and satellite indicated extreme precipitation values, often exceeding the intense precipitation threshold established by the Meteorological Service of Catalonia (20 mm in 30 minutes). Table 2 provides a summary of the case studies and the number of stations that exceeded selected precipitation thresholds on an hourly and daily scale. This approach allowed us to construct a database representing extreme precipitation episodes, facilitating the assessment of the remote sensing systems' capabilities in such events.

Table 2: Selected case studies and number of stations (N) exceeding selected threshold during the day on an hourly and daily scale. An asterisk (∗) denotes days when any of the stations exceeded the intense precipitation threshold established by the SMC (≥ 100 mm/day), and double asterisks (∗∗) indicate days classified by the SMC as exceptional meteorological episodes in the region.

Dates	**1h∗∗ (mm/h)**			**24h (mm/day)**		
	N ≥ 0.5	**N ≥ 15**	**N ≥ 30**	**N ≥ 1**	**N ≥ 50**	**N ≥ 100**
09/05/2021	49	0	0	100	1	0
17/06/2021∗∗	81	13	3	141	10	0
31/07/2021	98	13	1	183	4	0
25/08/2021	25	8	2	88	3	0
01/09/2021∗∗	69	5	2	114	7	2
09/09/2021	31	3	2	97	0	0
18/09/2021	55	3	1	125	0	0
23/11/2021∗∗	121	6	3	184	37	9
12/03/2022∗	181	2	0	187	24	3
20/03/2022∗	66	2	0	132	3	2
17/08/2022	32	9	4	94	4	0
24/08/2022	45	3	0	72	1	0
25/08/2022	80	7	0	123	2	0
23/09/2022∗∗	99	11	0	167	8	2
29/06/2023∗∗	113	16	0	170	6	1
27/07/2023	89	16	0	139	0	0
03/09/2023∗∗	25	8	5	44	11	7
15/09/2023∗∗	139	10	5	185	16	1

2.3.2 Point- Pixel comparison method

The validation process considered both hourly and daily temporal aggregations. For the temporal aggregations of the IMERG and H68 products, we checked that at least 100% of the semi-hourly data was available, there by guaranteeing the comparison of these products at hourly scale. At the daily scale, H68 product was not used due to insufficient data; instead, H64 was employed as indicated in Table 1.

A point-to-pixel (Gentilucci et al., 2022; R. Li et al., 2022; Y. Li et al., 2018; Xie et al., 2022) analysis was conducted in the study area to compare the time series of the selected rain gauge stations with the corresponding pixel values of the selected satellite products. The implicit assumption of this methodology is that the rain gauges are representative observations of the respective pixels of the products. For the H61 product, due to its high spatial resolution (approximately 3 km in the study area), each pixel was associated with only one rain gauge (Figure 1). Following the so-called fuzzy verification approach the point-to-pixel comparison considered the 9-pixel neighborhood closest to the rain gauge. Among these nine pixels, the one with the precipitation value closest to that estimated by the rain gauge was used for comparison. Naturally, only cells with at least one reporting station were selected for computation. For the other products, in cases where a pixel contained two or more rain gauges, the areal-average precipitation was calculated as the arithmetic average of all rain gauges located within that pixel. Although the satellite products analyzed have different spatial resolutions, studies such as Baez-Villanueva et al. (2018) and Wang et al. (2019) suggest that there are no substantial improvements when applying a resampling method between them. In this case, we also believe that products such as H61 and even IMERG would be significantly more affected if this technique were applied to bring them to the resolution of H68 and H64.

Additionally, prior to the final choice of the method used in this study, we performed a sensitivity analysis by varying the method to spatially match the records of satellite products and those obtained through rain gauges. Although all are variants of the point-to-pixel method, three variants were evaluated: (1) In case there was more than one rain gauge in one satellite pixel, the independence of the precipitation records in each one was maintained for the comparison; (2) we compared the rain gauge information with the eight pixels neighboring the one containing it and selected for the comparison the one with the least bias and (3) in case there was more than one rain gauge per pixel we took the arithmetic mean of the rain gauge records and compared it directly with the pixel containing them. Finally, the results obtained by these variants yielded results without substantial differences between them, so variant 2 was applied to H61 due to its high spatial resolution and variant 3 to the rest of the products.

2.4 Verification Scores

Three continuous statistics were calculated to quantify the magnitude of differences between satellite estimates and rain gauges: modified Kling-Gupta Efficiency (KGE), Correlation Coefficient (CC), percent bias (Rbias), and Root Mean Square Error (RMSE). RBIAS describes the deviation of satellite products from gauge data. KGE describes overall accuracy as a multi-component metric integrating correlation coefficient (CC), bias ratio (β), and variability ratio (γ), proposed by Gupta et al. (2009) and revised by Kling et al. (2012). The range of KGE is $(-\infty,\ 1]$, with a perfect value of 1. Higher values of KGE indicate better accuracy. The Rbias ranges from $-\infty$ to ∞, with a perfect value of 0. The sign of Rbias (positive or negative) indicates the direction of deviation (overestimation or underestimation) and absolute value reflects the magnitude of deviation. RMSE measures the size of the average error, giving more weight to large errors without showing the direction of deviation between satellite products and rain gauges. Table 3 shows details of the calculation of these statistics.

Table 3: List of the continuous verification metrics used to evaluate satellite products.

Name	Formula	Unit	Perfect score
Kling-Gupta Efficiency (KGE)	$KGE = 1 - \sqrt{(r-1)^2 + \left(\frac{\sigma_s}{\sigma_o} - 1\right)^2 + (\mu_s - \mu_o)^2}$	-	1
Correlation Coefficient (CC)	$CC = \frac{\sum_{i=1}^{n}(S_i - \bar{S})(O_i - \bar{O})}{\sqrt{\sum_{i=1}^{n}(S_i - \bar{S})^2}\sqrt{\sum_{i=1}^{n}(O_i - \bar{O})^2}}$	-	1
Relative Bias (Rbias)	$Rbias = \left(\frac{\sum_{i=1}^{n}(S_i - O_i)}{\sum_{i=1}^{n} O_i}\right) \times 100\%$	%	0
Root-Mean Square Error (RMSE)	$RMSE = \sqrt{\frac{1}{n}\sum_{i=1}^{n}(S_i - O_i)^2}$	mm	0

S_i - value of satellite precipitation estimates for the i^{th} event, O_i - value of rain-gauge observation for the i^{th} event, $\bar{S}$ and $\bar{O}$ - corresponding mean values, n - number of observed records, $\beta = \bar{S}/\bar{O}$, $\gamma = (\bar{S}/\sigma_{S_i})/(\bar{O}/\sigma_{O_i})$, σ_{S_i} and σ_{O_i} - corresponding standard deviations.

Additionally, two categorical indices based on contingency tables were used. The first approach involved a 2 $\times$ 2 contingency table with four possible scenarios for a given threshold (see Table 4). Two categorical scores were computed (see Table 5), including a combined index, the Hansen and Kuipers (HK) categorical score (Jolliffe & Stephenson, 2012; Trapero et al., 2013). The HK statistic measures the forecasting system's ability to distinguish observed "yes" and "no" cases. Critical Success Index (CSI) was also calculated, that quantifies the proportion of correct predictions relative to the total number of event and non-event predictions, focusing on the model's ability to detect events (Ebert, 2008).

Table 4: Contingency table for comparing rainfall observed by RG and estimated by IMERG for a given threshold.

Estimated rainfall	**Observed rainfall**	
	Gauge rainfall ≥ threshold	**Gauge rainfall < threshold**
IMERG rainfall ≥ threshold	Hits (H)	False alarms (F)
IMERG rainfall < threshold	Misses (M)	Correct Negatives (CN)

Table 5: List of categorical verification metrics used to evaluate satellite products.

Name of metric	**Formula**	**Perfect score**
Probability of Detection (POD)	$POD = \frac{H}{H+M}$	1
False Alarm Ratio (POFD)	$POFD = \frac{F}{F+CN}$	0
Hanssen and Kuipers Discriminant (HK)	$HK = POD - POFD$	1
Critical Success Index (CSI)	$CSI = \frac{H}{H+M+F}$	1

For statistical analysis, only precipitation records determined by the following thresholds were considered: 0.5 mm in 1 hour and 1 mm in 24 hours. Additionally, in a second part of the study, results were stratified according to predefined intensity thresholds for rain gauge data. At hourly scale (mm/h) the thresholds selected were RR $\geq$ 2, RR $\geq$ 10, RR $\geq$ 15, and RR $\geq$ 30. Similarly, at the daily scale (mm/24h): RR $\geq$ 10, RR $\geq$ 30, RR $\geq$ 50, and RR $\geq$ 100.

3 Results and Discussion

3.1 Performance of satellite products at hourly and daily scales

This section presents the evaluation of precipitation retrievals from all satellite products using rain gauge data as a reference, with detection thresholds of 0.5 mm for hourly scales and 1 mm for daily scales. Figure 2) shows the probability distributions of precipitation occurrence from rain gauge observations and estimates from each satellite product at both hourly and daily resolutions. The number of data points considered in each analysis is indicated in the title of each panel. As illustrated, both H68 at the hourly scale and H64 at the daily scale represent a much smaller sample compared to the other products. This is because both products rely solely on microwave sensors, making them subject to the availability of retrievals based on orbital geometry.

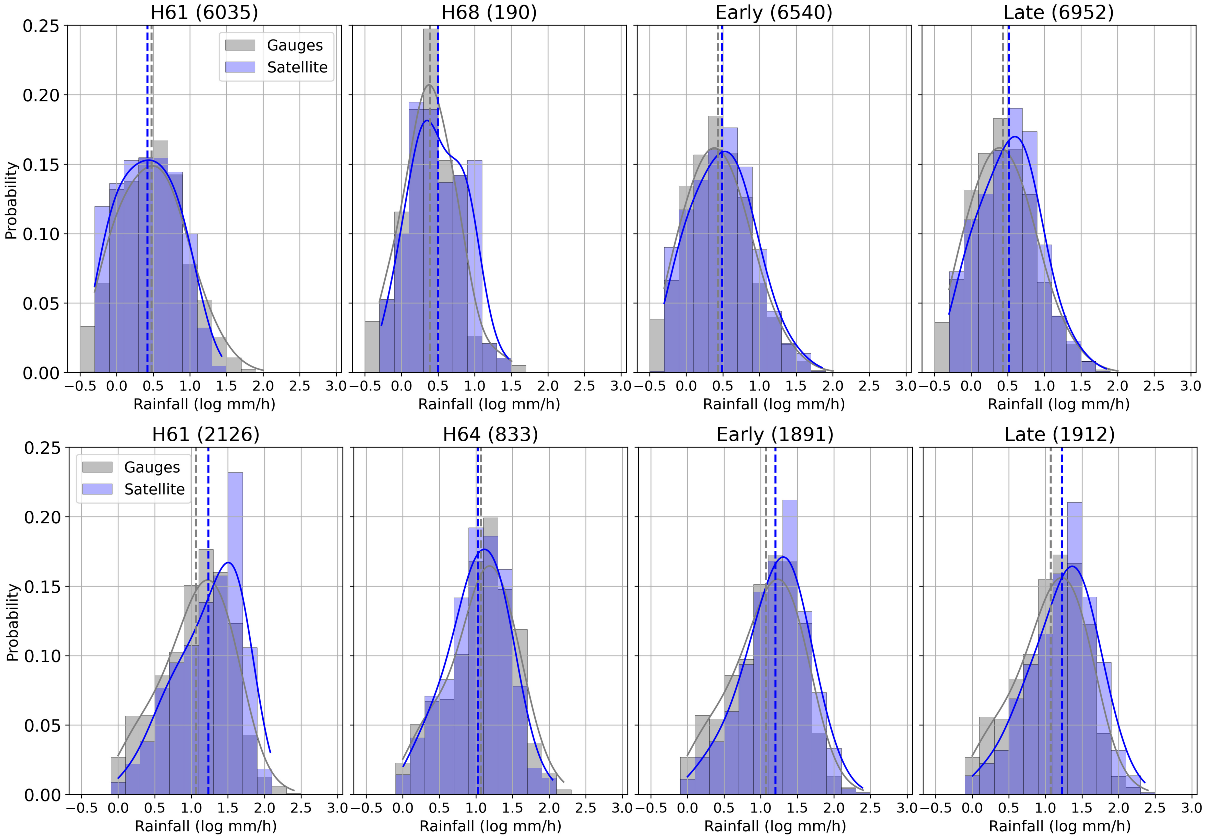

Figure 2: Probability distribution of precipitation for each product and the corresponding rain gauge records at the hourly scale (top panel) and at the daily scale (bottom panel). Dashed lines represent the median of the distributions.

While the distributions are generally similar in shape across all cases, there is a tendency to overestimate precipitation accumulations, except for H61 at the hourly scale and H64 at the daily scale. 6) summarizes the continuous metrics (KGE, RBIAS, and RMSE) between rain gauge data and satellite products at hourly and daily scales. Considering the thresholds for detecting a precipitation event (0.5 mm at the hourly scale and 1 mm at the daily scale), the CSI and HK indices obtained for each product are also included.

Table 6: Continuous and categorical errors obtained at hourly and daily resolutions. Best and worst values for each score are indicated in green and red, respectively.

Hourly					
Product	**KGE**	**Rbias**	**RMSE**	**HK**	**CSI**
H61	0.26	-23.47	6.67	0.48	0.37
H68	0.22	25.77	4.96	0.79	0.52
Early	0.18	12.36	8.01	0.57	0.41
Late	0.22	11.68	7.50	0.60	0.41
Daily					
Product	**KGE**	**Rbias**	**RMSE**	**HK**	**CSI**
H61	0.21	33.91	24.77	0.27	0.72
H64	0.38	-15.81	19.54	0.27	0.72
Early	0.32	26.09	26.31	0.30	0.72
Late	0.33	38.60	26.74	0.36	0.75

The variability in KGE, Rbias, and RMSE values among the products suggests that the accuracy and efficiency of satellite products can vary significantly depending on the temporal scale and each product. KGE values were relatively low for all products regardless of the temporal aggregation, indicating that there exit challenges in replicating the temporal variability and magnitude of precipitation measured by rain gauges. The highest value was observed for H64 at the daily scale, although it does not exceed 0.4. Despite not being very satisfactory, IMERG showed improved efficiency in retrievals with increased temporal aggregation. Several studies have noted this behavior (Chen et al., 2018; Peinó et al., 2022; Xu et al., 2019), as longer temporal aggregations smooth out short-term precipitation variations, leading to better alignment with rain gauge observations.

H61 exhibits a significant negative bias (-23.47%) at the hourly scale, nearly equivalent in magnitude but opposite in sign to H68 (25.77%). IMERG products at this scale showed similar values and the best performance, though they also tended to overestimate. RMSE values were quite similar across products, and although H68 demonstrated the best performance, this metric emphasizes larger errors, so the limited number of high-intensity records may have positively influenced the result.

At the daily scale, relative bias indicated substantial overestimation, especially for H61 and IMERG Late, which exceeded 30%, while H64 showed underestimation to a lesser extent and exhibited the best performance. The products reflected substantial systematic errors in daily precipitation estimation algorithms (between 19 and 26 mm/day). These discrepancies are likely influenced by precipitation intensity and limitations in spatial and temporal resolution used in comparisons between satellite products and rain gauges.

Overall, notable differences were observed between hourly and daily scales concerning the products' ability to detect precipitation events. CSI values increased at the daily scale compared to the hourly scale, while the products' ability to discriminate between events and non-events decreased. At the hourly scale, H68 demonstrated superior capability to distinguish between events and non-events (HK = 0.79) with moderately high accuracy in predicting correct events (CSI = 0.52). H61 showed slightly lower performance in these aspects. Conversely, at the daily scale, IMERG Late stood out with the best discrimination capability (HK = 0.36), though it did not exceed 0.5, while all products maintained high accuracy in event prediction (CSI = 0.72). This indicates that while temporal aggregation improves event detection accuracy, the ability to discriminate these events decreases due to a high false alarm rate affecting the index.

3.2 Spatial Distribution of Errors

Figure 3 presents the validation results at the hourly scale for each pixel according to the spatial resolution of each satellite product in terms of KGE. To better interpret the results, a scale was added where reddish colors represent poor product performance in these pixels, and green colors indicate better skill (ATBD, 2022). H68 shows poor performance with a high KGE index in several regions (more than 70% of pixels rated unsatisfactory), particularly in the Pyrenees area. H61 displays high spatial variability, with areas of unsatisfactory performance (68% of unsatisfactory pixels), particularly in coastal regions, and generally better performance in inland areas. IMERG products exhibit globally poor values, with only a few acceptable and very good pixels (4% and 12% of good pixels for Early and Late, respectively), indicating a limited ability to provide accurate and consistent estimates at this scale based on this index.

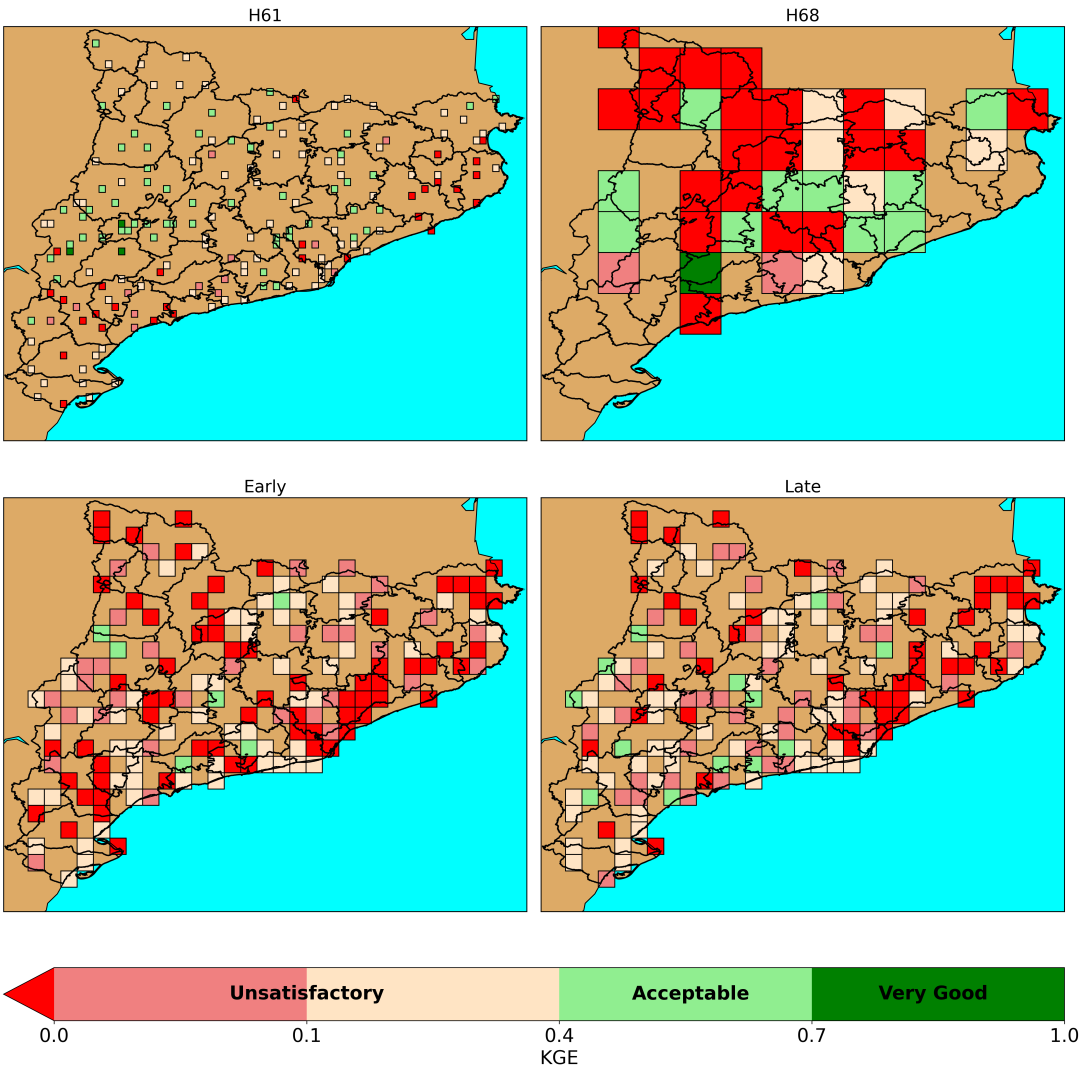

Figure 3: Distribution of KGE values at hourly scale in each pixel of all satellite products.

Figure 4 illustrates the behavior of KGE at the daily scale. Although it is challenging to establish clear spatial patterns of better performance among these products, it is noteworthy that all of them show the best results in the southwest of the region. The H64 product stands out as the most suitable, with 32% of pixels showing KGE values considered acceptable. The main limitations of this product are evident in the Pyrenees and the northeastern part of the region. H61 exhibits substantially lower KGE values across almost the entire domain, except near the Ebro Valley, where IMERG products also show the best results. Coastal areas north of this basin are notably affected by the largest errors. It is important to mention that many case studies (**see Appendix A**) coincidentally recorded the highest precipitation accumulations in this region, suggesting that this behavior is directly related to the intensity of precipitation events.

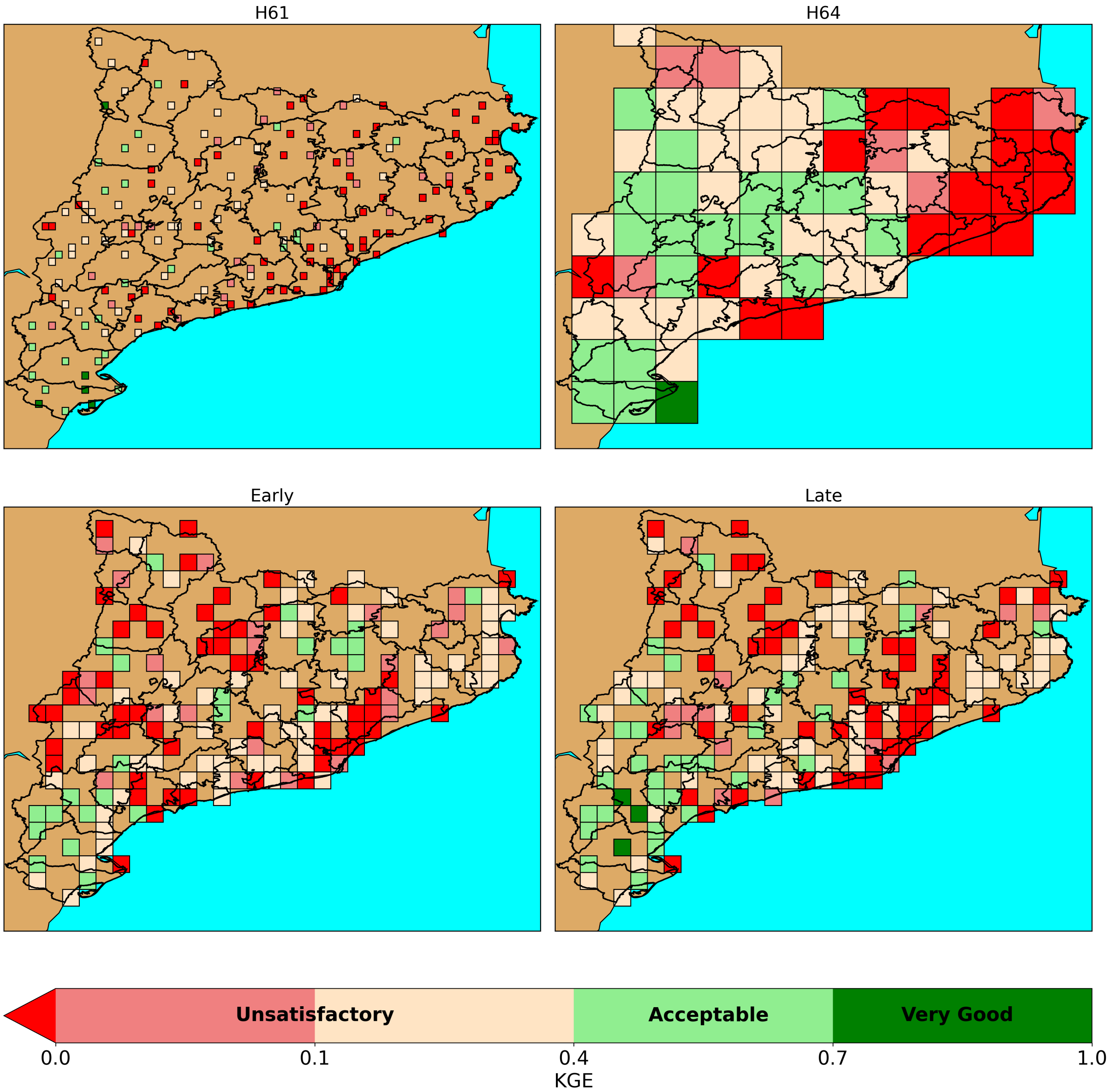

Figure 4: Same as Figure 3 but at daily scale.

The comparison between hourly and daily results shows that products with lower spatial resolution, such as H64, demonstrate the highest accuracy in terms of KGE. This may be primarily due to the limitations of the point-to-pixel method, which can struggle with high-resolution data due to the mismatch between the spatial resolution of satellite products and the spatial scale of ground-based measurements. IMERG products consistently perform poorly at both scales, indicating substantial limitations in their retrievals; however, the Late version generally outperforms the Early version, especially at the daily scale. Conversely, H61 shows better performance at the hourly scale, which could be attributed to its algorithm for constructing daily accumulations. Additionally, the high spatial resolution of H61 may make it more susceptible to the high variability of precipitation, making it more challenging for spaceborne sensors to accurately capture these variations.

3.3 Evaluation according to rainfall intensity

Figure 5 illustrates the distribution of hourly (top panel) and daily (bottom panel) precipitation accumulations for each satellite product and the corresponding rain gauge records used for validation. The four sections in the figure are identified according to different precipitation intensity thresholds in the reference rain gauges: RR (rain rate) = 2, 10, 15, and 30 mm/h (hourly scale) and RR = 10, 30, 50, and 100 mm/day (daily scale).

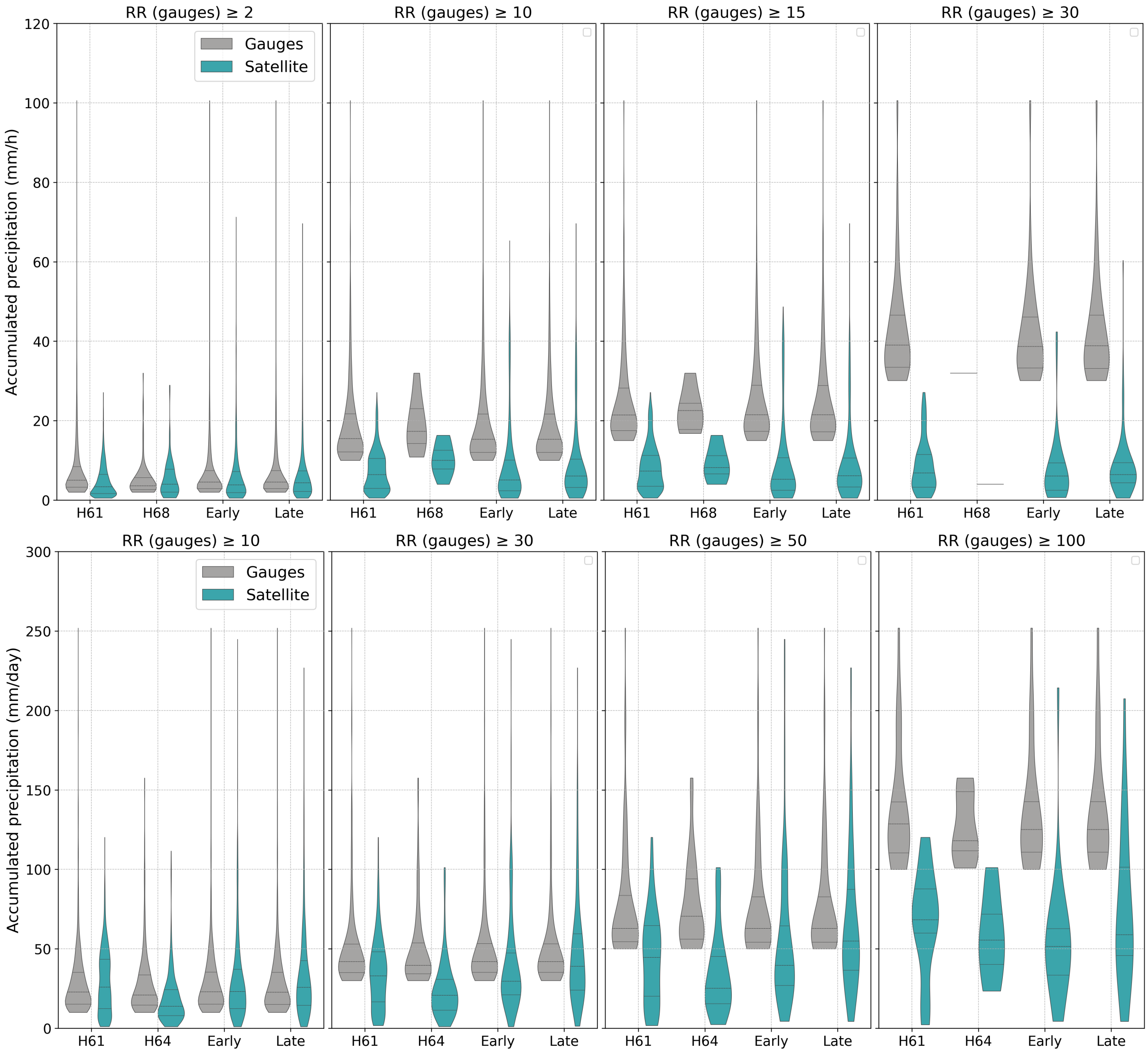

Figure 5: Violin plots at hourly (top panel) and daily (bottom panel) scale rain gauge observations (gray) and satellite products (green) for the four-rainfall intensity (mm/h) thresholds considered.

According to the results found here, satellite products tend to systematically underestimate precipitation accumulations, both hourly and daily, compared to rain gauge data, with this discrepancy becoming more pronounced as precipitation intensity increases. Notably, for the highest intensities (RR > 30 mm/h and RR > 100 mm/day), both H61 and H64 show minimal detection in these ranges and H68 lacked sufficient data at these intensities to establish a distribution. IMERG products exhibit similar performance among themselves and are the only ones capable of recording comparable precipitation accumulations at high-intensity ranges defined by rain gauges, although this does not imply perfect spatial and temporal alignment. The greater variability in rain gauge measurements at all intensity thresholds indicates that satellite products do not adequately capture this variability.

(Table 7) summarizes the key continuous statistics calculated for each satellite product at both hourly and daily temporal resolutions for the four predefined intensity thresholds. Generally, all products show a decrease in KGE, and an increase in negative bias and RMSE as the precipitation threshold increases, though values are slightly better at the daily scale. At the hourly scale, H68 tends to exhibit the lowest bias at lower thresholds, while both IMERG Late and H61 show better performance at low and moderate thresholds, regardless of temporal aggregation.

Table 7: Continuous and categorical scores for different intensity thresholds.Best and worst values for each score are indicated in green and red, respectively.

Hourly				**Daily**			
Product	**KGE**	**Rbias**	**RMSE**	**Product**	**KGE**	**Rbias**	**RMSE**
$\geq$ 2 **mm/h**				$\geq$ 10 **mm/day**			
H61	0.23	-38.17	8.01	H61	0.32	1.41	24.82
H68	0.22	2.41	5.67	H64	0.30	-33.17	22.23
Early	0.13	-11.19	9.36	Early	0.29	2.34	29.28
Late	0.18	-10.11	8.81	Late	0.37	15.24	29.11
$\geq$ 10 **mm/h**				$\geq$ 30 **mm/day**			
H61	-0.07	-61.90	16.22	H61	0.31	-31.70	31.14
H68	-0.75	-45.99	13.01	H64	0.09	-50.64	33.43
Early	-0.58	-54.55	17.74	Early	0.03	-19.53	39.74
Late	-0.40	-51.93	17.38	Late	0.22	-6.29	36.98
$\geq$ 15 **mm/h**				$\geq$ 50 **mm/day**			
H61	-0.25	-67.16	21.08	H61	0.19	-43.40	47.46
H68	-1.01	-59.19	16.11	H64	-0.39	-55.65	51.66
Early	-0.90	-64.70	22.19	Early	-0.27	-29.33	59.96
Late	-0.74	-63.73	22.12	Late	0.03	-16.28	52.73
$\geq$ 30 **mm/h**				$\geq$ 100 **mm/day**			
H61	-0.89	-79.93	37.22	H61	-0.14	-51.72	81.33
H68		-87.54	27.99	H64	-0.91	-54.56	73.54
Early	-1.88	-81.83	36.76	Early	-1.01	-59.99	96.88
Late	-1.41	-80.23	37.17	Late	-0.72	-45.96	84.20

According to the categorical statistics shown in Figure 6, all satellite products significantly decrease their ability to detect correct precipitation events at thresholds above 2 mm/h and 10 mm/day. Although there are no dramatically marked differences, indicators improve with increased temporal aggregation, which is particularly notable in the IMERG products. Similar behavior has been reported in other studies (Peinó et al., 2022), which have also shown significant improvements when dealing with precipitation values over longer time scales, such as monthly, quarterly, and annual periods.

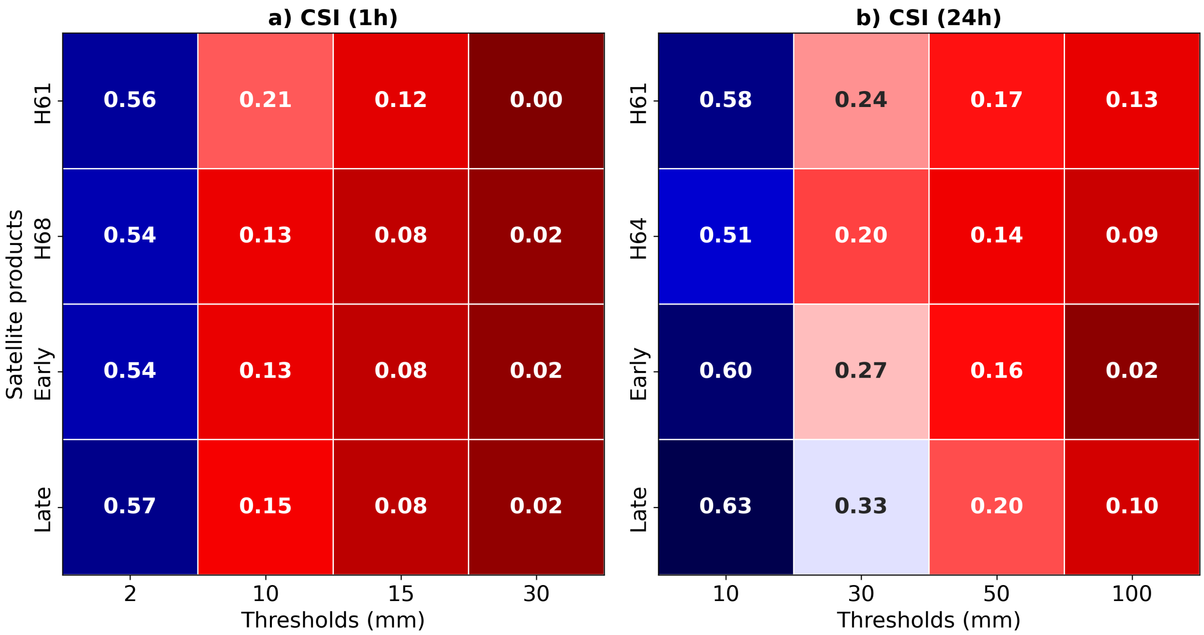

Figure 6: Critics Success Index score for each satellite product on an hourly scale (left column) and on a daily scale (right column) considering different intensity thresholds. Darker bluish colors (darker reddish) indicate good (bad) performance of the satellite estimates.

4 Conclusions

The performance of three H SAF products (H61, H64, H68) and the IMERG Early and Late versions were validated using hourly and daily precipitation records from 186 rain gauges distributed over a Mediterranean coastal region. A point-to-pixel method was used to establish spatial matches between the two datasets, and several metrics were analyzed to quantify the discrepancies in precipitation accumulations. The validation and intercomparison of these products' performance also considered four precipitation intensity thresholds at both hourly and daily scales. The main findings can be summarized as follows:

- In general satellite estimates tend to overestimate observed values. This overestimation is most noticeable in H68 products at hourly resolution and H61 at the daily scale.
- From a quantitative perspective, the results of KGE, RBIAS, and RMSE showed that all products have limited capacity for estimating hourly precipitation, and while the indices improve at the daily scale, there are no substantial improvements. Particularly, H64 stands out for exhibiting the lowest errors at the daily scale, while H61, unlike the other products, showed a substantially negative bias (-23.37%) at the hourly scale.
- Intense precipitation is rarely captured by the satellite products; indeed, all satellite products significantly reduce their ability to detect correct precipitation at thresholds above 2 mm/h and 10 mm/day. H68 presents the worst errors and the lowest ability to detect high-intensity precipitation, while IMERG Late, despite maintaining significant biases, was the best product for detecting such events.

The results of this study not only validate a range of satellite precipitation estimation products but also facilitate comparisons among them, providing valuable information to users for various applications.

The overall agreement between the rain gauge and satellite estimates was weak, indicating that although the products can capture extreme precipitation values, they do not always align with ground observations. This limitation reduces their utility in hydrometeorological applications such as disaster management and highlights the need for continued detailed validation efforts to enhance the accuracy and effectiveness of precipitation retrieval algorithms.

References

ATBD. (2020). Algorithm Theoretical Baseline Document (ATBD) for product H61 P-AC-SEVIRI-PMW and H90 P-AC-SEVIRI_e. https://hsaf.meteoam.it/CaseStudy/GetDocumentUserDocument?fileName=saf_hsaf_atbd-61b-90b_1_0.pdf&tipo=ATBD

ATBD. (2021). Algorithm Theoretical Baseline Document (ATBD) for product H68 (P-IN-PMW). https://hsaf.meteoam.it/CaseStudy/GetDocumentUserDocument?fileName=SAF_HSAF_ATBD-H68_v3.0.pdf&tipo=ATBD

ATBD. (2022). Algorithm Theoretical Baseline Document (ATBD) for product H64 P-AC-SM2RAIN. https://hsaf.meteoam.it/CaseStudy/GetDocumentUserDocument?fileName=SAF_HSAF_ATBD-H64_2_1.pdf&tipo=ATBD

Baez-Villanueva, O. M., Zambrano-Bigiarini, M., Ribbe, L., Nauditt, A., Giraldo-Osorio, J. D., & Thinh, N. X. (2018). Temporal and spatial evaluation of satellite rainfall estimates over different regions in Latin-America. *Atmospheric Research*, *213*, 34–50. https://doi.org/10.1016/j.atmosres.2018.05.011

Brocca, L., Ciabatta, L., Massari, C., Moramarco, T., Hahn, S., Hasenauer, S., Kidd, R., Dorigo, W., Wagner, W., & Levizzani, V. (2014). Soil as a natural rain gauge: Estimating global rainfall from satellite soil moisture data [ISBN: 2169-897X Publisher: Wiley Online Library]. *Journal of Geophysical Research: Atmospheres*, *119*(9), 5128–5141.

Chen, C., Chen, Q., Duan, Z., Zhang, J., Mo, K., Li, Z., & Tang, G. (2018). Multiscale Comparative Evaluation of the GPM IMERG v5 and TRMM 3B42 v7 Precipitation Products from 2015 to 2017 over a Climate Transition Area of China [Number: 6 Publisher: Multidisciplinary Digital Publishing Institute]. *Remote Sensing*, *10*(6), 944. https://doi.org/10.3390/rs10060944

Ciabatta, L., Massari, C., Brocca, L., Gruber, A., Reimer, C., Hahn, S., Paulik, C., Dorigo, W., Kidd, R., & Wagner, W. (2018). SM2RAIN-CCI: A new global long-term rainfall data set derived from ESA CCI soil moisture [ISBN: 1866-3508 Publisher: Copernicus GmbH]. *Earth System Science Data*, *10*(1), 267–280.

Ebert, E. E. (2008). Fuzzy verification of high-resolution gridded forecasts: A review and proposed framework [_eprint: https://onlinelibrary.wiley.com/doi/pdf/10.1002/met.25]. *Meteorological Applications*, *15*(1), 51–64. https://doi.org/10.1002/met.25

Force, I. A. (2024). Precipitation Products list. Retrieved August 1, 2024, from https://hsaf.meteoam.it/Products/ProductsList?type=precipitation

Furl, C., Ghebreyesus, D., & Sharif, H. O. (2018). Assessment of the Performance of Satellite-Based Precipitation Products for Flood Events across Diverse Spatial Scales Using GSSHA Modeling System [Number: 6 Publisher: Multidisciplinary Digital Publishing Institute]. *Geosciences*, *8*(6), 191. https://doi.org/10.3390/geosciences8060191

Gentilucci, M., Barbieri, M., & Pambianchi, G. (2022). Reliability of the IMERG product through reference rain gauges in Central Italy. *Atmospheric Research*, *278*, 106340. https://doi.org/10.1016/j.atmosres.2022.106340

Gupta, H. V., Kling, H., Yilmaz, K. K., & Martinez, G. F. (2009). Decomposition of the mean squared error and NSE performance criteria: Implications for improving hydrological modelling. *Journal of Hydrology*, *377*(1), 80–91. https://doi.org/10.1016/j.jhydrol.2009.08.003

Huffman, G. J., Bolvin, D. T., Braithwaite, D., Hsu, K., Joyce, R., Xie, P., & Yoo, S.-H. (2015). NASA global precipitation measurement (GPM) integrated multi-satellite retrievals for GPM (IMERG). https://gpm.nasa.gov/sites/default/files/2020-05/IMERG_ATBD_V06.3.pdf

Huffman, G. J., Bolvin, D. T., Braithwaite, D., Hsu, K.-L., Joyce, R. J., Kidd, C., Nelkin, E. J., Sorooshian, S., Stocker, E. F., Tan, J., Wolff, D. B., & Xie, P. (2020). Integrated Multi-satellite Retrievals for the Global Precipitation Measurement (GPM) Mission (IMERG). In V. Levizzani, C. Kidd, D. B. Kirschbaum, C. D. Kummerow, K. Nakamura, & F. J. Turk (Eds.), *Satellite Precipitation Measurement: Volume 1* (pp. 343–353). Springer International Publishing. https://doi.org/10.1007/978-3-030-24568-9_19

Jansa, A., Alpert, P., Arbogast, P., Buzzi, A., Ivancan-Picek, B., Kotroni, V., Llasat, M. C., Ramis, C., Richard, E., & Romero, R. (2014). MEDEX: A general overview [ISBN: 1561-8633 Publisher: Copernicus GmbH]. *Natural Hazards and Earth System Sciences*, *14*(8), 1965–1984.

Jolliffe, I. T., & Stephenson, D. B. (2012, January). *Forecast Verification: A Practitioner's Guide in Atmospheric Science* [Google-Books-ID: DCxsKQeaBH8C]. John Wiley & Sons.

Kidd, C., Huffman, G., Maggioni, V., Chambon, P., & Oki, R. (2021). The Global Satellite Precipitation Constellation: Current Status and Future Requirements [Publisher: American Meteorological Society Section: Bulletin of the American Meteorological Society]. *Bulletin of the American Meteorological Society*, *102*(10), E1844–E1861. https://doi.org/10.1175/BAMS-D-20-0299.1

Kidd, C., & Levizzani, V. (2019). Quantitative precipitation estimation from satellite observations. In *Extreme Hydroclimatic Events and Multivariate Hazards in a Changing Environment* (pp. 3–39). Elsevier. https://doi.org/10.1016/B978-0-12-814899-0.00001-8

Kirschbaum, D. B., Huffman, G. J., Adler, R. F., Braun, S., Garrett, K., Jones, E., McNally, A., Skofronick-Jackson, G., Stocker, E., Wu, H., & Zaitchik, B. F. (2017). NASA's Remotely Sensed Precipitation: A Reservoir for Applications Users [Publisher: American Meteorological Society Section: Bulletin of the American Meteorological Society]. *Bulletin of the American Meteorological Society*, *98*(6), 1169–1184. https://doi.org/10.1175/BAMS-D-15-00296.1

Kling, H., Fuchs, M., & Paulin, M. (2012). Runoff conditions in the upper Danube basin under an ensemble of climate change scenarios. *Journal of Hydrology*, *424-425*, 264–277. https://doi.org/10.1016/j.jhydrol.2012.01.011

Koster, R. D., Brocca, L., Crow, W. T., Burgin, M. S., & De Lannoy, G. J. (2016). Precipitation estimation using L-band and C-band soil moisture retrievals [ISBN: 0043-1397 Publisher: Wiley Online Library]. *Water Resources Research*, *52*(9), 7213–7225.

Lanza, L. G., & Stagi, L. (2008). Certified accuracy of rainfall data as a standard requirement in scientific investigations [ISBN: 1680-7359 Publisher: Copernicus Publications Göttingen, Germany]. *Advances in geosciences*, *16*, 43–48.

Lei, H., Li, H., Zhao, H., Ao, T., & Li, X. (2021). Comprehensive evaluation of satellite and reanalysis precipitation products over the eastern Tibetan plateau characterized by a high diversity of topographies [ISBN: 0169-8095 Publisher: Elsevier]. *Atmospheric Research*, *259*, 105661.

Li, R., Qi, D., Zhang, Y., & Wang, K. (2022). A new pixel-to-object method for evaluating the capability of the GPM IMERG product to quantify precipitation systems. *Journal of Hydrology*, *613*, 128476. https://doi.org/10.1016/j.jhydrol.2022.128476

Li, Y., Wang, W., & Lu, H. (2018). Evaluation of the Latest Satellite-Based Precipitation Products Through Pixel-Point Comparison and Hydrological Application Over the Mekong River Basin [ISSN: 2153-7003]. *IGARSS 2018 - 2018 IEEE International Geoscience and Remote Sensing Symposium*, 3043–3046. https://doi.org/10.1109/IGARSS.2018.8519448

Li, Z., Yang, D., & Hong, Y. (2013). Multi-scale evaluation of high-resolution multi-sensor blended global precipitation products over the Yangtze River. *Journal of Hydrology*, *500*, 157–169. https://doi.org/10.1016/j.jhydrol.2013.07.023

Llabrés-Brustenga, A., Rius, A., Rodríguez-Solà, R., & Casas-Castillo, M. C. (2020). Influence of regional and seasonal rainfall patterns on the ratio between fixed and unrestricted measured intervals of rainfall amounts. *Theoretical and Applied Climatology*, *140*(1), 389–399. https://doi.org/10.1007/s00704-020-03091-w

Llabrés-Brustenga, A., Rius, A., Rodríguez-Solà, R., Casas-Castillo, M. C., & Redaño, A. (2019). Quality control process of the daily rainfall series available in Catalonia from 1855 to the present. *Theoretical and Applied Climatology*, *137*(3), 2715–2729. https://doi.org/10.1007/s00704-019-02772-5

Llasat, M. C., Marcos, R., Turco, M., Gilabert, J., & Llasat-Botija, M. (2016). Trends in flash flood events versus convective precipitation in the Mediterranean region: The case of Catalonia. *Journal of Hydrology*, *541*, 24–37. https://doi.org/10.1016/j.jhydrol.2016.05.040

Llasat, M. C., Marcos, R., Llasat-Botija, M., Gilabert, J., Turco, M., & Quintana-Seguí, P. (2014). Flash flood evolution in north-western Mediterranean [ISBN: 0169-8095 Publisher: Elsevier]. *Atmospheric research*, *149*, 230–243.

Massari, C., Crow, W., & Brocca, L. (2017). An assessment of the performance of global rainfall estimates without ground-based observations [ISBN: 1027-5606 Publisher: Copernicus GmbH]. *Hydrology and earth system sciences*, *21*(9), 4347–4361.

Moazami, S., Na, W., Najafi, M. R., & de Souza, C. (2022). Spatiotemporal bias adjustment of IMERG satellite precipitation data across Canada. *Advances in Water Resources*, *168*, 104300. https://doi.org/10.1016/j.advwatres.2022.104300

Mugnai, A., Casella, D., Cattani, E., Dietrich, S., Laviola, S., Levizzani, V., Panegrossi, G., Petracca, M., Sanò, P., & Di Paola, F. (2013). Precipitation products from the hydrology SAF [ISBN: 1684-9981 Publisher: Copernicus Publications Göttingen, Germany]. *Natural Hazards and Earth System Sciences*, *13*(8), 1959–1981. https://doi.org/https://doi.org/10.5194/nhess-13-1959-2013

Navarro, A., García-Ortega, E., Merino, A., Sánchez, J. L., & Tapiador, F. J. (2020). Orographic biases in IMERG precipitation estimates in the Ebro River basin (Spain): The effects of rain gauge density and altitude [ISBN: 0169-8095 Publisher: Elsevier]. *Atmospheric Research*, *244*, 105068.

Panegrossi, G., Casella, D., Cattani, E., Dietrich, S., Laviola, S., Levizzani, V., Mugnai, A., Sanò, P., Biron, D., & De Leonibus, L. (2012). Precipitation products from the Hydrology SAF. *Proceedings of the 2012 EUMETSAT Meteorological Satellite Conference, Sopot, Poland*, 3–7.

Peinó, E., Bech, J., & Udina, M. (2022). Performance Assessment of GPM IMERG Products at Different Time Resolutions, Climatic Areas and Topographic Conditions in Catalonia [Number: 20 Publisher: Multidisciplinary Digital Publishing Institute]. *Remote Sensing*, *14*(20), 5085. https://doi.org/10.3390/rs14205085

Peinó, E., Bech, J., Udina, M., & Polls, F. (2024). Disentangling Satellite Precipitation Estimate Errors of Heavy Rainfall at the Daily and Sub-Daily Scales in the Western Mediterranean [Number: 3 Publisher: Multidisciplinary Digital Publishing Institute]. *Remote Sensing*, *16*(3), 457. https://doi.org/10.3390/rs16030457

Pradhan, R. K., Markonis, Y., Vargas Godoy, M. R., Villalba-Pradas, A., Andreadis, K. M., Nikolopoulos, E. I., Papalexiou, S. M., Rahim, A., Tapiador, F. J., & Hanel, M. (2022). Review of GPM IMERG performance: A global perspective. *Remote Sensing of Environment*, *268*, 112754. https://doi.org/10.1016/j.rse.2021.112754

Puca, S., Porcu, F., Rinollo, A., Vulpiani, G., Baguis, P., Balabanova, S., Campione, E., Ertürk, A., Gabellani, S., Iwanski, R., Jurašek, M., Kaňák, J., Kerényi, J., Koshinchanov, G., Kozinarova, G., Krahe, P., Lapeta, B., Lábó, E., Milani, L., . . . Gattari, F. (2014). The validation service of the hydrological SAF geostationary and polar satellite precipitation products [Publisher: Copernicus GmbH]. *Natural Hazards and Earth System Sciences*, *14*(4), 871–889. https://doi.org/10.5194/nhess-14-871-2014

Rojas, Y., Minder, J. R., Campbell, L. S., Massmann, A., & Garreaud, R. (2021). Assessment of GPM IMERG satellite precipitation estimation and its dependence on microphysical rain regimes over the mountains of south-central Chile. *Atmospheric Research*, *253*, 105454. https://doi.org/10.1016/j.atmosres.2021.105454

Serrat-Capdevila, A., Valdes, J. B., & Stakhiv, E. Z. (2014). Water Management Applications for Satellite Precipitation Products: Synthesis and Recommendations. *JAWRA Journal of the American Water Resources Association*, *50*(2), 509–525. https://doi.org/10.1111/jawr.12140

Skofronick-Jackson, G., Petersen, W. A., Berg, W., Kidd, C., Stocker, E. F., Kirschbaum, D. B., Kakar, R., Braun, S. A., Huffman, G. J., & Iguchi, T. (2017). The Global Precipitation Measurement (GPM) mission for science and society [ISBN: 0003-0007 Publisher: American Meteorological Society]. *Bulletin of the American Meteorological Society*, *98*(8), 1679–1695.

Tan, J., Huffman, G. J., Bolvin, D. T., & Nelkin, E. J. (2019). IMERG V06: Changes to the Morphing Algorithm. *Journal of Atmospheric and Oceanic Technology*, *36*(12), 2471–2482. https://doi.org/10.1175/JTECH-D-19-0114.1

Trapero, L., Bech, J., Duffourg, F., Esteban, P., & Lorente, J. (2013). Mesoscale numerical analysis of the historical November 1982 heavy precipitation event over Andorra (Eastern Pyrenees) [Publisher: Copernicus GmbH]. *Natural Hazards and Earth System Sciences*, *13*(11), 2969–2990. https://doi.org/10.5194/nhess-13-2969-2013

Trapero, L., Bech, J., Rigo, T., Pineda, N., & Forcadell, D. (2009). Uncertainty of precipitation estimates in convective events by the Meteorological Service of Catalonia radar network. *Atmospheric Research*, *93*(1), 408–418. https://doi.org/10.1016/j.atmosres.2009.01.021

Trenberth, K. E., Fasullo, J. T., & Kiehl, J. (2009). Earth's Global Energy Budget [Publisher: American Meteorological Society Section: Bulletin of the American Meteorological Society]. *Bulletin of the American Meteorological Society*, *90*(3), 311–324. https://doi.org/10.1175/2008BAMS2634.1

Vicente-Serrano, S. M., Beguería, S., & López-Moreno, J. I. (2010). A Multiscalar Drought Index Sensitive to Global Warming: The Standardized Precipitation Evapotranspiration Index. *Journal of Climate*, *23*(7), 1696–1718. https://doi.org/10.1175/2009JCLI2909.1

Wang, S., Liu, J., Wang, J., Qiao, X., & Zhang, J. (2019). Evaluation of GPM IMERG V05B and TRMM 3B42V7 Precipitation Products over High Mountainous Tributaries in Lhasa with Dense Rain Gauges [Number: 18 Publisher: Multidisciplinary Digital Publishing Institute]. *Remote Sensing*, *11*(18), 2080. https://doi.org/10.3390/rs11182080

WMO, G. (1994). Guide to hydrological practices: Data aquisition and processing, analysis, forecasting and other applications [Publisher: (Geneva)(Switzerland) WMO].

Xie, W., Yi, S., Leng, C., Xia, D., Li, M., Zhong, Z., & Ye, J. (2022). The evaluation of IMERG and ERA5-Land daily precipitation over China with considering the influence of gauge data bias [Publisher: Nature Publishing Group]. *Scientific Reports*, *12*(1), 8085. https://doi.org/10.1038/s41598-022-12307-0

Xu, J., Ma, Z., Tang, G., Ji, Q., Min, X., Wan, W., & Shi, Z. (2019). Quantitative evaluations and error source analysis of Fengyun-2-based and GPM-based precipitation products over mainland China in summer, 2018 [ISBN: 2072-4292 Publisher: MDPI]. *Remote Sensing*, *11*(24), 2992.

Yang, M., Liu, G., Chen, T., Chen, Y., & Xia, C. (2020). Evaluation of GPM IMERG precipitation products with the point rain gauge records over Sichuan, China. *Atmospheric Research*, *246*, 105101. https://doi.org/10.1016/j.atmosres.2020.105101

Yu, C., Hu, D., Liu, M., Wang, S., & Di, Y. (2020). Spatio-temporal accuracy evaluation of three high-resolution satellite precipitation products in China area. *Atmospheric Research*, *241*, 104952. https://doi.org/10.1016/j.atmosres.2020.104952

Zhang, D., Yang, M., Ma, M., Tang, G., Wang, T., Zhao, X., Ma, S., Wu, J., & Wang, W. (2022). Can GPM IMERG Capture Extreme Precipitation in North China Plain? [Number: 4 Publisher: Multidisciplinary Digital Publishing Institute]. *Remote Sensing*, *14*(4), 928. https://doi.org/10.3390/rs14040928

Appendix A Performance of daily precipitation accumulations in all selected case studies of each satellite product versus the records of all rain gauges in the domain.

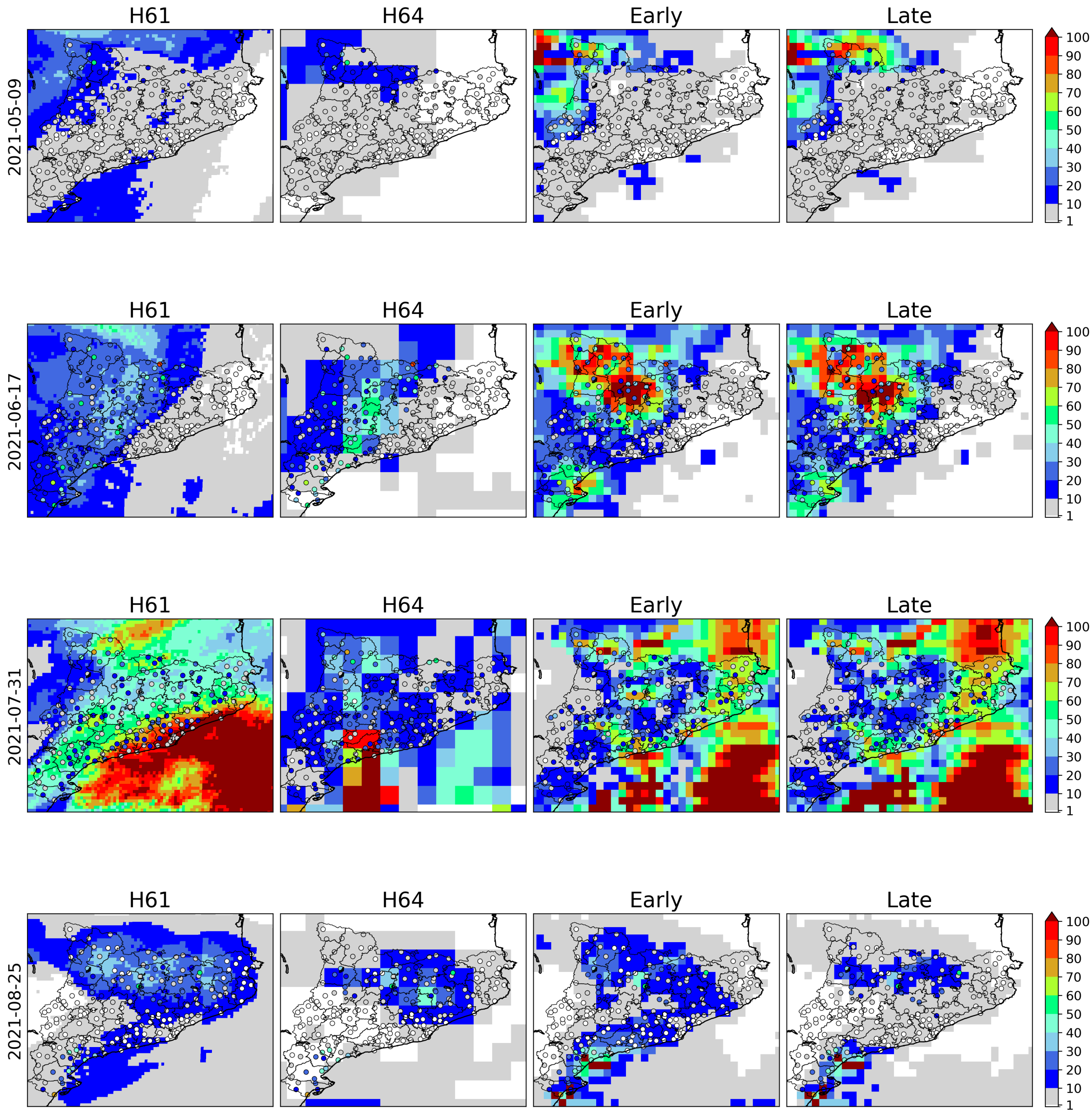

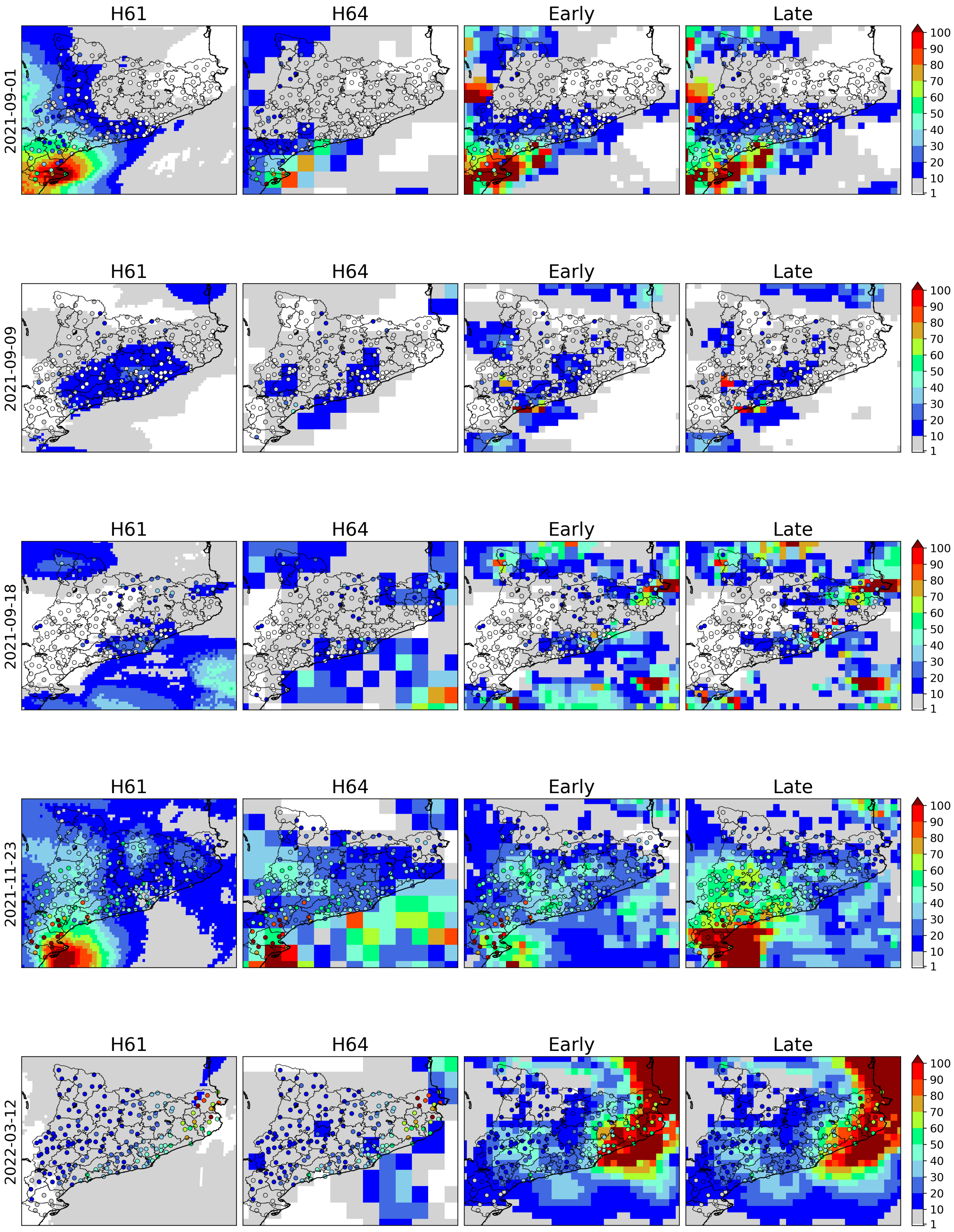
H61
H64
Early
Late
2021-09-01
2021-09-09
2021-09-18
2021-11-23
2022-03-12
100
90
80
70
60
50
40
30
20
10
1

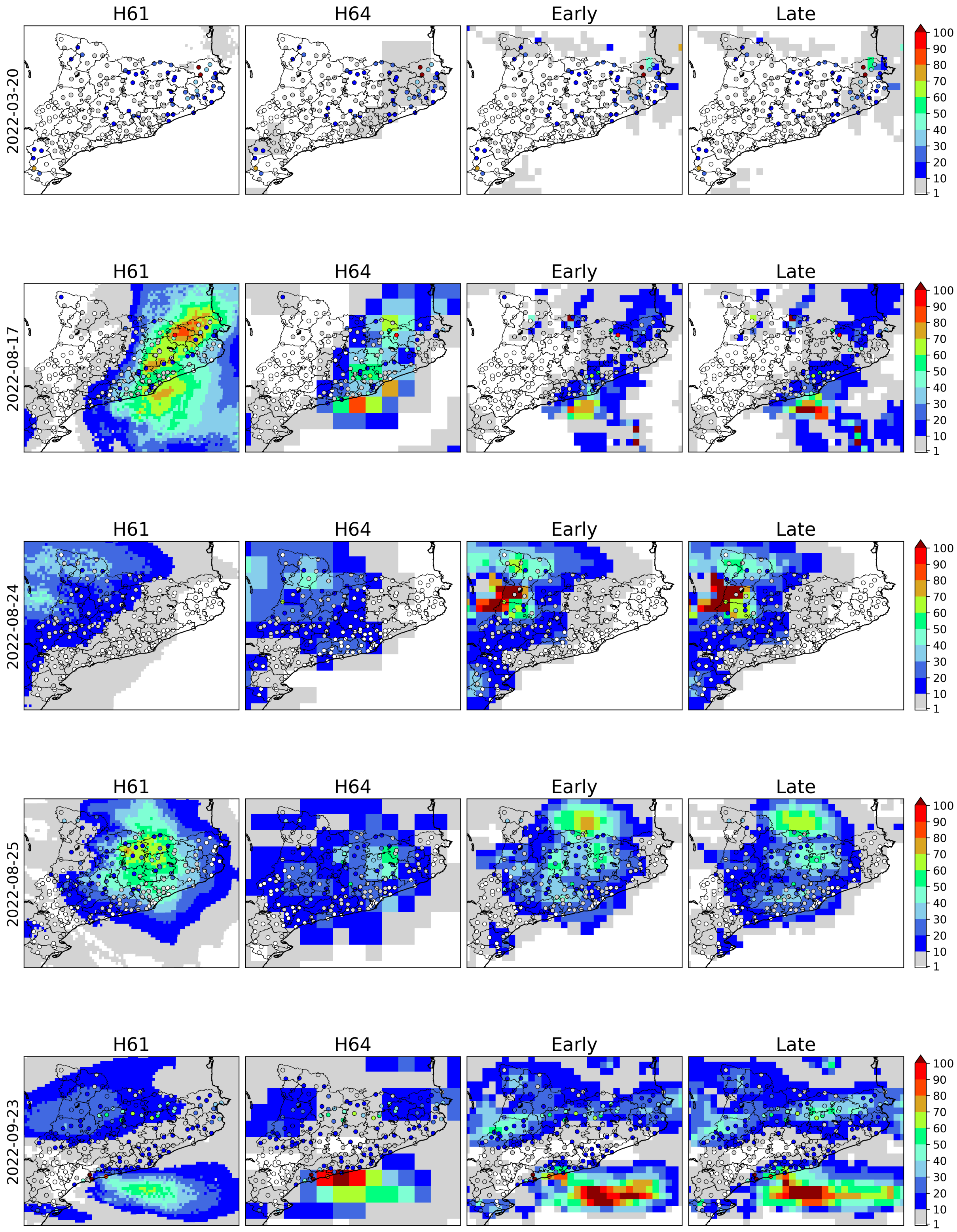
H61
H64
Early
Late
2022-03-20
2022-08-17
2022-08-24
2022-08-25
2022-09-23
100
90
80
70
60
50
40
30
20
10
1

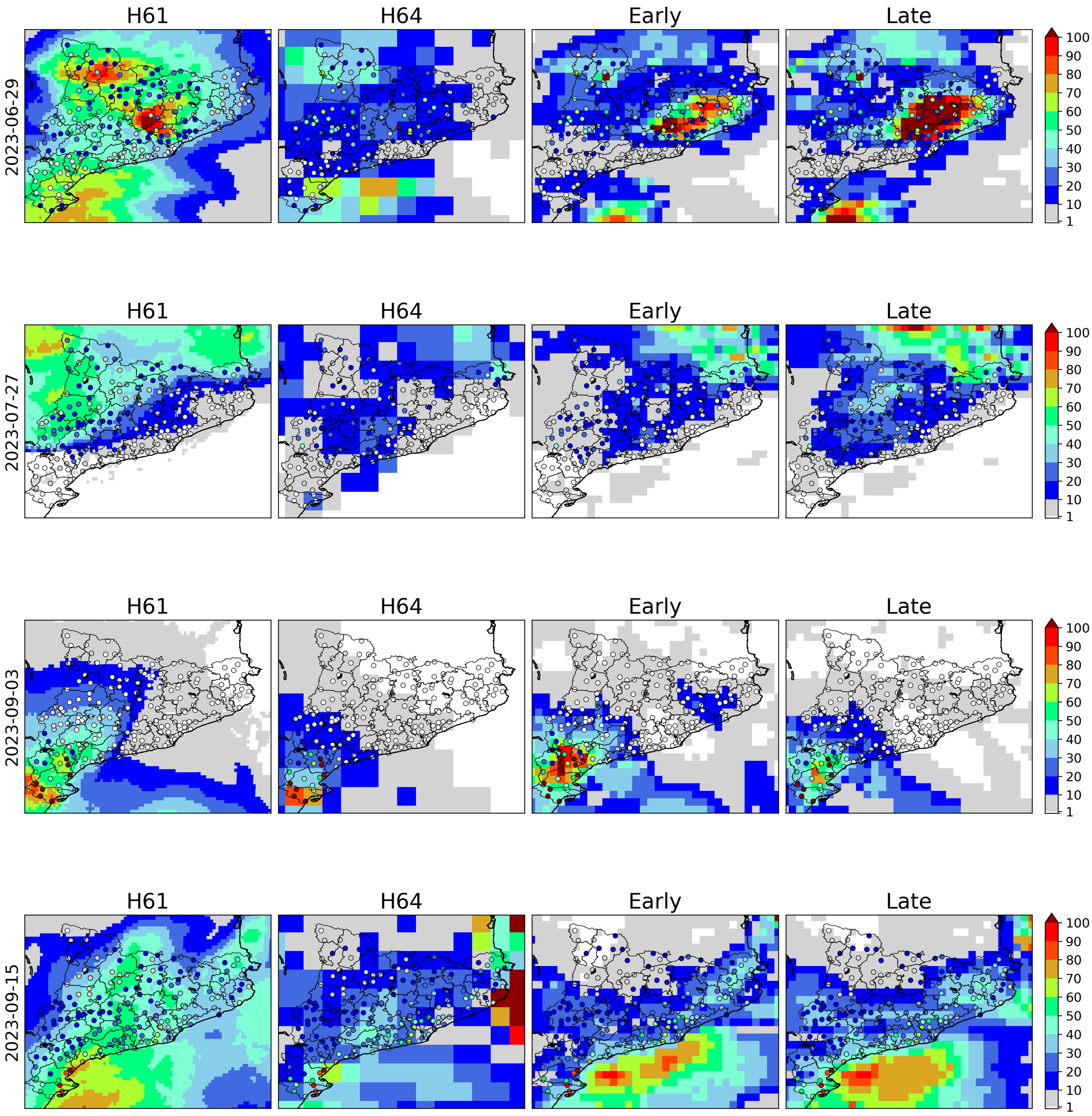
H61
H64
Early
Late
2023-06-29
2023-07-27
2023-09-03
2023-09-15
100
90
80
70
60
50
40
30
20
10
1

CHAPTER

5

Physical validation

5.1 Validation of GPM DPR rainfall and Drop Size Distributions using disdrometer observations in the Western Mediterranean

5.1.1 Summary

In this chapter the focus is on the evaluation and validation of the Global Precipitation Measurement (GPM) Dual-frequency Precipitation Radar (DPR) rainfall estimates and Drop Size Distributions (DSD) using ground-based disdrometer observations in the Western Mediterranean region. Specifically, the Section 4.1, provides a detailed analysis of how well the GPM DPR's version 07B data captures various precipitation microphysical parameters.

This study utilizes data from seven Parsivel disdrometers, strategically located across different topographical zones in the Western Mediterranean, to validate satellite-derived estimates of rainfall intensity, radar reflectivity factors (Z_{Ku} and Z_{Ka}), and key DSD parameters such as the mass-weighted mean diameter (D_m) and the intercept parameter (N_w). The data spans nearly a decade, from 2014 to 2023, allowing for a comprehensive assessment.

Four comparison techniques were employed to evaluate the agreement between satellite overpasses and ground-based observations. Furthermore, the study tested the convective and stratiform classification of precipitation provided by the GPM DPR, uncovering a significant overestimation of stratiform cases compared to the disdrometer observations. The chapter discusses these findings within the context of spatial and temporal sampling discrepancies between the satellite and ground-based instruments, emphasizing the importance of understanding these limitations for improving precipitation retrieval algorithms.

This validation study is particularly significant as it represents one of the first comprehensive validations of the GPM DPR in the Iberian Peninsula and Mediterranean climate regions, especially considering the updates introduced in version 7. The results provide valuable insights into the potential applications and limitations of satellite-based precipitation observations, which are crucial for refining future satellite precipitation retrievals and enhancing our understanding of precipitation processes in this region.

5.1.2 Article

Peinó, E., Bech, J., Polls, F., Udina, M., Petracca, M., Adirosi, E., Gonzalez, S., Boudevillain, B., 2024. Validation of GPM DPR rainfall and Drop Size Distributions using disdrometer observations in the Western Mediterranean. Remote Sensing 16, 2594.

Table 5.1: Summary of the impact and quality of the journal in which the third paper in accordance with this thesis was published. The data correspond to the year 2023 (last year available at the date of preparation of this document) according to Scientific Journal Rankings (SJR). IF: Impact Factor .

Journal Name	**Description**	**Journal Metrics**
Remote Sensing	Remote Sensing is an international, peer-reviewed, open access journal about the science and application of remote sensing technology. It is published semimonthly online by Multidisciplinary Digital Publishing Institute (MDPI).	IF: 4.2 (2023), 5-Year IF: 4.9, CiteScore: 8.3, Quartile: Q1 Earth and Planetary Sciences (miscellaneous)

remote sensing

Article

Validation of GPM DPR Rainfall and Drop Size Distributions Using Disdrometer Observations in the Western Mediterranean

Eric Peinó [1], Joan Bech [1,2,*], Francesc Polls [1], Mireia Udina [1], Marco Petracca [3], Elisa Adirosi [3], Sergi Gonzalez [4] and Brice Boudevillain [5]

1 Department Applied Physics—Meteorology, Universitat de Barcelona, 08028 Barcelona, Spain; epeino@meteo.ub.edu (E.P.); fpolls@meteo.ub.edu (F.P.); mudina@meteo.ub.edu (M.U.)
2 Water Research Institute, Universitat de Barcelona, 08028 Barcelona, Spain
3 National Research Council of Italy, Institute of Atmospheric Sciences and Climate (CNR-ISAC), 00133 Rome, Italy; m.petracca@isac.cnr.it (M.P.); elisa.adirosi@artov.isac.cnr.it (E.A.)
4 WSL Institute for Snow and Avalanche Research SLF, CH–7260 Davos, Switzerland; sergi.gonzalez@slf.ch
5 Institute for Geosciences and Environmental Research, University Grenoble Alpes, CNRS, INRAE, IRD, Grenoble INP, IGE, 38000 Grenoble, France; brice.boudevillain@univ-grenoble-alpes.fr
* Correspondence: joan.bech@ub.edu

Abstract: Dual-frequency precipitation radar (DPR) on the Core GPM satellite provides spaceborne three-dimensional observations of precipitation fields and surface rainfall rate with quasi-global coverage. The present study evaluates the behavior of liquid precipitation intensity, radar reflectivity factor (Z_{Ku} and Z_{Ka}) and drop size distribution (DSD) parameters (weighted mean diameter D_m and intercept parameter N_w) of the GPM DPR-derived products, version 07, from 2014 to 2023. Observations from seven Parsivel disdrometers located in different topographic zones in the Western Mediterranean are taken as ground references. Four matching techniques between satellite estimates and ground level observations were tested, and the best results were found for the so-called optimal comparison approach. Overall, GPM DPR products captured the variability of the observed DSD well at different rainfall intensities. However, overestimation of the mean D_m and underestimation of the mean N_w were observed, being much more sensitive to errors in drop diameters larger than 1.5 mm. Moreover, the lowest errors were found for radar reflectivity factor and D_m, and the highest for N_w and rainfall rate. In addition, the GPM DPR convective and stratiform classification was tested, and a substantial overestimation of stratiform cases compared to disdrometer observations were found.

Keywords: dual-frequency precipitation radar (DPR); GPM; disdrometer; ground validation; precipitation estimates; Western Mediterranean

Citation: Peinó, E.; Bech, J.; Polls, F.; Udina, M.; Petracca, M.; Adirosi, E.; Gonzalez, S.; Boudevillain, B. Validation of GPM DPR Rainfall and Drop Size Distributions Using Disdrometer Observations in the Western Mediterranean. *Remote Sens.* **2024**, *16*, 2594. https://doi.org/10.3390/rs16142594

Academic Editor: Won-Ho Nam

Received: 7 June 2024
Revised: 10 July 2024
Accepted: 11 July 2024
Published: 16 July 2024

1. Introduction

Satellite precipitation estimates are an essential input to provide a complete perspective of the hydrological cycle at the global scale, including the monitoring of extreme events and complementing traditional ground-based observation methods based on rain gauge and weather radar networks [1]. The Tropical Rainfall Measuring Mission (TRMM) of the National Aeronautics and Space Administration (NASA) and Japan Aerospace Exploration Agency (JAXA), launched in 1997, was the first satellite equipped with weather radar, operating at Ku-band (13.6 GHz), dedicated to measuring precipitation at latitudes between 35° S and 35° N [2]. In 2014, the same agencies launched the Core Observatory satellite (CO) on the Global Precipitation Measurement (GPM) mission [3] to provide precipitation estimates between 65° S and 65° N and become the basis for future long-term analyses [4]. To this end, GPM CO became the first spaceborne dual-frequency precipitation radar (DPR), operating at Ka- (35.5 GHz) and Ku-band (13.6 GHz) to offer three-dimensional measurements of the precipitation structure. Compared to TRMM precipitation radar, DPR is more sensitive to light rainfall rates, and because of simultaneous measurements from overlapping Ka/Ku bands, new information on the drop size distribution over moderate precipitation intensities can be obtained [5].

Because of the valuable information provided by the DPR and their multiple applications, validation exercises are essential. In fact, GPM precipitation recovery algorithms have been subject to frequent updates (seven versions in the first 10 years). Therefore, it is necessary to identify biases and improve future versions, with ground validation being an important component for evaluating and improving the performance of the DPR algorithm [6]. Some of the DPR-derived variables are estimated at ground level, so specific information about precipitation drop size distributions (DSDs) at that level is needed for their verification. For this reason, ground-based disdrometers, able to measure DSDs from which integral rainfall parameters, such as reflectivity, intensity and liquid water content can be computed, are a key instrument for the verification of DPR-derived products. A number of field campaigns promoted by the NASA Ground Validation program and other research groups have been carried out in recent years [7] deploying different disdrometer types (two-dimensional video disdrometer (2DVD) from Joanneum Research, Inc. in Graz, Austria; OTT Parsivel Model 2; and Joss–Waldvogel) [8]. Table 1 lists different GPM DPR validation studies using disdrometers and their region of study.

Table 1. Validation studies of GPM DPR products using disdrometers.

DPR Version	Disdrometer Type	Variables Studied *	Region of Study	Reference
-	OTT Parsivel [2]	RR, N_w, D_m, Z, k	Iowa, USA	Liao et al., (2014) [9]
V03	RD-80	RR, N_w, D_m, Z, k	Gadanki, India	Radhakrishna et al., (2016) [10]
V05	2DVD	RR, DSD, Z	Italian Peninsula	D’Adderio et al., (2019) [11]
V06	OTT Parsivel [2]	RR, N_w, D_m, Z, μ	Jianghuai, China	Wu et al., (2019) [12]
V06	2DVD	RR, D_m	Several international sites	Chase et al., (2020) [13]
V06	OTT Parsivel [2]	RR, N_w, D_m, Z, k	Central Andes, Peru	Del Castillo-Velarde et al., (2021) [14]
V06	Thies, OTT Parsivel [2]	RR, N_w, D_m, Z	Italian Peninsula	Adirosi et al., (2021) [15]
V07	Joss–Waldvogel	RR, N_w, D_m, Z	North Taiwan	Seela et al., (2023) [8]

* Variables considered are rain rate (RR), mass weighted mean drop diameter (D_m), intercept parameter (N_w), shape parameter (μ), radar reflectivity (Z), specific attenuation (k).

A first study was performed simulating the DPR algorithm before the GPM CO launch with disdrometer data [9]. In a comparative DPR-disdrometer study over Gadanki, India [10], it was observed that the D_m values obtained from GPM DPR were severely underestimated at high rainfall rates (R > 8 mm/h) during the SW monsoon season. Meanwhile D’Adderio et al. [11] obtained statistical scores that did not differ significantly between land and sea [13,14] and found that the GPM DPR showed superior performance in estimating rainfall parameters in stratiform precipitation than in convective precipitation. Adirosi et al. [15] compared the precipitation and drop size distribution parameters of a large network of disdrometers in Italy with the DPR GPM. The sensitivity analysis revealed, regardless of the type of DPR algorithm (dual- or single-frequency algorithm), a superior agreement for the mass-weighted mean raindrop diameter (D_m) and a lower agreement for the normalized gamma DSD intercept parameter (N_w), similar to the results of [8,11,16]. Del Castillo-Velarde et al. [14] concluded that differences with respect to convective rainfall could be associated with the setting of the shape parameter (μ) in the DPR algorithm. They also suggested that in the central Andes, the estimation of DSD parameters in stratiform rainfall is strongly affected by the limitation of the dual-frequency (DF) algorithm in estimating D_m < 1 mm.

The number of verification studies using disdrometer data has been growing over the years, but it is still much lower than the number of studies with rain gauges, limited to comparing precipitation amounts. As disdrometers are not frequently deployed in operational networks, their observations are relatively scarce, so the difficulties of sampling satellite overpasses matching precipitation events is an important limitation of such studies. For instance, in the Mediterranean basin, an area vulnerable to climate change, hydrometeorological extremes and uncertainty of projections regarding precipitation [17], studies of this type have focused only on the area over Italy using DPR products V05 and V06A. Therefore, the limited number of geographical regions examined and the continuous upgrade of DPR product versions require more validation studies of this type. To contribute to fill this gap, the objective of this study is to evaluate the behavior of the precipitation intensity, radar reflectivity factor (Z_{Ku} and Z_{Ka}) and DSD parameters (D_m, N_w) of the GPM DPR level 2 version 07B, the latest available. For this purpose, data from seven disdrometers (OTT Parsivels [1,2]) covering the period 2015 to 2024 located in different topographic areas of Catalonia, Spain were used as references.

The remainder of this paper is organized as follows. Section 2 provides a description of the study area, datasets used (disdrometers and GPM DPR data), the comparison methodology adopted in this study and the evaluation metrics employed. Section 3 shows results using disdrometer data, DPR data and their matches, the latter validated considering four different approaches. The most significant results are discussed in Section 4, and a summary and conclusion are provided in Section 5.

2. Materials and Methods

2.1. Datasets

2.1.1. GPM-DPR

The GPM CO operates in low Earth orbit, carrying two instruments to measure the Earth's precipitation and serving as a calibration standard for other members of the GPM satellite constellation [18]. The satellite was developed and tested in-house at NASA's Goddard Space Flight Center and launched from the Tanegashima Space Center, Japan, on 27 February 2014 [5]. The orbit height has been 442 km since November 2023, and the orbit inclination is 65°.

GPM-DPR Version 07B Level 2 products provide three main classes of precipitation products: (1) Ku-band frequency, derived over a 245 km-wide swath in so-called full scan (FS, low sensitivity) mode; (2) Ka-band frequency, which, as of May 2018, occupies a 125 km-wide swath in FS mode and the rest of the swath in high scan mode (HS, high sensitivity); and (3) dual-frequency-derived data in FS and HS modes. Finally, the swath structures can be categorized into single- and double-beam pixels based on the availability of radar reflectivity within the Ku and Ka bands [19].

The derivation of the DSD using the single-frequency (SF) and dual-frequency (DF) algorithms in the liquid phase intervals assumes a gamma-shaped droplet size distribution with three parameters: N_w, D_m and the shape parameter (μ). To reduce the number of unknown parameters from three to two, GPM DPR algorithms consider a constant value for μ, set to $\mu = 3$ [6]. To determine D_m and N_w, relationships between D_m and k/Z_e or DFR are used, where k is the specific attenuation in dB/km, Z_e is the effective reflectivity factor, and DFR is the dual-frequency ratio. A brief summary of SF and DF algorithms is shown in Appendix A and further information is available in [19–21].

An important relationship is assumed between the precipitation rate R and D_m [15]. In the current version, V07B, the R-D_m relationship is given by

$$R = \varepsilon^{\tau} \alpha D_m^{\beta} \tag{1}$$

where R is the precipitation rate in mm/h for temperatures between −50 °C and 50 °C and α, β and τ are constants of 0.392, 6.131 and 4.815, respectively. To reconcile possible inconsistencies arising from the use of different attenuation estimation techniques [22], the equation includes an adjustment factor ε. Different R-D_m relations were tested by varying ε from 0.2 to 5.0. Assuming a gamma DSD with a fixed shape parameter, it is possible to establish a relationship between R and D_m for various effective reflectivity values [20]. Thus, given ε = 1.25, a pair (R, D_m) can be obtained.

In this study, DF (DPR) and SF (Ku-band and Ka-band) products were used in the FS mode of the GPM DPR version 07B from 2014 to 2023. Note that the FS format is available in version V07 for observations recorded both before and after the scan pattern change of the Ka-band in May 2018 [21]. The output variables selected to be evaluated were the precipitation intensity (precipRateNearSurface, mm/h) estimated in the clutter-free bin closest to the surface (binClutterFreeBottom, CFB), the reflectivity factor with attenuation correction at the CFB (zFactorFinalNearSurface, dBZ), the normalized gamma DSD parameters (paramDSD) and N_w (dB) and D_m (mm) evaluated at the CFB, as well as the precipitation type (TypePrecip) for the case of the DF product. It is worth mentioning that HS mode data results were not yet available for processing during this study.

2.1.2. Disdrometer Locations

Data from seven disdrometers deployed at different sites in the region of study were used. The Department of Applied Physics–Meteorology of the University of Barcelona manages six disdrometers. Three of them, plus a fourth one from the University of Grenoble–Alpes, were used during the Land Surface Interactions with the Atmosphere over the Iberian Semi-Arid Environment (LIAISE) field campaign in the Eastern Ebro subbasin [23]. The rest of the disdrometers were at Das Aerodrome (in the Eastern Pyrenees, during the Cerdanya-2017 [24] and the ARTEMIS field campaigns), the roof of the Faculty of Physics of the University of Barcelona and the Fabra Observatory of Royal Academy of Sciences and Arts of Barcelona also supporting the ARTEMIS campaign. Table 2 provides detailed information about each site, including temporal period covered and valid rainfall data for each site after quality control (for details, see next section).

Table 2. Information about the Parsivel disdrometers (model 1 and 2 as indicated by the superindex) used in the present study.

Disdrometer Type	Disdrometer Site	Label (Subregions)	Lon (°E)	Lat (°N)	Height (m)	Start Date	End Date	Valid Data (min)
Parsivel ^{1}	Barcelona University	C01 (Coast)	2.11	41.38	98	1 January 2015	1 February 2024	51,679
Parsivel ^{2}	Fabra Observatory	C02 (Coast)	2.12	41.42	411	26 July 2022	13 February 2024	12,537
Parsivel ^{1,2}	Das	M01 (Mountain)	1.87	42.39	1097	9 December 2016	8 February 2024	59,388
Parsivel ^{2}	Tarrega	P01 (Plain)	1.16	41.67	427	4 May 2021	14 June 2022	10,218
Parsivel ^{2}	Mollerussa	P02 (Plain)	0.87	41.62	247	27 April 2021	5 December 2022	12,855
Parsivel ^{2}	Tordera	P03 (Plain)	1.22	41.68	388	30 April 2021	14 June 2022	12,035
Parsivel ^{2}	Cendrosa	P04 (Plain)	0.93	41.69	239	9 April 2021	12 October 2021	3616

The locations of the disdrometers are representative of three key areas with different climatic and orographic characteristics typical of Catalonia: mountain (in the Pyrenees mountains), plain (inland plain of the Segre River Valley) and coast. The disdrometers of Tordera, Mollerussa, Tarrega and Cendrosa are in the plain subregion, characterized by flat terrain with few orographic contrasts and an arid Köppen climate (Figure 1), conditioned by precipitation deficit. Disdrometers located at the Faculty of Physics and Fabra Observatory represent the coast subregion with a hot-summer Mediterranean Köppen climate, more exposed to Mediterranean heavy precipitation. The disdrometer at Das was in a valley at 1094 m a.s.l. in the mountain subregion and had a temperate Köppen climate.

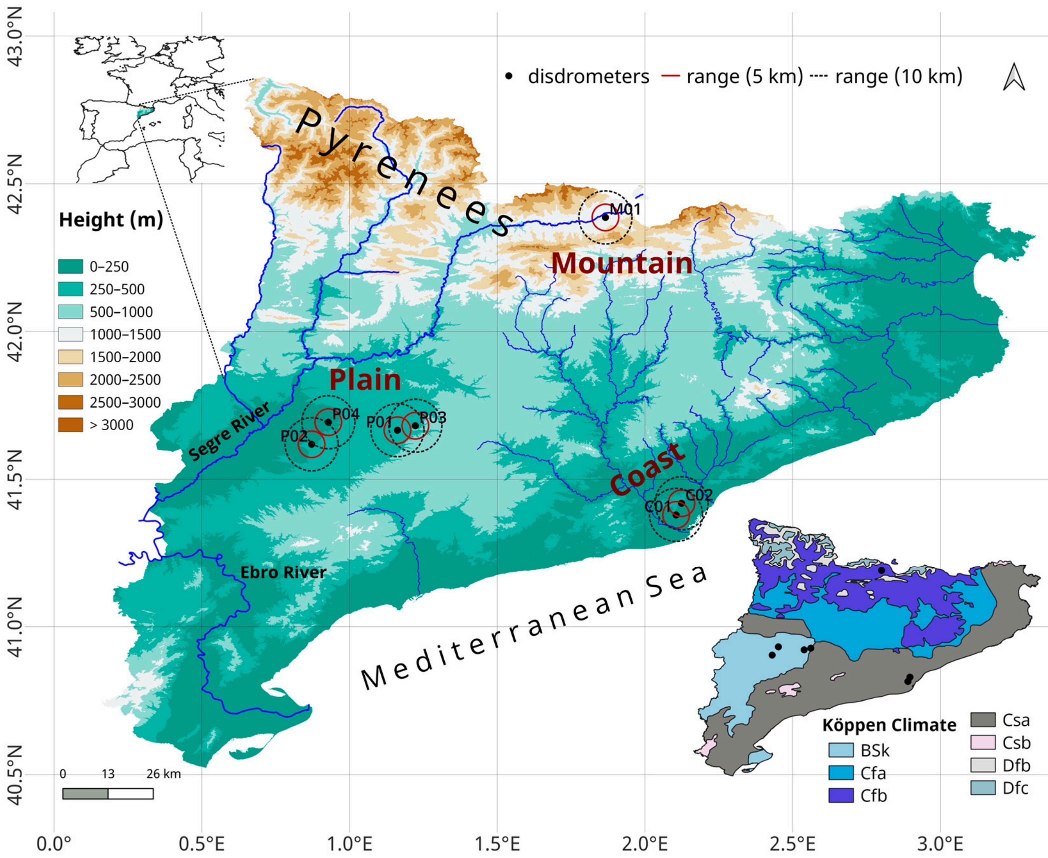

Figure 1. Digital elevation model of the region of study and the three subregions considered (mountain, plain and coast) and disdrometer sites (black dots), showing range circles of 5 km (thin red line) and 10 km (black dotted line) around each site where GPM-DPR data were collected for the present study. The lower right corner shows a map with the Köppen climate classification of the region and the disdrometer locations.

2.1.3. Disdrometer Data

The OTT Parsiveloptical disdrometer uses a 650 nm laser device with a power of 3 mW [25,26]. The laser emits a horizontal sheet of light 30 mm wide and 180 mm long. With a horizontal sampling area of 54 cm^2, particles passing through it cause a reduction in light intensity, resulting in the measurement of their size. The signal duration and particle size allow the estimation of particle velocity [27]. The size and fall speed of each particle is classified into 32 classes ranging from 0.05 to 20 m/s and 32 particle diameter classes ranging from 0.062 mm to 24.5 mm. Based on the recorded size and fall speed spectra, different variables are computed, including the present weather type (synop code 4677 [25]). Temporal resolution was set to 1 min aggregation periods for all disdrometers.

Quality control was applied, consisting of the following conditions: (1) to exclude non-liquid particles and errors associated with boundary effects [28], particle fall speeds did not differ more than ±50% from the empirical terminal fall speed V(D) [29]; (2) to further ensure liquid precipitation, the reported present weather (code 4677) was checked discarding all types containing solid particles [30]; (3) to compute DSD parameters consistently a minimum of 11 drops had to be present in each 1 min sample [15]. The DSD was computed according to the following expression:

$$\mathrm{N}(\mathrm{D_i}) = \frac{1}{\mathrm{A_{eff}}(\mathrm{D_i}) \times \mathrm{t} \times \Delta\mathrm{D_i}} \sum_{j=1}^{32} \frac{\mathrm{n_{ij}}}{\mathrm{V_{D_i}}} \tag{2}$$

where A_{eff} is the effective sampling area (m^2), t is the sampling time (60 s), ΔD_i is the bin width (mm), n_{ij} is the number of drops measured in the ith diameter class and jth drop velocity class, and V_{D_i} is the drop velocity according to the theoretical diameter–drop velocity relationship [29]. In this case, as in [27,28], the edge effects mentioned above are considered: $A_{eff}(D_i) = L(W - 0.5Di)$ where L = 180 mm and W = 30 mm (laser beam length and width, respectively). Finally, for each DSD, $Z_{Ka,Ku}$, R, D_m, N_w and μ were calculated based on the *n*th-order moment (M*n*) of the drop size distribution [8,31–33] using the following:

$$R(mm/h) = 3.6\frac{\Pi}{6}10^{-3}\sum_{i=1}^{32} N(D_i)V(D_i)D^3\Delta D_i \tag{3}$$

$$Z_{K_a,K_u}\left(mm^6m^{-3}\right) = \frac{\lambda^4_{K_u,K_a}}{\Pi^5|K_w|^2}\sum_{i=1}^{32}\sigma_{K_u,K_a}(D_i)N(D_i)\Delta D_i \tag{4}$$

$$M_n\left(mm^n m^{-3} mm^{-1}\right) = \sum_{i=1}^{32} D_i^n N(D_i)\Delta D_i \tag{5}$$

$$D_m(mm) = \frac{M_4}{M_3} \tag{6}$$

$$LWC\left(gm^{-3}\right) = \frac{\Pi 10^{-3}\rho_w}{6}\sum_{i=1}^{32}(D)D^3\Delta D_i \tag{7}$$

$$N_w\left(m^{-3}mm^{-1}\right) = \frac{4^4}{\Pi}\frac{LWC}{D_m^4} \tag{8}$$

$$\mu = \frac{(7-11A) - \sqrt{(7-11A)^{\prime 2} - 4(A-1)(30A-12)}}{2(A-1)} \tag{9}$$

$$A = \frac{M_4^2}{M_2 M_6} \tag{10}$$

where LWC is the liquid water content (gm^{-3}), λ is the wavelength (mm), K_w is the complex dielectric constant of water, ρ_w is the density of water (1 g/cm^3), and $\sigma_{K_u,K_a}\left(mm^2\right)$ is the backscatter radar cross-section for the Ku and Ka bands of a droplet of equivalent diameter D. For the calculation of the cross-sections, the T-matrix [34,35] estimation method was applied assuming (1) an ambient temperature of 20 °C; (2) the shape of hydrometeors according to the model proposed by Thurai et al. [36]; and (3) the distribution of hydrometeor canting angles modeled with a Gaussian distribution with mean 0° and standard deviation 10° [15]. These calculations were performed using the Python package pyTMatrix 0.3.3 [37].

Additionally, considering that the GPM assumes a normalized gamma-type DSD to estimate the DSD parameters (Equations (A1) and (A2), Appendix A) and based on Equations (A3)–(A8), the DSD measurements recorded by the disdrometers were used to compute k (specific attenuation), as well as the k/Z_e and DFR (dB) ratios, by setting $\mu = 3$ [10,14].

2.2. Methodology

As indicated above, the number of satellite overpasses coincident with rainfall events may be an important limiting factor when comparing satellite and disdrometer observations. To overcome or partly mitigate this problem, some previous studies considered not only satellite matches but also datasets of the area of study of both the disdrometers and the satellite without necessarily including satellite overpass matches [8,10]. Then these two relatively independent datasets (as opposed to the datasets with matches) can be compared, for example, by checking if biases are present, to better interpret the comparison of satellite matches with ground observations. According to this idea, below are described the comparison of the so-called independent (non-matching) DPR and disdrometer datasets and the matching approaches considered.

2.2.1. Comparison of Independent Datasets

To select DPR data comparable to the reference disdrometer data, precipitation DPR observations within a 10 km radius around the location of the disdrometer sites were considered. Duplicate information due to overlapping of the selected areas was eliminated to avoid redundant data that could affect the characterization statistics (Figure 1). The results of this analysis were stratified according to each disdrometer separately, into three geographic areas with different climatic and orographic characteristics and considering all the data together. For each subregion, it was ensured that only one data record existed at any given time (in cases where more than one existed, only one was selected randomly). The characterization of the entire domain was considered based on the union of all valid data from the three subregions.

According to GPM documentation, the minimum detectable radar reflectivity and rainfall rate for the Ku- and Ka-bands are 13 dBZ, 17 dBZ and 0.5 and 0.2 mm/h, respectively. However, previous studies have observed improved detection of light precipitation using GPM DPR [38]. In addition, GPM DPR estimates over the study region showed minimum precipitation rates of 0.1 mm/h, therefore, in this work this threshold [8,15] was selected to fix precipitation events for both GPM DPR and disdrometer data.

2.2.2. Matching Approaches

Four different matching approaches were considered, based on similar previous studies [8,15]. An attempt was made to determine the most appropriate strategy considering the performance of each GPM DPR scanning mode (Ka-FS, Ku-FS and DPR-FS). The four methods are as follows:

a. Point: The disdrometer location was found within the footprint of the DPR (within the 5 km^2 pixel area) and so could be compared directly.
b. Mean 5 km: Disdrometer data were compared with the average of all DPR pixels within a 5 km radius of the disdrometer.
c. Mean 10 km: Disdrometer data were compared with the average of all DPR pixels within a radius of 10 km of the disdrometer.
d. Optimal: Disdrometer data were compared with the DPR pixel closest to the disdrometer within a 5 km radius and the nine DPR pixels containing the disdrometer. Finally, among these nine pixels, the pixel with closest radar reflectivity factor to that of the disdrometer was selected for comparison.

The methods proposed aim to reduce the spatiotemporal uncertainties that arise when comparing instantaneous measurements from space with ground-based measurements from disdrometers. Additionally, considering various methodologies allows us to understand the impact on the results and compare them with previous studies. As proposed by Adirosi et al. [15], due to advection processes, the significant DPR estimates determined in the CFB may not correspond to the corresponding pixel on the surface. To address this limitation, averaging methods are employed. The choice of a 5 km radius is based on the results of a sensitivity study and the physical considerations described by Adirosi et al. [15]. Similarly, in this work, a 10 km radius was used, which, while not considerably increasing the number of cases, yielded better results for some variables. A larger radius was not considered because, particularly in coastal areas, it would include parts of the sea, affecting the homogeneity of the selected terrain and potentially altering the microphysical characteristics of precipitation. Finally, the so-called optimal method, based on the work of Silvestro et al. [39], comparing ground-based weather radar observations with rain gauge data, primarily seeks to determine if the DPR can detect the characteristics of rain measured by the disdrometer, at least in its vicinity.

After selecting the GPM overpasses in rainy conditions, the 1-min DSD samples from the disdrometers were averaged over a 10-min window to reduce the time and space sampling problems between the GPM-DPR and the disdrometers. The results for the total number of precipitation exceedances and matches following these methodologies are shown in the results section. The comparison was made in terms of D_m (mm), R (mm/h), $Z_{Ku,Ka}$ (mm^6m^{-3}) and N_w (dB).

2.2.3. Verification Metrics

The comparison between the GPM DPR and disdrometer data was performed considering verification scores for both continuous variables and categorical events (Table 3).

Table 3. List of verification metrics used to evaluate DPR products.

Name	Formula	Perfect Score
Correlation Coefficient (CC)	$CC = \frac{\Sigma(O_i - \overline{O_i})(S_i - \overline{S_i})}{\sqrt{\Sigma(O_i - \overline{O_i})^2 \Sigma(S_i - \overline{S_i})^2}}$	1
Normalized Mean Bias (NBias)	$NBIAS = \frac{\frac{1}{n}\sum_{i=1}^{n}(S_i - O_i)}{\overline{O_i}} \times 100$	0
Normalized Mean Absolute Error (MAE)	$NMAE = \frac{\frac{\sum_{i=1}^{n}\lvert S_i - O_i\rvert}{n}}{\overline{O_i}}$	0
Normalized Root Mean Square Error (RMSE)	$NRMSE = \frac{\sqrt{\frac{1}{n}\sum_{i=1}^{n}(S_i - O_i)^2}}{\overline{O_i}}$	0
Accuracy	$\frac{TP}{\text{All classifications}}$	1
Precision	$\frac{TP}{TP+FP}$	1
Recall	$\frac{TP}{TP+FN}$	1

S_i is the value of satellite precipitation estimates for the ith event, O_i is the value of disdrometer observation for the ith event, and n is the number of observed records. $\overline{S_i}$ and $\overline{O_i}$ are the mean of satellite and observations, respectively. The values of TP and FP are based on the confusion matrix (Table 4).

Table 4. Confusion Matrix for multi-class classification (3 × 3).

		Observed Class			
		A	B	C	Total
Predicted Class	A	TP_A	F_{BA}	F_{CA}	$TP_A + F_{BA} + F_{CA}$
	B	F_{AB}	TP_B	F_{CB}	$F_{AB} + TP_B + F_{CB}$
	C	F_{AC}	F_{BC}	TP_C	$F_{AC} + F_{BC} + TP_C$
	Total	$TP_A + F_{AB} + F_{AC}$	$F_{BA} + TP_B + F_{BC}$	$F_{CA} + F_{CB} + TP_C$	All classifications

Note that the scores considered for verification of categorical forecasts are based on the so-called confusion matrix, also called the contingency table [40]. These scores are typically used in machine learning applications [41] but in this case are applied to multi-category events [42] considering a 3 × 3 confusion matrix (Table 4). As shown, TP_A, TP_B and TP_C are the number of true positive samples in classes A, B and C, respectively. False negatives (FN) of any class, which are in a column, can be calculated by adding the errors in that class/column, whereas the false positives for any predicted class, which are in a row, represent the sum of all errors in that row. For example, the false positive rate in class A (FP_A) is calculated as $FP_A = F_{BA} + F_{CA}$ and the false negative rate in the A class is $FN_A = F_{AB} + F_{AC}$ [43].

3. Results

3.1. GPM CO vs. Disdrometer-Derived Independent Estimates

Figure 2 shows the histograms of the probability of occurrence with respect to the following variables: reflectivity factor ($Z_{Ka,Ku}$), precipitation intensity (R) and DSD parameters (D_m, N_w, μ) obtained for both GPM DPR and disdrometer independent datasets. The dashed lines represent the median of the distribution of each dataset, and the solid curve represents the kernel density estimation (KDE) curve associated with each distribution.

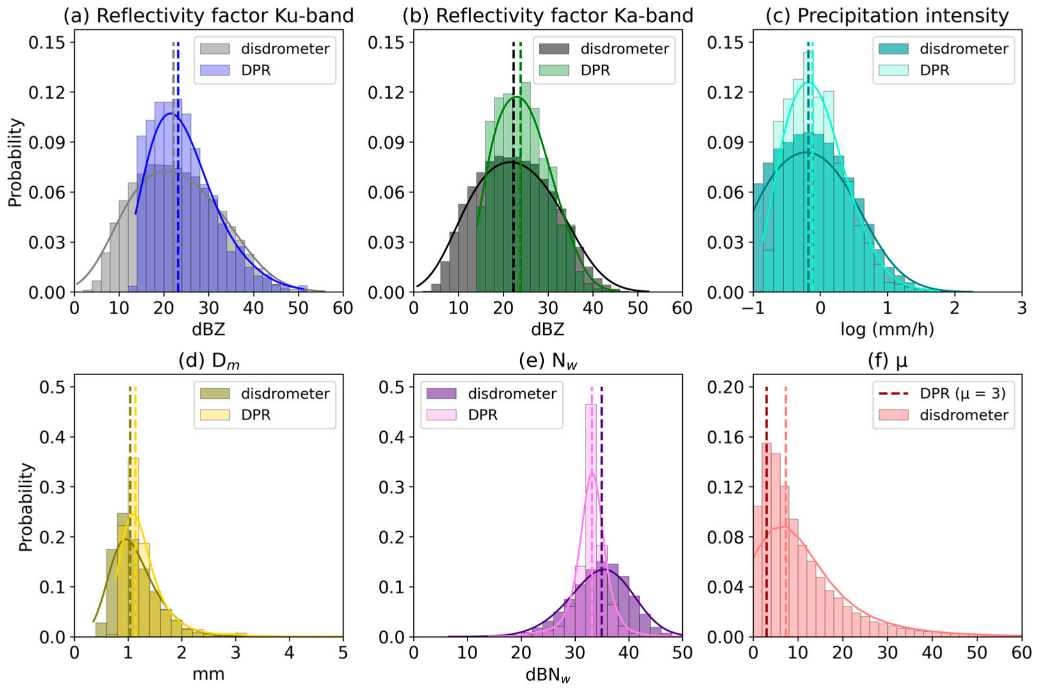

Figure 2. Histograms of (**a**) Z_{Ku}, (**b**) Z_{Ka}, (**c**) $\log_{10}(R)$, (**d**) D_m, (**e**)$10 \log_{10} (N_w)$ and (**f**) shape parameter (µ) derived from all disdrometer and GPM DPR (DF) datasets.

Despite the differences in the number of samples and period of record in the two independent datasets, important similarities can be observed in the distributions. However, the DPR distributions are slightly shifted to higher values compared to the disdrometer distributions in reflectivity (Z_{Ka} and Z_{Ku}), precipitation intensity and D_m, which might indicate little skill in detecting the lower thresholds in these variables with respect to the data taken as reference. Specifically, in the case of D_m, while in the disdrometers, the highest probability of occurrence occurs for values less than 1 mm, in the DPR, this occurs between 1.0 and 1.5 mm. In contrast, the N_w values obtained from the DSD of the disdrometers had a wider range, especially with a tendency to detect higher thresholds and a higher mean than that of the DPR. Figure 2f shows the discrepancies between the mean µ close to 10 in the case of the reference data, which is different from that set by the DPR algorithm (µ = 3). Several authors [8,9,28] discussed the limitations of setting this parameter.

Tables 5 and 6 show the number and median and maximum values of each variable analyzed for each dataset. In addition, to evaluate how the location of the disdrometers might affect the precipitation and DSD parameters, three zones with different orographic and climatic characteristics were analyzed. The plain, coastal and mountain regions were constructed by combining the data from the disdrometers that compose these homogeneous regions (Figure 1).

In general, there is little variability among the disdrometer statistics according to geographic location. The median reflectivity values range between 20 and 24 dBZ, precipitation intensities between 0.48 and 0.89 mm/h, D_m close to 1 mm and the intercept parameter (N_w) around 35 dB. Similarly, in the analysis of the observations in regions with different climatologies, the behavior of the variables was similar. The coastal area shows slightly higher median values, and the maximum intensity is reported at the Fabra Observatory, which is consistent with previous rain gauge-based climatologies in this region reporting higher rainfall rates near or at the coast compared to inland areas [44]. This behavior of the variables can be compared with the results obtained by Adirosi et al. [15] in Italy, where median values of 23.4, 21.9, 0.73, 35.72 and 1.05 (see Table 5 last row) were obtained for the variables Z_{Ka}, Z_{Ku}, R, N_w and D_m, respectively.

Table 5. Statistics of the different rainfall and DSD parameters for each single dataset, three similar orographic and climatic regions and all datasets together from the disdrometers.

Dataset		Z_{Ka} (dBZ)		Z_{Ku} (dBZ)		R (mm/h)		N_w (dB)		D_m (mm)	
	N	Median	Max	Median	Max	Median	Max	Median	Max	Median	Max
C01	51,679	24.77	47.27	24.92	51.86	0.89	60.83	33.75	51.61	1.19	6.28
C02	12,537	22.79	52.40	22.68	55.83	0.77	183.27	35.23	53.06	1.04	4.40
M01	59,388	21.13	49.74	20.92	54.88	0.60	107.70	36.16	52.04	0.96	7.86
P01	10,218	20.30	47.83	20.04	52.47	0.48	74.61	34.77	50.17	0.98	3.85
P02	12,855	21.49	50.26	21.38	53.97	0.54	115.74	34.09	49.98	1.06	4.91
P03	12,035	21.04	50.16	20.79	53.76	0.56	114.86	35.27	50.00	1.00	7.59
P04	3616	21.56	50.71	21.44	55.20	0.54	132.65	34.75	50.88	1.04	4.75
Coast	60,570	24.26	52.40	24.34	55.83	0.85	183.27	34.04	53.06	1.16	6.28
Mountain	59,388	21.13	49.74	20.92	54.88	0.60	107.70	36.16	52.04	0.96	7.86
Plain	24,254	20.44	50.71	20.21	55.20	0.48	132.65	34.43	50.88	1.01	7.59
All	144,212	22.28	52.40	22.16	55.83	0.66	183.27	34.97	53.06	1.04	7.86

Table 6. Same as Table 4, but with dual-frequency DPR data. Note that the number of Ka-band reflectivity data is different from other variables because only the Ka inner swath was available.

Dataset		Z_{Ka} (dBZ)			Z_{Ku} (dBZ)		R (mm/h)		N_w (dB)		D_m (mm)	
	N	Median	Max	N	Median	Max	Median	Max	Median	Max	Median	Max
C01	291	25.10	45.70	351	24.46	51.13	0.96	57.07	33.19	51.29	1.19	3.00
C02	312	25.00	42.34	376	24.24	51.13	0.90	36.33	33.24	51.29	1.18	4.45
M01	360	23.47	37.54	423	23.25	46.34	0.78	18.49	33.04	50.65	1.16	3.00
P01	262	23.16	41.37	304	22.38	51.05	0.68	27.75	33.11	43.93	1.12	5.00
P02	203	24.23	38.67	232	23.18	44.61	0.75	11.71	33.34	41.34	1.12	3.00
P03	269	23.63	41.37	304	22.20	51.05	0.67	27.75	33.13	43.93	1.11	4.99
P04	234	23.42	37.44	273	22.38	47.42	0.68	13.18	33.34	41.51	1.11	3.56
Coast	603	25.05	45.70	727	24.40	51.13	0.92	57.07	33.21	51.29	1.18	4.45
Mountain	360	23.47	37.54	423	23.25	46.34	0.78	18.49	33.04	50.65	1.16	3.00
Plain	968	23.55	41.37	1113	22.59	51.05	0.69	27.75	33.21	43.93	1.11	5.00
All	1931	23.89	45.70	2263	23.19	51.12	0.77	57.07	33.17	51.29	1.14	5.00

The statistics obtained from DPR data showed higher median values for all variables, except N_w. However, DPR data can capture the variability between different zones, exhibiting the highest median values in the coastal zones. Similarly, the maximum values observed by disdrometers were much higher in all datasets than those recorded by the DPR DF. Although other studies have commented on the limitations in the detection of extreme values by remote sensing products [45], in this case, we cannot draw any conclusions because such values are subject to the availability of DPR data at the time of the occurrence of this type of extreme event.

3.1.1. Rain Rate Effects

The DSD-derived precipitation characteristics were stratified into six rain rate intensity classes. For this purpose, the disdrometer and DPR DF records were considered together and grouped according to the three subregions (plain, mountain and coast) mentioned above. Figure 3 (top panel) shows the normalized density distributions for the datasets. A necessary condition to obtain the mean of these variables in each precipitation intensity interval was that they had at least 10 records. It is evident that all datasets behave similarly, with a high representation of data -as expected-, at lower precipitation intensities and much lower for moderate and high intensities. Despite the lack of temporal concurrence between the disdrometers and the DPR, both sources provide relatively similar results with similar qualitative behavior.

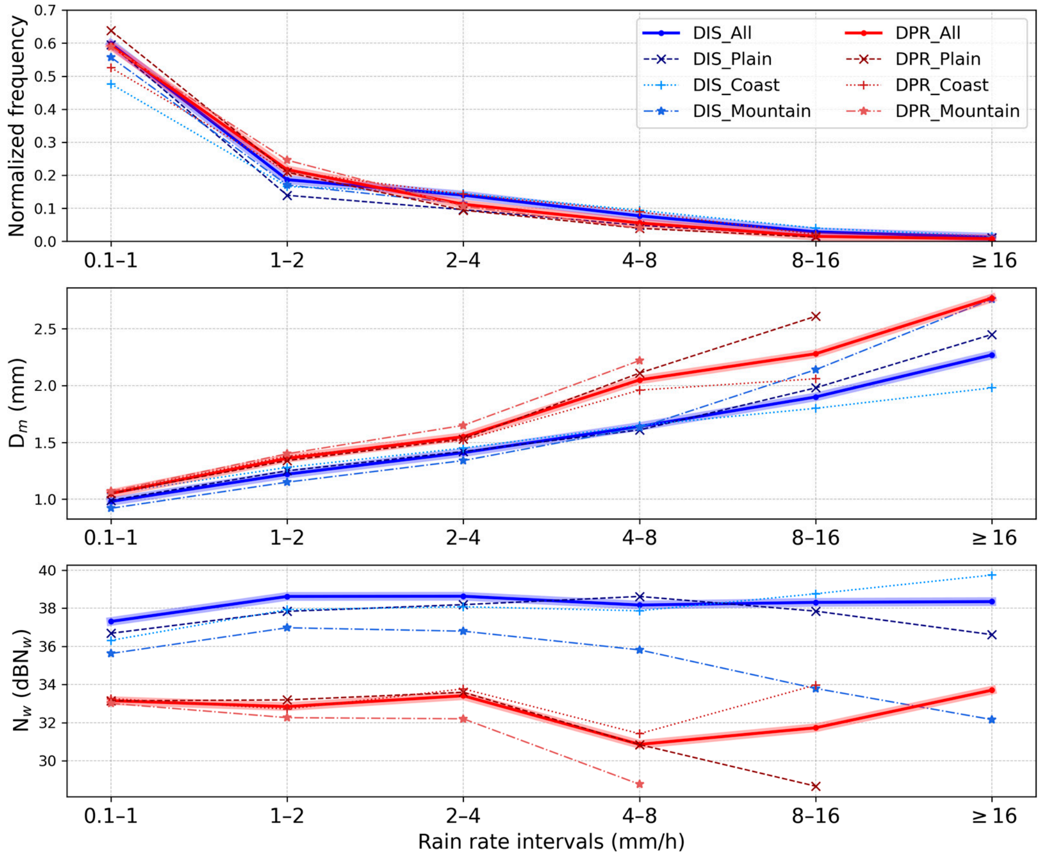

Figure 3. Comparison of normalized frequency distribution showing the ratio of data at each rain rate interval for disdrometer (in blue) and DPR (in red) data (top panel) and, similarly, comparison of DSD parameters D_m (middle panel) and N_w (bottom panel). All panels show values for the subregions plain (dashed line), coast (dotted line), mountain (semi-dashed line) and the whole region (all, thick line), for both disdrometer (DIS_) and DPR (DPR_) data.

Figure 3 (middle and bottom panels) illustrates the variation in the mean D_m and N_w observed and estimated using the DF DPR algorithm as a function of precipitation intensity. The DSD parameters were similar in all regions for intensities below 4 mm/h. At thresholds higher than 16 mm/h, the D_m for example differs by more than 0.5 mm between coastal and mountain areas according to the disdrometer data. The intercept parameter begins to differentiate in the regions from intensities between 8–16 mm/h with a difference of more than 5 dB between coastal and inland areas according to the DPR and close to 6 dB between coastal and mountain areas according to disdrometer data.

From these figures, the DSD parameters obtained by the DF algorithms capture the variability observed at different intensities, although with overestimates of the mean D_m and underestimates of the mean N_w, showing the greatest differences at moderate and high intensities and being much more sensitive to errors in drops greater than 1.5 mm. These results are similar to those found by Del Castillo-Velarde [14], in which it is stated that the DF algorithm is susceptible to the uncertainty of μ fixation, which causes an underestimation of N_w.

Comparisons of the DSD parameters show an overestimation of D_m of about 0.1 mm at low and moderate precipitation rates (0.1–1, 1–2, 2–4 mm/h) and of 0.4 mm at precipitation rates higher than 4 mm/h by the DF algorithm with respect to the disdrometer. In contrast, the behavior of N_w was underestimated by the DPR, with a maximum value close to 6 dB at moderate precipitation rates (4–8 mm/h). Compared to the studies of [10], the magnitudes of underestimation and overestimation of D_m and N_w are very similar. However, here the behavior of the DSD parameters occurs in reverse; that is, the mean value of D_m is overestimated and N_w is underestimated. This sensitivity analysis shows that the results presented here are consistent and that differences with other studies may be due to spatial and temporal sampling factors and differences arising from the use of other types of disdrometers [46,47].

3.1.2. Stratiform vs. Convective Regimes

In this section, we analyze the stratiform and convective regimes associated with the DPR and disdrometer data, as well as different related microphysical processes. For this purpose, we consider the classification for a given rainfall DSD proposed by Dolan et al. [48] based on the clustering of D_o and N_w values obtained from global disdrometric records. From this perspective, six groups with independent characteristics were defined: Group 1, Group 3, Group 5 and Group 6 (Figure 4b) are characterized by convective precipitation processes, while the Group 2 and Group 4 are stratiform precipitation processes, with increasing D_0 and decreasing N_w. Complementarily, we also considered the DPR algorithm classification, in which each pixel is assigned a so-called precipitation type label: stratiform, convective or other. Figure 4 plots all disdrometer records in the D_o-log (N_w) space overlaid with the diagram proposed by Dolan et al. [48].

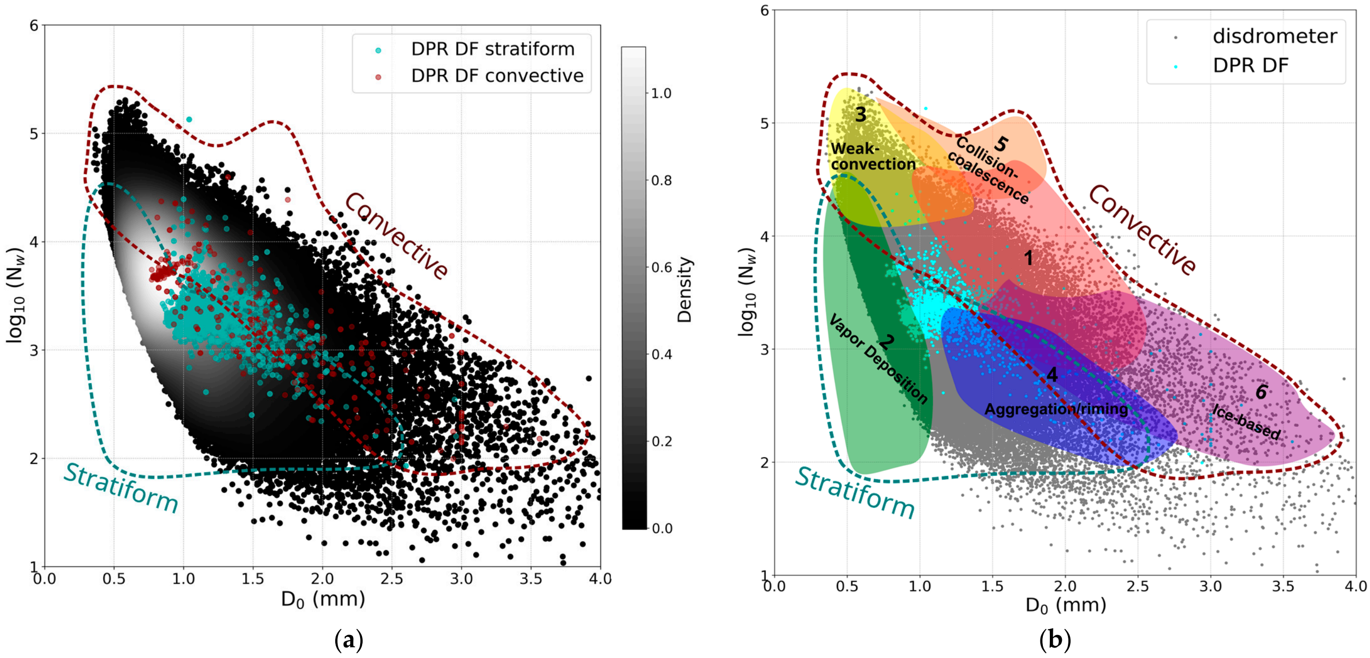

Figure 4. (**a**) Scatter density plot of raindrop size distribution measurements from all disdrometers in the D_0-log(N_w) space overlapped by the stratiform region (limited by turquoise dashed line) and convective region (limited by red dashed line) defined by Dolan et al. [48]. Disdrometer data density increase from dark to white dots, and DPR DF convective and stratiform types are indicated by red and turquoise dots, respectively. (**b**) Convective, stratiform and microphysical dominant process regions in the D_0-log(N_w) space according to Dolan et al. [48] overlapped by disdrometer (grey dots) and DF DPR (cyan dots) data.

Note that in Figure 4a, most of the measurements were in the stratiform part of the plot, which is consistent with the values of the disdrometer parameters discussed above (low liquid water content and small mean droplet diameters). In the same figure, the values classified as stratiform (turquoise dots) and convective (red dots) by the DPR DF algorithm are plotted. Although the highest percentage of data are in the stratiform domain, there is a large scatter of data that does not fit this classification, especially for events classified as convective rain (Table 7).

Table 7. Percentage (%) of data according to the rainfall regime considering stratiform, convective, ambiguous (between stratiform and convective) and outlier (out of the stratiform and convective classification domain) according to Dolan et al. [48].

	Stratiform	Convective	Ambiguous	Outlier
Disdrometer	53	31	13	2
GPM DPR (DF)	73	18	8	1

Figure 4b provides information on the dominant precipitation mechanisms in the disdrometer and DPR DF records following Dolan et al. [48]. According to this classification, the disdrometer stratiform rainfall was dominant (Table 7) and strongly influenced by vapor deposition followed by riming processes (Table 8). Convective events, on the other hand, are not associated with a single well-defined microphysical mechanism. Moreover, an important part of the events (13%) are classified as ambiguous (neither convective nor stratiform) and are associated with different microphysical mechanisms. DPR records have a large percentage of data (46%) in areas that fall outside the classification range, although the influence of stratiform precipitation processes by riming can be appreciated (Table 8).

Table 8. Percentage (%) of data associated with microphysical precipitation mechanism groups proposed by Doan et al. [48] (see Figure 4b).

	Group 1	Group 2	Group 3	Group 4	Group 5	Group 6		
		Vapor Deposition	Weak Convection	Aggregation/ Riming	Collision–Coalescence	Ice-Based	Ambiguous	Outlier
Disdrometer	4	29	4	14	0	1	12	32
GPM DPR (DF)	4	15	0	22	0	2	11	46

3.2. Analysis of Satellite Overpass Events Coincident with Disdrometer Data

This section evaluates the performance of the GPM-DPR estimates for the different matching methods with disdrometer data described in Section 2.2. Table 9 shows the number of overpasses of the GPM-DPR (2014–2023) with precipitation, and the number of matches from the different proposed methods. A comparison was carried out for the two algorithms: DPR DF and SF in the FS mode. Analyses of the variables Z, R, D_m and N_w were considered.

Table 9. Summary of overpasses over disdrometer sites without (Group A) and with (Group B) concurrent disdrometer rainfall data for DPR, Ka and Ku FS modes. Matching methods between GPM observations and disdrometer sites are point, 5 km, 10 km, 9 pixels (Group A) and optimal (Group B).

GPM Product	Group A: GPM CO Overpasses with Rain without Necessarily Matching Disdrometer Data				Group B: GPM CO Overpasses with Rain Matching Disdrometer Data			
Matching Method	Point	5 km	10 km	9 pixels	Point	Mean 5 km	Mean 10 km	Optimal
DPR-FS	142	272	460	567	19	33	39	40
Ka-FS	69	157	289	328	12	27	33	34
Ku-FS	142	270	463	569	20	34	41	41

Between March 2014 and November 2023, the GPM CO passed (at least one footprint) over the region of Catalonia 2089 times and, of them, 1126 had at least one footprint with rainfall (hereafter rain overpasses). It is important to mention that the Ka-band presents a lower number of cases compared to the others (Table 9) because only inner swath data are available due to the DPR scan pattern change in May 2018. After that change, the data were reprocessed, leaving the payoffs in HS scan mode in the outer swath, for which no data are available as of the date of this study. The differences in the number of overpasses between the DPR and Ku-band products in both Group A and Group B, although insignificant in this case, are due to differences in the precipitation estimation algorithms around the 0.1 mm/h threshold.

The main statistics for quantifying the error between the DPR estimates at the CFB and disdrometer ground-based values are shown in Table 10. Values marked in red represent the worst scores and those in green the best scores for each group of variables and error statistics analyzed.

Table 10. Statistics of the comparison between the GPM DF and SF products and disdrometer data for different variables and matching methods. Statistical significance of CC is indicated with an asterisk(*) and was tested with the *t*-test using a significance level of 0.05. The best and worst statistics obtained for each product, method and variable are marked in green and red, respectively. Note that all variables listed in the table are dimensionless.

		Point				Mean 5 km				Mean 10 km				Optimal			
		NBIAS	NMAE	NRMSE	CC	NBIAS	NMAE	NRMSE	CC	NBIAS	NMAE	NRMSE	CC	NBIAS	NMAE	NRMSE	CC
R	DF	−46.12	0.70	1.20	0.48 *	−39.21	0.66	1.02	0.31	−16.88	0.59	0.90	0.70 *	0.26	0.61	1.60	0.77 *
	SF	−49.84	0.69	1.18	0.37 *	−46.93	0.64	1.01	0.30 *	−31.63	0.66	0.99	0.44 *	−35.35	0.43	0.78	0.78 *
Z_{Ka}	DF	−6.07	0.19	0.27	0.61	−7.55	0.17	0.22	0.61 *	−4.68	0.18	0.23	0.66 *	−2.58	0.09	0.14	0.88 *
	SF	−13.55	0.16	0.20	0.27	−11.58	0.16	0.19	0.42 *	−7.37	0.17	0.21	0.48 *	−2.81	0.10	0.16	0.77 *
Z_{Ku}	DF	−10.23	0.20	0.29	0.63 *	−10.75	0.18	0.25	0.63 *	−8.27	0.20	0.26	0.66 *	−6.04	0.12	0.16	0.88 *
	SF	−9.23	0.20	0.29	0.63 *	−11.53	0.18	0.27	0.64 *	−8.12	0.20	0.25	0.65 *	−5.37	0.10	0.16	0.88 *
D_m	DF	−1.08	0.24	0.28	0.65 *	2.05	0.21	0.27	0.56 *	1.82	0.22	0.28	0.51 *	0.96	0.14	0.18	0.83 *
	SF	−1.68	0.23	0.27	0.67 *	2.82	0.23	0.32	0.38 *	5.30	0.23	0.34	0.33 *	2.99	0.14	0.19	0.83 *
N_w	DF	−7.01	0.12	0.16	0.34	−7.59	0.11	0.14	0.32	−5.83	0.09	0.12	0.35 *	−5.12	0.11	0.13	0.39 *
	SF	−6.77	0.12	0.15	0.34	−8.61	0.12	0.15	0.16	−8.36	0.12	0.15	−0.01	0.29	0.12	0.14	0.19

Figure 5 shows the scatterplots of rainfall rate R (mm/h), Z_{Ka} (dBZ), Z_{Ku} (dBZ), mass-weighted mean drop diameter (D_m, mm) and N_w (dB) of the GPM DPR and disdrometers. Regarding rainfall intensity, the point and mean methods show a certain dispersion of the data in general around the 1:1 line (dashed line). Although it is less evident in the optimal methods, for intensity values higher than 4 mm/h, it is again marked in all methodologies. In fact, the correlation values are generally higher than 0.7 in the optimal method, and in the point and mean methods most cases are lower than 0.5, showing a worse performance in the SF algorithm.

In the analysis of the intensity of precipitation, the optimal and mean 10 km methods, generally, show the lowest values of NBIAS, NMAE and NRMSE, as well as higher values of correlation, displaying also a substantial improvement of the DF algorithm over the SF over a mean of 10 km. For the rest of the methods, the behavior of the SF and DF is similar. The NBIAS shows a marked difference in the DF algorithm between the point method (−46%) and optimal (0.26%); however, this could be due to error compensation, a disadvantage associated with this statistic.

The errors associated with the reflectivity in both Ka and Ku-bands are generally below 10%. Again, the worst results are observed with the point method and are better in the optimal method, with errors not exceeding 6%. It should be noted that the optimal method precisely optimizes the comparison with respect to reflectivity. The improvements in SF and DF behave similarly, although a slight improvement is observed in the SF returns associated with the Ka-band, which may be associated with a smaller number of records in the selected sample. A higher dispersion of the Ka-band reflectivity can also be observed, which can be verified with slightly lower correlation values and errors in the Ku-band. In terms of the MAE and RMSE, there were hardly any differences between the point and mean methods. However, these values were almost halved, with values barely exceeding 0.15 in the optimal method.

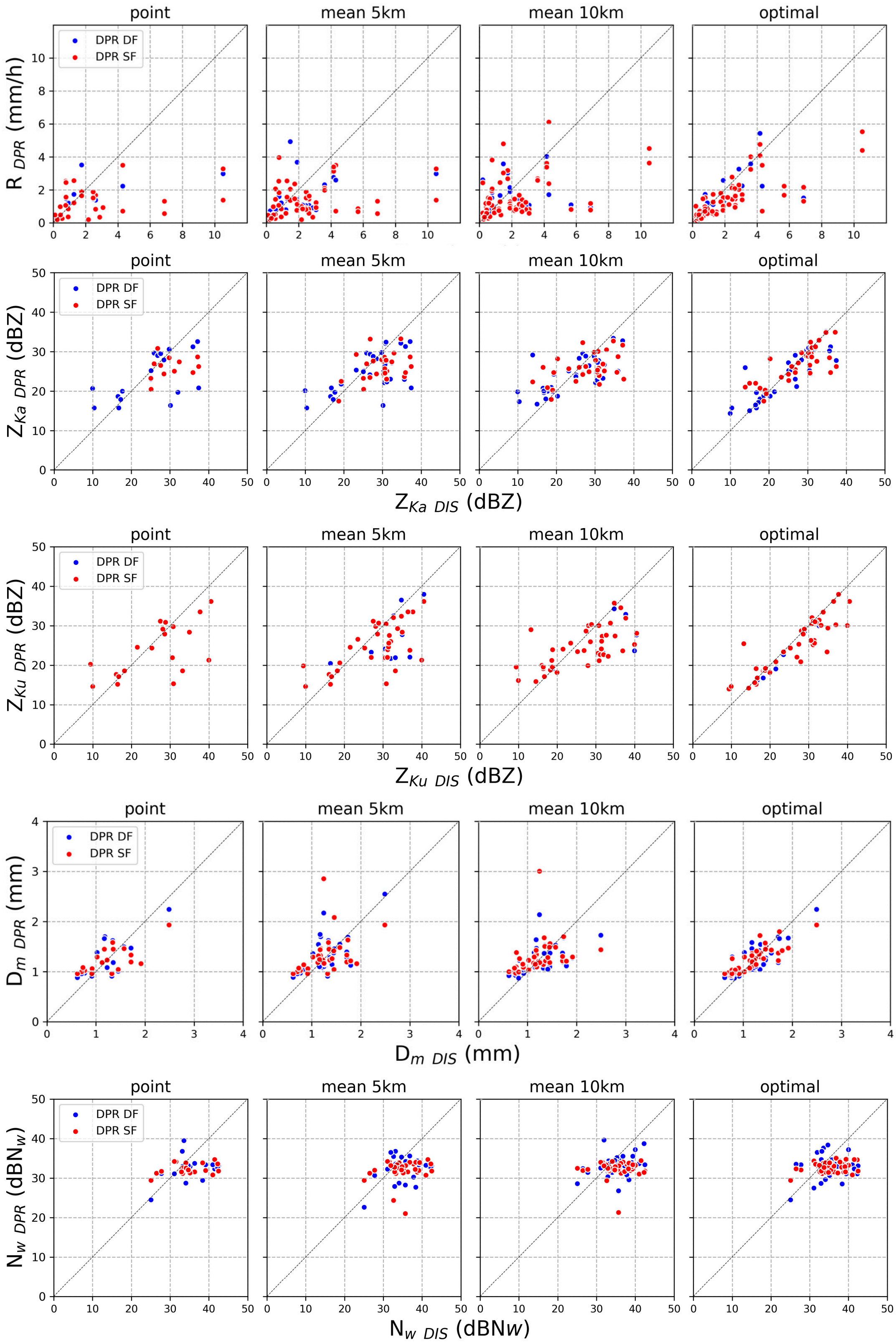

Figure 5. Scatterplots between disdrometer (x-axis) and GPM products (y-axis) considering rainfall rate (first row), Z_{Ka} (second row), Z_{Ku} (third row), D_m (fourth row) and dBN_w (fifth row) and four matching methods (point, mean 5 km, mean 10 km and optimal).

Agreement with respect to the D_m values depends on the method applied to the selection of cases. In the point method, unlike the others, the D_m values tended to be underestimated by approximately 1 mm and 1.7 mm under the SF and DF algorithms, respectively. However, the mean methods show an overestimation that reaches a maximum value of 5.3 mm in the SF (mean 10 km). In these methods, the lowest correlation values were also obtained, whereas the best values were recorded in the optimal method with 0.83, and the highest point was 0.65. There is a clear improvement in the DF algorithms with respect to SF, especially in the mean methods, where values of 1 and 2 mm are overestimated, and values higher than 2 mm are underestimated.

As in the results of Adirosi et al. [15], the concordance in terms of N_w was not satisfactory. Although the correlations this time turned out to be better, they lack statistical significance: the NMAE values were very similar, close to 12% in all cases, while the NBIAS was higher, similar to the work of Seela et al. [8], increasing the underestimation in our cases. Although earlier versions of the DPR were used in those works, it is shown that the deficiencies in N_w estimates remain. This may support the idea that the discrepancies between satellite- and disdrometer-based N_w may be due to the parameterization used by the GPM to model DSD.

3.2.1. Single- vs. Dual-Frequency-derived Estimates

Figure 6 shows the behavior of N_w versus D_m comparing all disdrometer data and two overpass matching methods (9-pixels and optimal) with GPM CO single- and dual-frequency estimates. The GPM data follow the typical D_m-$10\log_{10} N_w$ behavior reported by Adirosi et al. [15], although they are concentrated, mainly SF, at approximately 30–35 dBN_w. As illustrated in Figure 6, comparing single- vs. dual-frequency estimates, it is apparent that the dual-frequency pattern in the D_m-$10\log_{10} N_w$ space is closer to disdrometer data than the single-frequency pattern, which is consistent with the improved scores obtained by DF-derived estimates seen in Table 10.

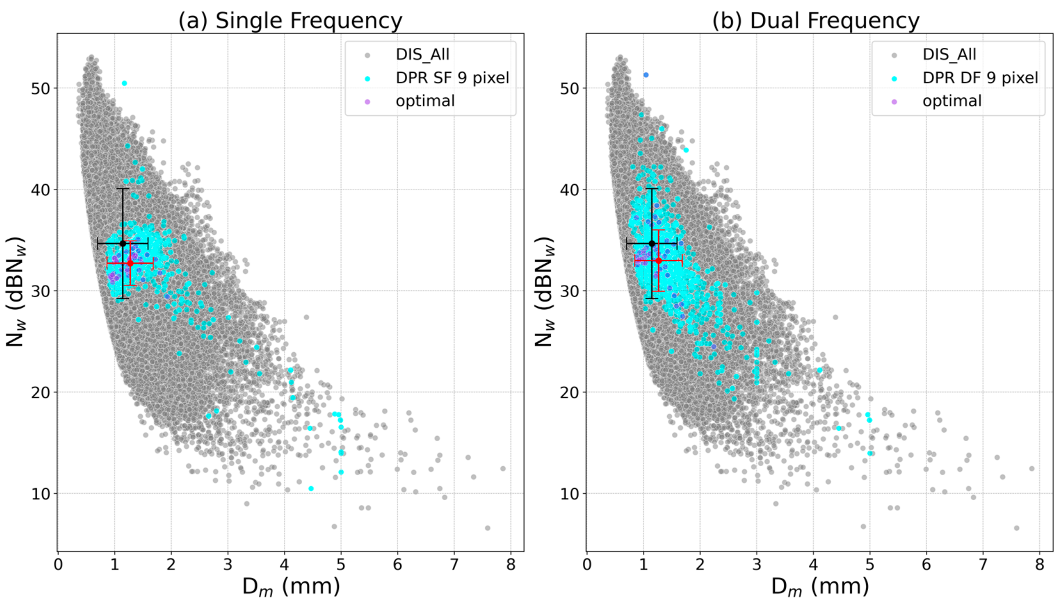

Figure 6. D_m vs. N_w for all available disdrometer data (grey dots), GPM data of nine pixels around the disdrometers (cyan dots) and GPM data coincident with disdrometers (violet dots) under optimal method showing GPM single-frequency (**a**)- and dual-frequency (**b**)-derived estimates. The black and red dots with the error bars represent the averages and standard deviations of the disdrometer dataset and GPM 9 pixels method.

Further insight about differences between single- and dual-frequency-derived estimates can be seen in Figure 7, which shows a Taylor Diagram that displays the STD-normalized CC and RMSE with the data obtained by the point method and the optimal method for the five variables of analysis. The benchmark represents the standard deviation and the correlation coefficient equal to unity. We observe an improvement using the optimal method, especially in the estimates of $Z_{Ka,Ku}$ and D_m. However, considering the analysis of precipitation intensity using the DF algorithm, the optimal yielded worse results. The differences between the methods may be related to the variability in precipitation in the pixels around the disdrometer.

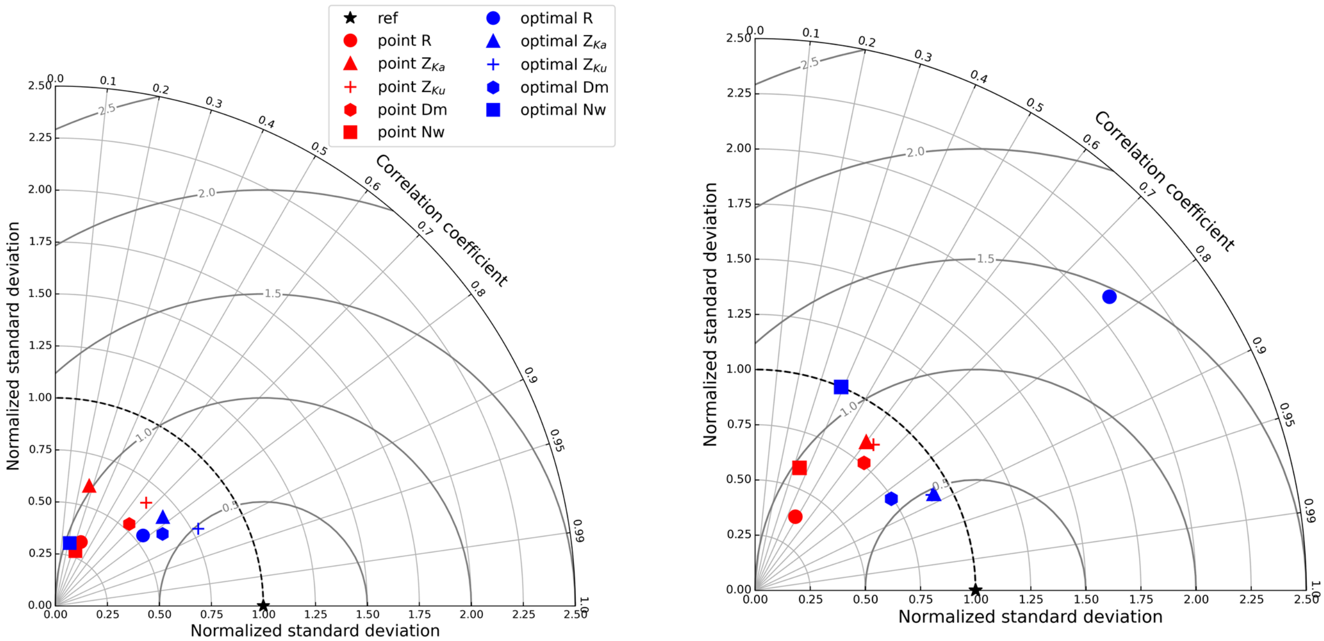

(**a**) (**b**)

Figure 7. Taylor diagram with the data obtained by the point and the optimal methods for R, Z_{Ka}, Z_{Ku}, D_m and N_w for single-frequency (**a**) and dual-frequency (**b**) GPM-derived estimates.

3.2.2. Stratiform vs. Convective Regimes

The precipitation type classification (including stratiform, convective and other regimes) provided by the DPR (variable named TypePrecip) was compared with the classification proposed by Dolan et al. [48] applied to disdrometer data. Table 11 shows the confusion matrix obtained by comparing the two datasets and considering the matches with the optimal method. Note that an "ambiguous" class appears to classify records that do not belong to stratiform or convective regimes using either method.

Table 11. Confusion matrix between ambiguous, stratiform and convective regimes classified by DPR DF and disdrometer data matched with the optimal approach, listing totals for each regime.

		Disdrometer			
		Ambiguous	**Convective**	**Stratiform**	**Total**
DPR DF	**Ambiguous**	1	0	1	2
	Convective	2	0	0	2
	Stratiform	5	15	17	37
	Total	8	15	18	41

According to Table 11, disdrometer data presents a similar proportion of convective (37%) and stratiform cases (44%) and a smaller ratio of ambiguous cases. However, this is not the case for the DPR data where stratiform cases are clearly predominant (90%) and convective and ambiguous cases are marginal (5% each). The overall DPR classification is rather limited according to the value of the accuracy (below 0.50), as only 46% (precision of 0.46) of the predominant predicted regime (stratiform) is correctly done, despite 94% of cases identified as stratiform by the disdrometers where correctly predicted. Worse scores are obtained for convective cases.

4. Discussion

As discussed in previous research, discrepancies observed in DSD parameter values between disdrometer data and GPM-DPR estimates may be associated with spatial and/or temporal sampling problems [49,50]. The spatial sampling uncertainties are due to the difference in the observation area of the two instruments, as the disdrometer has a sampling area of about 50 cm^2 and the GPM-DPR footprint circular radius is 5 km at nadir [10]. Another aspect to consider is the effect of updrafts and downdrafts present from the lowest GPM-DPR measurement to the ground, which can actually modify the estimated DSD at ground level [51]. As mentioned above there is also a problem associated with the limited GPM-DPR overpasses over a given region which implies a low probability of coincidence with observing precipitation over the disdrometer sites.

Similarly to other investigations [14], results found here indicate the DF algorithm overestimated the mean D_m values and underestimated the intercept parameter N_w. Such a problem has been primarily associated with the DPR assumption of a constant shape parameter. In Section 3.1, Figure 2f, we compared the μ distribution observed by disdrometers with the fixed value set by DPR (μ = 3) finding that it corresponded to the mode value but differed from the median (μ = 7). To better understand the limitation of fixing the shape parameter μ in the calculation of DSD-derived variables, we examine the k/Z_e ratio vs. the D_m, and the DFR vs. D_m with the disdrometer DSD (Figure 8). The k/Z_e ratio was calculated assuming the SF algorithm applied to Z_{Ku} and the DFR was calculated considering the DF algorithm.

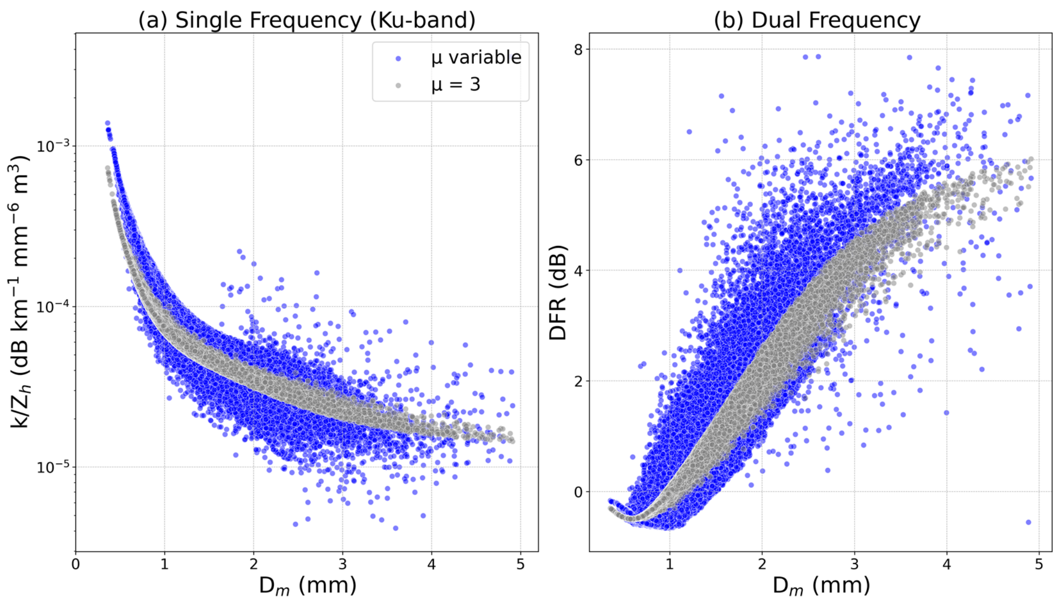

Figure 8. (**a**) Attenuation (k) to reflectivity (Z_h) ratio as a function of D_m at Ku-band frequency obtained from disdrometer measurements without and with fixed shape parameter (μ = 3). (**b**) As panel (**a**) but for DFR estimated with the dual-frequency algorithm.

Each panel of Figure 8 shows the variable considered in two ways: fixing the shape parameter (grey dots) and not fixing it (blue dots). When μ is set to 3 in both single- and dual-frequency algorithms (Figure 8a,b), a much higher variability of the data is observed. Radhakrishna et al. [10] posited that the high scatter in the values of (k/Z_h) and DFR is caused by the high variability in the DSD of convective rainfall. When μ is fixed, part of this variability is lost, increasing the uncertainty in the estimates. These results and the strong correlation between μ and N_w [33,52] are among the factors that generate the differences in the DSD parameter values between the disdrometers and the DPR DF. In addition, Del Castillo-Velarde [14] and Radhakrishna et al. [10] showed that the DF algorithm has limitations when attempting to estimate D_m for DFR values less than 0 dB, where there are two possible D_m values for a DFR measurement as the DF algorithm selects the drop with the highest D_m if two solutions exist [19]. Here we also observe that, for DFR values below 0 dB, D_m grows when DFR decreases for Dm below 0.5 mm as reported [10,14].

As seen in Equation (1), the GPM DPR rainfall rate computation is based on an adjustable R-D_m relationship linked to ε. In version 6 of the DPR algorithm, ε was assumed to be invariant, which imposed constraints on rainfall retrieval and caused the natural DSD variations along the rainfall column to be missed. In version 7, a two-scale model of ε was introduced, allowing it to vary with range [6]. To assess the consistency of this approach with our disdrometer observations, the D_m vs R observations were plotted overlaid with the corresponding GPM DPR curves computed for values of ε equal to 1.25 and 0.2 and 5.0 thus covering the possible range of values (Figure 9).

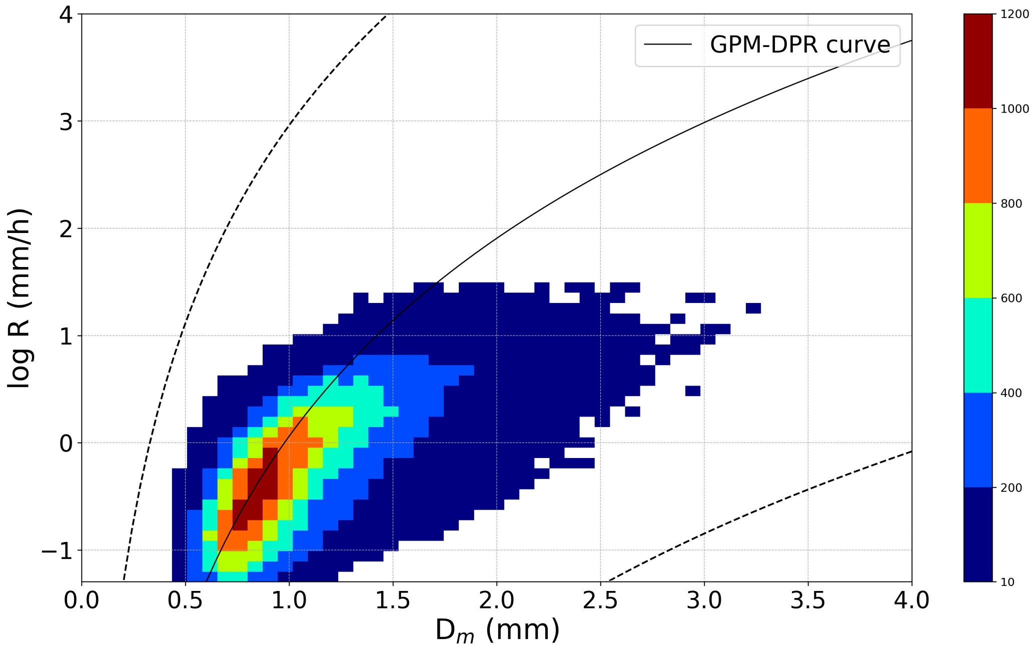

Figure 9. Scatter density plot of $\log_{10}$ (R) vs. D_m observed by disdrometers overlayed with the relation used in the GPM DPR algorithm for ε equal to 0.2 (upper dashed line), 1.25 (solid line) and 5.0 (lower dashed line).

The disdrometer data are clearly contained in the region limited by the GPM DPR lines and higher observation densities correspond well to the ε = 1.25 for D_m < 1.5 mm, but for larger diameters, the GPM DPR relationships tend to underestimate R. As posited by [8,15], this may be due to the use of predefined constants (α, β and τ) in the relationships between the precipitation rate and mass-weighted mean diameter (Equation (1)) that may not be adequate for the rainfall characteristics of the region of study. In addition, factors such as the attenuation effect, multiple scattering, non-uniform beam filling, and terrain interference directly affect the accuracy of the GPM DPR parameter estimation [6,53].

The results of the analysis of the matches between GPM DPR overpasses with disdrometers were consistent with those of similar studies [8,15]. The superiority of the optimal matching approach and the lower errors associated with the radar reflectivity factor and the mass-weighted mean diameter, as well as the poorer agreement between the intercept parameter and the rainfall rate, are indications of limitations in the DPR algorithm. In addition, it is worth mentioning that there is no clear trend of improvement of the DF algorithms over SF in version 07, which agrees with what was observed with version 6 by Adirosi et al. [15]. Finally, the limited ability to detect the convective precipitation type, documented in studies analyzing previous GPM DPR previous versions [11,13,14], is also found here for version 07 as reported by Seela et al. [8].

5. Conclusions

In this study, more than nine years of data ranging from March 2014 to November 2023 recorded by the GPM DPR over different geographical areas of the northeastern Iberian Peninsula were analyzed. Based on information from seven disdrometers, the first part of the study focuses on the characterization and comparison of DSD-derived parameters obtained from both datasets independently considering 162,328 and 2263 min of precipitation records observed by disdrometers and the GPM DPR, respectively. Results were stratified by orographic and climatic characteristics and several rainfall rate intensity thresholds. The second part of the study focused on validating four spatial matching methods between DPR overpasses and disdrometers. The main results are as follows:

1. The behavior of DSD-derived variables among the plain, mountain and coastal subregions showed some differences according to the disdrometer data, which were captured by the DPR DF algorithm. However, the GPM DSD parameters show an overestimation of D_m by about 0.1 mm at low and moderate precipitation rates (0.1–1, 1–2, 2–4 mm/h) and by 0.4 mm at precipitation rates greater than 4 mm/h by the DF algorithm with respect to the disdrometer. In contrast, the behavior of N_w was underestimated by the DPR, with a maximum value close to 6 dBN_w at moderate precipitation rates (4–8 mm/h).
2. Disdrometer data indicated that the shape parameter mode over the area of study corresponds to the DPR fixed value ($\mu = 3$), but the median was higher ($\mu = 7$). Moreover, μ presents a distribution with a substantial natural variability which implies an increase in the uncertainty of DSD estimates based on the constant value assumption.
3. The superiority of the optimal matching approach was observed when validating the GPM DPR rainfall parameters with disdrometers. The GPM DPR estimates showed better verification statistics for the radar reflectivity factor in both Ku and Ka bands and the mass-weighted mean diameter, while worse results were found for the rainfall rate and the shape parameter N_w.
4. According to the available sample of overpass matches (41 cases) the DPR DF rainfall classification algorithm showed little ability to detect events identified as convective by the disdrometers.

To the authors' knowledge, this validation study is the first of its kind covering the Iberian Peninsula and one of the few carried out in areas with a Mediterranean climate. Moreover, this is one of the first analyses in which recent updates incorporated in version 7 are validated. Results reported here may contribute to enhance our understanding of potential applications and limitations of satellite precipitation observations and can be considered in the development of future satellite precipitation retrievals.

Author Contributions: Conceptualization, E.P. and J.B.; methodology, E.P. and J.B.; formal analysis, E.P.; investigation, E.P. and J.B.; data curation, E.P., F.P., J.B., M.U., S.G. and B.B.; writing—original draft preparation, E.P. and J.B.; writing—review and editing, E.P., J.B., F.P., M.U., M.P., E.A., S.G. and B.B.; visualization, E.P.; supervision, J.B. and M.U. All authors have read and agreed to the published version of the manuscript.

Funding: This research was partly funded by the projects WISE-PreP (RTI2018-098693-B-C32), ARTEMIS (PID2021-124253OB-I00 MINECO/FEDER) and the Water Research Institute (IdRA) of the University of Barcelona.

Data Availability Statement: Data are contained within the article.

Acknowledgments: Satellite and gauge data for this study were provided by NASA/JAXA. The authors wish to acknowledge the Fabra Observatory of the Royal Academy of Sciences and Arts of Barcelona and the support from the Secretariat for Universities and Research of the Ministry of Business and Knowledge of the Government of Catalonia and the European Social Fund.

Conflicts of Interest: The authors declare no conflicts of interest.

Appendix A

The GPM algorithm assumes a gamma-type DSD (normalized version) to estimate the DSD parameters of the form:

$$N(D) = N_w f(D; \mu;\ D_m) \tag{A1}$$

$$f(D; \mu;\ D_m) = \frac{6(\mu+4)^{(\mu+4)}}{4^4\Gamma(\mu+4)}\left(\frac{D}{D_m}\right)^{\mu} \exp\left[\frac{-(\mu+4)D}{D_m}\right] \tag{A2}$$

where $N(D)$ is the drop size distribution (in $mm^{-1}m^{-3}$), D is the diameter of the raindrop (mm), D_m (mm) is the mass-weighted mean diameter which represents a mean particle size of the distribution. N_w is the normalized scaling parameter for concentration ($mm^{-1}m^{-3}$), μ the shape parameter for gamma distribution and Γ denotes the gamma function. Letting σ_b (in mm^2) and σ_e (in mm^2) be the backscattering cross section and the extinction cross section of raindrops at a given temperature, respectively, K as a constant defined as a function of complex refractive index and λ the radar wavelength (in mm), the equivalent reflectivity Z (in mm^6/m^3) and specific attenuation k (in dB/km) are expressed as follows:

$$Z_e = N_w F(\lambda; \mu; D_m) \tag{A3}$$

$$F(\lambda; \mu; D_m) = \frac{\lambda^4}{\Pi^5|K|^2}\int f(D; \mu;\ D_m)\sigma_b \Delta D \tag{A4}$$

$$k = \ N_w G(D; \mu; D_m) \tag{A5}$$

$$G(D; \mu; D_m) = 4.343 \times 10^{-3}\int f(D; \mu;\ D_m)\sigma_e \Delta D \tag{A6}$$

Equations (A3) and (A5) are used by the SF and DF algorithms to determine the DSD parameters. The terms $F(\lambda; \mu; D_m)$ and $G(D; \mu; D_m)$ refer to normalized radar reflectivity and specific attenuation (in dB/km) and are the same as $F(D_m)$ and $G(D_m)$ in [19] and Ib (D_m, μ, λ) and Ie (D_m, μ, λ) in [9]. To determine parameters D_m and N_w, the GPM-DPR uses the SF and DF algorithms defined by Equations (A7) and (A8), respectively.

$$\frac{k}{Z_e} = \frac{G(D; \mu; D_m)}{F(\lambda; \mu; D_m)} \tag{A7}$$

$$DFR = 10\ \log_{10}\left(\frac{F(\lambda_{1;}\mu; D_m)}{F(\lambda_{2;}\mu; D_m)}\right) \tag{A8}$$

The aim of these algorithms is to define a monotonic function that only depends on D_m [10,14,19]. It means that from measurements of k/Ze or DFR we will obtain a value of D_m and then, N_w can be calculated by replacing D_m in (A3) or (A5).

References

1. Sun, Q.; Miao, C.; Duan, Q.; Ashouri, H.; Sorooshian, S.; Hsu, K.-L. A Review of Global Precipitation Data Sets: Data Sources, Estimation, and Intercomparisons. *Rev. Geophys.* **2018**, *56*, 79–107. [CrossRef]
2. Kummerow, C.; Barnes, W.; Kozu, T.; Shiue, J.; Simpson, J. The Tropical Rainfall Measuring Mission (TRMM) Sensor Package. *J. Atmos. Ocean. Technol.* **1998**, *15*, 809–817. [CrossRef]
3. Hou, A.Y.; Kakar, R.K.; Neeck, S.; Azarbarzin, A.A.; Kummerow, C.D.; Kojima, M.; Oki, R.; Nakamura, K.; Iguchi, T. The Global Precipitation Measurement Mission. *Bull. Am. Meteorol. Soc.* **2014**, *95*, 701–722. [CrossRef]
4. Adler, R.F.; Gu, G.; Huffman, G.J.; Sapiano, M.R.; Wang, J.-J. GPCP and the Global Characteristics of Precipitation. *Satell. Precip. Meas.* **2020**, *2*, 677–697.
5. GPM Core Observatory. Available online: https://gpm.nasa.gov/missions/GPM/core-observatory (accessed on 8 April 2024).
6. Liao, L.; Meneghini, R. GPM DPR Retrievals: Algorithm, Evaluation, and Validation. *Remote Sens.* **2022**, *14*, 843. [CrossRef]

7. Tokay, A.; D'Adderio, L.P.; Wolff, D.B.; Petersen, W.A. Development and Evaluation of the Raindrop Size Distribution Parameters for the NASA Global Precipitation Measurement Mission Ground Validation Program. *J. Atmos. Ocean. Technol.* **2020**, *37*, 115–128. [CrossRef]
8. Seela, B.K.; Janapati, J.; Lin, P.-L.; Lan, C.-H.; Huang, M.-Q. Evaluation of GPM DPR Rain Parameters with North Taiwan Disdrometers. *J. Hydrometeorol.* **2023**, *25*, 47–64. [CrossRef]
9. Liao, L.; Meneghini, R.; Tokay, A. Uncertainties of GPM DPR Rain Estimates Caused by DSD Parameterizations. *J. Appl. Meteorol. Climatol.* **2014**, *53*, 2524–2537. [CrossRef]
10. Radhakrishna, B.; Satheesh, S.K.; Narayana Rao, T.; Saikranthi, K.; Sunilkumar, K. Assessment of DSDs of GPM-DPR with Ground-Based Disdrometer at Seasonal Scale over Gadanki, India. *J. Geophys. Res. Atmos.* **2016**, *121*, 11–792. [CrossRef]
11. D'Adderio, L.P.; Porcù, F.; Panegrossi, G.; Marra, A.C.; Sanò, P.; Dietrich, S. Comparison of the GPM DPR Single- and Double-Frequency Products over the Mediterranean Area. *IEEE Trans. Geosci. Remote Sens.* **2019**, *57*, 9724–9739. [CrossRef]
12. Wu, Z.; Zhang, Y.; Zhang, L.; Hao, X.; Lei, H.; Zheng, H. Validation of GPM Precipitation Products by Comparison with Ground-Based Parsivel Disdrometers over Jianghuai Region. *Water* **2019**, *11*, 1260. [CrossRef]
13. Chase, R.J.; Nesbitt, S.W.; McFarquhar, G.M. Evaluation of the Microphysical Assumptions within GPM-DPR Using Ground-Based Observations of Rain and Snow. *Atmosphere* **2020**, *11*, 619. [CrossRef]
14. Del Castillo-Velarde, C.; Kumar, S.; Valdivia-Prado, J.M.; Moya-Álvarez, A.S.; Flores-Rojas, J.L.; Villalobos-Puma, E.; Martínez-Castro, D.; Silva-Vidal, Y. Evaluation of GPM Dual-Frequency Precipitation Radar Algorithms to Estimate Drop Size Distribution Parameters, Using Ground-Based Measurement over the Central Andes of Peru. *Earth Syst. Environ.* **2021**, *5*, 597–619. [CrossRef]
15. Adirosi, E.; Montopoli, M.; Bracci, A.; Porcù, F.; Capozzi, V.; Annella, C.; Budillon, G.; Bucchignani, E.; Zollo, A.L.; Cazzuli, O.; et al. Validation of GPM Rainfall and Drop Size Distribution Products through Disdrometers in Italy. *Remote Sens.* **2021**, *13*, 2081. [CrossRef]
16. Sun, Y.; Dong, X.; Cui, W.; Zhou, Z.; Fu, Z.; Zhou, L.; Deng, Y.; Cui, C. Vertical Structures of Typical Meiyu Precipitation Events Retrieved from GPM-DPR. *J. Geophys. Res. Atmos.* **2020**, *125*, e2019JD031466. [CrossRef]
17. Cramer, W.; Guiot, J.; Fader, M.; Garrabou, J.; Gattuso, J.-P.; Iglesias, A.; Lange, M.A.; Lionello, P.; Llasat, M.C.; Paz, S.; et al. Climate Change and Interconnected Risks to Sustainable Development in the Mediterranean. *Nat. Clim. Change* **2018**, *8*, 972–980. [CrossRef]
18. Kidd, C.; Huffman, G.; Maggioni, V.; Chambon, P.; Oki, R. The Global Satellite Precipitation Constellation: Current Status and Future Requirements. *Bull. Am. Meteorol. Soc.* **2021**, *102*, E1844–E1861. [CrossRef]
19. Seto, S.; Iguchi, T.; Oki, T. The Basic Performance of a Precipitation Retrieval Algorithm for the Global Precipitation Measurement Mission's Single/Dual-Frequency Radar Measurements. *IEEE Trans. Geosci. Remote Sens.* **2013**, *51*, 5239–5251. [CrossRef]
20. Seto, S.; Iguchi, T.; Meneghini, R.; Awaka, J.; Kubota, T.; Masaki, T.; Takahashi, N. The Precipitation Rate Retrieval Algorithms for the GPM Dual-Frequency Precipitation Radar. *J. Meteorol. Soc. Jpn. Ser. II* **2021**, *99*, 205–237. [CrossRef]
21. Iguchi, T.; Seto, S.; Meneghini, R.; Yoshida, N.; Awaka, J.; Le, M.; Chandrasekar, V.; Kubota, T. GPM/DPR Level-2 Algorithm Theoretical Basis Document. 2021. Available online: https://gpm.nasa.gov/sites/default/files/2022-06/ATBD_DPR_V07A.pdf (accessed on 15 May 2024).
22. Seto, S.; Iguchi, T. Intercomparison of Attenuation Correction Methods for the GPM Dual-Frequency Precipitation Radar. *J. Atmos. Ocean. Technol.* **2015**, *32*, 915–926. [CrossRef]
23. Udina, M.; Peinó, E.; Polls, F.; Mercader, J.; Guerrero, I.; Valmassoi, A.; Paci, A.; Bech, J. Irrigation Impact on Boundary Layer and Precipitation Characteristics in Weather Research and Forecasting Model Simulations during LIAISE-2021. *Q. J. R. Meteorol. Soc.* **2024**, 1–23. [CrossRef]
24. González, S.; Bech, J.; Garcia-Benadí, A.; Udina, M.; Codina, B.; Trapero, L.; Paci, A.; Georgis, J.-F. Vertical Structure and Microphysical Observations of Winter Precipitation in an Inner Valley during the Cerdanya-2017 Field Campaign. *Atmos. Res.* **2021**, *264*, 105826. [CrossRef]
25. OTT HydroMet. *Operating Instructions Present Weather Sensor OTT Parsivel 2*; OTT HydroMet: Kempten, Germany, 2016; p. 52.
26. OTT Messtechnik. *Operating Instructions: Present Weather Sensor–Parsivel*; OTT Messtechnik: Kempten, Germany, 2009.
27. Friedrich, K.; Higgins, S.; Masters, F.J.; Lopez, C.R. Articulating and Stationary PARSIVEL Disdrometer Measurements in Conditions with Strong Winds and Heavy Rainfall. *J. Atmos. Ocean. Technol.* **2013**, *30*, 2063–2080. [CrossRef]
28. Casanovas, C.; Salio, P.; Galligani, V.; Dolan, B.; Nesbitt, S.W. Drop Size Distribution Variability in Central Argentina during RELAMPAGO-CACTI. *Remote Sens.* **2021**, *13*, 2026. [CrossRef]
29. Atlas, D.; Srivastava, R.C.; Sekhon, R.S. Doppler Radar Characteristics of Precipitation at Vertical Incidence. *Rev. Geophys.* **1973**, *11*, 1–35. [CrossRef]
30. WMO CODE TABLE 4677. Available online: https://www.nodc.noaa.gov/archive/arc0021/0002199/1.1/data/0-data/HTML/WMO-CODE/WMO4677.HTM (accessed on 8 April 2024).
31. Bringi, V.N.; Chandrasekar, V.; Hubbert, J.; Gorgucci, E.; Randeu, W.L.; Schoenhuber, M. Raindrop Size Distribution in Different Climatic Regimes from Disdrometer and Dual-Polarized Radar Analysis. *J. Atmos. Sci.* **2003**, *60*, 354–365. [CrossRef]
32. Seela, B.K.; Janapati, J.; Lin, P.-L.; Reddy, K.K.; Shirooka, R.; Wang, P.K. A Comparison Study of Summer Season Raindrop Size Distribution between Palau and Taiwan, Two Islands in Western Pacific. *J. Geophys. Res. Atmos.* **2017**, *122*, 11–787. [CrossRef]
33. Ulbrich, C.W.; Atlas, D. Rainfall Microphysics and Radar Properties: Analysis Methods for Drop Size Spectra. *J. Appl. Meteorol. Climatol.* **1998**, *37*, 912–923. [CrossRef]

34. Leinonen, J. High-Level Interface to T-Matrix Scattering Calculations: Architecture, Capabilities and Limitations. *Opt. Express OE* **2014**, *22*, 1655–1660. [CrossRef]
35. Mishchenko, M.I.; Travis, L.D.; Mackowski, D.W. *T*-Matrix Computations of Light Scattering by Nonspherical Particles: A Review. *J. Quant. Spectrosc. Radiat. Transf.* **1996**, *55*, 535–575. [CrossRef]
36. Thurai, M.; Huang, G.J.; Bringi, V.N.; Randeu, W.L.; Schönhuber, M. Drop Shapes, Model Comparisons, and Calculations of Polarimetric Radar Parameters in Rain. *J. Atmos. Ocean. Technol.* **2007**, *24*, 1019–1032. [CrossRef]
37. Pytmatrix/Pytmatrix/Tmatrix_aux.Py at Master·Jleinonen/Pytmatrix. Available online: https://github.com/jleinonen/pytmatrix/blob/master/pytmatrix/tmatrix_aux.py (accessed on 9 February 2024).
38. Hamada, A.; Takayabu, Y.N. Improvements in Detection of Light Precipitation with the Global Precipitation Measurement Dual-Frequency Precipitation Radar (GPM DPR). *J. Atmos. Ocean. Technol.* **2016**, *33*, 653–667. [CrossRef]
39. Silvestro, F.; Rebora, N.; Ferraris, L. An Algorithm for Real-Time Rainfall Rate Estimation by Using Polarimetric Radar: RIME. *J. Hydrometeorol.* **2009**, *10*, 227–240. [CrossRef]
40. Brooks, H.E.; Flora, M.L.; Baldwin, M.E. A Rose by Any Other Name: On Basic Scores from the 2 × 2 Table and the Plethora of Names Attached to Them. *Artif. Intell. Earth Syst.* **2024**, *3*, e230104. [CrossRef]
41. Ghada, W.; Casellas, E.; Herbinger, J.; Garcia-Benadí, A.; Bothmann, L.; Estrella, N.; Bech, J.; Menzel, A. Stratiform and Convective Rain Classification Using Machine Learning Models and Micro Rain Radar. *Remote Sens.* **2022**, *14*, 4563. [CrossRef]
42. Livezey, R.E. Deterministic Forecasts of Multi-Category Events. In *Forecast Verification: A Practitioner's Guide in Atmospheric Science*; Jolliffe, I.T., Stephenson, D.B., Eds.; Willey-Blackwell: West Sussex, UK, 2011; pp. 61–75.
43. Tharwat, A. Classification Assessment Methods. *Appl. Comput. Inform.* **2020**, *17*, 168–192. [CrossRef]
44. Gonzalez, S.; Bech, J. Extreme Point Rainfall Temporal Scaling: A Long Term (1805–2014) Regional and Seasonal Analysis in Spain. *Int. J. Climatol.* **2017**, *37*, 5068–5079. [CrossRef]
45. Peinó, E.; Bech, J.; Udina, M.; Polls, F. Disentangling Satellite Precipitation Estimate Errors of Heavy Rainfall at the Daily and Sub-Daily Scales in the Western Mediterranean. *Remote Sens.* **2024**, *16*, 457. [CrossRef]
46. Adirosi, E.; Roberto, N.; Montopoli, M.; Gorgucci, E.; Baldini, L. Influence of Disdrometer Type on Weather Radar Algorithms from Measured DSD: Application to Italian Climatology. *Atmosphere* **2018**, *9*, 360. [CrossRef]
47. Park, S.-G.; Kim, H.-L.; Ham, Y.-W.; Jung, S.-H. Comparative Evaluation of the OTT PARSIVEL2 Using a Collocated Two-Dimensional Video Disdrometer. *J. Atmos. Ocean. Technol.* **2017**, *34*, 2059–2082. [CrossRef]
48. Dolan, B.; Fuchs, B.; Rutledge, S.A.; Barnes, E.A.; Thompson, E.J. Primary Modes of Global Drop Size Distributions. *J. Atmos. Sci.* **2018**, *75*, 1453–1476. [CrossRef]
49. Bringi, V.N.; Huang, G.-J.; Munchak, S.J.; Kummerow, C.D.; Marks, D.A.; Wolff, D.B. Comparison of Drop Size Distribution Parameter (D0) and Rain Rate from S-Band Dual-Polarized Ground Radar, TRMM Precipitation Radar (PR), and Combined PR–TMI: Two Events from Kwajalein Atoll. *J. Atmos. Ocean. Technol.* **2012**, *29*, 1603–1616. [CrossRef]
50. Bringi, V.N.; Tolstoy, L.; Thurai, M.; Petersen, W.A. Estimation of Spatial Correlation of Drop Size Distribution Parameters and Rain Rate Using NASA's S-Band Polarimetric Radar and 2D Video Disdrometer Network: Two Case Studies from MC3E. *J. Hydrometeorol.* **2015**, *16*, 1207–1221. [CrossRef]
51. Watters, D.C. The Global Precipitation Measurement Mission: Product Validation and Model Evaluation Studies. Ph.D Thesis, University of Leicester, Leicester, UK, 30 November 2021. [CrossRef]
52. Ulbrich, C.W. Natural Variations in the Analytical Form of the Raindrop Size Distribution. *J. Appl. Meteorol. Climatol.* **1983**, *22*, 1764–1775. [CrossRef]
53. Meneghini, R.; Liao, L.; Iguchi, T. A Generalized Dual-Frequency Ratio (DFR) Approach for Rain Retrievals. *J. Atmos. Ocean. Technol.* **2022**, *39*, 1309–1329. [CrossRef]

CHAPTER

6

Conclusions

6.1 Original Contributions

This thesis offers a comprehensive validation of the Global Precipitation Measurement (GPM) satellite products over the Western Mediterranean region. By conducting four specific studies using traditional surface observation data, it provides a deeper understanding of the accuracy of precipitation estimates derived from NASA-JAXA GPM mission products at mid-latitudes. The main contributions of this research are as follows:

- It represents one of the first studies in the Iberian Peninsula that evaluates IMERG products with a detailed focus on orographic and climatic factors, as well as precipitation intensity, at a high temporal resolution.
- This research is among the few that utilize half-hourly resolution data to investigate extreme precipitation events in the Mediterranean region. It also assesses the impact of retrievals obtained from microwave and infrared sensors and their relationship to cloud microphysical characteristics.
- For the first time, it compares IMERG product retrievals with several products from the H SAF program in a study region outside the scope of the Validation Program.
- This is the first validation in a Mediterranean region to evaluate recent updates incorporated in version 7 of the GPM DPR. Precipitation microphysics parameters were thoroughly assessed using a network of disdrometers representing diverse climatic regions.

6.2 Key Findings

The key findings of this thesis related to the Specific Objectives (SO) of the thesis are:

- **SO1: Evaluating the precipitation estimates from the three IMERG (Integrated Multi-satellite Retrievals for GPM) runs (Early, Late, and Final) at various temporal scales (half-hourly, hourly, daily, monthly, seasonal, and annual).**

  IMERG generally captures the spatial and temporal pattern of average annual precipitation, although with discrepancies in the estimated magnitude. At monthly, seasonal, and annual scales, IMERG performs reasonably well, with IMERG Final standing out for a significant reduction in estimation error (2%) compared to IMERG Early and IMERG Late (20%). However, at sub-daily temporal scales, such as half-hourly, there are high bias values and low correlation values, particularly during the summer, indicating that satellite retrievals still face challenges in estimating precipitation at high temporal resolution. Additionally, the underestimation of precipitation values in IMERG Final compared to the other versions is notable, in mountainous areas, when incorporating calibration with GPCC data .

- **SO2. To analyze the IMERG estimates at the highest temporal resolution (30 minutes), considering different orographic features, climatic conditions, and precipitation intensity thresholds, to understand their performance under varying conditions.**

  The high temporal resolution analysis showed that IMERG tends to overestimate precipitation in flat areas and under BSk climates. Orographic (valleys, plains, ridges) and climatic conditions types (BSk, Csa, Csb, Dfb) affected IMERG's performance, with difficulties in identifying extreme events and underestimating intense precipitation. IMERG's ability to identify precipitation events improves at scales greater than a day, but it faces challenges in identifying extreme events at shorter scales and detecting light precipitation that may be influenced by processes such as evaporation not considered by the algorithm. These conclusions highlight the achievements in the detailed evaluation of IMERG at different temporal scales and conditions, as well as the areas that require improvement for greater accuracy in detecting extreme events and in varied orographic and climatic conditions.

- **SO3. To quantify the errors associated with IMERG in estimating heavy rainfall events at daily and sub-daily scales, considering different intensity thresholds, to identify and address sources of error.**

  IMERG products tend to underestimate precipitation as the rainfall intensity threshold and temporal resolution increase. IMERG Late shows no significant advantages over IMERG Early in detecting extreme events. The underestimation is widespread, although less pronounced when direct PMW data are used compared to IR sensor data, which increase the negative bias. High false alarm rates are associated with PMW-direct sensors, while the MORPH+IR combination is linked to higher omission rates of precipitation events. These results suggest that the main sources of error stem from the incorporation of IR sensor data and IMERG's tendency to underestimate intense precipitation, especially at finer temporal scales.

- **SO4. To investigate the impact of the contribution of different sensors to IMERG retrievals and their linkage to the microphysical properties of precipitating cloud tops, focusing on the estimation of heavy rainfall events.**

  The study indicates that IMERG performs better in the presence of ice clouds compared to warm and mixed clouds. Uncertainties in extreme precipitation estimation are related to microphysical characteristics, such as cloud optical thickness (COT) and cloud top effective radius (R_{eff}), especially in warm clouds, which show the worst results. PMW-direct sensors generate high false alarm rates, while the MORPH+IR combination is associated with higher omission rates of precipitation events. These findings highlight the importance of PMW-direct sensors in improving the detection of extreme events and the need to address deficiencies in estimating intense precipitation in warm and mixed clouds.

- **SO5. Comparing the performance of three HSAF products and the Early and Late versions of IMERG in the estimation of extreme precipitation events at hourly and daily scales.**

  The comparison of the three H SAF products (H61, H64, H68) and the Early and Late versions of IMERG, based on hourly and daily precipitation records from 186 rain gauges in the Catalonia region, revealed that, in general, satellite estimates tend to overestimate observed values. This overestimation is more notable in H68 products at hourly scale and in H61 at daily scale. From a quantitative perspective, the results of the KGE, RBIAS, and RMSE metrics indicated that all products have limited capability in estimating hourly precipitation, with modest improvements at daily scale. The H64 product stood out by presenting the lowest errors at the daily scale, while H61 showed a substantial negative bias (-23.37%) at hourly scale. In terms of KGE error distribution, H61 stood out at hourly scale and H64 at daily scale. The ability of satellite products to capture intense precipitation is limited; all products significantly reduce their capacity to detect correct precipitation at thresholds above 2 mm/h and 10 mm/day, with H68 showing the worst errors and the lowest ability to detect high-intensity precipitation. Despite maintaining significant biases, IMERG Late was the best product for detecting extreme precipitation events.

  The overall weak agreement between satellite estimates and ground measurements indicates that while the products may capture extreme precipitation values, they do not always align with observations, limiting their usefulness in hydrometeorological applications and highlighting the need for continued detailed validation efforts to improve the accuracy and effectiveness of precipitation retrieval algorithms.

- **SO6. To evaluate the precipitation intensity, radar reflectivity factors, and drop size distribution (DSD) parameters of GPM's Dual-frequency Precipitation Radar (DPR) Level 2 version 07B considering a network of disdrometers.**

  The study, covering GPM DPR data from March 2014 to November 2023, reveals that the DPR DF algorithm tends to overestimate the mean drop diameter (D_m) by approximately 0.1 mm at low and moderate precipitation rates (0.1–1, 1–2, 2–4 mm/h), and by 0.4 mm at rates above 4 mm/h compared to disdrometers. On the other hand, the intercept parameter (N_w) variable is underestimated by the DPR, showing a maximum value close to 6 dBNw at moderate precipitation rates (4–8 mm/h). Additionally, disdrometer data indicate that the mode of the drop shape parameter (μ) in the study area correspond reasonably well to the fixed DPR value ($\mu = 3$), but the median is higher ($\mu = 7$), showing considerable natural variability that increases uncertainty in DSD estimates based on its constant value assumption.

The validation of spatial matching methods between DPR overpasses and disdrometers highlighted the superiority of the so-called optimal approach, showing that DPR estimates had better verification statistics for radar reflectivity factors in the Ku and Ka bands and mass-weighted mean diameter, while the results were worse for precipitation rate and the intercept parameter. The DPR DF precipitation classification algorithm showed limited ability to detect events identified as convective by the disdrometers in the available sample of 41 overpass matches.

This study is pioneering in the Iberian Peninsula and one of the few conducted in areas with a Mediterranean climate. It is also one of the first evaluations of recent updates incorporated in version 7 of the DPR, which evaluates microphysical parameters. The results provide a deeper understanding of the potential applications and limitations of satellite precipitation observations and can be considered in the development of future satellite precipitation retrievals.

6.3 Main research limitations

A key limitation in this study stems from the inherent challenges in comparing point-based precipitation measurements, such as those from rain gauges or disdrometers, with gridded satellite-derived products. The fundamental difference in spatial scales between the point measurements, which capture precipitation at a single location, and satellite grids, which average precipitation over a larger area, can lead to significant discrepancies. These differences are often exacerbated in regions with high precipitation variability, where localized events may be captured by ground instruments but diluted or missed entirely in the satellite grid. This variability can introduce biases and affect the accuracy of comparisons, making it crucial to consider these limitations when interpreting the results. Understanding and accounting for these discrepancies is essential for accurate analysis and meaningful conclusions in satellite precipitation validation studies.

Another important limitation identified in this research is related to a geolocation error in the IMERG V06 grid code, discovered in the summer of 2022 by the product developers. As shown in Figure 6.1, this error caused IMERG's PMW estimates to be incorrectly geolocated by 0.1° eastward in the latitude band 75°N-S, affecting V06 and all preceding versions. This geolocation error primarily impacts the PMW component of IMERG V06, with its effects propagating through the morphing algorithm, thereby influencing most of the precipitation estimates.

The nature of this error is such that it cannot be corrected in any of the precipitation outputs because it occurs at the initial step of the IMERG algorithm. Consequently, studies utilizing IMERG V06 data are particularly affected by this issue, especially those involving fine-resolution data. The error's impact is more pronounced for GPM PMW constellation sensors with finer footprint sizes, such as GMI and AMSR2. However, analyses using aggregated IMERG data—such as those compiling histograms over time and space—are less affected, as demonstrated by the minimal changes in mean relative bias. Despite the correction in IMERG V07, this limitation is a significant concern for any research relying on V06 or earlier versions, as it introduces biases that cannot be easily mitigated. Specifically, in two of the articles published

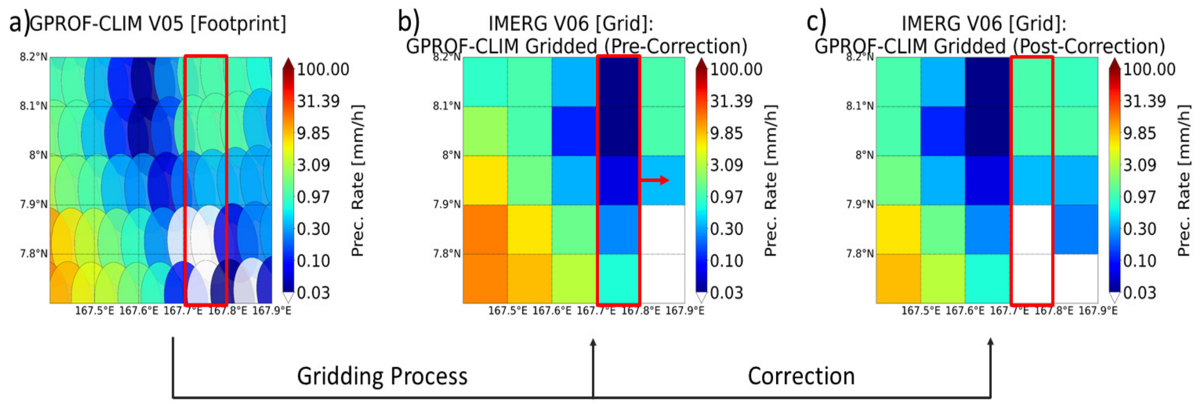

Figure 6.1: An example of the IMERG PMW gridder geolocation error and the necessary correction corresonding to July 12, 2019. a) GPROF climate product (GPROF-CLIM) V05B precipitation estimates computed from the GMI footprint measurements. b) The original gridding of the GPROF-CLIM V05B precipitation estimates by the IMERG V06B algorithm, which includes the geolocation error. c) Corrected version of the IMERG V06B gridding (showing a 0.1° one-pixel shift westward for all grid boxes). The red box highlights cases where the geolocation error in the IMERG gridding is clear; however, note that the one-gridbox offset applies to all gridboxes. Also, note that these gridded values are not yet calibrated, which happens in computing the HQprecipitation variable (Huffman et al., 2023).

in this study (Chapter 3 and Chapter 4), this limitation may have affected some of the calculated statistics, although we consider that, as shown in (Huffman et al., 2023), it does not represent a serious error and should only be taken into account for comparison in future research.

6.4 Future Perspectives

The future of the GPM mission and its associated products is centered on ensuring and expanding the global capability for precipitation observation by leveraging both existing and emerging technologies. While GPM has significantly advanced our understanding of the global cycle of precipitation, the continuation of these observations is critical. As the current satellite constellation ages, with many satellites exceeding their expected operational lifespans, it becomes imperative to develop and deploy new sensors to maintain the quality and continuity of precipitation observations.

Future versions of products like IMERG are expected to incorporate new constellations of low-cost satellites equipped with passive microwave radiometers and advanced radars. This integration will not only enhance spatial and temporal coverage but also improve the accuracy of precipitation estimates, particularly for extreme events and daily variability. Additionally, the inclusion of radars in non-sun-synchronous orbits, such as those in the upcoming GPM-CO mission, will allow for more precise cross-calibrations and consistent data retrieval across different sensors and orbits.

Future precipitation observation missions must address several key challenges. Maintaining a long-term strategy is crucial—not only to ensure the continuity of observations but also to incorporate technological innovations like CubeSats and SmallSats. These smaller, more cost-effective platforms could play a critical role in increasing the frequency and coverage of observations, especially in regions where precipitation exhibits significant temporal and spatial variability. Moreover, mitigation strategies need to be implemented in precipitation retrieval schemes to maximize the use of suboptimal observations and ensure continuous and reliable sampling, even in the event of sensor failure or channel loss.

I am particularly interested in continuing and expanding the use of satellite and in situ observation data to quantify precipitation. While validation exercises for these estimates in different regions and climates remain a core interest of mine, I am eager to explore further. I am especially keen to study the applicability of these data and their potential integration into numerical models to improve short- and long-term predictions of meteorological events. Fundamentally, I aim to investigate how the combination of satellite observations with advanced atmospheric circulation models can enhance the accuracy of extreme precipitation event estimates, such as tropical cyclones, in the context of climate change.

References

Adirosi, E., Montopoli, M., Bracci, A., Porcù, F., Capozzi, V., Annella, C., Budillon, G., Bucchignani, E., Zollo, A. L., Cazzuli, O., Camisani, G., Bechini, R., Cremonini, R., Antonini, A., Ortolani, A., & Baldini, L. (2021). Validation of GPM Rainfall and Drop Size Distribution Products through Disdrometers in Italy [Number: 11 Publisher: Multidisciplinary Digital Publishing Institute]. *Remote Sensing*, *13*(11), 2081. https://doi.org/10.3390/rs13112081

Adirosi, E., Porcù, F., Montopoli, M., Baldini, L., Bracci, A., Capozzi, V., Annella, C., Budillon, G., Bucchignani, E., Zollo, A. L., Cazzuli, O., Camisani, G., Bechini, R., Cremonini, R., Antonini, A., Ortolani, A., Melani, S., Valisa, P., & Scapin, S. (2023). Database of the Italian disdrometer network [Publisher: Copernicus GmbH]. *Earth System Science Data*, *15*(6), 2417–2429. https://doi.org/10.5194/essd-15-2417-2023

Adler, R. F., Sapiano, M. R., Huffman, G. J., Wang, J.-J., Gu, G., Bolvin, D., Chiu, L., Schneider, U., Becker, A., & Nelkin, E. (2018). The Global Precipitation Climatology Project (GPCP) monthly analysis (new version 2.3) and a review of 2017 global precipitation [ISBN: 2073-4433 Publisher: MDPI]. *Atmosphere*, *9*(4), 138. https://doi.org/https://doi.org/10.3390/atmos9040138

Ahrens, C. D. (2015). *Meteorology today: An introduction to weather, climate, and the environment*. Cengage Learning Canada Inc.

Allan, R. P., Barlow, M., Byrne, M. P., Cherchi, A., Douville, H., Fowler, H. J., Gan, T. Y., Pendergrass, A. G., Rosenfeld, D., Swann, A. L. S., Wilcox, L. J., & Zolina, O. (2020). Advances in understanding large-scale responses of the water cycle to climate change [_eprint: https://onlinelibrary.wiley.com/doi/pdf/10.1111/nyas.14337]. *Annals of the New York Academy of Sciences*, *1472*(1), 49–75. https://doi.org/10.1111/nyas.14337

Aonashi, K., Awaka, J., Hirose, M., Kozu, T., Kubota, T., Liu, G., Shige, S., Kida, S., Seto, S., & Takahashi, N. (2009). GSMaP passive microwave precipitation retrieval algorithm: Algorithm description and validation [ISBN: 0026-1165 Publisher: Journal of the Meteorological Society of Japan. Ser. II]. *Journal of the Meteorological Society of Japan. Ser. II*, *87*, 119–136. https://doi.org/https://doi.org/10.2151/jmsj.87A.119

Arkin, P. A., Joyce, R., & Janowiak, J. E. (1994). The estimation of global monthly mean rainfall using infrared satellite data: The GOES precipitation index (GPI) [Publisher: Taylor & Francis _eprint: https://doi.org/10.1080/02757259409532261]. *Remote Sensing Reviews*, *11*(1-4), 107–124. https://doi.org/10.1080/02757259409532261

Bartsotas, N. S., Anagnostou, E. N., Nikolopoulos, E. I., & Kallos, G. (2018). Investigating Satellite Precipitation Uncertainty Over Complex Terrain. *Journal of Geophysical Research: Atmospheres*, *123*(10), 5346–5359. https://doi.org/10.1029/2017JD027559

Battaglia, A., Kollias, P., Dhillon, R., Roy, R., Tanelli, S., Lamer, K., Grecu, M., Lebsock, M., Watters, D., Mroz, K., Heymsfield, G., Li, L., & Furukawa, K. (2020). Spaceborne Cloud and Precipitation Radars: Status, Challenges, and Ways Forward. *Reviews of Geophysics (Washington, D.C.: 1985)*, *58*(3), e2019RG000686. https://doi.org/10.1029/2019RG000686

Bech, J., Codina, B., Lorente, J., & Bebbington, D. (2003). The Sensitivity of Single Polarization Weather Radar Beam Blockage Correction to Variability in the Vertical Refractivity Gradient [Publisher: American Meteorological Society Section: Journal of Atmospheric and Oceanic Technology]. *Journal of Atmospheric and Oceanic Technology*, *20*(6), 845–855. https://doi.org/10.1175/1520-0426(2003)020<0845:TSOSPW>2.0.CO;2

Beck, H. E., Van Dijk, A. I., Levizzani, V., Schellekens, J., Miralles, D. G., Martens, B., & De Roo, A. (2017). MSWEP: 3-hourly 0.25 global gridded precipitation (1979–2015) by merging gauge, satellite, and reanalysis data [ISBN: 1027-5606 Publisher: Copernicus GmbH]. *Hydrology and Earth System Sciences*, *21*(1), 589–615. https://doi.org/https://doi.org/10.5194/hess-21-589-2017

Berg, P., Moseley, C., & Haerter, J. O. (2013). Strong increase in convective precipitation in response to higher temperatures [ISBN: 1752-0908 Publisher: Nature Publishing Group]. *Nature Geoscience*, *6*(3), 181–185. https://doi.org/https://doi.org/10.1038/ngeo1731

Bogerd, L., Leijnse, H., Overeem, A., & Uijlenhoet, R. (2024). Assessing sampling and retrieval errors of GPROF precipitation estimates over the Netherlands [Publisher: Copernicus GmbH]. *Atmospheric Measurement Techniques*, *17*(1), 247–259. https://doi.org/10.5194/amt-17-247-2024

Bringi, V. N., Tolstoy, L., Thurai, M., & Petersen, W. A. (2015). Estimation of Spatial Correlation of Drop Size Distribution Parameters and Rain Rate Using NASA's S-Band Polarimetric Radar and 2D Video Disdrometer Network: Two Case Studies from MC3E [Publisher: American Meteorological Society Section: Journal of Hydrometeorology]. *Journal of Hydrometeorology*, *16*(3), 1207–1221. https://doi.org/10.1175/JHM-D-14-0204.1

Carr, N., Kirstetter, P.-E., Hong, Y., Gourley, J. J., Schwaller, M., Petersen, W., Wang, N.-Y., Ferraro, R. R., & Xue, X. (2015). The Influence of Surface and Precipitation Characteristics on TRMM Microwave Imager Rainfall Retrieval Uncertainty [Publisher: American Meteorological Society Section: Journal of Hydrometeorology]. *Journal of Hydrometeorology*, *16*(4), 1596–1614. https://doi.org/10.1175/JHM-D-14-0194.1

Casellas, E., Bech, J., Veciana, R., Pineda, N., Rigo, T., Miró, J. R., & Sairouni, A. (2021). Surface precipitation phase discrimination in complex terrain. *Journal of Hydrology*, *592*, 125780. https://doi.org/10.1016/j.jhydrol.2020.125780

Ciach, G. J. (2003). Local Random Errors in Tipping-Bucket Rain Gauge Measurements [Publisher: American Meteorological Society Section: Journal of Atmospheric and Oceanic Technology]. *Journal of Atmospheric and Oceanic Technology*, *20*(5), 752–759. https://doi.org/10.1175/1520-0426(2003)20<752:LREITB>2.0.CO;2

Ciach, G. J., & Krajewski, W. F. (1999). Radar–Rain Gauge Comparisons under Observational Uncertainties [Publisher: American Meteorological Society Section: Journal of Applied

Meteorology and Climatology]. *Journal of Applied Meteorology and Climatology*, *38*(10), 1519–1525. https://doi.org/10.1175/1520-0450(1999)038<1519:RRGCUO>2.0.CO;2

Clark, M. P., & Slater, A. G. (2006). Probabilistic Quantitative Precipitation Estimation in Complex Terrain [Publisher: American Meteorological Society Section: Journal of Hydrometeorology]. *Journal of Hydrometeorology*, *7*(1), 3–22. https://doi.org/10.1175/JHM474.1

Colle, B. A., Naeger, A. R., & Molthan, A. (2017). Structure and Evolution of a Warm Frontal Precipitation Band during the GPM Cold Season Precipitation Experiment (GCPEx) [Publisher: American Meteorological Society Section: Monthly Weather Review]. *Monthly Weather Review*, *145*(2), 473–493. https://doi.org/10.1175/MWR-D-16-0072.1

Dolan, B., Fuchs, B., Rutledge, S. A., Barnes, E. A., & Thompson, E. J. (2018). Primary Modes of Global Drop Size Distributions [Publisher: American Meteorological Society Section: Journal of the Atmospheric Sciences]. *Journal of the Atmospheric Sciences*, *75*(5), 1453–1476. https://doi.org/10.1175/JAS-D-17-0242.1

Duchon, C. E., & Essenberg, G. R. (2001). Comparative rainfall observations from pit and aboveground rain gauges with and without wind shields [ISBN: 0043-1397 Publisher: Wiley Online Library]. *Water Resources Research*, *37*(12), 3253–3263. https://doi.org/https://doi.org/10.1029/2001WR000541

Fabry, F. (2018). *Radar meteorology: Principles and practice*. Cambridge University Press. https://doi.org/10.1017/CBO9781107707405

Fennig, K., Schröder, M., Andersson, A., & Hollmann, R. (2020). A fundamental climate data record of SMMR, SSM/I, and SSMIS brightness temperatures [ISBN: 1866-3508 Publisher: Copernicus GmbH]. *Earth System Science Data*, *12*(1), 647–681. https://doi.org/https://doi.org/10.5194/essd-12-647-2020

Funk, C., Peterson, P., Landsfeld, M., Pedreros, D., Verdin, J., Shukla, S., Husak, G., Rowland, J., Harrison, L., & Hoell, A. (2015). The climate hazards infrared precipitation with stations—a new environmental record for monitoring extremes [ISBN: 2052-4463 Publisher: Nature Publishing Group]. *Scientific data*, *2*(1), 1–21. https://doi.org/https://doi.org/10.1038/sdata.2015.66

Gergel, D. R., Nijssen, B., Abatzoglou, J. T., Lettenmaier, D. P., & Stumbaugh, M. R. (2017). Effects of climate change on snowpack and fire potential in the western USA. *Climatic Change*, *141*(2), 287–299. https://doi.org/10.1007/s10584-017-1899-y

Grecu, M., Olson, W. S., Munchak, S. J., Ringerud, S., Liao, L., Haddad, Z., Kelley, B. L., & McLaughlin, S. F. (2016). The GPM Combined Algorithm [Publisher: American Meteorological Society Section: Journal of Atmospheric and Oceanic Technology]. *Journal of Atmospheric and Oceanic Technology*, *33*(10), 2225–2245. https://doi.org/10.1175/JTECH-D-16-0019.1

Haddad, Z. S., Smith, E. A., Kummerow, C. D., Iguchi, T., Farrar, M. R., Durden, S. L., Alves, M., & Olson, W. S. (1997). The TRMM 'day-1'radar/radiometer combined rain-profiling algorithm [ISBN: 0026-1165 Publisher: Meteorological Society of Japan]. *Journal of the Meteorological Society of Japan. Ser. II*, *75*(4), 799–809. https://doi.org/https://doi.org/10.2151/jmsj1965.75.4_799

Harrison, D. L., Driscoll, S. J., & Kitchen, M. (2000). Improving precipitation estimates from weather radar using quality control and correction techniques [ISBN: 1469-8080 Publisher: Cambridge University Press]. *Meteorological Applications*, *7*(2), 135–144. https://doi.org/https://doi.org/10.1017/S1350482700001468

Hong, Y., Hsu, K.-L., Sorooshian, S., & Gao, X. (2004). Precipitation Estimation from Remotely Sensed Imagery Using an Artificial Neural Network Cloud Classification System [Publisher: American Meteorological Society Section: Journal of Applied Meteorology and Climatology]. *Journal of Applied Meteorology and Climatology*, *43*(12), 1834–1853. https://doi.org/10.1175/JAM2173.1

Hou, A. Y., Kakar, R. K., Neeck, S., Azarbarzin, A. A., Kummerow, C. D., Kojima, M., Oki, R., Nakamura, K., & Iguchi, T. (2014). The Global Precipitation Measurement Mission [Publisher: American Meteorological Society Section: Bulletin of the American Meteorological Society]. *Bulletin of the American Meteorological Society*, *95*(5), 701–722. https://doi.org/10.1175/BAMS-D-13-00164.1

Houze, R. A. (1997). Stratiform Precipitation in Regions of Convection: A Meteorological Paradox? [Publisher: American Meteorological Society Section: Bulletin of the American Meteorological Society]. *Bulletin of the American Meteorological Society*, *78*(10), 2179–2196. https://doi.org/10.1175/1520-0477(1997)078<2179:SPIROC>2.0.CO;2

Houze, R. A., McMurdie, L. A., Petersen, W. A., Schwaller, M. R., Baccus, W., Lundquist, J. D., Mass, C. F., Nijssen, B., Rutledge, S. A., Hudak, D. R., Tanelli, S., Mace, G. G., Poellot, M. R., Lettenmaier, D. P., Zagrodnik, J. P., Rowe, A. K., DeHart, J. C., Madaus, L. E., Barnes, H. C., & Chandrasekar, V. (2017). The Olympic Mountains Experiment (OLYMPEX) [Publisher: American Meteorological Society Section: Bulletin of the American Meteorological Society]. *Bulletin of the American Meteorological Society*, *98*(10), 2167–2188. https://doi.org/10.1175/BAMS-D-16-0182.1

Huang, G.-J., Bringi, V. N., Moisseev, D., Petersen, W. A., Bliven, L., & Hudak, D. (2015). Use of 2D-video disdrometer to derive mean density–size and Ze–SR relations: Four snow cases from the light precipitation validation experiment. *Atmospheric Research*, *153*, 34–48. https://doi.org/10.1016/j.atmosres.2014.07.013

Huffman, G. J., Bolvin, D. T., Braithwaite, D., Hsu, K., Joyce, R., Xie, P., & Yoo, S.-H. (2015). NASA global precipitation measurement (GPM) integrated multi-satellite retrievals for GPM (IMERG). https://gpm.nasa.gov/sites/default/files/2020-05/IMERG_ATBD_V06.3.pdf

Huffman, G. J., Bolvin, D. T., Braithwaite, D., Hsu, K.-L., Joyce, R. J., Kidd, C., Nelkin, E. J., Sorooshian, S., Stocker, E. F., Tan, J., Wolff, D. B., & Xie, P. (2020). Integrated Multi-satellite Retrievals for the Global Precipitation Measurement (GPM) Mission (IMERG). In V. Levizzani, C. Kidd, D. B. Kirschbaum, C. D. Kummerow, K. Nakamura, & F. J. Turk (Eds.), *Satellite Precipitation Measurement: Volume 1* (pp. 343–353). Springer International Publishing. https://doi.org/10.1007/978-3-030-24568-9_19

Huffman, G. J., Bolvin, D. T., Joyce, R., Kelley, O. A., Nelkin, E. J., Portier, A., Stocker, E. F., Tan, J., Watters, D. C., & West, B. J. (2023). IMERG V07 Release Notes. https://gpm.nasa.gov/sites/default/files/2024-01/IMERG_V07_ReleaseNotes_231220.pdf

Huffman, G. J., Bolvin, D. T., Nelkin, E. J., Wolff, D. B., Adler, R. F., Gu, G., Hong, Y., Bowman, K. P., & Stocker, E. F. (2007). The TRMM Multisatellite Precipitation Analysis (TMPA): Quasi-Global, Multiyear, Combined-Sensor Precipitation Estimates at Fine Scales [Publisher: American Meteorological Society Section: Journal of Hydrometeorology]. *Journal of Hydrometeorology*, *8*(1), 38–55. https://doi.org/10.1175/JHM560.1

Iguchi, T., Matsui, T., Tao, W.-K., Khain, A. P., Phillips, V. T. J., Kidd, C., L'Ecuyer, T., Braun, S. A., & Hou, A. (2014). WRF–SBM Simulations of Melting-Layer Structure in Mixed-Phase Precipitation Events Observed during LPVEx [Publisher: American Meteorological Society Section: Journal of Applied Meteorology and Climatology]. *Journal of Applied Meteorology and Climatology*, *53*(12), 2710–2731. https://doi.org/10.1175/JAMC-D-13-0334.1

Iguchi, T. (2020). Dual-Frequency Precipitation Radar (DPR) on the Global Precipitation Measurement (GPM) Mission's Core Observatory. In V. Levizzani, C. Kidd, D. B. Kirschbaum, C. D. Kummerow, K. Nakamura, & F. J. Turk (Eds.), *Satellite Precipitation Measurement: Volume 1* (pp. 183–192). Springer International Publishing. https://doi.org/10.1007/978-3-030-24568-9_11

Iguchi, T., Seto, S., Meneghini, R., Yoshida, N., Awaka, J., Le, M., Chandrasekar, V., & Kubota, T. (2021). GPM/DPR level-2 algorithm theoretical basis document [Publisher: Greenbelt]. https://gpm.nasa.gov/resources/documents/gpmdpr-level-2-algorithm-theoretical-basis-document-atbd

Ikuta, Y. (2016). Data assimilation using GPM/DPR at JMA. CAS/JSC WGNE. *Research Activities in Atmospheric and Oceanic Modeling*, 1.11–1.13. https://www.wcrp-climate.org/WGNE/BlueBook/2016/individual-articles/01_Ikuta_Yasutaka_Space_Radar_Assimilation.pdf

IPCC. (2013). Climate Change 2013: The Physical Science Basis. Contribution of Working Group I to the Fifth Assessment Report of the Intergovernmental Panel on Climate Change [Stocker, T.F., D. Qin, G.-K. Plattner, M. Tignor, S.K. Allen, J. Boschung, A. Nauels, Y. Xia, V. Bex and P.M. Midgley (eds.)]. Cambridge University Press, Cambridge, United Kingdom and New York, NY, USA, 1535 pp. https://www.ipcc.ch/site/assets/uploads/2017/09/WG1AR5_Frontmatter_FINAL.pdf

Jensen, M. P., Petersen, W. A., Bansemer, A., Bharadwaj, N., Carey, L. D., Cecil, D. J., Collis, S. M., Genio, A. D. D., Dolan, B., Gerlach, J., Giangrande, S. E., Heymsfield, A., Heymsfield, G., Kollias, P., Lang, T. J., Nesbitt, S. W., Neumann, A., Poellot, M., Rutledge, S. A., ... Zipser, E. J. (2016). The Midlatitude Continental Convective Clouds Experiment (MC3E) [Publisher: American Meteorological Society Section: Bulletin of the American Meteorological Society]. *Bulletin of the American Meteorological Society*, *97*(9), 1667–1686. https://doi.org/10.1175/BAMS-D-14-00228.1

Joyce, R. J., Janowiak, J. E., Arkin, P. A., & Xie, P. (2004). CMORPH: A Method that Produces Global Precipitation Estimates from Passive Microwave and Infrared Data at High Spatial and Temporal Resolution [Publisher: American Meteorological Society Section: Journal of Hydrometeorology]. *Journal of Hydrometeorology*, *5*(3), 487–503. https://doi.org/10.1175/1525-7541(2004)005<0487:CAMTPG>2.0.CO;2

Kidd, C. (2018). NASA global precipitation measurement (GPM) precipitation retrieval and profiling scheme (PRPS). https://pps.gsfc.nasa.gov/Documents/20180203_SAPHIR-ATBD.pdf

Kidd, C., & Huffman, G. (2011). Global precipitation measurement. *Meteorological Applications*, *18*(3), 334–353. https://doi.org/10.1002/met.284

Kidd, C., Huffman, G., Maggioni, V., Chambon, P., & Oki, R. (2021). The Global Satellite Precipitation Constellation: Current Status and Future Requirements [Publisher: American Meteorological Society Section: Bulletin of the American Meteorological Society]. *Bulletin of the American Meteorological Society*, *102*(10), E1844–E1861. https://doi.org/10.1175/BAMS-D-20-0299.1

Kidd, C., & Levizzani, V. (2019). Quantitative precipitation estimation from satellite observations. In *Extreme Hydroclimatic Events and Multivariate Hazards in a Changing Environment* (pp. 3–39). Elsevier. https://doi.org/10.1016/B978-0-12-814899-0.00001-8

Kidd, C., Takayabu, Y. N., Skofronick-Jackson, G. M., Huffman, G. J., Braun, S. A., Kubota, T., & Turk, F. J. (2020). The Global Precipitation Measurement (GPM) Mission. In V. Levizzani, C. Kidd, D. B. Kirschbaum, C. D. Kummerow, K. Nakamura, & F. J. Turk (Eds.), *Satellite Precipitation Measurement: Volume 1* (pp. 3–23). Springer International Publishing. https://doi.org/10.1007/978-3-030-24568-9_1

Kirschbaum, D., & Stanley, T. (2018). Satellite-Based Assessment of Rainfall-Triggered Landslide Hazard for Situational Awareness. *Earth's Future*, *6*(3), 505–523. https://doi.org/10.1002/2017EF000715

Kirschbaum, D. B., Huffman, G. J., Adler, R. F., Braun, S., Garrett, K., Jones, E., McNally, A., Skofronick-Jackson, G., Stocker, E., Wu, H., & Zaitchik, B. F. (2017). NASA's Remotely Sensed Precipitation: A Reservoir for Applications Users [Publisher: American Meteorological Society Section: Bulletin of the American Meteorological Society]. *Bulletin of the American Meteorological Society*, *98*(6), 1169–1184. https://doi.org/10.1175/BAMS-D-15-00296.1

Kochendorfer, J., Rasmussen, R., Wolff, M., Baker, B., Hall, M. E., Meyers, T., Landolt, S., Jachcik, A., Isaksen, K., & Brækkan, R. (2017). The quantification and correction of wind-induced precipitation measurement errors [ISBN: 1027-5606 Publisher: Copernicus GmbH]. *Hydrology and Earth System Sciences*, *21*(4), 1973–1989. https://doi.org/https://doi.org/10.5194/hess-21-1973-2017

Kubota, T., Shige, S., Hashizume, H., Aonashi, K., Takahashi, N., Seto, S., Hirose, M., Takayabu, Y. N., Ushio, T., & Nakagawa, K. (2007). Global precipitation map using satellite-borne microwave radiometers by the GSMaP project: Production and validation [ISBN: 0196-2892 Publisher: IEEE]. *IEEE Transactions on Geoscience and Remote Sensing*, *45*(7), 2259–2275. https://doi.org/10.1109/TGRS.2007.895337

Kummerow, C., Barnes, W., Kozu, T., Shiue, J., & Simpson, J. (1998). The Tropical Rainfall Measuring Mission (TRMM) Sensor Package [Publisher: American Meteorological Society Section: Journal of Atmospheric and Oceanic Technology]. *Journal of Atmospheric and Oceanic Technology*, *15*(3), 809–817. https://doi.org/10.1175/1520-0426(1998)015<0809:TTRMMT>2.0.CO;2

Kummerow, C. D., Randel, D. L., Kulie, M., Wang, N.-Y., Ferraro, R., Munchak, S. J., & Petkovic, V. (2015). The Evolution of the Goddard Profiling Algorithm to a Fully Parametric Scheme [Publisher: American Meteorological Society Section: Journal of Atmospheric and Oceanic Technology]. *Journal of Atmospheric and Oceanic Technology*, *32*(12), 2265–2280. https://doi.org/10.1175/JTECH-D-15-0039.1

Kyriakidis, P. C., Kim, J., & Miller, N. L. (2001). Geostatistical Mapping of Precipitation from Rain Gauge Data Using Atmospheric and Terrain Characteristics [Publisher: American Meteorological Society Section: Journal of Applied Meteorology and Climatology]. *Journal of Applied Meteorology and Climatology*, *40*(11), 1855–1877. https://doi.org/10.1175/1520-0450(2001)040<1855:GMOPFR>2.0.CO;2

Laviola, S., & Levizzani, V. (2011). The 183-WSL fast rain rate retrieval algorithm: Part I: Retrieval design. *Atmospheric Research*, *99*(3), 443–461. https://doi.org/10.1016/j.atmosres.2010.11.013

Laviola, S., Levizzani, V., Cattani, E., & Kidd, C. (2013). The 183-WSL fast rain rate retrieval algorithm. Part II: Validation using ground radar measurements [ISBN: 0169-8095 Publisher: Elsevier]. *Atmospheric research*, *134*, 77–86. https://doi.org/https://doi.org/10.1016/j.atmosres.2013.07.013

Liao, L., Meneghini, R., & Tokay, A. (2014). Uncertainties of GPM DPR Rain Estimates Caused by DSD Parameterizations [Publisher: American Meteorological Society Section: Journal of Applied Meteorology and Climatology]. *Journal of Applied Meteorology and Climatology*, *53*(11), 2524–2537. https://doi.org/10.1175/JAMC-D-14-0003.1

Luini, L., & Capsoni, C. (2012). The impact of space and time averaging on the spatial correlation of rainfall [ISBN: 1944-799X Publisher: AGU]. *Radio Science*, *47*(03), 1–10. https://doi.org/10.1029/2011RS004915

Lundquist, J., Abel, M. R., Gutmann, E., & Kapnick, S. (2019). Our Skill in Modeling Mountain Rain and Snow is Bypassing the Skill of Our Observational Networks [Publisher: American Meteorological Society Section: Bulletin of the American Meteorological Society]. *Bulletin of the American Meteorological Society*, *100*(12), 2473–2490. https://doi.org/10.1175/BAMS-D-19-0001.1

Maggioni, V., & Massari, C. (2018). On the performance of satellite precipitation products in riverine flood modeling: A review. *Journal of Hydrology*, *558*, 214–224. https://doi.org/10.1016/j.jhydrol.2018.01.039

Maggioni, V., Meyers, P. C., & Robinson, M. D. (2016). A Review of Merged High-Resolution Satellite Precipitation Product Accuracy during the Tropical Rainfall Measuring Mission (TRMM) Era [Publisher: American Meteorological Society Section: Journal of Hydrometeorology]. *Journal of Hydrometeorology*, *17*(4), 1101–1117. https://doi.org/10.1175/JHM-D-15-0190.1

Maggioni, V., Nikolopoulos, E. I., Anagnostou, E. N., & Borga, M. (2017). Modeling Satellite Precipitation Errors Over Mountainous Terrain: The Influence of Gauge Density, Seasonality, and Temporal Resolution [Conference Name: IEEE Transactions on Geoscience and Remote Sensing]. *IEEE Transactions on Geoscience and Remote Sensing*, *55*(7), 4130–4140. https://doi.org/10.1109/TGRS.2017.2688998

Maidment, R. I., Allan, R. P., & Black, E. (2015). Recent observed and simulated changes in precipitation over Africa. *Geophysical Research Letters*, *42*(19), 8155–8164. https://doi.org/10.1002/2015GL065765

Manz, B., Páez-Bimos, S., Horna, N., Buytaert, W., Ochoa-Tocachi, B., Lavado-Casimiro, W., & Willems, B. (2017). Comparative Ground Validation of IMERG and TMPA at Variable Spatiotemporal Scales in the Tropical Andes [Publisher: American Meteorological Society Section: Journal of Hydrometeorology]. *Journal of Hydrometeorology*, *18*(9), 2469–2489. https://doi.org/10.1175/JHM-D-16-0277.1

Mugnai, A., Casella, D., Cattani, E., Dietrich, S., Laviola, S., Levizzani, V., Panegrossi, G., Petracca, M., Sanò, P., & Di Paola, F. (2013). Precipitation products from the hydrology SAF [ISBN: 1684-9981 Publisher: Copernicus Publications Göttingen, Germany]. *Natural Hazards and Earth System Sciences*, *13*(8), 1959–1981. https://doi.org/https://doi.org/10.5194/nhess-13-1959-2013

Navarro, A., García-Ortega, E., Merino, A., Sánchez, J. L., Kummerow, C., & Tapiador, F. J. (2019). Assessment of IMERG Precipitation Estimates over Europe [Number: 21 Publisher: Multidisciplinary Digital Publishing Institute]. *Remote Sensing*, *11*(21), 2470. https://doi.org/10.3390/rs11212470

Ng, J. L., Abd Aziz, S., Huang, Y. F., Wayayok, A., & Rowshon, M. (2018). Generation of a stochastic precipitation model for the tropical climate. *Theoretical and Applied Climatology*, *133*(1), 489–509. https://doi.org/10.1007/s00704-017-2202-x

Okamoto, K., Aonashi, K., Kubota, T., & Tashima, T. (2016). Experimental Assimilation of the GPM Core Observatory DPR Reflectivity Profiles for Typhoon Halong (2014) [Publisher: American Meteorological Society Section: Monthly Weather Review]. *Monthly Weather Review*, *144*(6), 2307–2326. https://doi.org/10.1175/MWR-D-15-0399.1

Olson, W. S., Yang, S., Stout, J. E., & Grecu, M. (2007). The Goddard Profiling Algorithm (GPROF): Description and Current Applications. In V. Levizzani, P. Bauer, & F. J. Turk (Eds.), *Measuring Precipitation From Space: EURAINSAT and the Future* (pp. 179–188). Springer Netherlands. https://doi.org/10.1007/978-1-4020-5835-6_14

Palomino-Ángel, S., Anaya-Acevedo, J. A., & Botero, B. A. (2019). Evaluation of 3B42V7 and IMERG daily-precipitation products for a very high-precipitation region in northwestern South America. *Atmospheric Research*, *217*, 37–48. https://doi.org/10.1016/j.atmosres.2018.10.012

Petersen, W. A., Kirstetter, P.-E., Wang, J., Wolff, D. B., & Tokay, A. (2020). The GPM Ground Validation Program. In V. Levizzani, C. Kidd, D. B. Kirschbaum, C. D. Kummerow, K. Nakamura, & F. J. Turk (Eds.), *Satellite Precipitation Measurement: Volume 2* (pp. 471–502). Springer International Publishing. https://doi.org/10.1007/978-3-030-35798-6_2

Petracca, M., D'Adderio, L. P., Porcù, F., Vulpiani, G., Sebastianelli, S., & Puca, S. (2018). Validation of GPM Dual-Frequency Precipitation Radar (DPR) Rainfall Products over Italy [Publisher: American Meteorological Society Section: Journal of Hydrometeorology]. *Journal of Hydrometeorology*, *19*(5), 907–925. https://doi.org/10.1175/JHM-D-17-0144.1

Pradhan, R. K., Markonis, Y., Vargas Godoy, M. R., Villalba-Pradas, A., Andreadis, K. M., Nikolopoulos, E. I., Papalexiou, S. M., Rahim, A., Tapiador, F. J., & Hanel, M. (2022).

Review of GPM IMERG performance: A global perspective. *Remote Sensing of Environment*, *268*, 112754. https://doi.org/10.1016/j.rse.2021.112754

Prakash, S., Mitra, A. K., AghaKouchak, A., Liu, Z., Norouzi, H., & Pai, D. S. (2018). A preliminary assessment of GPM-based multi-satellite precipitation estimates over a monsoon dominated region. *Journal of Hydrology*, *556*, 865–876. https://doi.org/10.1016/j.jhydrol.2016.01.029

Rysman, J.-F., Panegrossi, G., Sanò, P., Marra, A. C., Dietrich, S., Milani, L., & Kulie, M. S. (2018). SLALOM: An All-Surface Snow Water Path Retrieval Algorithm for the GPM Microwave Imager [Number: 8 Publisher: Multidisciplinary Digital Publishing Institute]. *Remote Sensing*, *10*(8), 1278. https://doi.org/10.3390/rs10081278

Saltikoff, E., Friedrich, K., Soderholm, J., Lengfeld, K., Nelson, B., Becker, A., Hollmann, R., Urban, B., Heistermann, M., & Tassone, C. (2019). An Overview of Using Weather Radar for Climatological Studies: Successes, Challenges, and Potential [Publisher: American Meteorological Society Section: Bulletin of the American Meteorological Society]. *Bulletin of the American Meteorological Society*, *100*(9), 1739–1752. https://doi.org/10.1175/BAMS-D-18-0166.1

Sanò, P., Panegrossi, G., Casella, D., Marra, A. C., D'Adderio, L. P., Rysman, J. F., & Dietrich, S. (2018). The Passive Microwave Neural Network Precipitation Retrieval (PNPR) Algorithm for the CONICAL Scanning Global Microwave Imager (GMI) Radiometer. *Remote Sensing*, *10*(7), 1122. https://doi.org/10.3390/rs10071122

Sanò, P., Panegrossi, G., Casella, D., Marra, A. C., Di Paola, F., & Dietrich, S. (2016). The new Passive microwave Neural network Precipitation Retrieval (PNPR) algorithm for the cross-track scanning ATMS radiometer: Description and verification study over Europe and Africa using GPM and TRMM spaceborne radars [ISBN: 1867-1381 Publisher: Copernicus GmbH]. *Atmospheric Measurement Techniques*, *9*(11), 5441–5460. https://doi.org/https://doi.org/10.5194/amt-9-5441-2016

Sapiano, M. R., Berg, W. K., McKague, D. S., & Kummerow, C. D. (2012). Toward an intercalibrated fundamental climate data record of the SSM/I sensors [ISBN: 0196-2892 Publisher: IEEE]. *IEEE Transactions on Geoscience and Remote Sensing*, *51*(3), 1492–1503. https://doi.org/10.1109/TGRS.2012.2206601

Scofield, R. A., & Kuligowski, R. J. (2003). Status and Outlook of Operational Satellite Precipitation Algorithms for Extreme-Precipitation Events [Publisher: American Meteorological Society Section: Weather and Forecasting]. *Weather and Forecasting*, *18*(6), 1037–1051. https://doi.org/10.1175/1520-0434(2003)018<1037:SAOOOS>2.0.CO;2

Seela, B. K., Janapati, J., Lin, P.-L., Lan, C.-H., & Huang, M.-Q. (2023). Evaluation of GPM DPR rain parameters with north Taiwan disdrometers [Publisher: American Meteorological Society Section: Journal of Hydrometeorology]. *Journal of Hydrometeorology*, *-1*(aop). https://doi.org/10.1175/JHM-D-23-0027.1

Shawky, M., Moussa, A., Hassan, Q. K., & El-Sheimy, N. (2019). Performance Assessment of Sub-Daily and Daily Precipitation Estimates Derived from GPM and GSMaP Products over an Arid Environment [Number: 23 Publisher: Multidisciplinary Digital Publishing Institute]. *Remote Sensing*, *11*(23), 2840. https://doi.org/10.3390/rs11232840

Simpson, J., Adler, R. F., & North, G. R. (1988). A Proposed Tropical Rainfall Measuring Mission (TRMM) Satellite [Publisher: American Meteorological Society Section: Bulletin of the American Meteorological Society]. *Bulletin of the American Meteorological Society*, *69*(3), 278–295. https://doi.org/10.1175/1520-0477(1988)069<0278:APTRMM>2.0.CO;2

Skofronick-Jackson, G., Hudak, D., Petersen, W., Nesbitt, S. W., Chandrasekar, V., Durden, S., Gleicher, K. J., Huang, G.-J., Joe, P., Kollias, P., Reed, K. A., Schwaller, M. R., Stewart, R., Tanelli, S., Tokay, A., Wang, J. R., & Wolde, M. (2015). Global Precipitation Measurement Cold Season Precipitation Experiment (GCPEX): For Measurement's Sake, Let It Snow. *Bulletin of the American Meteorological Society*, *96*(10), 1719–1741. https://doi.org/10.1175/BAMS-D-13-00262.1

Skofronick-Jackson, G., Kirschbaum, D., Petersen, W., Huffman, G., Kidd, C., Stocker, E., & Kakar, R. (2018). The Global Precipitation Measurement (GPM) mission's scientific achievements and societal contributions: Reviewing four years of advanced rain and snow observations. *Quarterly Journal of the Royal Meteorological Society*, *144*(S1), 27–48. https://doi.org/10.1002/qj.3313

Skofronick-Jackson, G., Petersen, W. A., Berg, W., Kidd, C., Stocker, E. F., Kirschbaum, D. B., Kakar, R., Braun, S. A., Huffman, G. J., & Iguchi, T. (2017). The Global Precipitation Measurement (GPM) mission for science and society [ISBN: 0003-0007 Publisher: American Meteorological Society]. *Bulletin of the American Meteorological Society*, *98*(8), 1679–1695.

Sorooshian, S., Hsu, K.-L., Gao, X., Gupta, H. V., Imam, B., & Braithwaite, D. (2000). Evaluation of PERSIANN System Satellite-Based Estimates of Tropical Rainfall [Publisher: American Meteorological Society Section: Bulletin of the American Meteorological Society]. *Bulletin of the American Meteorological Society*, *81*(9), 2035–2046. https://doi.org/10.1175/1520-0477(2000)081<2035:EOPSSE>2.3.CO;2

Tan, J., Cho, N., Oreopoulos, L., & Kirstetter, P. (2022). Evaluation of GPROF V05 Precipitation Retrievals under Different Cloud Regimes [Publisher: American Meteorological Society Section: Journal of Hydrometeorology]. *Journal of Hydrometeorology*, *23*(3), 389–402. https://doi.org/10.1175/JHM-D-21-0154.1

Tan, J., Petersen, W. A., Kirstetter, P.-E., & Tian, Y. (2017). Performance of IMERG as a Function of Spatiotemporal Scale [Publisher: American Meteorological Society Section: Journal of Hydrometeorology]. *Journal of Hydrometeorology*, *18*(2), 307–319. https://doi.org/10.1175/JHM-D-16-0174.1

Tan, J., Petersen, W. A., & Tokay, A. (2016). A Novel Approach to Identify Sources of Errors in IMERG for GPM Ground Validation [Publisher: American Meteorological Society Section: Journal of Hydrometeorology]. *Journal of Hydrometeorology*, *17*(9), 2477–2491. https://doi.org/10.1175/JHM-D-16-0079.1

Trenberth, K. E., Fasullo, J. T., & Kiehl, J. (2009). Earth's Global Energy Budget [Publisher: American Meteorological Society Section: Bulletin of the American Meteorological Society]. *Bulletin of the American Meteorological Society*, *90*(3), 311–324. https://doi.org/10.1175/2008BAMS2634.1

Ushio, T., Sasashige, K., Kubota, T., Shige, S., Okamoto, K., Aonashi, K., Inoue, T., Takahashi, N., Iguchi, T., & Kachi, M. (2009). A Kalman filter approach to the Global Satellite Mapping of Precipitation (GSMaP) from combined passive microwave and infrared radiometric data. *Journal of the Meteorological Society of Japan. Ser. II*, *87*, 137–151. https://doi.org/https://doi.org/10.2151/jmsj.87A.137

Watters, D. C. (2021). *The Global Precipitation Measurement Mission: Product Validation and Model Evaluation Studies* [Doctoral dissertation, University of Leicester]. https://doi.org/10.25392/leicester.data.17099396.v1

Wentz, F. J., & Draper, D. (2016). On-Orbit Absolute Calibration of the Global Precipitation Measurement Microwave Imager [Publisher: American Meteorological Society Section: Journal of Atmospheric and Oceanic Technology]. *Journal of Atmospheric and Oceanic Technology*, *33*(7), 1393–1412. https://doi.org/10.1175/JTECH-D-15-0212.1

Xie, W., Yi, S., Leng, C., Xia, D., Li, M., Zhong, Z., & Ye, J. (2022). The evaluation of IMERG and ERA5-Land daily precipitation over China with considering the influence of gauge data bias [Publisher: Nature Publishing Group]. *Scientific Reports*, *12*(1), 8085. https://doi.org/10.1038/s41598-022-12307-0

Note: References listed here refer to those quoted in the text but do not include those quoted in the three articles and the preprint (to see those, please refer to the corresponding article reference sections)

CHAPTER

A

Contributions

This chapter includes a list of the contributions and relevant activities carried out during the predoctoral period.

A.1 Peer-reviewed Papers

- Méndez, B., Saenz, E., Pires, Ó., Cantero, E., Bech, J., Polls, F., Peinó, E., Udina, M., and Garcia-Benadí, A. (2024). Experimental campaign for the characterization of precipitation in a complex terrain site using high resolution observations. Journal of Physics: Conference Series, 2767(4), 042016. https://doi.org/10.1088/1742-6596/2767/4/042016

- Peinó, E., Bech, J., and Udina, M. (2022). Performance assessment of GPM IMERG products at different time resolutions, climatic areas and topographic conditions in Catalonia. Remote Sensing, 14(20), 5085: https://doi.org/10.3390/rs14205085.

- Peinó, E., Bech, J., Udina, M., and Polls, F. (2024). Disentangling Satellite Precipitation Estimate Errors of Heavy Rainfall at the Daily and Sub-Daily Scales in the Western Mediterranean. Remote Sensing, 16(3), 457: https://doi.org/10.3390/rs16030457.

- Udina, M., Peinó, E., Polls, F., Mercader, J., Guerrero, I., Valmassoi, A., Paci, A., and Bech, J. (2024). Irrigation impact on boundary layer and precipitation characteristics in WRF model simulations during LIAISE-2021. Quarterly Journal of the Royal Meteorological Society: https://doi.org/10.1002/qj.4756.

- Peinó, E., Bech, J., Polls, F., Udina, M., Petracca, M., Adirosi, E., Gonzalez, S., Boudevillain, B., 2024. Validation of GPM DPR rainfall and Drop Size Distributions using disdrometer observations in the Western Mediterranean. Remote Sensing 16, 2594: https://doi.org/10.3390/rs16142594.

A.2 Research Stays

- (3-months) Institute of Atmospheric Sciences and Climate (CNR-ISAC), Rome, Italy. Financed by the Montcelimar Foundation.

A.3 Conference presentations

- **Peinó, E.**, Bech, J., Polls, F., Udina, M., Petracca, M., Adirosi, E., Gonzalez, S., and Boudevillain, B.: Validation of GPM DPR rainfall and Drop Size Distribution through disdrometers in the Northeastern Iberian Peninsula, EMS Annual Meeting 2024, Barcelona, Spain, 1–6 Sep 2024, EMS2024-503, https://doi.org/10.5194/ems2024-503,2024.
- **Bech, J.**, García-Benadí, A., Udina, M., Polls, F., Peinó, E., Paci, A., and Boudevillain, B.: A case study of rainfall evaporation using a simple drop size distribution column model and Micro Rain Radar observations, EMS Annual Meeting 2024, Barcelona, Spain, 1–6 Sep 2024, EMS2024-352, https://doi.org/10.5194/ems2024-352,2024.
- **Polls, F.**, Peinó, E., Udina, M., and Bech, J.: Investigating ground-level relative humidity and radar reflectivity using C-band weather radar observations in two contiguous irrigated and rainfed areas, EMS Annual Meeting 2024, Barcelona, Spain, 1–6 Sep 2024, EMS2024-453, https://doi.org/10.5194/ems2024-453,2024.
- **Udina, M.**, Peinó, E., Polls, F., Mercader, J., Guerrero, I., Valmassoi, A., Paci, A., and Bech, J.: Irrigation impact on boundary layer and precipitation in WRF model simulations (LIAISE-2021), EMS Annual Meeting 2024, Barcelona, Spain, 1–6 Sep 2024, EMS2024-78, https://doi.org/10.5194/ems2024-78,2024.
- **Bech, J.**, Garcia-Benadí, A., Udina, M., Polls, F., Peinó, E., Balagué, M., Paci, A., and Boudevillain, B. (2024, January). Analysis of Rainfall Characteristics and Evaporation Processes using Vertically Pointing Doppler Radars during the LIAISE Field Campaign. In 104th AMS Annual Meeting. AMS.
- **Peinó, E.**: How well can IMERG products capture precipitation events over Catalonia? (jun-2023). In VI Jornada de Joves Investigadors de l'IdRA, Universitat de Barcelona.
- **Udina, M.**, Peinó, E., Bech, J., Polls, F., Mercader, and J., Guerrero: Boundary layer and precipitation changes by introducing irrigation parameterization in WRF, 9th International Conference on Meteorology and Climatology of the Mediterranean, Genoa, Italy, 22/05/2023–24/05/2023.
- **Bech, J.**, Udina, M., Peinó, E., Polls, F., García-Benadí, A., and Balagué, M.: Precipitation observations and simulations during the LIAISE-2021 field campaign, EGU General Assembly 2023, Vienna, Austria, 24–28 Apr 2023, EGU23-9890, https://doi.org/10.5194/egusphere-egu23-9890, 2023.
- **Peinó, E.**, Bech, J., and Udina, M.: Dependence of GPM IMERG products on precipitation intensity in Catalonia., EGU General Assembly 2023, Vienna, Austria, 24–28 Apr 2023, EGU23-12109, https://doi.org/10.5194/egusphere-egu23-12109, 2023.
- **Udina, M.**, Bech, J., Peinó, E., and Mercader, J. (2022). Irrigation Impact on Precipitation Forecasts During the LIAISE-2021 Field Campaign (No. EMS2022-613). Copernicus Meetings.

- **Udina, M.**, Bech, J., Peinó, E., Polls, F., and Balagué, M. (2022). Precipitation characteristics and related boundary-layer processes during LIAISE 2021 (No. EMS2022-674). Copernicus Meetings.

- Bech, J., Udina, M., and **Peinó, E.**: Preliminary results of irrigation impact on precipitation forecasts during the LIAISE-2021 field campaign, EGU General Assembly 2022, Vienna, Austria, 23–27 May 2022, EGU22-10647, https://doi.org/10.5194/egusphere-egu22-10647, 2022.

- **Peinó, E.**, Bech, J., and Udina, M.: Assessment of GPM- IMERG precipitation products over Catalonia at different time resolutions, EGU General Assembly 2022, Vienna, Austria, 23–27 May 2022, EGU22-2933, https://doi.org/10.5194/egusphere-egu22-2933, 2022.

- **Peinó, E.**: Assessment of GPM- IMERG precipitation products over Catalonia. (jun-2022). In V Jornada de Joves Investigadors de l'IdRA, Universitat de Barcelona.

A.4 Posters

- **Peinó, E.**, Bech, J., Polls, F., Udina, M., Petracca, M., Adirosi, E., Gonzalez, S., and Boudevillain, B.:An evaluation of satellite GPM-DPR precipitation estimates with ground-based disdrometers in a Mediterranean region. 12th European Conference on Radar in Meteorology and Hydrology. 09/09/2024 – 13/09/2024, Rome, Italy

- **Peinó, E.**, Bech, J., Udina, M. and Polls, F. Satellite Precipitation Estimates of Heavy Rainfall Events at Daily and Sub-daily Scales Compared with a Dense Rain Gauge Network. 104th AMS Annual Meeting. 28/01/2024 – 01/02/2024. Baltimore, Maryland, US

- **Peinó, E.**, Bech, J., and Udina, M. Half-hourly evaluation of GPM-IMERG precipitation products using rain-gauge precipitation products in Catalonia. 11th European Conference on Radar in Meteorology and Hydrology. 29/08/2022 – 02/09/2022, Locarno, Switzerland

- **Peinó, E.**, Bech, J., and Udina, M. Assessment of IMERG products on Catalonia: preliminary results. XXVII Jornades de meteorologia Eduard Fontserè. 27/11/2021. Barcelona, Spain

A.5 Relevant Training Courses

- International Autumn School on Satellites Data Applications. Organized by Hellenic National Meteorological Service and EUMETSAT, Athens, Greece, 23/10/2023 – 27/10/2023.

- International School on Applications with the Newest Multi-spectral Environmental Satellites. Hosted by the Italian Operational Center for Meteorology (COMet) and supported by EUMETSAT, Ostia, Italy, 20/06/2023–28/06/2023.

- 1st MedCyclones workshop and trainning school. University of Athenas, Greece, 27/06/2022 – 02/07/2022.

- Advanced remote sensing techniques for risk managment. Spring School 2021 (virtual) Instituto de Altos Estudios Espaciales “Mario Gulich” (IG), Universidad Nacional de Córdoba (UNC). Comisión Nacional de Actividades Espaciales (CONAE), 20/09/2021 – 24/09/2021.
- Data Scientist (big data analyst and data scientist). Consorci per a la Formació Contínua de Catalunya, Catalonia, Spain, 28/03/2022–13/06/2022.

A.6 Teaching

- History and Instrumentation (2 hours). Curse 21-22, 22-23, 23-24. Astronomy and Meteorology. University of Experience, University of Barcelona
- Meteorology and climatology (64 hours). Curse 22-23. Degree in Physics, University of Barcelona
- Instrumentation workshop (2 hours). Degree in Physics, University of Barcelona
- Physics experiments: Invisible light (8 hours). Faculty of physics, University of Barcelona